

Replication of Functional Polymeric Micro- and Nanostructures



TU Dortmund
Fakultät Elektrotechnik und Informationstechnik
Arbeitsgebiet Mikrostrukturtechnik

Dissertation
zur Erlangung des akademischen Grades
Doktor der Ingenieurwissenschaften

von
MSc. MNT, Christian Rytka
Bad Säckingen

Tag der mündlichen Prüfung: 15. April 2016

Hauptreferent: Prof. Dr. Andreas Neyer
Korreferent: Prof. Dr. Per Magnus Kristiansen

Abstract

Surfaces of polymer products are increasingly being functionalized with micro- and nanostructures using mass replication techniques such as injection moulding. The complex transcription process requires a deep understanding of material and process interrelations in order to accurately replicate the desired functional structures over many hundreds of thousands of production cycles. The goal of this thesis was the investigation of differences in filling and demoulding behaviour of macro-, micro-, and nanostructures, focussing on the influences of the type of injection moulding process, processing parameters and polymer properties. For this purpose the replication quality of functional structures was investigated using four different moulding processes employing polymers differing in rheology and wetting behaviour. Representative 2D and 3D micro- and nanostructures were transferred into various mould insert materials (nickel, brass, steel and high performance polymers) and replicated by iso- and variothermal injection moulding with and without compression and compared with filling simulations. Importantly, it was found that a parallel compression phase reduces the internal pressure and stresses in the cavity leading to less demoulding damage but without significant influence on replication fidelity. Moreover, variothermal heating was favourable especially for filling of high aspect ratio structures. However, clear differences in replication were shown between the glass transition and no-flow temperature as upper mould temperature, also in context of the influence of holding pressure.

With regards to geometric correlations, a parabolic relationship is demonstrated between the replicated height and the structure width for the replication of microstructures. On this scale, the polymer melt viscosity is clearly more relevant than capillary effects as flow resistance and frozen layer formation are the main reasons for incomplete filling. On the nanoscale, capillary effects become increasingly dominant depending on the surface energy of the polymer and the parabolic correlation is superimposed by wetting phenomena.

The dewetting potential Ω_s of a polymer is proposed as a simple rationale for estimation of the replicability. The value of Ω_s was determined by integrating the spreading coefficient over the range from melt processing temperature to no-flow temperature. Ω_s correlates well with the replicated height for four different structures covering both the micro and the nano range for different mould surfaces and polymers with different spreading coefficients. It is clearly shown that a lower Ω_s leads to a better replication accuracy.

As flow simulations can cut down both costs and time for the development of polymer parts with functional surfaces, experimental trials were compared with detailed 3D multiscale Moldflow simulations. Additionally, thermal transfer and 2D filling simulations were carried out with Comsol. By adjusting the heat transfer coefficient and the transition temperature it was possible both for micro- and nanostructures to achieve a good correlation with experimental findings at different processing conditions. The macroscopic model with a microstructure can be scaled down in volume and number of elements to save computational time as long as boundary conditions such as the flow front speed are correctly transferred.

Finally, the developed knowledge of the filling and demoulding, focussing on heat transfer and no-flow temperature was successfully applied to the reproducible production of nanostructured samples for cell growth tests, and a fast prototyping method based on pattern transfer onto high performance polymer inserts was established.

The novel experimental and simulated findings about micro- and nanostructure replication provide a valuable contribution to the development of injection moulded surface-structured polymeric products in the areas of life science and optics / photonics.

Kurzfassung

Die Oberflächen von Kunststoffprodukten werden zunehmend mit Mikro- und Nanostrukturen funktionalisiert. Als etablierte Massenverarbeitungsmethode bietet sich hierfür das Spritzgießverfahren an. Jedoch ist für die Replikation der Strukturen ein tieferes Verständnis der Zusammenhänge zwischen Material und Prozess nötig. Aus diesem Grund war das Ziel dieser Dissertation, Unterschiede in der Ab- und Entformung von Makro- im Vergleich zu Mikro- und Nanostrukturen, mit Fokus auf dem Einfluss von Prozessen, Verarbeitungsparametern und Polymereigenschaften zu untersuchen. Die Abformqualität dieser Strukturen wurde deshalb zwischen vier verschiedenen Spritzgussverfahren mit Polymeren unterschiedlicher Viskosität und unterschiedlichem Benetzungsverhalten verglichen. Hierfür wurden repräsentative 2D und 3D Strukturen mittels iso- und variothermem Spritzgießen/-prägen repliziert und mit detaillierten FEM-Füllsimulationen verglichen.

Als ein wichtiger Prozesseinfluss stellte sich heraus, dass durch die geringeren Spannungen und Drücke beim Spritzprägen im Vergleich zum klassischen Spritzguss, vor allem Entformungsprobleme reduziert werden können, allerdings ohne nennenswerten Einfluss auf die erreichte Abformhöhe. Eine variotherme Temperierung ist vorteilhaft bei Strukturen mit hohem Aspekt-Verhältnis. Es zeigten sich dabei klare Unterschiede in der Replizierbarkeit zwischen Glasübergangs- und No-flow Temperatur als obere Werkzeugtemperatur im Moment des Einspritzens, insbesondere auch im Zusammenhang mit der Wirkungszeit des Nachdrucks.

In Bezug auf geometrische Zusammenhänge wurde gezeigt, dass zwischen abgeformter Höhe und Strukturbreite eine quadratische Abhängigkeit bei der Replikation von Mikrostrukturen besteht. Auf dieser Skala spielt die Schmelzeviskosität des Polymers eine dominante Rolle, da der Fließwiderstand und die Bildung einer erstarrten Randschicht die Hauptgründe für eine unvollständige Füllung sind, während für Nanostrukturen der Kapillareffekt zusätzlich an Bedeutung gewinnt und der quadratische Zusammenhang durch Benetzungseffekte überlagert wird.

Das Entzernetzungspotential von Polymeren Ω_s wird deshalb zur einfachen Abschätzung der Replizierbarkeit vorgeschlagen und wurde durch Integrieren des Spreitkoeffizienten im Bereich zwischen Schmelze- und No-flow Temperatur ermittelt. Ω_s korreliert mit der abgeformten Höhe verschiedener Strukturen auf der Nano- und Mikroskala sowohl für verschiedene Werkzeugoberflächen, als auch für Polymere mit unterschiedlichen Spreitkoeffizienten. Es wird klar aufgezeigt, dass ein niedriges Ω_s mit guter Abformtreue korreliert.

Die Verwendung von Fließsimulationen bietet das Potential, Kosten und Zeit für die Entwicklung von Kunststoffbauteilen mit funktionellen Strukturen zu reduzieren. Aus diesem Grund wurden Spritzversuche mit 3D Moldflow Füllsimulationen verglichen. Zusätzlich wurden Wärmetransfer- und 2D Füllsimulationen mit Comsol durchgeführt. Durch Anpassung des Wärmeübergangskoeffizienten und der Übergangstemperatur ist es möglich, sowohl für Mikro- als auch für Nanostrukturen eine gute Korrelation mit den Experimenten für verschiedene Prozessbedingungen zu erzielen. Um Rechenzeit zu sparen, kann das Volumen und die Anzahl der Elemente des makroskopischen Modells reduziert werden, unter der Voraussetzung, dass Randbedingungen wie die Fließfrontgeschwindigkeit entsprechend korrekt übertragen werden.

Abschließend wurde das erarbeitete Wissen zum Füll- und Entformungsverhalten, insbesondere im Hinblick auf Wärmetransfer und No-flow Temperatur, erfolgreich auf die reproduzierbare Herstellung von nanostrukturierten Musterbauteilen für Zellwachstumsversuche angewendet. Hierfür wurde eine Methode zur schnellen Strukturübertragung für Kleinserien, basierend auf Inserts aus Hochleistungsthermoplasten, demonstriert.

Die neu gewonnenen Erkenntnisse aus Experimenten und Simulationen zur Abformung von Mikro- und Nanostrukturen liefern einen wertvollen Beitrag zur Entwicklung von z.B. spritzgegossenen oberflächenstrukturierten Produkten für Anwendungen in den Bereichen Life Science und Optik/Photonik.

Je (unendlich) kleiner die Dinge werden,
umso näher kommen sie ihrer eigenen (unendlichen) Perfektion.

Diese Arbeit ist meiner Frau Rafaela und meiner Tochter Merle gewidmet.

Danksagung

Vielen Dank an alle, die mich bei meiner Dissertation unterstützt haben. In der heutigen Zeit ist es wohl kaum mehr möglich, völlig eigenständig gute wissenschaftliche Resultate hervorzubringen.

Ganz herzlich möchte ich mich deshalb bei meinen beiden Betreuern Prof. Dr. Andreas Neyer und Prof. Dr. Per Magnus Kristiansen für die ausgezeichnete Betreuung und wichtigen Tipps zur richtigen Zeit bedanken.

Außerdem danke ich Prof. Clemens Dransfeld und Prof. Dr. Jens Gobrecht, die alle administrativen Hürden aus dem Weg geräumt haben, damit es mir möglich war, eine Dissertation "on the job" überhaupt durchzuführen. In diesem Zusammenhang danke ich auch Prof. Jürg Christener und Prof. Rainer Schnaidt, die das FHNW-Exzellenzprogramm zur Finanzierung meiner Dissertation letztendlich bewilligt haben. Einen besonderen Dank an Dr. Helmut Schift, der mir regelmäßig wertvolle Ideen gab und mir meine Konferenzvorträge an der DTU in Dänemark und an der Mahatma Gandhi University in Indien ermöglichte.

Einen großen Dank auch an alle meine Kollegen, insbesondere an Dr. Sonja Neuhaus, Oskar Häfeli, Daniel Zürcher, Dr. Kunal Masania, an meine Praktikanten, insbesondere an Nadia Opara, Ruut Kummala und Steffen Fagerland und an meine Studenten, vor allem Simon Aubry, Christian Sager und Pascal Krämer, die mich bei der Erstellung meiner Arbeit unterstützt haben. Roger Bischofberger möchte ich für die Herstellung der Nickelinserts danken, Dr. Celestino Padeste für die Antihafbeschichtungen. Dr. Harun Solak danke ich für den Phable Insert, Dr. Jörn Lungershausen für die gelagerten Mikrostrukturen und Dr. Felix Holzer und Dr. Philip Paul für die 3D Nanostrukturen. Nis Korsgaard Andersen und Rebecca Huber danke ich für die inspirierende Zusammenarbeit, Evelyn Drabiniok für die guten Diskussionen in Dortmund und den schönen Doktor-Hut. Regina Neugebauer möchte ich für die Unterstützung bei den rheologischen Messungen und Bruno Manhart für die Hilfe mit Moldflow danken.

Schließlich danke ich auch meiner Frau Rafaela und meiner Tochter Merle, die mich während zahlreicher Wochenenden und Ferien mit meinem Laptop teilen mussten.

Eidesstattliche Versicherung

In Kenntnis der Bedeutung einer eidesstattlichen Versicherung und der Strafbarkeit der Abgabe einer falschen eidesstattlichen Versicherung versichere ich hiermit an Eides statt, dass ich die vorliegende Dissertation mit dem Titel

Replication of Functional Polymeric Micro- and Nanostructures

selbstständig und ohne unzulässige fremde Hilfe angefertigt habe. Ich habe keine anderen als die angegebenen Quellen und Hilfsmittel benutzt sowie wörtliche und sinngemäße Zitate kenntlich gemacht.

Bad Säckingen,
10. August 2016



Ort, Datum

Unterschrift

Table of Contents:

Abstract	I
Acknowledgements	II
1. INTRODUCTION.....	1
1.1 MOTIVATION: APPLICATIONS WITH POLYMERIC MICRO- AND NANOSTRUCTURES	1
1.1.1 <i>Sensors and microfluidic devices</i>	1
1.1.2 <i>Surface cell interactions</i>	2
1.1.3 <i>Bionic structures: Biomimetic modification of polymeric surfaces</i>	3
1.1.4 <i>Optical structures: Diffraction, reflection and diffusion of light</i>	4
1.2 SCOPE OF RESEARCH AND OBJECTIVES.....	4
1.3 STATE-OF-THE-ART	6
1.3.1 <i>Manufacturing of micro- and nanostructured moulds</i>	6
1.3.2 <i>Influences on the replication fidelity</i>	7
1.4 STRUCTURE OF THE THESIS	10
2. FUNDAMENTALS.....	11
2.1 POLYMER MOLECULE SIZE IN COMPARISON TO NANOSTRUCTURES	11
2.2 RHEOLOGY OF POLYMERS	12
2.2.1 <i>Melt temperature - viscous thermal dissipation</i>	14
2.2.2 <i>Wall boundaries and micro-viscosity</i>	15
2.3 WETTING BEHAVIOUR AT THE POLYMER/MOULD INTERFACE	16
2.4 PRESSURES AND FORCES IN MICRO- AND NANOSTRUCTURES	17
2.5 HEAT TRANSFER PROCESS IN INJECTION MOULDING	17
3. MATERIALS AND METHODS	19
3.1 POLYMERS AND POLYMER PROPERTIES	19
3.1.1 <i>General description of the polymers used for injection moulding</i>	19
3.1.2 <i>General and mechanical properties</i>	21
3.1.3 <i>Thermal and processing relevant properties</i>	22
3.1.4 <i>Rheological properties</i>	25
3.2 POLYMER AND STRUCTURE ANALYSIS	27
3.2.1 <i>No-flow temperature measurement</i>	27
3.2.2 <i>Surface tension measurements</i>	28
3.2.3 <i>Microscope structure analysis</i>	30
3.3 INJECTION MOULDING MACHINE, MOULD AND SENSORS.....	30
3.3.1 <i>Temperature and pressure sensors</i>	32
3.3.2 <i>Dynamic heating: Variothermal process control</i>	33
3.3.3 <i>Online viscosity measurements with pressure and temperature sensors</i>	34
3.4 ISO- AND VARIOTHERMAL INJECTION (COMPRESSION) MOULDING PROCESS	36
3.4.1 <i>Forces and pressures in the compression moulding cycle</i>	37
3.4.2 <i>Processing parameters</i>	38
3.5 GENERAL OVERVIEW OF MOULD MASTER INSERTS	39

4. PROCESS VARIATIONS: ISO- AND VARIOTHERMAL INJECTION (COMPRESSION) MOULDING.....	41
4.1 INJECTION MOULDING PROCESSES.....	41
4.2 MOULD MASTER INSERTS: STRUCTURE DESIGN AND FABRICATION TECHNOLOGY	41
4.2.1 <i>V-groove microstructures</i>	41
4.2.2 <i>Nickel inserts produced by mask based displacement Talbot UV photolithography</i>	42
4.2.3 <i>Nickel insert produced by thermal scanning probe lithography and electroplating</i>	44
4.3 PROCESSING PARAMETERS	45
4.4 POLYMERS AND POLYMER PROPERTIES	47
4.5 PRE-TRIALS: REPLICATION OF MACROSTRUCTURES & VARIATION OF MOULD TEMP.	49
4.5.1 <i>Replication of macro-grooves and pillars</i>	49
4.5.2 <i>Dependence of microstructure replication fidelity on mould temperature</i>	51
4.6 RESULTS & DISCUSSION: VARIATION OF MOULDING PROCESSES & STRUCT. GEOMETRIES..	52
4.6.1 <i>Pressure and frozen-in stresses</i>	52
4.6.2 <i>Replication of v-groove microstructure: Variation of processes and materials</i>	53
4.6.3 <i>Calculation of filling resistance and capillary force in the microstructure</i>	56
4.6.4 <i>Large - area transcription from Ni-pillars to polymer holes</i>	57
4.6.5 <i>Transcription of Ni 3D nanostructures</i>	63
4.6.6 <i>Transcription of Ni nanolines</i>	65
4.6.7 <i>Capillary and flow resistance regime depending on aspect ratio</i>	68
4.7 CONCLUSIONS.....	70
5. ON THE ROLE OF WETTING, STRUCTURE WIDTH AND FLOW CHARACTERISTICS IN POLYMER REPLICATION.....	71
5.1 MATERIALS AND METHODS	71
5.1.1 <i>Injection moulding processes and mould master inserts</i>	71
5.1.2 <i>Polymers and processing temperatures</i>	73
5.2 CORRELATION OF DEWETTING POTENTIAL WITH REPLICATED HEIGHT.....	74
5.2.1 <i>No-flow temperature measurements</i>	74
5.2.2 <i>Comparison of surface tension and polymer viscosity with replicated height</i>	75
5.2.3 <i>Correlation of dewetting potential with replicated height of microstructures</i>	79
5.2.4 <i>Correlation of dewetting potential with replicated height of nanostructures</i>	81
5.3 REPLICABILITY OF HIERARCHICAL STRUCTURES	82
5.3.1 <i>Influence of width to pitch ratio on replication height of micro-squares</i>	82
5.3.2 <i>Replication of hierarchical structures by variothermal injection moulding</i>	84
5.4 CONCLUSIONS.....	86
6. 3D MULTI-SCALE SIMULATION IN COMPARISON TO INJECTION MOULDING TRIALS	87
6.1 MOTIVATION AND STATE-OF-THE-ART.....	87
6.2 POLYMERS AND PROCESS	88
6.2.1 <i>Mould master inserts</i>	88
6.2.2 <i>Processing parameters</i>	89
6.2.3 <i>No-flow temperature</i>	89
6.3 SIMULATION SETTINGS WITH MOLDFLOW AND COMSOL.....	90
6.3.1 <i>Governing equations</i>	91
6.3.2 <i>Analysis sequences</i>	92
6.3.3 <i>Mesh density and model scaling</i>	92
6.3.4 <i>Simulation parameters in Moldflow</i>	94

TABLE OF CONTENTS

6.4	VALIDATION OF MACROSCOPIC BOUNDARY CONDITIONS	95
6.4.1	<i>Shear rates</i>	96
6.4.2	<i>Viscosities: Comparison of simulation with online measurements</i>	97
6.4.3	<i>Flow front velocities</i>	98
6.4.4	<i>Pressure</i>	99
6.5	HEAT TRANSFER AND COOLING RATE OF MICRO- AND NANOSTRUCTURES	99
6.6	CORRELATION OF EXPERIMENTS WITH SIMULATION	103
6.6.1	<i>Short-shot: Replication of microstructures during the filling phase</i>	103
6.6.2	<i>Impact of injection velocity on microstructure replication</i>	103
6.6.3	<i>Variation of mould temperature</i>	108
6.6.4	<i>Replication of nanostructures</i>	111
6.6.5	<i>Influence of wall boundary condition</i>	112
6.7	CONCLUSIONS	114
7.	DEMOULDING OF MICRO- AND NANOSTRUCTURES.....	115
7.1	INTRODUCTION	115
7.2	FRACTURE TOUGHNESS AND DEMOULDING ISSUES OF DIFFERENT MOULD MATERIALS	116
7.3	ANTI-ADHESION COATINGS FOR BETTER DEMOULDING	117
7.4	CORRELATION OF DEMOULDING ISSUES WITH WORK OF ADHESION & ADHESION FORCES	118
7.5	EXPLANATIONS FOR DEMOULDING ISSUES	121
7.6	CONCLUSIONS.....	122
8.	POLYMER MOULDS FOR THE FAST FABRICATION OF NANOSTRUCTURED POLYMERIC SAMPLES FOR CELL GROWTH TESTS	123
8.1	INTRODUCTION	123
8.2	INJECTION MOULDING AND MOULD INSERT PROCESS CHAIN	124
8.3	THERMAL PROPERTIES OF MOULD MATERIALS	125
8.4	CONTACT TEMPERATURES AT THE POLYMER MELT/MOULD INTERFACE	125
8.5	REPLICATION OF SINTERED NANO-DOTS FOR CELL TESTS	127
8.6	CONCLUSIONS.....	128
9.	SUMMARY, CONCLUSIONS AND OUTLOOK.....	129
9.1	SUMMARY	129
9.2	CONCLUSIONS.....	130
9.3	OUTLOOK.....	132
10.	LIST OF SYMBOLS AND ABBREVIATIONS	133
11.	BIBLIOGRAPHY	135
12.	LIST OF OWN PUBLICATIONS & CONFERENCE PRESENTATIONS.....	143
13.	CURRICULUM VITAE	145

1. INTRODUCTION

On our lovely planet earth surfaces of solid materials, plants, animals or human beings interact with gases, fluids and solids. As part of the evolution, mankind created artificial materials such as steel or synthetic polymers, and surfaces have been functionalised especially with coatings, for example to prevent corrosion of metals or to reduce friction. Instead of adding a second material onto the first one, surface functionality can be modified by structuring. In the macroscopic world the difference between a structured and a smooth surface is evident when cycling on a single trail full of stones and roots in comparison to an asphalted road. But the precise behaviour of a polymer melt flowing with high speed over a structured or smooth surface on the micro- or nanoscale is less obvious. This is exactly what happens when polymeric parts with structures are replicated by injection moulding. Only with a detailed understanding of the influence of polymer properties like viscosity or wetting and the processing on the filling and demoulding of functional micro- and nanostructures, highly sophisticated applications, for example in the field of optics or life science, can be developed.

1.1 Motivation: Applications with polymeric micro- and nanostructures

Since several decades a technological contest towards more miniaturization and higher complexity of polymeric parts can be observed. The track pitches in sound storage mediums decreased continuously from roughly 1.6 μm for compact discs to 300 nm for Blu-ray discs. In this context, the integration of functional micro- and nanostructures on polymeric surfaces boost a wide range of potential applications for different markets, because a variety of surface properties can be adapted without changing the chemical composition of the material, which is of particular relevance for the life science and medical diagnostics sector.

1.1.1 Sensors and microfluidic devices

The major applications for micro- and nanostructures with an enormous market forecast are sensors (Urwyler et al., 2013) and microfluidic devices (Attia et al., 2009), so called lab-on-the-chip, or micro total analysis systems (μTAS) for the transport of fluids like e.g. blood and urine and in-situ diagnostics of proteins, bacteria, diseases (Chin et al., 2011) or DNA as shown by (Utiko et al., 2011). (Graß et al., 2001) proposed a PMMA-microchip device for electrophoretic methods that could be not only used for clinical diagnostics but also for process control or food and environmental analysis.

Integrated micro-devices offer the advantage of running fast parallel analysis processes on chips with the size of a credit card. Detection can be realized optically with integrated waveguides as presented among others by (Fleger and Neyer, 2006). An example for a μTAS is shown in Fig. 1.1a. Whereas blood cells are in the range of some μm , viruses and DNA are only in nm size (Fig. 1.6), which is the reason why current channel dimensions in the range of 10 to 200 μm are supplemented by submicron structures. Integrated nano-grooves in micro-channels were, for instance, proposed by (Senn et al., 2010) to enhance the fluid flow with parallel oriented channels and to block the fluid flow at distinct locations with perpendicular oriented ones. Such technological progresses make the entire replication chain more complex and challenging, because small defects can cause functional failure like low signal to noise ratio, interrupted flow of fluidics or bonding issues. A variety of methods how to seal the micro- and nano-channels were reviewed by (Temiz et al., 2015). Most of the microfluidic structures have an aspect ratio of below one. But with increasing demand on flow speed for faster analysis also higher aspect ratios are considered in the design of microfluidic devices, which can lead to demoulding (Fig. 1.1b) and filling issues (Fig. 1.1c, d) when using standard isothermal injection moulding for the replication process.

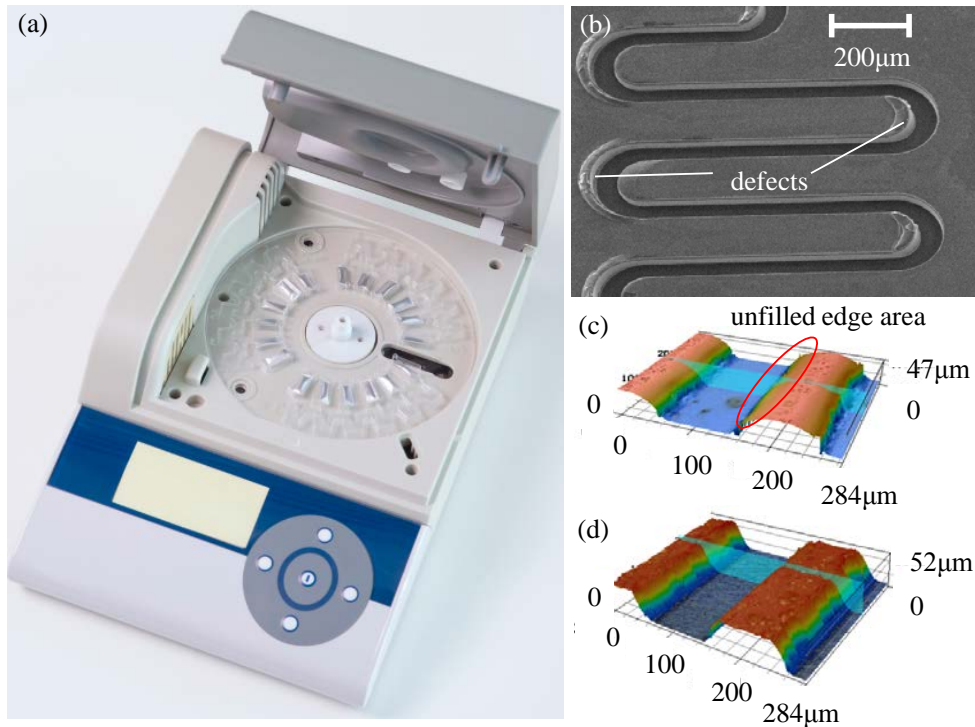


Fig. 1.1: (a) Example of a complex lab-on-a-chip (courtesy of Bernd Müller for IMTEK & Hahn-Schickard); (b) tilted SEM picture showing microdefects of a replicated PMMA channel caused by demoulding problems of high aspect ratio structures; (c) and (d) 3D CLSM picture of an unfilled channel with a width of $50\ \mu\text{m}$ compared to a completely filled one.

1.1.2 Surface cell interactions

The interaction of surface topographies with cells is of particular interest for tissue engineering (Padeste et al., 2011) and implant surfaces, also in the context of bactericidal surfaces (Bixler et al., 2014), (Magin et al., 2010). The design of a nano-pattern can influence migration, focal adhesion, and spreading of proteins and cells (Cavalcanti-Adam et al., 2008). (Franco et al., 2011) demonstrated that on hot-embossed micro-gratings in cycloolefin copolymer (COC) the onset of endothelial spreading is 40% faster than on flat surfaces. Artificial microstructured surfaces allow the reconstitution of physiological in situ conditions for controlled in vitro cell culture and have been used to reveal fundamental cell morphogenetic processes. By manipulating microstructured shapes, cells were shown to precisely adapt their cytoskeleton architecture to the geometry of their microenvironment (Théry, 2010). In Fig. 1.2 a cell interacts with a nanostructured surface:

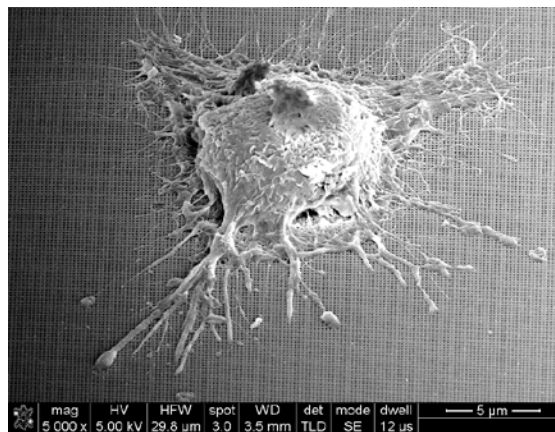


Fig. 1.2: SEM image of a human epithelial carcinoma cell (HeLa) on $100\ \text{nm}$ wide holes in COC (Matschuk, 2011).

Especially for bio-assays or micro-containers for cell cultivation, as shown by (Piotter et al., 2002), cheap and reproducible samples are needed to obtain statistically relevant results, which is the main driver for the substitution of silicon and glass by polymers in such applications.

1.1.3 Bionic structures: Biomimetic modification of polymeric surfaces

Many functional surface topographies can be discovered in nature and their transfer into polymers has been investigated among others by (Gadegaard et al., 2003). (Baum et al., 2014) showed that snake-inspired anisotropic microstructures on epoxy reduce the friction and stick-slip effect. Structural micro- and nanostructures on butterflies, moths, peacocks, beetles or fungi generate brilliant colours (Kinoshita et al., 2008), (Steindorfer et al., 2012). Some animals are even able to vary their colour when exposed to stress by adapting the distance between structures or by varying the amount of liquid in the gaps between them (Liu et al., 2009). The practical use of such structural colours can reach from decorative effects to security features or sensors as already mentioned above. Other functions based on nanostructures such as anti-reflection (Christiansen et al., 2014), drag reduction (Bechert et al., 2000) or adhesion (Gorb et al., 2007) can also be found in nature, which is the reason for terms like moth eye, shark skin or gecko feet effect. Adhesion related studies are not limited to geckos but were enlarged to frogs that adhere well to moist surfaces. (Iturri et al., 2015) produced such frog-inspired hexagonal μ -pillar arrays in polydimethylsiloxane (PDMS). Another example for bionic structures is described by (Drabiniok and Neyer, 2014) who designed micro-pores and cooling channels for photovoltaic cells based on evaporation, imitating the water transport mechanism of trees. Maybe the best known nanostructure is that of the lotus-leaf. (Michaeli and Klaiber, 2010) proposed an easy way to produce such super-hydrophobic structures. The polymer gets stuck in laser-machined holes with small undercuts and is stretched in a more or less controlled way. The mould temperature needs to be high enough to fill the undercuts, but for ejection the mould temperature is reduced again to prevent a rupture of the structures. The influence of such a microstructure on the water contact angle is shown in Fig. 1.3.

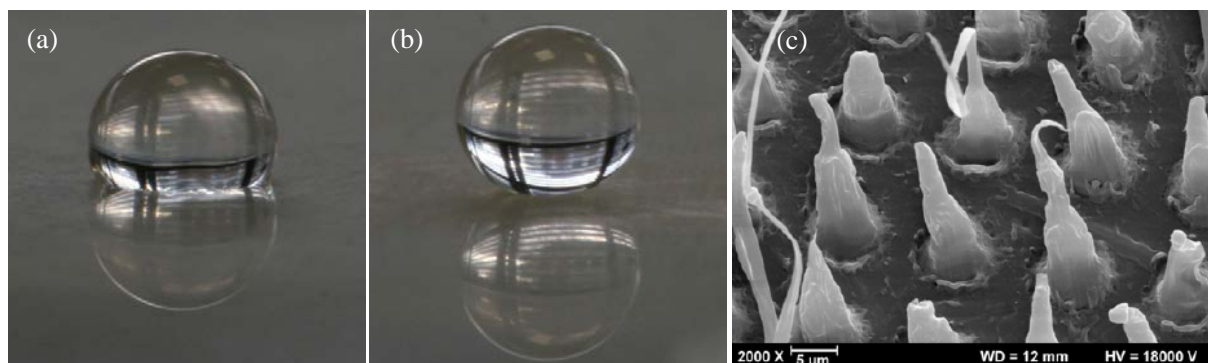


Fig. 1.3: (a) Water droplet on an unstructured surface with a contact angle of $\sim 90^\circ$; (b) water droplet on a stretched polypropylene (PP) structure increasing the contact angle to 160° ; (c) SEM picture of the stretched PP structure (Bekesi et al., 2010).

An alternative way to produce super hydrophobic surfaces on polypropylene was proposed by (Andersen and Taboryski, 2015) who replicated electroformed nickel foils with randomly distributed microstructures by injection moulding. The tuning of wetting and adhesion in order to produce biomimetic polymer surfaces was also studied by many other groups, e.g. (Shahsavani et al., 2012) or (Feng et al., 2009) who produced super-hydrophobic surfaces in polyethylene with simple manufacturing methods like stretched controlled embossing in an oven. (Zhang et al., 2015) achieved super hydrophobicity with bio-inspired hierarchical PDMS microstructures and could even tune the adhesive forces of the water droplet on the PDMS from extremely low ($\sim 8.3 \mu\text{N}$) to very high ($\sim 57 \mu\text{N}$) levels.

1.1.4 Optical structures: Diffraction, reflection and diffusion of light

Micro- and nanostructures have already been used in various optical applications, such as light guiding plates as demonstrated by (Huang and Chung, 2011) or (Tengler et al., 2014). There is growing industrial interest of optical structures for redirection of sunlight (Klammt et al., 2012) as well as diffractive and holographic structures (Kalima et al., 2007). Diffractive optical elements (DOE) are used for example in low-cost infrared spectrometers, as described by (Lovhaugen et al., 2004). The anti-reflective effect of nanostructures as investigated among others by (Burr et al., 2003) is based on a gradual transition in the refractive index preventing the light from escaping. In order to avoid diffractive effects, statistical nanostructures can be used to decrease reflection as shown by (Saarikoski et al., 2009), who proposed a hierarchical structure design combining micro- and nanostructures on polycarbonate. Optical microstructures were also integrated in a multimode fibre connector as shown by (Piotter et al., 2002).

A low replication quality with surface defects can strongly reduce the functionality of optical polymer surfaces, as can be seen in Fig. 1.4. The precisely replicated pillar array, shown in Fig. 1.4b, leads to distinct diffraction orders, which become blurred in the presence of surface defects.

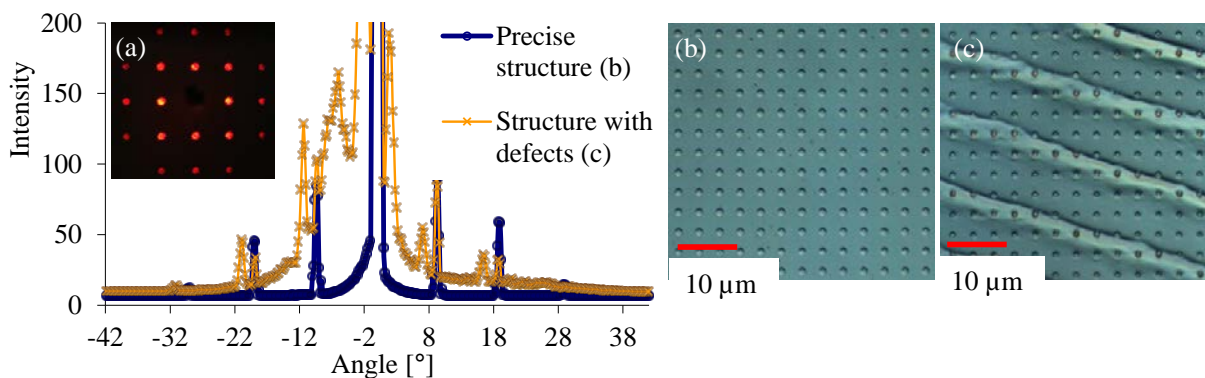


Fig. 1.4: (a) Transmission laser diffraction pattern with (b) a defect-free microstructure on amorphous polyamide (A-PA) showing a regular pattern (blue line); (c) A-PA part with defects in the microstructure showing an unregular pattern (orange line); (Rytka, 2009).

The examples above show that the geometry and size of the designed structure on the polymer substrate can vary a lot, depending on the required function of the final product.

In order to manufacture polymeric parts with additional functionality, it is therefore of high importance to fully understand the replication process of micro- and nanostructures compared to standard macro-moulding processes.

1.2 Scope of research and objectives

As technologies are developing, functional structures can nowadays be produced artificially by micro-machining, laser ablation or lithographic methods. Once the functional structure is produced, it can be replicated by different methods such as injection moulding (Rytka et al., 2015), reaction injection moulding (Hanemann et al., 2002), hot embossing (Schift, 2015) and roll embossing or thermoforming (Heckele and Schomburg, 2004).

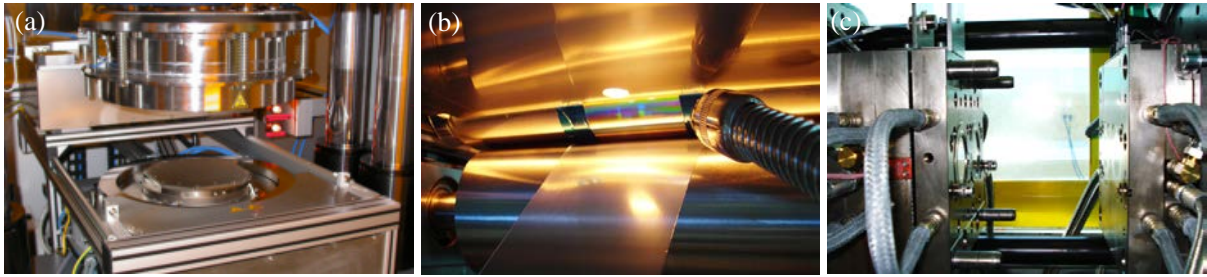


Fig. 1.5: Most important replication methods of micro- and nanostructures: (a) press for hot embossing; (b) roll and film with IR sensor for roll embossing; (c) mould for injection moulding.

The most important method for mass replication of complex 3D polymeric parts is still injection moulding (Fig. 1.5c), which is also the focus of this work.

Micro- and nanostructure replication differs from conventional macro injection moulding because of substantial differences in the surface to volume ratio at the melt/mould interface. Therefore, the heat transfer becomes more relevant, and an increased solidification speed of the polymer melt is observed in contact with the mould.

Table 1-1 summarizes the most probable differences between filling of macro-, micro- and nanoscale cavities and addresses some working hypotheses investigated and discussed in this work.

Table 1-1: Summary of possible differences between macro-, micro- and nanoreplication.

Structure size	Macro > 200 μm	Micro $\sim 200 \mu\text{m} \rightarrow \sim 1 \mu\text{m}$	Nano $\sim 1 \mu\text{m} \rightarrow \sim 1 \text{nm}$
Surface tension Wetting Capillary forces	Less relevant	Relevant	Capillary forces dominating?
Friction Flow resistance	Hagen-Poiseuille	Hagen-Poiseuille; low flow velocity*	Probably very low flow velocity*
Holding pressure	Filling before applying holding pressure	Relevance depends on heat transfer	Interrelation with shrinkage and heat transfer?
Heat transfer	Frozen layer at the edge and fluid centre	Thinner fluid centre & increased heat transfer	Probably no fluid centre, very fast heat transfer?
Size dependent viscosity Molecule orientation	Shear thinning Navier-Stokes	Less shear thinning because of low flow velocity*	Wall thickness comparable with polymer radius of gyration
Gas occlusions Gas solubility	Venting channels: $\sim 100 - 200 \mu\text{m}$	Vacuum advantageous	Air becomes supercritical \rightarrow diffusion?
Demoulding issues	Depending on roughness, geometry (draft angles, undercuts, aspect ratio), inhomogeneous stresses and pressures		

*only valid if micro- and nanostructures are filled in parallel with the macro-areas, thus, the macro-part will be filled first with high velocity because of lower flow resistance, and the flow into the micro- and nanostructures would be decelerated

In the scientific literature, many experimental studies on the replication of micro- and nanostructures by isothermal injection moulding can be found, in which important processing parameters such as mould temperature, injection speed or holding pressure have been varied. However, most of these studies do not discuss the influence of other relevant parameters like polymer viscosity, surface tension, wall slip and adhesion, filling and cooling speed, as well as local pressures and shear rates on the

filling and demoulding of such structures. One particular focus of this work is to find out to which extent the melt viscosity and wetting behaviour of the polymer and associated changes in spreading coefficient and capillary effects influence the replication quality of micro- and nanostructures, respectively. Process variations related to elevated temperatures at the interface between polymer and mould, uniform pressure distribution and controlled polymer solidification are necessary to optimize the replication of functional micro- and nanostructures. In order to gain a deeper understanding of polymer replication on different length scales, the relevance and impact of the different variables mentioned above needs to be elucidated. Possible differences between macro-, micro- and nano-replication are formulated in Table 1-1. The aim of this work is to prove some of these hypotheses.

For the investigation of all these physical effects, the processing has an additional important influence. In particular, variothermal compression moulding offers the highest potential to achieve the best replication quality, but nonetheless has found little attention in the scientific community. For this reason, a detailed comparative study of four different process variants has been carried out (Chapter 4).

In conclusion, the goal of this work is to compare theoretical considerations and models with practical tests on the injection compression moulding machine running four different variations of injection moulding on the same mould. By carrying out simulations and calculations with isothermal and variothermal processes and different filling modes with changing pressures, temperatures and shear rates, the fundamental differences between nano-, micro- and macro-structures will be discussed, also taking into account the behaviour of different polymers on various mould material surfaces. For that reason the processes and polymers will be evaluated in the context of replication accuracy (height and shape of the structures), homogeneity, defects, stresses and suitability for mass production (stability, demouldability and filling pressure).

1.3 State-of-the-art

1.3.1 Manufacturing of micro- and nanostructured moulds

Depending on size, geometry and material of the structure, different production methods are used for the manufacturing of micro- and nanostructured moulds which are summarized in Fig. 1.6.

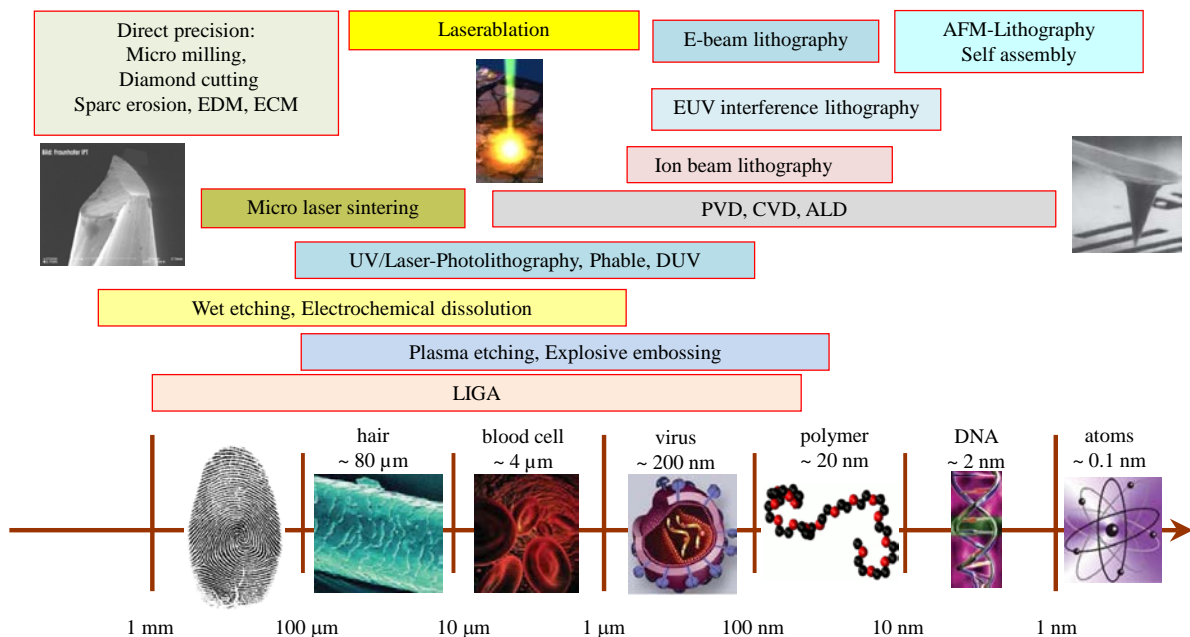


Fig. 1.6: Overview of feature sizes, dependent on top-down and bottom-up manufacturing technologies of micro- and nanostructures.

Technologies for manufacturing methods of micro- and nanostructures were extensively reviewed by (Heckele and Schomburg, 2004), (Giboz et al., 2007), (Tawfick et al., 2012) and (Zhiltsova et al., 2013). For structures down to around 10 - 50 μm , direct precision mechanical technologies like high speed diamond cutting and milling, electro discharge machining (EDM), electro chemical machining (ECM) or spark erosion can be used. The advantage of these methods is that structures are directly implemented onto steel or aluminium moulds, which is also true for wet etching, as demonstrated, for instance in the investigation of (Feng et al., 2010). On the other hand, surface quality with respect to roughness, dimensional control and structure size is rather poor if feature sizes below 10 μm are needed.

For structures < 10 μm , lithographic methods combined with electroplating have to be used, commonly referred to as LIGA. Laser ablation, as applied by (Hanemann et al., 2002) for the rapid fabrication of micro components, bridges the gap between direct precision methods and lithography. But similar to mechanical technologies above, the surface roughness of the structures is rather high ($R_a > 200 \text{ nm}$), which is the reason why laser ablation is sometimes combined with chemical or physical polishing methods. In order to get more precise structures with complicated shapes, the manufacturing methods of micro- and nanostructures have been continuously improved. (Kirchner et al., 2015), for instance, combined grayscale electron beam lithography with selective thermal polymer reflow so that very smooth transitions from steep and high aspect ratio areas to shallow regions within the same structure area were applicable. (Huovinen et al., 2014) presented a simple method to manufacture hierarchical multiscale patterns in nickel with a micro-roughening technique.

In this thesis, mainly laser ablation, mask based displacement Talbot UV photolithography and mask less thermal scanning probe lithography combined with electroplating were used to manufacture moulds.

1.3.2 Influences on the replication fidelity

The realisation of applications in polymers requires fast and efficient mass production methods allowing functional structures to be integrated into the product in a versatile and cost-effective manner. Most of the functional structures are replicated by injection moulding, roll or hot embossing (Fig. 1.5). The biggest differences between these methods are contact time with the mould, output speed and geometry of the replica. Roll embossing is mainly used for high throughput replication of 2D films or plates with rather short mould contact times whereas injection moulding is also suitable for 3D parts and the integration of structured films or inserts by back moulding. Also hot embossing or nano-imprint lithography (NIL) is mainly used for 2D replication (Schift, 2015), although current research deals with 3D imprint and the optimisation of cycle times of NIL. The melt transcription process was proposed by (Ito et al., 2007) as an alternative replication method. This process is a combination of coating and compression and apparently results in good replication quality and low stresses.

Low aspect ratio structures, even if they are as small as 18 nm, are still possible to be replicated by standard isothermal injection moulding (IIM) as shown by (Holzer et al., 2010). With increasing complexity of the functional surface topography, perfect replication becomes more difficult, particularly for high aspect ratio (AR) structures and polymers with high melt viscosity. To overcome these limitations, variothermal injection moulding (VIM) has been proposed, among others, by (Yoo et al., 2009) and (Hattori et al., 2010), but requires sophisticated mould design and peripheral equipment. Despite the substantially longer cycle times in comparison to IIM, VIM is already in use to achieve glossy surfaces as investigated by (Lucchetta and Fiorotto, 2013) without weld lines for automotive parts or mobile phone covers (Park et al., 2010). Another disadvantage of IIM is the high level of internal stresses, which is the reason why CDs, DVDs, or lenses with a low level of internal stresses and precise geometry are produced by isothermal injection compression moulding (IICM) as shown by

(Michaeli et al., 2007) and (Stricker et al., 2009). (Rohde et al., 2009) investigated the influence of processing parameters on the replication of microstructures for IICM.

However, the highest potential for accurate replication, combined with low stress level and part thickness precision as determined by (Hong et al., 2014), is offered by variothermal injection compression moulding (VICM). (Michaeli et al., 2008) investigated all four process variants for the replication of microstructures with POM and PMMA using inductive heating for the variothermal process and showed that only VICM allowed the full height of 100 μm of 40 μm wide honeycomb structures to be replicated. Unfortunately, no correlation to viscosities and surfaces energies of the polymers were discussed and no nanostructures were replicated. An alternative way to replicate high aspect ratio structures was proposed by (Stormonth-Darling et al., 2014) using heat-retarding polymeric inserts. However, most of the master structures are still made in well-established nickel as investigated by (Nagato et al., 2011).

In the context of accurate filling, the aspect ratio (AR) of the structure and the replication ratio (RR) play an important role and are therefore defined in Fig. 1.7.

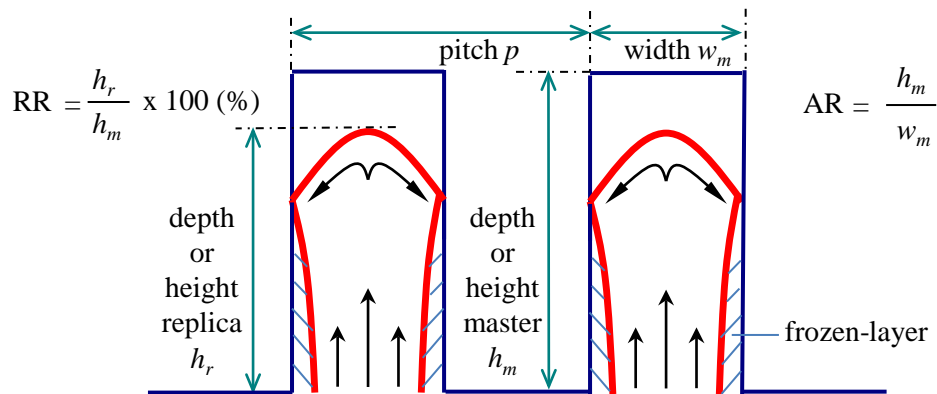


Fig. 1.7: Flow of polymer melt into a structure with definitions of aspect ratio (AR) and replication ratio (RR).

In order to fill especially high aspect ratio structures, a high mould temperature, ideally above the transition or no-flow temperature of the polymer is favourable, whereas for demoulding, the polymer has to be solid enough for being ejected without deformation. For that reason, a variothermal process is clearly a compromise between replication quality and cycle time.

Influence of processing parameters on the replication quality

Many investigations about replication of microstructures were already carried out by standard injection moulding with different processing parameters. In some of these studies the mould temperature was found to have the biggest influence on the replication quality. (Bekesi et al., 2010) replicated polypropylene (PP) by inductive VIM and created hairy super-hydrophobic structures that were stretched in a laser-machined mould with rough undercuts and perfectly filled with a high mould temperature (Fig. 1.3). (Matschuk and Larsen, 2013) demonstrated the importance of high mould temperature of nickel nanostructures with cycloolefin copolymers (COC) for an accurate replication, but if the temperatures were too high, sticking of the polymer to the mould surface could be observed. (Kalima et al., 2007), (Xu et al., 2005) and (Tofteberg and Andreassen, 2008) showed the positive effect of high injection speed with significant differences between various polymers. However, the maximum injection pressure of the injection moulding machine limits the injection speed and, additionally, surface quality may suffer as the polymer melt is subjected to high shear forces in the cavity, especially at wall thickness transitions. (Tofteberg et al., 2010) investigated the influence of holding pressure on the replication of microstructures and found that an increasing holding pressure can have either a positive or a negative effect on the replication fidelity.

Influence of vacuum venting and geometry on replication quality

(Han et al., 2006) demonstrated the positive effect of vacuum venting on the replication quality of microstructures (around 10 % increase in RR) especially at very high injection velocities, as the air has probably less time to diffuse into the material or to be pressed out of the cavity. The small effect of vacuum venting on the replication of microstructures was also found by (Sorgato and Lucchetta, 2015), who observed no improvement with polystyrene (PS) but an increase of 13.6 % in RR with cycloolefin polymer (COC). Interestingly, these differences were explained with differences in viscosity and wettability of the two polymers. To improve the μ -IM process in general, meaning less air traps and diesel effect, the use of vacuum methods are highly recommended according to the investigations of (Griffiths et al., 2011).

The state-of-the-art in replication of surface texture and topography at the micro- and nanoscale was discussed, for instance, by (Hansen et al., 2011). In another investigation of (Han and Yokoi, 2006) it was shown that a smaller wall thickness of the macro part is favourable for the filling of μ -v-grooves. (Schift et al., 2000b) replicated low aspect ratio μ -v-grooves with polycarbonate (PC) under variation of the mould temperature and also analysed the effect of radial shrinkage on structures at different positions of the sample.

(Jung et al., 2007) replicated machined microstructures with AR = 10 with two different COC grades and showed that structures with widths of 100, 150 and 200 μm were completely replicated, whereas structures of 50 μm width were not entirely filled. Unfortunately, no explanations for the observed differences in filling were presented referring to material viscosity, glass transition or mould temperature.

In most of those studies only one or two injection moulding processes were investigated with focus either on the influence of different process parameters or on the comparison of different materials. However, systematic comparative studies on iso- and variothermal injection compression moulding methods employing the same mould are very rare and the replication process is hardly correlated to important polymer properties such as online measured melt viscosity, glass transition or no-flow temperature and wetting behaviour.

1.4 Structure of the thesis

The thesis is organized as follows. First of all, some fundamental aspects relevant to micro- and nanoscale replication are presented in Chapter 2, followed by a description of materials and methods in Chapter 3. Chapter 4 focuses on the comparison of four different injection moulding processes, taking into account the influences of mould temperature, compression and capillary effects on the filling of micro- and nanostructures. In Chapter 5, the role of wetting, structure width and flow characteristics on the resulting replication ratio are discussed. Chapter 6 deals with the simulation of the filling behaviour of micro- and nanostructures and the comparison to experimental results obtained in real injection moulding trials. Moldflow was used for the 3D filling simulation and Comsol for the simulation of heat transfer and the influence of wall boundary condition. Next, in Chapter 7, demoulding issues on both the replica and the master structures are discussed. The differences of polymeric in comparison to metal moulds for injection moulding are presented in Chapter 8 exemplary for the fast fabrication of reproducible samples with nano-hemispheres for cell tests. Finally, all results are summarized in Chapter 9 and an outlook is given on topics that warrant further in-depth investigations.

2. FUNDAMENTALS

2.1 Polymer molecule size in comparison to nanostructures

If small nanostructures below 100 nm are replicated, it is of high interest to consider the size of polymer chains, i.e. the radius of gyration, in relation to the structure dimensions to be filled by the polymer. In Fig. 2.1 the molecule geometry of polyethylene (PE) is visualized when flowing into a nanostructure.

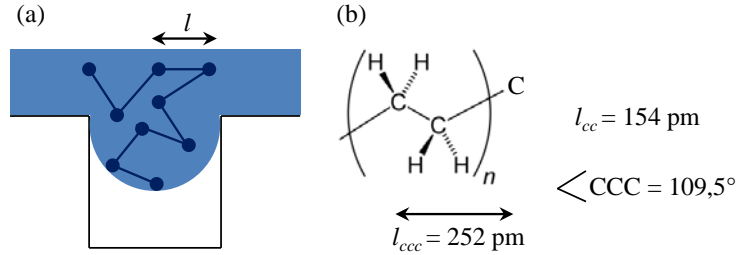


Fig. 2.1: (a) Visualization of theoretical molecule geometry for polyethylene (PE) in a small nanostructure; (b) distance between two carbon atoms $l_{cc} = 154$ pm with an angle of $109,5^\circ$ and the distance between three carbon atoms $l_{ccc} = 252$ pm.

In Table 2-1 the real and theoretical radius of gyration R and the molecule length l_M were calculated in dependence of the degree of polymerization N , the binding length l_B and the molecule enlargement factor C_∞ (= relation of the real expansion of the polymer chain to the theoretical expansion of imaginary chain using 3 for very flexible chains and 20 for stiff chains) for a PE and two hypothetical polymers P1 and P2.

Table 2-1: Theoretical calculation of the molecule radius R considering different degrees of polymerization N and different molecule enlargement factors C_∞ ; the equations and values for the calculation were taken from (Eliezer and Hayman, 1957); (Wang, 1990) and (Zhou et al., 1992).

Material		PE	P1	P2
Degree of polymerization	N	4000	7000	10000
Binding length between two carbon atoms	l_B [nm]	0.154	0.18	0.2
Molecule enlargement factor	C_∞	6.7	12	20
Mean theoretical Radius of gyration [nm]	$R = \sqrt{\frac{N \cdot l_B^2}{6}}$ (2-1)	4	6	8
Theoretical molecule length [nm]	$l_M = \sqrt{N \cdot l_B^2}$ (2-2)	10	15	20
Mean real Radius of gyration [nm]	$R = \sqrt{\frac{c_\infty \cdot N \cdot l_B^2}{6}}$ (2-3)	10	21	37
Real molecule length [nm]	$l_M = \sqrt{c_\infty \cdot N \cdot l_B^2}$ (2-4)	25	52	89

These simplified calculations are in good agreement with studies of (Yao and Kim, 2005), who mentioned the possible role of molecular effects, like steric forces and chain entanglement on the polymer flow into nanostructures. On the one hand, the replication of structures below 50 nm becomes very interesting because such structures would have a similar diameter like typical polymer chains with moderate chain flexibility C_∞ and a typical degree of polymerization N .

On the other hand, (Schift et al., 2000a), for example, impressively showed the replication of 25 nm line structures with aspect ratios of almost 2 with cycle times down to 4 seconds.

When using continuum theories, as it is the case in Moldflow and Comsol simulations and as will be shown in Chapter 6, one should be aware that rheological and heat transfer properties may vary significantly for the replication of structures on the length scale of polymer molecules in comparison to macroscopic moulding.

2.2 Rheology of polymers

The viscosity η of polymers has a huge effect on the filling of micro- and nanostructures and decreases with an increasing shear rate. This effect is called shear thinning and can be described with equation (2-5).

$$\tau = \eta \cdot \frac{dv_x}{dz} = \eta \cdot \dot{\gamma} \quad (2-5)$$

Where $\dot{\gamma}$ is the shear rate, v_x the velocity in x-direction and z refers to the wall thickness of the part.

Shear thinning is based on the orientation of macromolecules becoming more enhanced in the injection moulding process at high injection velocities and small wall thickness so that shear rates might increase to more than 10000 s^{-1} . If the melt cools down quickly (as it is the case in conventional injection moulding) these orientations are frozen-in and can be visualized between cross polarizers. Using compression moulding, it can be assumed that during the compression stroke the shear rate is getting very low.

If a non-Newtonian, isothermal flow is considered, the power-law model, as described in equations (2-6) and (2-7), can be used to represent the shear-thinning behaviour:

$$\eta = m \cdot \dot{\gamma}^{n-1} \quad (2-6)$$

$$m(T) = m_0 \cdot e^{-a_0(T_p - T_0)} \quad (2-7)$$

Where n is the power law index, m_0 and a_0 are material constants and T_0 is the reference temperature in the channel.

The Carreau-Yasuda model (Bird et al., 1987), described in equation (2-8), is for example implemented in simulation programs like Comsol by default.

$$\eta = \alpha_T \cdot \eta_0 \cdot \left[1 + (\alpha_T \cdot \lambda \cdot \dot{\gamma})^{a_1} \right]^{(n-1)/a_1} \quad (2-8)$$

Where η_0 is the zero shear viscosity, a_1 is a fitting parameter determining the width of the transition zone between Newtonian and the shear-thinning regime, λ is a time constant, α_T is the shift-factor according to the Williams-Landel-Ferry (WLF) equation (see also equation (2-11)) for considering the temperature influence on the viscosity.

The Cross-WLF model (Mezger, 2014) represents the dependence of viscosity on both temperature T and pressure P according to equation (2-9):

$$\eta(\dot{\gamma}, T, P) = \frac{\eta_0(T, P)}{1 + \left(\frac{\eta_0 \cdot \dot{\gamma}}{\tau^*} \right)^{1-n}} \quad (2-9)$$

$$n = \frac{\Delta(\lg \tau)}{\Delta(\lg \dot{\gamma})} \quad (2-10)$$

Many polymers exhibit a Newtonian plateau at low shear rates $\dot{\gamma}$, a transition region (τ^* represents the transition between Newtonian and shear thinning regime), and a power law regime (slope defined by the power law index n) as well modelled by the Cross-WLF equations.

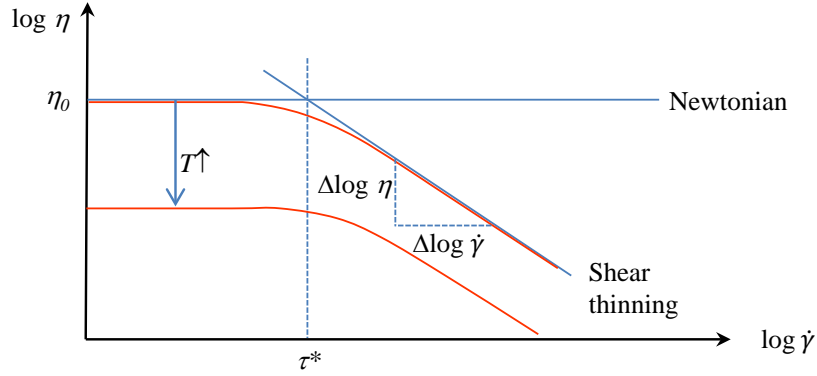


Fig. 2.2: Shear thinning behaviour based on Cross-WLF approach: τ^* represents the transition between Newtonian and shear thinning regime; the slope is defined by the power law index n .

The zero shear viscosity η_0 can be calculated with (2-11), (2-12) and (2-13), based on the time-temperature-transition according Williams, Landel and Ferry:

$$\eta_0(T, P) = D_1 \cdot \exp \left[- \frac{A_1 (T_p - T_g)}{A_2 + (T_p - T_g)} \right] \quad (2-11)$$

$$A_2 = A_3 + D_3 \cdot P \quad (2-12)$$

$$T_g = D_2 + D_3 \cdot P \quad (2-13)$$

Where T_p is the polymer melt processing temperature and T_g is the glass transition temperature; D_1 , D_2 , D_3 , A_1 , A_2 and A_3 are polymer specific fitting parameters.

As the shear rate has such a strong influence on the viscosity, it is essential to know the precise shear rate in the structures during the injection, compression and packing phase. Especially during compression and packing the shear rates are rather low compared to the injection phase, and the viscous dissipation is negligible (Massé et al., 2004). The main disadvantage of the Cross-WLF model is the rather bad reproduction of the viscosity around the transition zone of the polymer (Kennedy and Zheng, 2013), (Tofteberg and Andreassen, 2010).

The Cross-WLF model for macroscopic flow is based on incompressible Navier-Stokes viscous fluid motion, also named creeping flow. In this model which was also used by (Kim and Turng, 2006) to describe the filling of an optical lens with micro features, advective inertial forces are not taken into consideration as they are dominated by viscous forces. The ratio between these viscous forces and the inertial effects can be expressed by the Reynolds number:

$$\text{Re} = \frac{\rho \cdot v \cdot w}{\eta} \quad (2-14)$$

Where ρ is the density, v is the flow velocity and w is the characteristic width (e.g. wall thickness or of the structure).

The macroscopic flow is a laminar flow with typically low Reynolds numbers (10^{-4} - 10^{-2}). Even lower Re values are found in the case of micro- and nanostructures. Therefore, the flow in these small-scale cavities can be assumed as inertialess or creeping (Gujrati and Leonov, 2010).

In some publications and commercial software (e.g. CMOULD) the flow in micro-features was modelled with the Hele-Shaw flow that is defined as a Stokes flow between two parallel flat plates separated by an infinitesimally small gap.

The Hele-Shaw model provides simplified governing equations for non-isothermal, non-Newtonian and inelastic flows but neglects inertia effect and exhibits other limitations. It cannot accurately represent 3D flow behaviour within thick and complex areas or at the melt front (fountain flow), at flow junctions or in regions with pronounced transitions in part thickness, which is obviously the case for macro filling in combination with micro-features.

The most accurate equations to simulate the flow are full 3D Navier-Stokes equations that are implemented in simulation software like Moldflow or Comsol. The Navier-Stokes equations are independent on dimensions, but the size of the cavity could play an important role if the structure dimensions are comparable to the polymer's radius of gyration, as already described in Chapter 2.1.

2.2.1 Melt temperature - viscous thermal dissipation

The polymer melt processing temperature T_p plays an important role for the replication of structures as shown by (Huang and Chung, 2011) for the filling of light guiding plates with v-grooved micro-features. In macroscopic injection moulding the melt temperature is increased by high shear rates close to the mould surface. With decreasing cavity width the shear rate profile changes, which results in different temperature profiles that can be seen in Fig. 2.3.

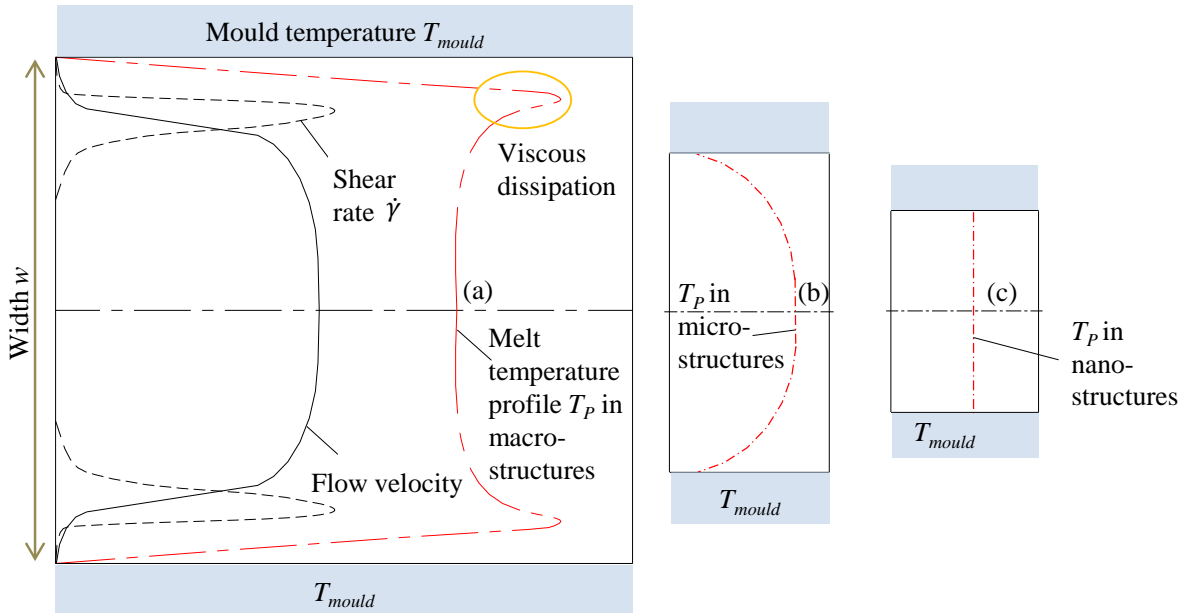


Fig. 2.3: Schematic melt temperature T_p profiles in (a) macro-, (b) micro- and (c) nanostructures, showing the increased impact of mould temperature and feature size on the cooling of the melt and the resulting viscous dissipation, adapted from (Yao and Kim, 2005).

The Brinkman number Br (2-15) represents the ratio of viscous dissipation and heat conduction resulting from the temperature difference ΔT between mould temperature T_{mould} and the bulk fluid temperature. For highly viscous fluids such as a polymer melt, viscous dissipation is one of the main contributions in the equation of energy conservation. For a polymer melt flowing in a plate-shaped cavity and assuming a constant viscosity, the Brinkman number Br can be expressed as:

$$Br = \frac{\eta \cdot \dot{\gamma}^2 \cdot w^2}{k \cdot \Delta T} \quad (2-15)$$

For a rough calculation of the Br number for isothermal injection moulding with, e.g. polymethylmethacrylate (PMMA), η can be assumed as 600 Pa s, $\dot{\gamma} = 600 \text{ s}^{-1}$; $k = 0.19 \text{ W m}^{-1} \text{ K}^{-1}$ and $\Delta T = 170^\circ\text{C}$. The resulting Br number as a function of the cavity width w is plotted in Fig. 2.4.

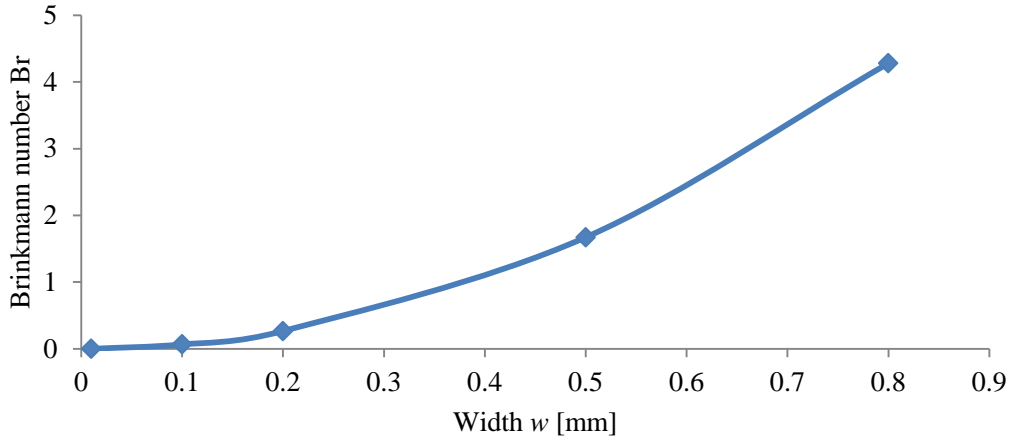


Fig. 2.4: Brinkman number Br plotted vs. structure width w .

As the Brinkman number decreases in dependence on the structure width to the power of two, heat conduction will quickly dominate over viscous dissipation. Therefore, viscous dissipation could be neglected for micro- and nanostructures (Yao and Kim, 2005) as already shown in Fig. 2.3, but not for the filling of the macro-part.

2.2.2 Wall boundaries and micro-viscosity

For a polymer flow in macro-cavities wall slip effects are usually neglected and viscosities are typically determined with capillary viscometer and plate-plate rheology.

However, in different publications it has been reported that wall slip effects may become dominant in micro- or nanostructures. In general, wall slip occurs if the melt flow becomes unstable, for example, because of wall thickness transitions and high shear forces that may cause disentanglement of polymer chains. (Yao, 2002) simulated wall slip and reported that the effect would have an impact on the flow velocity of the polymer melt for feature sizes below 1 μm . In these simulations a modified power-law slip model, previously introduced by (Rosenbaum and Hatzikiriakos, 1997) was used to describe the flow velocity u as:

$$u = \frac{a_{slip}}{1 + (\tau_c / \tau_w)^{k_{slip}}} \tau_w^n \quad (2-16)$$

Where τ_c and τ_w are the critical shear stress and the shear stress at the wall respectively; a_{slip} and k_{slip} are coefficients and n is the power law index.

However, because of the much lower velocity and shear in micro- and nanostructures it could be anticipated that no wall slip occurs and the reality may be better represented by wetted wall boundaries. Such boundary conditions are possible to implement for example in Comsol to simulate the filling of structures and will be shown in Chapter 6.6.5.

Polymer viscosity data is usually based on macroscopic measurements and may not be suitable to be used at the polymer mould/interface and in micro- and nano-filling, because of additional effects originating from surface tension, wall-slip, nano-roughness or changes in local heat transfer. Therefore, (Chien, 2005) tried to measure the polymer viscosity in micro-channels and claimed that wall-slip could reduce the viscosity within micro-channels by a factor of up to 4. The influence was supposed to become enhanced with increased melt viscosity. (Yao, 2002) applied a nonlocal continuum theory for viscous fluids under consideration of molecular orientation effects based on the equation of (Eringen and Okada, 1995). It turned out that the viscosity at the mould wall can increase by a factor of two due to the immobilisation of a layer of molecules in direct contact with the mould surface.

2.3 Wetting behaviour at the polymer/mould interface

The interfacial interactions become more relevant with decreasing feature size to be replicated. In this context, the surface tension and the surface energy play an important role.

For pure substances at constant temperature and pressure the surface free energy G_S is equal to the surface tension σ .

$$G_S = \left(\frac{dG}{dA} \right)_{T,P} = \sigma \quad (2-17)$$

Surface free energy arises from the unbalance of forces between atoms and molecules at the surface. The higher the surface energy of a material, the more bonding potential it has with other materials. In the case of a liquid on a solid surface in a gaseous environment, the contact angle θ can be defined as the angle formed by the liquid at the triple-phase boundary:

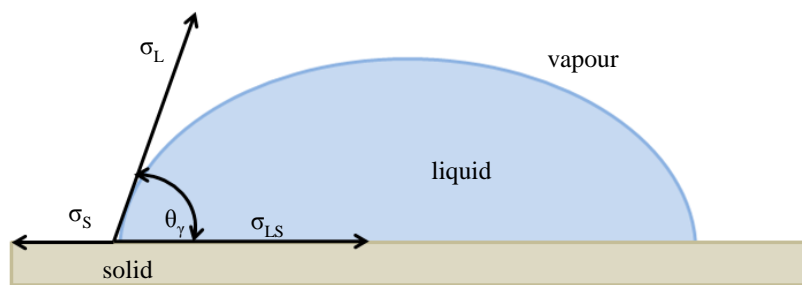


Fig. 2.5: Liquid at the vapour, liquid and solid interface.

Water for example has a rather high surface tension of about 73 mN m^{-1} and tends to form spherical droplets on surfaces to reduce its area A and thus energy.

Depending on the contact angle formed, the surfaces can be divided into different classes:

Hydrophilic for contact angles $\theta < 90^\circ$, hydrophobic for contact angles $\theta > 90^\circ$ and super hydrophobic for contact angles $\theta > 150^\circ$. If the drop completely flows over the surfaces it is called spreading.

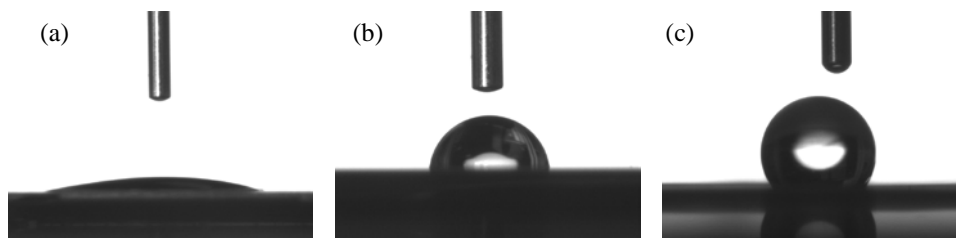


Fig. 2.6: Contact angle classes: (a) hydrophilic, (b) hydrophobic and (c) super hydrophobic.

The model of (Wenzel, 1936) predicts that roughness, which can be in the same range as functional micro- or nanostructures, enhances the natural tendency of the surface. For this reason, hydrophobicity ($\theta > 90^\circ$) would become more pronounced while the contact angle of hydrophilic surfaces ($\theta < 90^\circ$) would decrease with increasing roughness.

Surface free energy and its components for solids can be determined for example with contact angle measurements using different liquids and will be described in detail in Chapter 3.2.2.

2.4 Pressures and forces in micro- and nanostructures

The advancement of the polymer melt in a micro- or nano-sized cavity is influenced by different forces, such as surface tension, acting mainly at the flow front and extensional viscous forces, particularly at the entrance of the cavity. The filling is mainly forced by injection, holding and compression pressure. Additionally to the filling resistance, which depends linearly on the viscosity, capillary forces or, more generally, wetting of the cavity walls by the melt, can play a significant role, as the relative contribution of surface tension at the melt front will increase with smaller structures. Materials with a good wetting behaviour would improve the filling of the cavity, whereas materials with a low wetting behaviour can prevent a good flow. Most of the time, capillary forces are neglected in injection moulding. However, for small nano-cavities these forces can become relevant as described by (Jeong et al., 2006) who showed that nano-hairs can be produced with capillary force driven polymer melt into polyurethane acrylate (PUA) nano-holes. Moreover, the wetting at the interface between mould and polymer melt can have a contribution to the filling of the nanostructures at least in the very first milliseconds before a frozen-layer is formed, especially, for low injection speed with a slow increase in cavity pressure.

The capillary number Ca gives an indication of the ratio of viscous forces and surface tension:

$$Ca = \frac{\eta \cdot v}{\sigma_p} \quad (2-18)$$

With this simple equation it is possible to make a rough estimation of the impact of capillary effects, which is assumed to become relevant for small values ($Ca < 1$). When the melt comes into contact with the cold mould, the viscosity of the polymer is rather low in the first milliseconds. Depending on shear rate and temperature the polymers used in this work have a viscosity η in the order of 50 - 1000 Pa s (Fig. 3.9), increasing rapidly as the polymer solidifies. Typical flow velocities for macroscopic injection moulding are in the range of 0.01 - 0.1 m s⁻¹. The surface energies of the polymers used at processing temperature vary between 0.025 and 0.035 N m⁻¹.

Applying these values to equation (2-18), Ca numbers of 15 to 1200 result, which confirms that capillary effect in macroscopic filling is negligible compared to viscous effects. It is anticipated that this may be very different for nanostructures, which is one of the hypothesis to be investigated. The capillary effect will only be relevant in the very first milliseconds after contact with the cold mould surface leading to a rapid increase in viscosity, but at the same time to a drastic reduction in flow velocity.

(Zhang et al., 2012) proposed the following equation to estimate the filling height h or depth of micro- or nanostructures and included, additionally to injection pressure P_I and capillary pressure P_c , the air pressure P_{air} .

$$h = w \left[\frac{t_f (P_I - P_c - P_{air})}{12\eta} \right]^{1/2} \quad (2-19)$$

This simple equation may be reasonably suitable for macroscopic injection moulding. However, as will be shown, the correlation of filling height h and structure width w is not linear on the microscale. Moreover, it is rather difficult to calculate the real filling time t_f as the flow front velocity is unknown and varies over time close to the mould surface.

The implementation of air pressure is questionable because of two reasons. First, the cavities are not completely tight and the entrapped air can escape through venting channels or ejector pins. Secondly the air may diffuse into the polymer because of the high melt pressure.

2.5 Heat transfer process in injection moulding

The heat transfer between polymer melt and the heated mould surface probably has the biggest influence on the replication of micro- and nanostructures. It was shown in different investigations that the

heat transfer in the injection moulding process changes with time. The heat flux q can be calculated with equation (2-20) according to (Böckh von, 2011) as:

$$q = \frac{\partial Q}{\partial t} = A \cdot h_{tc} \cdot \Delta T \quad (2-20)$$

Where h_{tc} is the thermal transmittance or heat transfer coefficient, A the area and ΔT the difference between melt processing temperature T_P and mould temperature T_{mould} .

If different mould insert materials are combined, the resulting h_{tc} according to (Böckh von, 2011) can be calculated simply by:

$$\frac{1}{h_{tc}} = \frac{1}{h_{tc1}} + \frac{1}{h_{tc2}} + \dots + \frac{1}{h_{tci}} \quad (2-21)$$

For accurate simulations, correct material properties and parameters are of high importance. The melt temperature in the structures in contact with the colder mould influences the viscosity and therewith also the filling. The h_{tc} values at the polymer-mould and at the mould-cooling channel interface have a significant impact on the cooling speed. Moreover, the heat transfer coefficient depends on pressure, temperature, type of mould material, surface roughness and how intimate the polymer contacts the mould.

Different values were proposed for the heat transfer coefficient at the polymer-mould interface. (Tofteberg and Andreassen, 2010) claimed that the heat transfer in micro- and nanostructures can be as high as $30000 \text{ W m}^{-2} \text{ K}^{-1}$. (Xu et al., 2005) proposed a local variable heat transfer coefficient in a channel with a diameter of $50 \text{ }\mu\text{m}$ depending on a corrected Nusselt number (Nu) as defined in equation (2-22) below. They concluded that this local heat transfer would be $25000 \text{ W m}^{-2} \text{ K}^{-1}$ at the entrance of the channel and drops down to $4000 \text{ W m}^{-2} \text{ K}^{-1}$ at a filling length of $100 \text{ }\mu\text{m}$. (Nguyen-Chung et al., 2008) investigated the correlation between injection pressure and filling speed with the heat transfer coefficient and showed that a good correlation between Moldflow simulations and injection moulding could only be achieved by varying the h_{tc} from $15000 \text{ W m}^{-2} \text{ K}^{-1}$ to $25000 \text{ W m}^{-2} \text{ K}^{-1}$. In stark contrast, (Kim and Turng, 2006) showed a good correlation of numerical simulations with experiments when applying substantially lower values of h_{tc} between 500 and $1000 \text{ W m}^{-2} \text{ K}^{-1}$ depending on the flow velocity. (Dawson et al., 2008) determined an h_{tc} of $7000 \text{ W m}^{-2} \text{ K}^{-1}$ for PMMA in contact with a steel surface. (Cui et al., 2014) calculated the influence of increasing h_{tc} from 5000 to $20000 \text{ W m}^{-2} \text{ K}^{-1}$ and showed, as a result that the filling distance in a microstructure is reduced by a factor of 2.5 when the higher h_{tc} was applied. (Lin et al., 2010) used $9000 \text{ W m}^{-2} \text{ K}^{-1}$ in order to get a good correlation of analytical calculations with injection moulding.

The convective heat transfer coefficient is also included in the equation of the Nusselt number:

$$\text{Nu} = \frac{h_{tc} \cdot D}{k} \quad (2-22)$$

D is the characteristic length; in case of the cooling channel it would be the diameter and k is the thermal conductivity of the fluid, e.g. water or oil.

Instead of the thermal heat transfer coefficient the thermal contact resistance (t_{cr}) was used in various investigations for describing the heat transfer between polymer and mould as was done among others by (Delaunay et al., 2000). The t_{cr} is defined as:

$$t_{cr} = \frac{1}{h_{tc}} \quad (2-23)$$

The t_{cr} analysed by (Bendada et al., 2004) for PP in contact with a metal mould was in the range of 0.0001 to $0.0004 \text{ m}^2 \text{ K W}^{-1}$.

Obviously, there is a considerable high discrepancy between the various applied values of the heat transfer coefficients in literature.

3. MATERIALS AND METHODS

3.1 Polymers and polymer properties

3.1.1 General description of the polymers used for injection moulding

Polymethylmethacrylate (PMMA)

PMMA is a rather inexpensive amorphous thermoplastic polymer and quite commonly used for of titerplates, optical waveguides, automotive lighting, instrument cluster covers, optical lenses and displays. The chemical structure of PMMA is shown in Fig. 3.1:

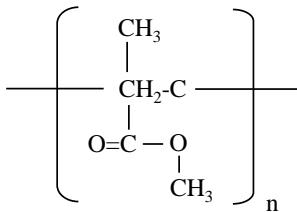


Fig. 3.1: Chemical structure of PMMA.

PMMA has the best UV-resistance of all transparent polymers because of its high light transmission also in the UV range. On the other hand it shows low stress cracking resistance in contact with solvents and is rather brittle. This brittleness can result in demoulding issues. The glass transition temperature of 100°C-120°C (dependent on the molecular weight) prevents the usage for high temperature applications.

In these investigations PMMA Plexiglas[®] 7N from Evonik (Marl, Germany) was used.

Amorphous Polyamide (A-PA)

Transparent polyamides are mainly used for sunglasses and frames, displays, filter bowls, flow meters, baby bottles but also for sensors and medical products.

A-PA has a high ductility which is favourable for demoulding. The overall stress-crack resistance is better compared to PMMA or PC. The glass transition temperature range is broad. Commercial grades are available with a T_g of up to 160°C, but with the disadvantage of an increasing viscosity.

For this work amorphous polyamide (A-PA, Grilamid[®] TR55LX) from EMS-Chemie (Domat-Ems, Switzerland) was chosen. Grilamid[®] TR55LX is a blend of PA12/MACMI and PA12.

The chemical structure of PA12/MACMI and PA12 is shown exemplarily in Fig. 3.2.

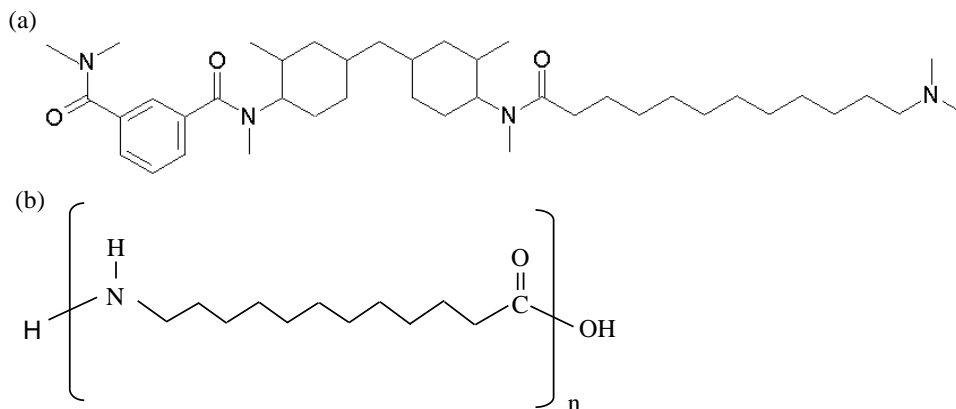


Fig. 3.2: Chemical structure of (a) PA12/MACMI and (b) PA12.

Cyclic Olefin Copolymer (COC)

COC is used for example in light guide panels. Other typical applications are blister packages, medical devices and diagnostics (micro titerplates, lab-CDs, micro-pumps).

Cyclic olefin copolymers are manufactured by chain copolymerization of cyclic monomers such as 8,9,10-trinorborn-2-ene (norbornene) or 1,2,3,4,4a,5,8,8a-octahydro-1,4:5,8-dimethanonaphthalene (tetracyclododecene) with ethene. Topas[®] is the trade name for cyclic olefin copolymers (COC) made by Topas[®] Advanced Polymers (Oberhausen, Germany). In contrast to the partially crystalline polyolefins like polyethylene (PE) or polypropylene (PP), the Topas[®] COC family, consists of amorphous, transparent copolymers based on cyclic and linear olefins. The chemical structure of COC is shown in Fig. 3.3:

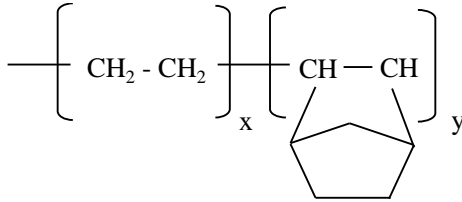


Fig. 3.3: Chemical structure of COC.

Characteristic properties of COC are low water absorption (< 0.01%), good biocompatibility, a refractive index of 1.53 and high light transmission also in the UV-range which makes it an ideal material for lab-on-the-chip diagnostics with optical bio-detection methods. By variation of the norbornene content, the glass transition temperature T_g can be varied over a wide range from 75°C to 180°C. But similar to PMMA, COC is very brittle and shows high sensitivity to stress cracking, especially in contact with oils and fats or apolar solvents like toluene or hexane.

In this investigation Topas[®] COC 5013L-10 was used. This grade contains also a release agent for better demoulding.

Polypropylene Copolymer (PP-C)

Polypropylenes are commodity polymers which are used for almost all kinds of applications. In contrast to homo-polymers (PP-H), the ductility can be improved by copolymerization with ethylene. The chemical structure of a block-copolymer (PP-B) is shown in Fig. 3.4:

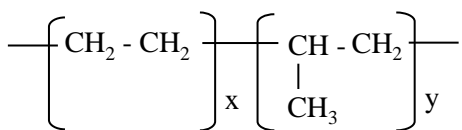


Fig. 3.4: Chemical structure of a block-copolymer (PP-B).

PP-C is a semi-crystalline polymer, inexpensive and easy to process.

In this investigation PPC-711-70RNA from Braskem (Sao Paulo, Brazil) was used. PPC-711-70 RNA is a high impact PP-B developed at Dow Chemicals (Michigan, US) especially for high speed thin wall injection moulding. It is a very low viscous copolymer featuring good impact strength, even at low temperatures. This good impact strength is based on the ethylene blocks embedded in the PP matrix.

Typical applications for this grade are packaging, household and medical products.

Compared to amorphous materials the crystallization process of PP during cooling causes more shrinkage with the result of more warpage and lower dimensional stability. During crystallisation heat is released which has an effect on solidification and viscosity. This is the reason why the flow simulation of semi-crystalline materials is generally much more difficult compared to amorphous polymers.

Polystyrene (PS)

Standard PS is amorphous, highly transparent, inexpensive but as PMMA rather brittle. It is used for packaging, food and beverage, household or medical products.

By copolymerization of styrene with butadiene the impact properties can be increased. The chemical structure of PS is shown in Fig. 3.5:

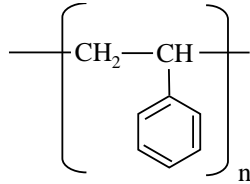


Fig. 3.5: Chemical structure of polystyrene (PS).

In this work a general purpose standard PS grade PS 158K from BASF (Ludwigshafen, Germany) was used. This specific grade has excellent clarity and good processability. Interestingly it is a rapid freezing grade which should have a negative influence on the replication fidelity.

Polyoxymethylene (POM)

POM is semi-crystalline and has a high strength, toughness and stiffness with low water absorption and low coefficient of friction. It is used for mechanical and electrical parts such as gears, valve bodies or connectors and for many other applications also in the medical and food industry.

The chemical structure of POM is shown in Fig. 3.6.

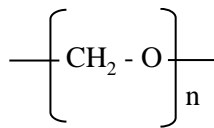


Fig. 3.6: Chemical structure of polyoxymethylene (POM).

In this work a Copolymer grade Hostaform[®] C9021 from Celanese (Kaiserslautern, Germany) was used. This specific grade is a standard injection moulding grade.

3.1.2 General and mechanical properties

In Table 3-1 the most important properties of the polymers used are summarized.

Shrinkage and mechanical properties are particularly relevant for demoulding. A low shrinkage is favourable for less demoulding issues because of lower shear and bending stresses in the ejection phase. Semi-crystalline materials like PP are more critical related to shrinkage on the one hand but are more flexible on the other hand. Ejection at higher temperatures would take place on a lower shrinkage level, which is also favourable for demoulding, but can result in more sticking and deterioration of the part geometry by irreversible plastic deformation.

High ductility (high impact strength) or more elasticity (low E and high yield strain) is favourable for less deformation in the ejection phase. Low water absorption is relevant for good dimensional stability of the product in humid environment.

Table 3-1: Overview of important material data (various source: material data sheets and brochures from producers, Moldflow and Campus database).

Property	Method	Evonik Plexiglas® 7N	Topas Topas® 5013L-10	Dow C711- 70RNA	BASF PS 158K	EMS Grilamid® TR55 LX	Celanese Hostaform® C9021
Product nomenclature	ISO 1874	PMMA	COC	PP-C	PS	A-PA	POM
Morphology		Amor- phous	Amor- phous	Semi- crystalline	Amor- phous	Micro- crystalline	Semi- crystalline
Tensile modulus (E) [MPa]	ISO 527- 1/-2	3200	3200	1250	3300	1900	2850
Yield strain [%]	ISO 527	3.5	1.7	7	3	6	9
Unnotched impact strength (Charpy) +23°C [kJ m⁻²]	ISO 179 1eU	20	13	no break	<25	no break	180
Notched impact strength (Charpy) +23°C [kJ m⁻²]	ISO 179 1eA; 23°C	2	1.6	8	3	9	6.5
Density [g cm⁻³]	ISO 1183, dry	1.19	1.02	0.90	1.05	1.04	1.41
Water absorption [%]	ISO 62, 23°C/sat.	2	0.01	-	0.1	2.5	0.65
Shrinkage [%]	ISO 294-4	0.3-0.6	0.4-0.7	2-3%	0.4-0.7	0.5-0.6	1.8-2

3.1.3 Thermal and processing relevant properties

For the injection moulding process, but also for wetting phenomena, the thermal polymer properties like glass transition temperature T_g , melt temperature T_m or no-flow temperature T_{no} are highly important with respect to replication fidelity and demouldability. Additionally, the recommended processing temperatures were used from data sheets of the polymer producers and the respective mould and cylinder temperatures T_{cyl} and T_{mould} were set specifically for each polymer. Except for PP and PS all materials were dried in a dry-air dryer as recommend in the material supplier data sheets.

Table 3-2: Relevant temperatures for the injection moulding process.

Property	ISO 1874	PMMA	COC	PP-C	PS	A-PA	POM
T_g and T_m [°C]	ISO 11357, dry	110	134	-10 / 160	100	110	-50 / 166
T_{cyl} [°C]	Applied	250	280	220	230	280	205
T_p [°C]	Recommended	220-260	240-300	190-260	180-280	250-280	190-230
T_{mould} [°C]	Recommended	60-90	95-125	20-50	10-60	40-70	80-120
T_{mould} [°C]	Applied	80	120	50	70	70	90
Pre-drying [°C; h]	Recommended	90; 3	100; 6	no	no	80; 4	120; 3

For comparative reasons the cylinder temperatures should be chosen according to a certain rule, e.g. $T_g + 140^\circ\text{C}$, as it is the case for PMMA. However, for moderate or high viscous polymers the maximum injection pressure of the machine would be reached which is the reason why materials like A-PA were processed at the upper limit of the recommended melt temperature ($T_g + 170^\circ\text{C}$). The mould temperatures were all set to the upper limit and even above the recommended temperature range in such a way that ejection was still possible without sticking. For specific investigations T_{mould} was varied and changes will be listed in the respective Chapter.

Thermal heat properties

For the calculation of the contact temperature, the frozen-layer thickness and other filling phenomena, the thermal properties at the particular polymer melt temperature were taken from the Moldflow data base and are listed in Table 3-3.

Table 3-3: Thermal properties (source: Moldflow database 2014).

Material	Polymer melt temperature T_p [°C]	Specific heat capacity c_p [J kg ⁻¹ K ⁻¹]	Coefficient of thermal conductivity k [W m ⁻¹ K ⁻¹]	Melt density ρ [kg m ⁻³]
PP	220	2700	0.153	738
PMMA	245	2120	0.19	1057
A-PA	265	2200	0.2	950
COC	270	2750	0.1875	905
PS	230	1975	0.155	946
POM	210	2168	0.224	1149

Especially for a precise modelling in simulations it is favourable if the temperature dependent specific heat capacity and thermal conductivity are available. Those data are implemented in Moldflow for PP and COC, as can be seen in Fig. 3.7, but not for the other polymers.

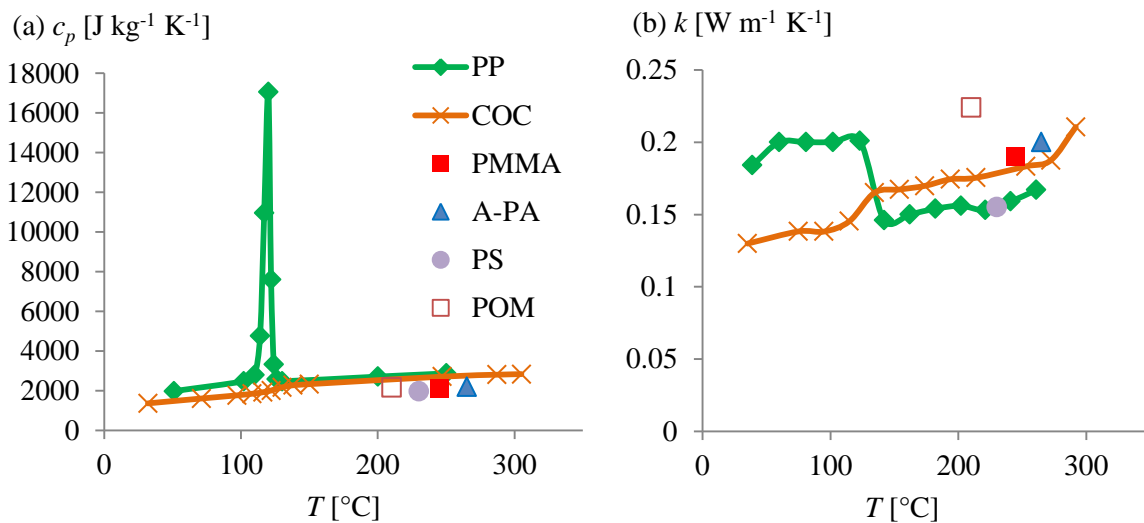


Fig. 3.7: Dependence of (a) specific heat capacity c_p and (b) thermal conductivity k on the temperature of the polymer (source: Moldflow database 2014).

The heat capacity further depends on the cooling speed which can be very high in injection moulding. If the heat capacity was measured with a lower cooling speed the introduced error for amorphous materials would not be as significant as for semi-crystalline materials according to (Kennedy and Zheng, 2013). The importance of correct thermal conductivity values for flow and cool simulations using Moldflow was shown by (Urquhart and Brown, 2004) who demonstrated an inverse correlation of thermal conductivity with the freezing time.

Shrinkage and pressure, volume, temperature (PvT)-curves

The densities or specific volumes of polymers depend on temperature and pressure as can be seen in the so called PvT-curves (Fig. 3.8). Volume contraction during solidification has a significant influence on the replication fidelity as well as the demoulding. Unfilled amorphous polymers display shrinkage in the range of 0.3 to 0.9% and semi-crystalline polymers exhibit values from 1.0 to 2.5% and beyond (more than 4%), depending on the crystallinity and section thickness (Fischer, 2012).

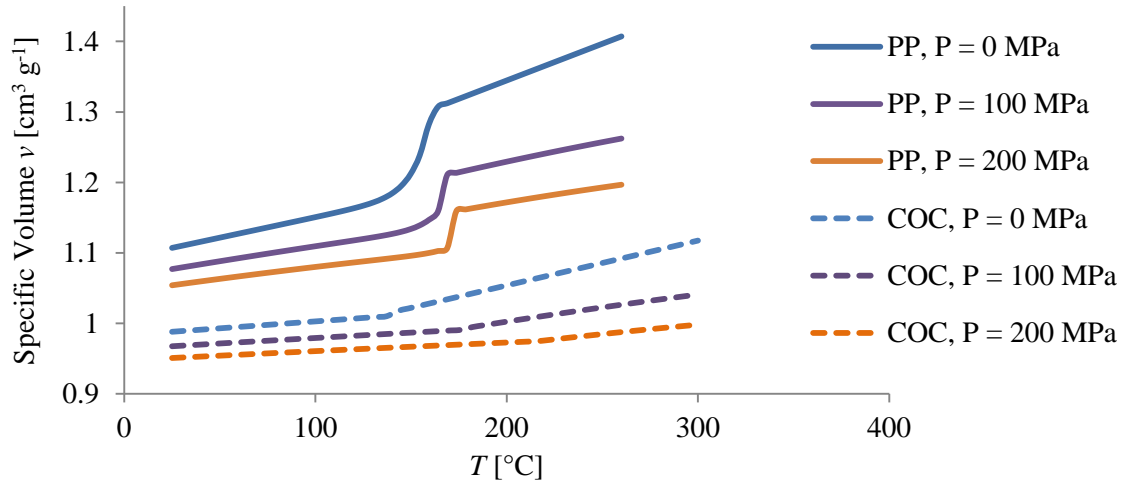


Fig. 3.8: Pressure, volume, temperature (PvT)-curves exemplary for amorphous polymers like COC and semi-crystalline polymers like PP showing significant differences in specific volume change dependent on temperature, taken from Moldflow data base.

In order to achieve a replication ratio of 100%, the shrinkage needs to be compensated during cooling by holding and/or compression pressure. If the shrinkage is irregular, deformations of structures can occur with the result of pronounced demoulding issues. (Schift et al., 2000b) investigated the radial shrinkage of an injection moulded compact disc with nano-features in PC dependent on the distance from the injection point at the disc centre and found that the overall shrinkage at the outer side of the disc was around 10% higher compared to the centre area.

The density or specific volume of the different polymers is represented in simulation programs like Moldflow by a modified 2-domain Tait-model according to the following equation:

$$\rho(T, P) = \{V_0(T)[1 - C \ln(P/B(T))] + V_i(T, P)\}^{-1} \quad (3-1)$$

Where B is the pressure sensitivity and C a universal constant equal to 0.894.

3.1.4 Rheological properties

The viscosity curves were also taken from the Moldflow database (Autodesk, 2014). These parameters were determined by the raw material producers with a capillary viscometer or modified injection moulding machine at specific processing conditions and were also used for the simulations with Comsol (cf. Chapter 6.6.5). In order to compare the different polymers with each other, all Cross-WLF coefficients were extracted from the database and compiled in Table 3-4:

Table 3-4: Cross-WLF coefficients extracted from Moldflow database.

Coefficient	unit	PMMA	PP	A-PA	COC	PS	POM
n	-	0.2813	0.2604	0.2	0.4027	0.2056	0.2075
τ^*	Pa	67160.3	5.74E+04	5.68E+05	4.61E+04	3.62E+04	311959
D_1	Pa s	3.26E+18	8.01E+19	1.40E+28	4.51E+17	2.96E+12	2.51E+15
D_2	K	377.15	263.15	200	343.15	373.15	223.15
D_3	K Pa ⁻¹	0	0	0	1.20E-07	0	0
A_1	-	46.032	49.706	66.125	44.743	28.314	34.878
A_2	K	51.6	51.6	51.6	51.6	51.6	51.6

The parameter D_3 represents the dependence of the transition temperature on pressure. Interestingly, this dependence is only implemented for COC. Based on these coefficients the viscosity curves for different polymers at the respective processing temperature (Fig. 3.9) can be plotted for the different polymers used in this thesis.

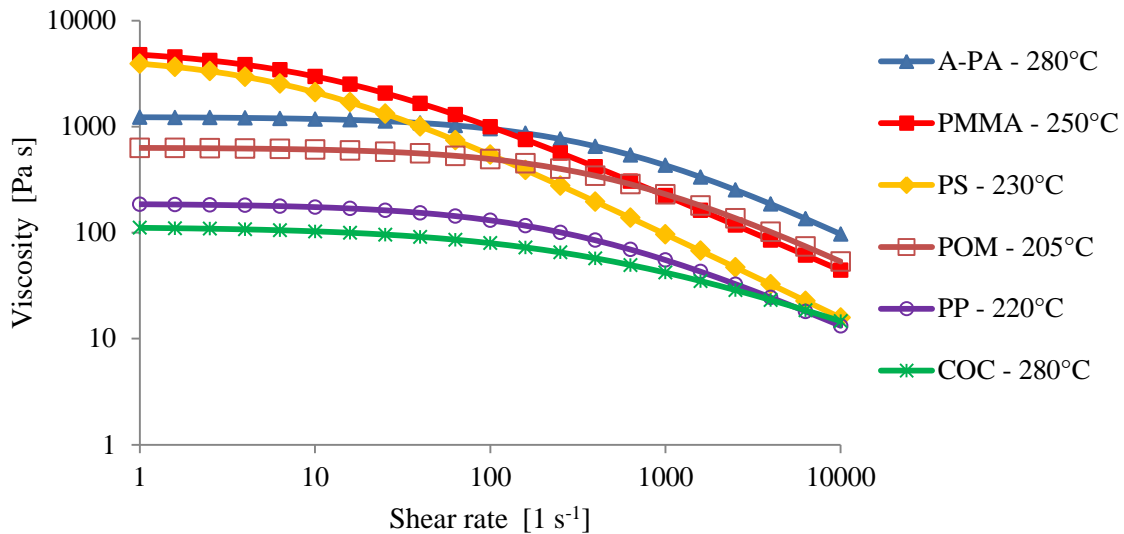


Fig. 3.9: Viscosity curves based on Cross-WLF coefficients taken from Moldflow data base.

It is worth to mention that the polymers show differently developed shear thinning which is the reason why the viscosity curves in Fig. 3.9 cross each other.

By comparing these curves a viscosity ranking can be made at different shear rates. The viscosity at zero shear rate η_0 could be important for the compression and for the filling of micro- and nanostructures in general, assuming low flow velocities in small features. The shear rate $\dot{\gamma}$ in the macro cavity was in the range of 600 - 700 s⁻¹ for most of the trials. For that reason the viscosity was compared at a shear rate of 631 s⁻¹. The comparison of zero shear viscosities η_0 are plotted in Fig. 3.10a, and those at 631 s⁻¹ in Fig. 3.10b.

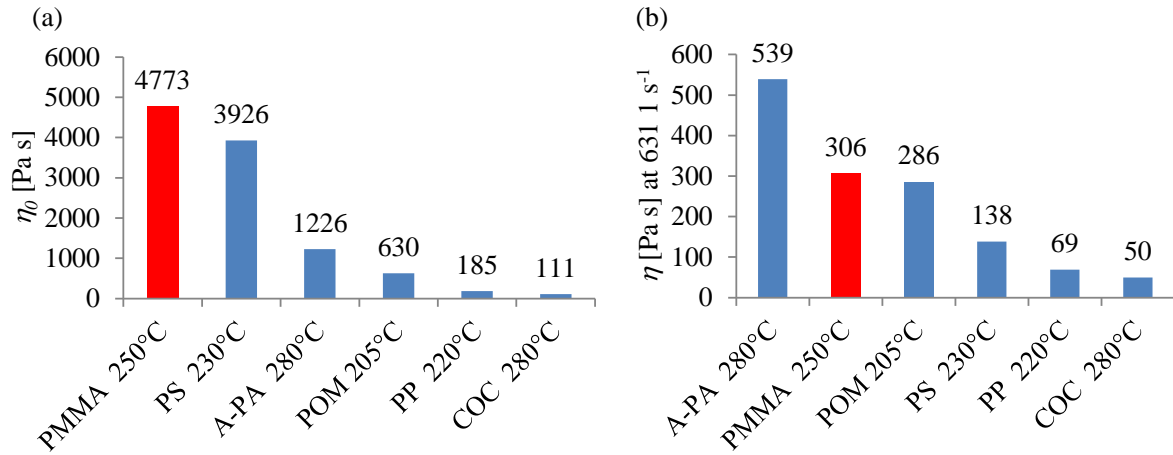


Fig. 3.10: Viscosity ranking of all polymers at a shear rate of (a) 10^{-2} s^{-1} (Newtonian plateau) and (b) 631 s^{-1} at the corresponding melt processing temperatures used for injection moulding.

According to the ranking in Fig. 3.10 the best replication should be possible with PP and COC. Less clear is the filling behaviour of PMMA and A-PA because the order of viscosity changes depending on the shear rate. That is one reason why the focus of all investigations was on PMMA in comparison to A-PA. COC and PP were used as high flow reference polymers. Additionally, differences between semi-crystalline and amorphous morphology were investigated when comparing PP with COC. Only in a few investigations PS was included.

One of the main issues is that this viscosity data is based on macroscopic scale measurements and may therefore not be suitable to be used in micro- and nanoscale filling because of additional effects originating from surface tension, wall-slip, nano-roughness or changes in the heat transfer. This is the reason why the viscosity was additionally measured online, directly in the injection mould, as will be described in detail in Chapter 3.3.3.

3.2 Polymer and structure analysis

3.2.1 No-flow temperature measurement

For accurate determination of the filling behaviour of functional structures it is important to know the temperature at which the polymer stops to flow. This so called no-flow temperature T_{no} or transition temperature T_{trans} (terminology used e.g. by Moldflow) has a strong influence on the replication fidelity but is rather difficult to determine. (Mannella et al., 2011) summarized various methods how to measure T_{no} and mentioned among other theories that T_{no} of amorphous polymers typically lie 20 to 70°C above T_g , whereas semi-crystalline polymers feature T_{no} values of 10 to 80°C below T_m depending on the super-cooling. Moreover, the rate of cooling influences the crystallization and also the viscosity. If a semi-crystalline polymer is cooled very fast, it may continue to flow even below the transition temperature (Kennedy and Zheng, 2013).

Thus, T_{no} is utmost important for the definition of the proper mould temperature in the injection moulding process. Values for T_{no} were determined with a melt flow index (MFI) measuring device MI-2 from Göttfert (Buchen, Germany) by detecting the melt temperature at which a zero melt flow mass rate (MFR) was observed. The melt was pressed with 21.6 kg and 26.6 kg through a capillary with a diameter of 2 mm, corresponding to pressures 33 MPa and 41.5 MPa, respectively. This dynamic method with fluid motion was originally introduced by Moldflow as an alternative to static methods like differential scanning calorimetry (DSC). However, in both methods cooling rates are rather low compared to the fast temperature decrease in injection moulding, which can distort the T_{no} measurements.

3.2.2 Surface tension measurements

The surface tension σ_L of the polymer melt was determined by the pendant drop method. The contact angle θ of the polymer melt on the mould materials with and without anti-adhesion coatings was measured by the sessile drop method. For both methods a hot chamber was used with a drop shape analysis system DSA100B Version 1.90.0.14 (2005) from Krüss, (Hamburg, Germany), described in detail by (Kwok et al., 1998), (Yang et al., 2010) and (Wulf et al., 1999).

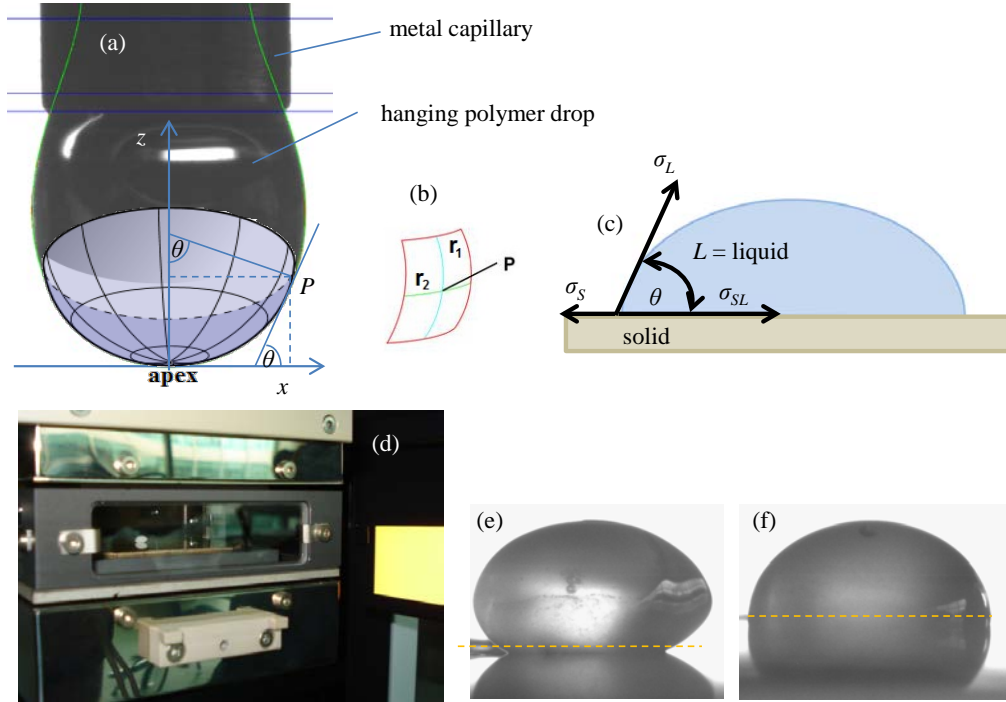


Fig. 3.11: (a) Principle of pendant-drop test: hanging polymer melt at the end of the metal capillary; (b) horizontal and vertical radii of curvature at point P; (c) principle of sessile drop method; (d) hot chamber used for sessile and pendant drop method; (e) start of melting a polymer granule (f) molten polymer granule at equilibrium used for measuring contact angles of polymers on inserts with circle fitting.

The drop shape method is based on gravity and surface tension. As soon as these forces are in hydro-mechanical equilibrium, the surface tension can be determined by analysing the shape of the drop using the Young's equation (3-4). Equation (3-2) describes the difference in pressure Δp between the inside (polymer melt) and outside (air or inert gas, e.g. N₂) of a curved object, for instance a drop with r_1 and r_2 , which are the main radii of curvature of a sectional area of the drop surface with respect to the interfacial tension σ .

$$\Delta p = \sigma \left(\frac{1}{r_1} + \frac{1}{r_2} \right) \quad (3-2)$$

In the hydro-mechanical equilibrium the following relationship can also be applied:

$$\Delta p_{apex} - \Delta p_p = z \cdot \Delta \rho_p \cdot g \quad (3-3)$$

With Δp_{apex} = pressure difference at apex; Δp_p = pressure difference at point P (x, z); z = vertical height above the reference plane; $\Delta \rho_p$ = difference in density between the drop liquid and its surroundings (melt densities were used from Moldflow database, listed in Table 3-5.); g = gravitational acceleration (negative for pendant drop).

Table 3-5: Melt densities ρ_{melt} at polymer melt temperature T_p (source: Moldflow database 2014).

Material	PP	PMMA	A-PA	COC	PS	POM
ρ_{melt} [kg m ⁻³]	738	1057	950	905	946	1149
T_p [°C]	220	245	265	270	230	205

The shape of the drop is mainly determined by the surface energy and the gravity. At the three-phase boundary the thermodynamic equilibrium can be described by the Young's equation (Lee, 1991).

$$\cos \theta = \frac{\sigma_s - \sigma_{LS}}{\sigma_L} \quad (3-4)$$

With σ_L = surface energy of the liquid; σ_s = surface energy of the solid; σ_{LS} = interfacial energy between liquid and solid; θ = contact angle.

The surface energy is based on different effects, driven by a sum of forces like dispersive forces, hydrogen bonds, polar interactions and acid/base forces.

$$\sigma_s = \sum \sigma_s^n \quad (3-5)$$

According to Owens, Wendt, Rabel and Kaelble the surface tension of each phase can be split up into a polar (P) and a dispersive (D) component.

$$\sigma_L = \sigma_L^D + \sigma_L^P \quad (3-6)$$

$$\sigma_s = \sigma_s^D + \sigma_s^P \quad (3-7)$$

Combined with the Young's equation (3-4) the result is as follows:

$$\sigma_L \cdot (1 + \cos \theta) = 2 \cdot \left(\sqrt{\sigma_s^D \cdot \sigma_L^D} + \sqrt{\sigma_s^P \cdot \sigma_L^P} \right) \quad (3-8)$$

Which can be rewritten as:

$$\frac{(1 + \cos \theta) \cdot \sigma_L}{\left(2 \cdot \sqrt{\sigma_L^D} \right)} = \sqrt{\sigma_s^P} \cdot \sqrt{\frac{\sigma_L^P}{\sigma_L^D}} + \sqrt{\sigma_s^D} \quad (3-9)$$

Equation (3-9) according (Fowkes, 1964), corresponds well to a linear regression curve $y = m x + b$ with:

$$x = \sqrt{\frac{\sigma_L^P}{\sigma_L^D}} \quad (3-10)$$

$$y = \frac{1}{2} \left[(1 + \cos \theta) \frac{\sigma_L}{\sqrt{\sigma_L^D}} \right] \quad (3-11)$$

$$m = \frac{dy}{dx} = \sqrt{\sigma_s^P} \quad (3-12)$$

$$b = \sqrt{\sigma_s^D} \quad (3-13)$$

In order to calculate the surface energy, the contact angle has to be determined for at least two different liquids with known surface tensions as listed in Table 3-6.

Table 3-6: Surface tension components of distilled water and diiodomethane at different temperatures.

Liquid	T [°C]	σ_L [mN m ⁻¹]	σ_{LD} [mN m ⁻¹]	σ_{LP} [mN m ⁻¹]
Distilled water	20	72.8	26.4	46.4
	45	68.8	20.6	48.2
	70	64.5	19.3	45.2
Diiodomethane	20	50.8	50.8	0
	45	47.2	47.2	0
	70	43.8	43.8	0

The surface tension values for distilled water and diiodomethane for different temperatures were calculated with equation (3-14) and (3-15), respectively, according to (Sun et al., 2006):

$$\sigma_L = 235.8 \left(\frac{374 - T}{647.15} \right)^{1.256} \left[1 - 0.625 \left(\frac{374 - T}{647.15} \right) \right] \quad (3-14)$$

$$\sigma_L = 53.48 - 0.14154T + 4.9567 \cdot 10^{-5} T^2 \quad (3-15)$$

3.2.3 Microscope structure analysis

The micro- and nanostructures were analysed with different microscopy techniques. A confocal laser scanning microscope (CLSM, VK-X200) from Keyence (Osaka, Japan) was used for topographical analysis of microstructures. The height was always measured at least at three different positions. The CLSM can be used for structures down to 500 nm. Two scanning electron microscopes (SEM), i.e. Tescan Vega 3 from Tescan (Brno, Czech Republic) and Zeiss Gemini Supra 55VP from Carl Zeiss Microscopy GmbH (Jena, Germany), were used for analysis of defects on the microstructures and for inspection of the nanostructured mould inserts. Additionally, detailed analysis of the latter was accomplished by atomic force microscopy (AFM, VEECO DI 3100) from Digital Instruments (New York, USA) with DP15/STING/AIBS cantilevers from MicroMasch (Tallinn, Estonia). High aspect ratio nanostructures were measured with AppNano Harta12-2 tips (12° tilt compensation, 2 µm spike length, 50 nm Al reflex coating, tip radius = 30 nm) from AppNano (Mountain View, USA). The AFM measurement data was processed and analysed with Gwyddion 2.36.

3.3 Injection moulding machine, mould and sensors

All trials were carried out on an injection moulding machine from Arburg (Lossburg, Germany), Type 320 A 600-170 with an hydraulic clamping unit with a maximum clamp force of 600 kN (60 t) and an electrical injection unit with a maximum injection velocity of 142 cm³ s⁻¹, a 3-zone screw with a diameter of 30 mm with a maximum injection volume of 77 cm³ and a maximum injection pressure of 2000 bar.

The variothermal injection compression mould (Fig. 3.12) was designed internally and produced at AdvalTech FOBOHA (Muri, Switzerland), constructed with a spring loaded compression plate with 10 springs (total spring force 100 kN) and four changeable inserts for testing of different structure designs. The cavities with the clamped inserts had a separate water circuit so that the temperature could be varied fast and independent from the rest of the mould.

The wall thickness range of the mould can be varied from 0.2 mm to 3 mm by using distance discs.

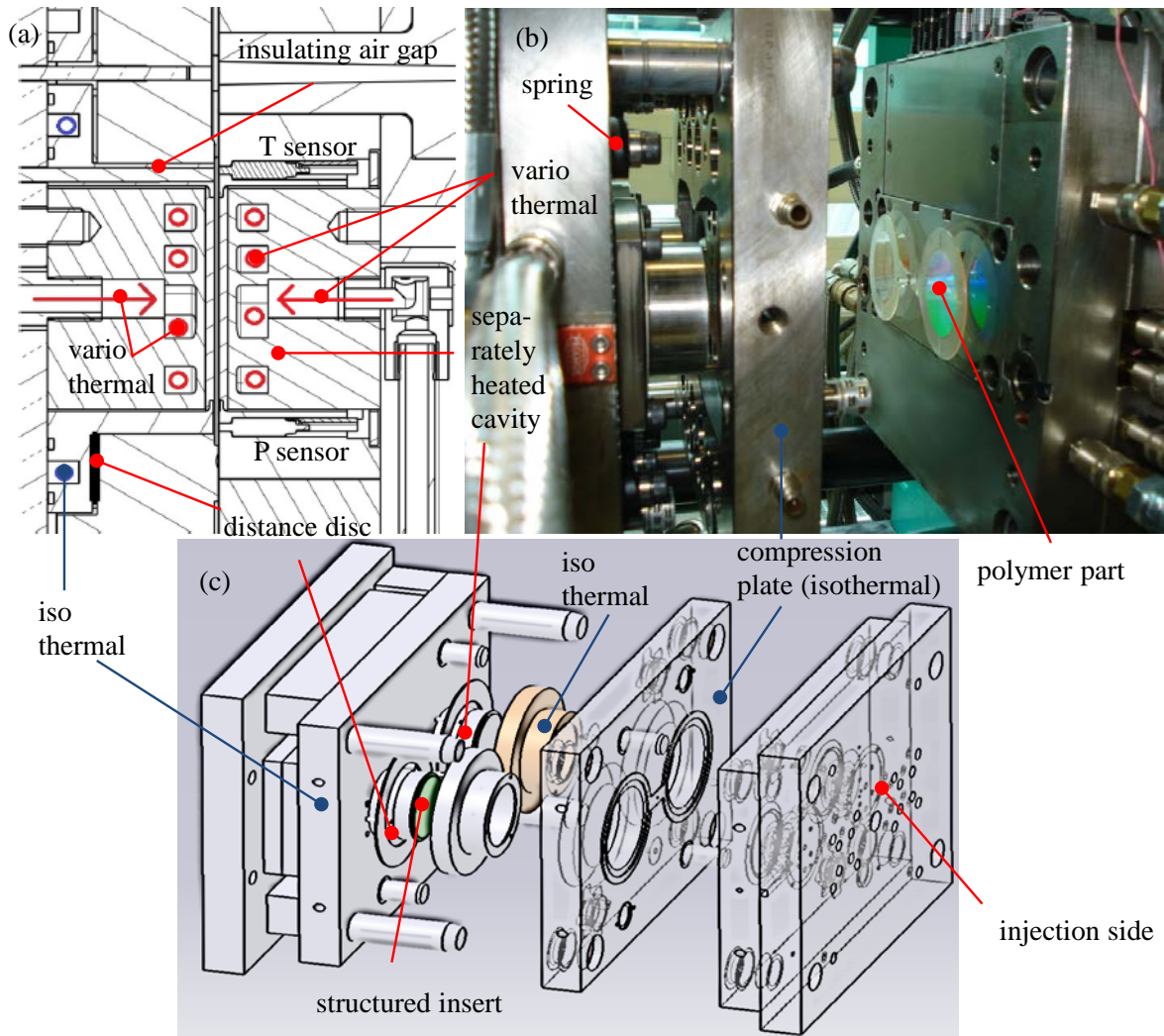


Fig. 3.12: (a) CAD cross-section of the dynamic heated cavities with T and P sensors; (b) photograph of injection compression mould with replicated polymer part on injection side; (c) 3D CAD drawing of the injection mould.

3.3.1 Temperature and pressure sensors

The mould was equipped with four temperature sensors (4003B, Blue Line 5080-16T) and three piezoelectric pressure sensors (6006BB, Blue Line 5080-16p) from Priamus (Schaffhausen, Switzerland) allowing precise process control (e.g. determination of switch over pressures) as well as online monitoring and data extraction during the moulding process.

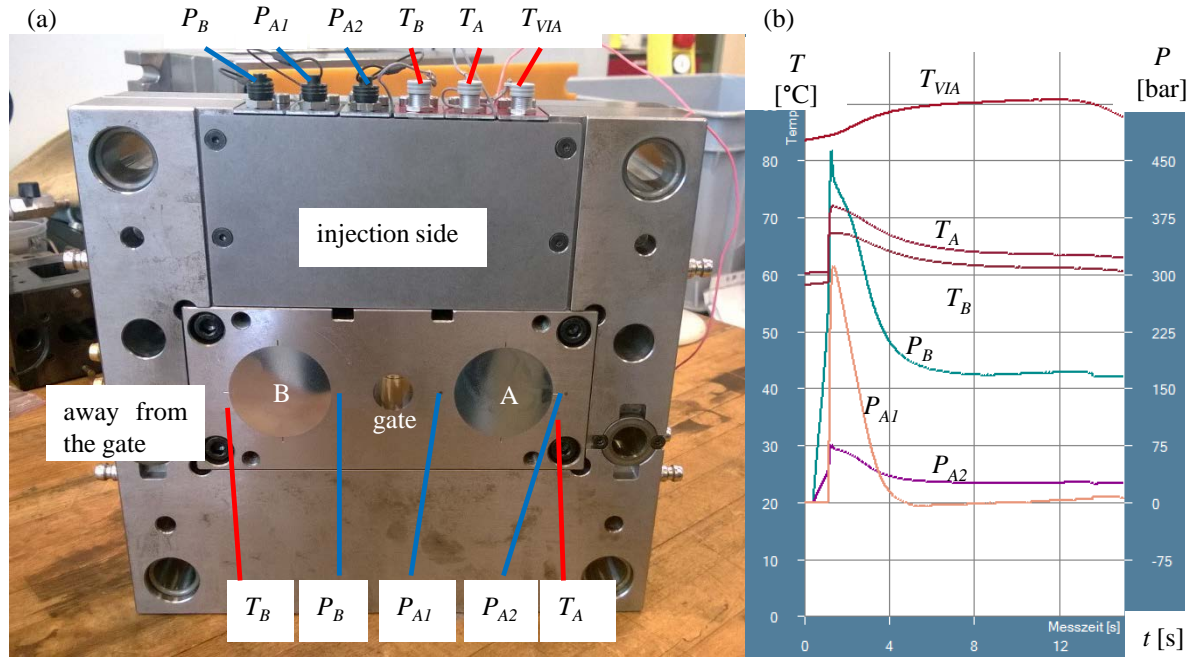


Fig. 3.13.: (a) Injection side of the mould showing the positions and connections of the temperature and pressure sensors; the temperature sensor T_{VIA} was embedded in the variothermal cylinder block on the injection side in cavity A to control the thermal cycles; (b) corresponding measured pressure and temperature curves.

3.3.2 Dynamic heating: Variothermal process control

The switching between hot and cold water was controlled with two temperature sensors embedded 1 mm behind the backside of the 2 mm thick insert and triggered by the signal from T_{VEA} (ejection side) whereas T_{VIA} (injection side) was used for control measurements. The total distance of the cooling channel to the cavity was 2 mm + insert thickness.

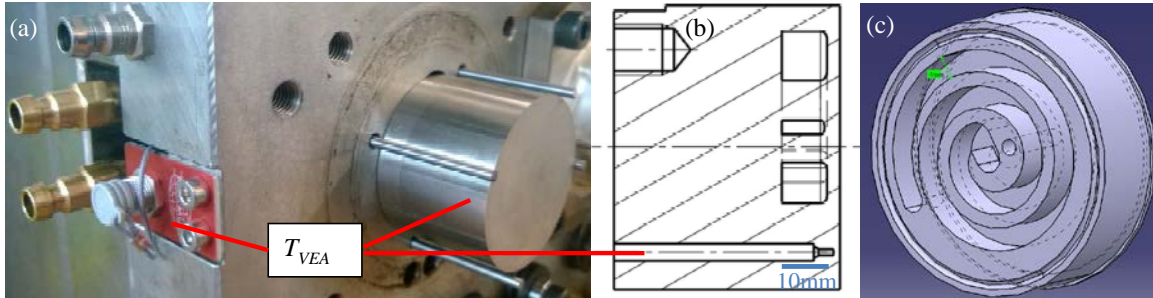


Fig. 3.14: (a) Ejection side with temperature sensor T_{VEA} for variothermal process control; (b) section drawing of variothermal cylinder with sensor; (c) 3D CAD drawing showing the flow cross-section of 8 mm x 4 mm channel.

Variothermal cycling of the mould temperature was accomplished with a two chamber water system composed of two control units (HB-160Z2) from HB-Therm (St. Gallen, Switzerland) operated at two temperatures between 20°C to 160°C with a pump capacity of 60 l min⁻¹ and a cooling power of 30 kW combined with a dedicated switching unit (HB-VS180-20).

The focus in this thesis was not to run tests with shortest cycle times but to achieve good replication fidelity with a simple, reliable and cost-efficient technology. For rapid temperature cycles, infrared, ceramic or inductive heating with heating rates of up to 60 K s⁻¹ (Michaeli et al., 2008) would be the faster technologies, especially if high mould temperatures (> 140°C) are necessary.

A good overview of different variothermal heating methods was presented by (Yao et al., 2008) and in the review article of (Zhiltsova et al., 2013). A representative curve showing the variothermal heating cycle can be seen in Fig. 3.15.

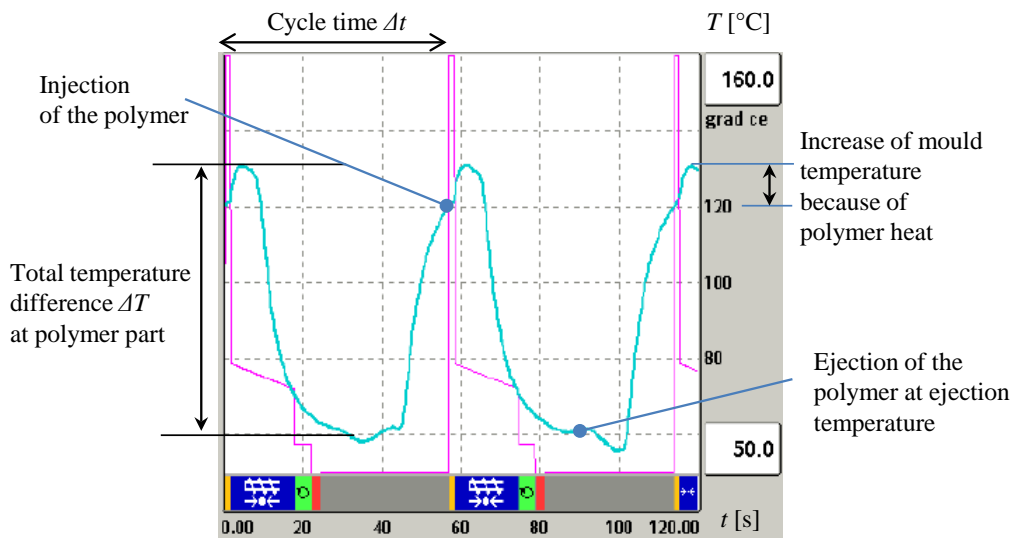


Fig. 3.15.: Measured mould temperature (blue) and hydraulic pressure (pink) curves of a variothermal heating process with temperature sensor T_{VEA} : The mould is heated dynamically with cold and hot water.

3.3.3 Online viscosity measurements with pressure and temperature sensors

Additionally to Cross-WLF rheology curves taken from Moldflow data base, the viscosity was measured online with a pressure (P_I) and temperature sensor (T_I) from Priamus:

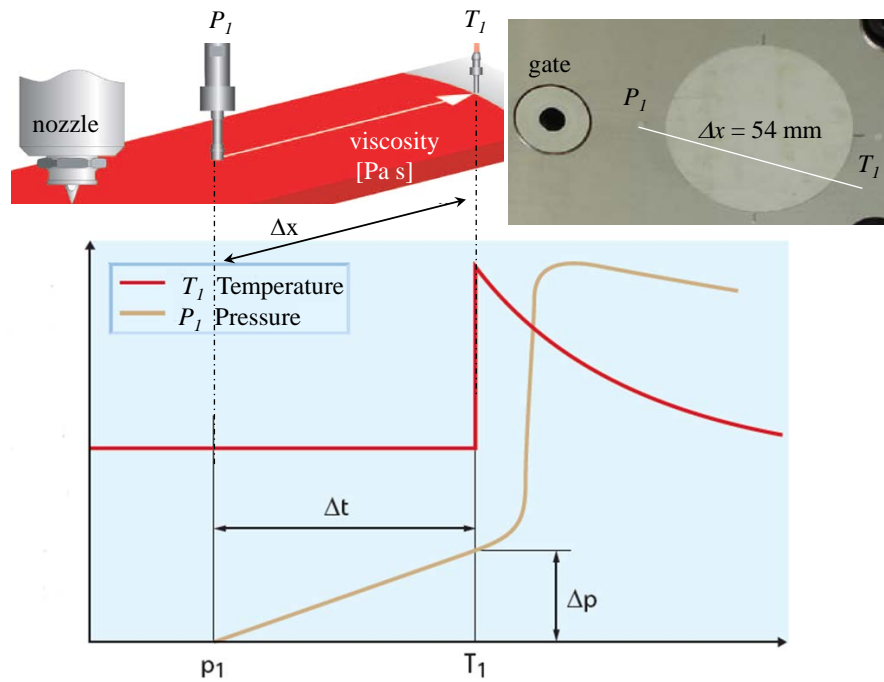


Fig. 3.16: Visualization of online measurement principle of polymer viscosity with a pressure and temperature sensor from Priamus (Bader and Zeller, 2010).

By adapting equation (2-5) to $\eta = \tau / \dot{\gamma}$, the viscosity can be calculated, provided that the distance Δx between P and T sensor and the part thickness z are known (for the mould used, Δx was 54 mm and $z = 1$ mm). The shear rate can be determined by measuring the time the melt needs to pass from the pressure sensor P to the temperature sensor T . The shear stress τ is approximated from the pressure increase ΔP measured at the pressure sensor near the gate after the time difference Δt when the melt contacts the temperature sensor at the end of the cavity.

The online viscosity measurements of four different polymers were compared with the values based on the Cross-WLF model, taken from the Moldflow data base (Fig. 3.17).

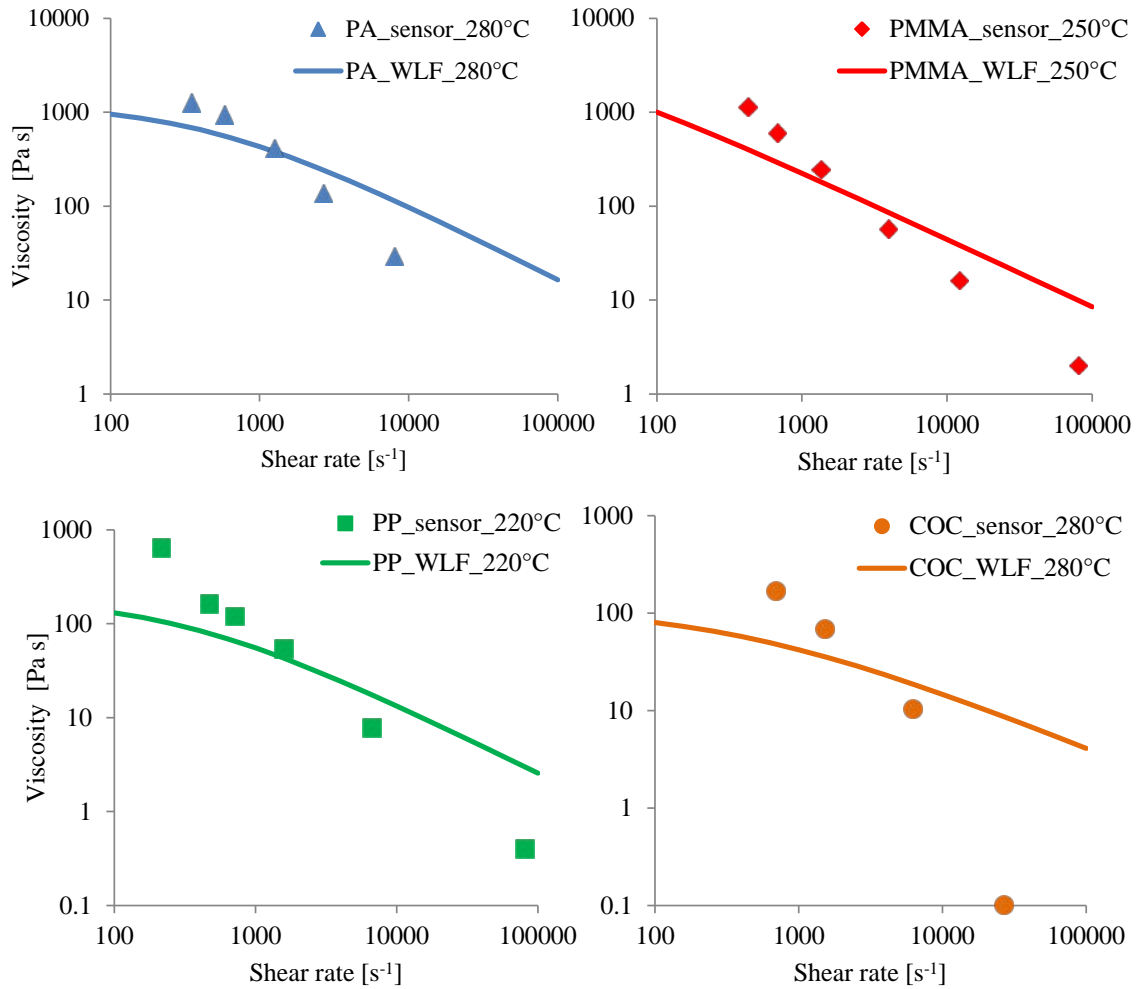


Fig. 3.17: Comparison between calculated Cross-WLF model viscosities and online sensor measurements showing good correlation for moderate shear rates ($600 - 4000 \text{ s}^{-1}$).

The online viscosity measurements reveal higher viscosities at low shear rates and lower viscosities at high shear rates compared to the Cross-WLF model. At low shear rates, the contact time with the mould is substantially longer and, thus, the melt cools down before reaching the temperature sensor at the end of the cavity. At very high shear rates, shear heating expectedly seems to dominate, and for this reason the online viscosity is lower. The higher viscosity for low shear rates correlates well with flow simulations (Chapter 6, Fig. 6.6) showing a fast increase of the viscosity in the polymer/mould interface, because of rapid cooling, in contrast to the bulk where viscosity remains on a low level until the cavity is filled completely. Another explanation for the differences in viscosity could be a result of wall-slip effects in the polymer/mould interface which are not implemented in Cross-WLF models.

3.4 Iso- and variothermal injection (compression) moulding process

Compared to standard isothermal injection moulding (IIM) where shrinkage is compensated only by holding pressure, in injection compression moulding (ICM) an additional compression stroke reduces the uneven stress distribution obtained in IIM. Dependent on the particular product, different compression moulding methods have been established. Expansion compression moulding is used especially for thick lenses in order to avoid sink marks. For variothermal process moulding a compression plate (shown in Fig. 3.12) is recommended because of fewer problems with thermal expansion of the cavities. Consequently, less tool damage is expected compared to standard compression moulding with a vertical flash face. The injection compression moulding process is schematically explained in Fig. 3.18:

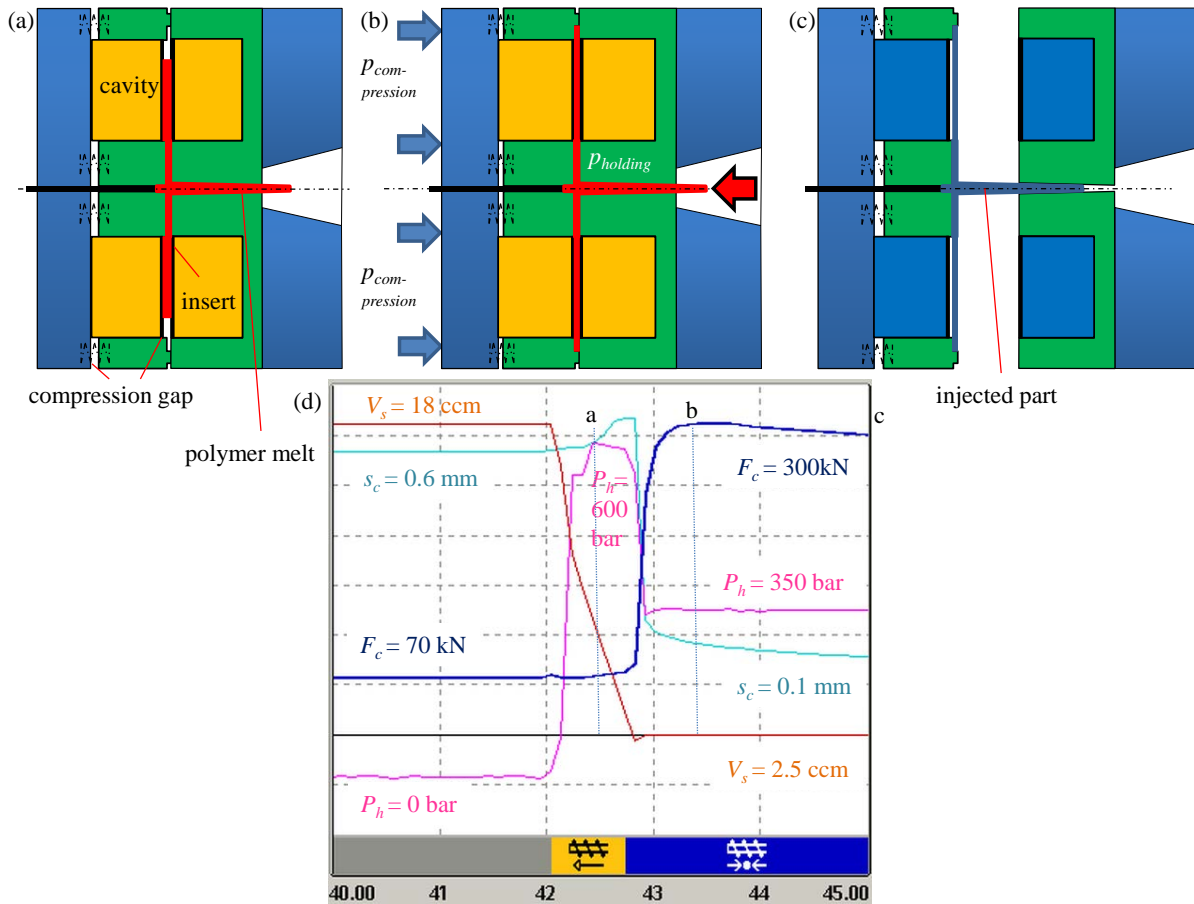


Fig. 3.18: Schematic example of a variothermal injection compression moulding process for PMMA: (a) polymer is injected into cavities that are heated either isothermally (IIM) below or variothermally (VIM) above the no-flow temperature (T_{no}) of the polymer; (b) holding pressure phase, optionally with compression stroke (blue arrows) in balance with holding pressure (red arrow) for homogenous pressure distribution (IICM or VICM); (c) polymer part is cooled down and part is ejected; the different sequences are implemented in the graph (d) showing the clamp force F_c , hydraulic pressure P_h , compression stroke s_c and polymer volume V_s in the front of the screw.

In Table 3-7 the main differences of all four processes are summarized:

Table 3-7: Overview of the four different injection moulding processes.

Process	IIM	ICM	VIM	VICM
Compression	No	Yes	No	Yes
Dynamic heating	No	No	Yes	Yes

3.4.1 Forces and pressures in the compression moulding cycle

During the compression moulding process different forces are interacting. On the one hand there is the injection/holding pressure (p_{inj}/p_{hold}) and the spring force (F_{spring}); on the other hand there is the clamp force (F_{clamp}) operating as counterforce and determining the compression gap. The gap is not necessarily closed completely in order to maintain the spring force during the compaction phase.

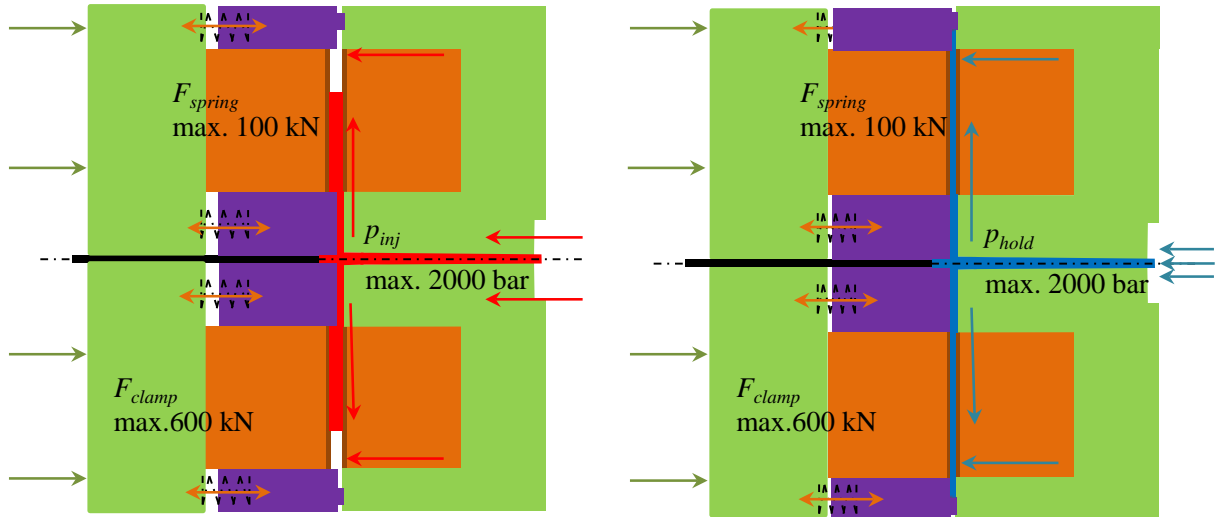


Fig. 3.19: Relationship of different forces during the injection compression moulding process.

$$F_{clamp} = F_{spring} + F_{injection} \text{ or } F_{clamp} = F_{spring} + F_{holding} \quad (3-16)$$

As soon as equation (3-16) is not in balance the compression gap would either get smaller or larger. Also, the spring power is not constant. The more the springs are compressed the higher the spring force gets as can be seen Fig. 3.20a. For that reason it is very important to control the compression gap and the pressures in the mould with precise sensors (Fig. 3.20b).

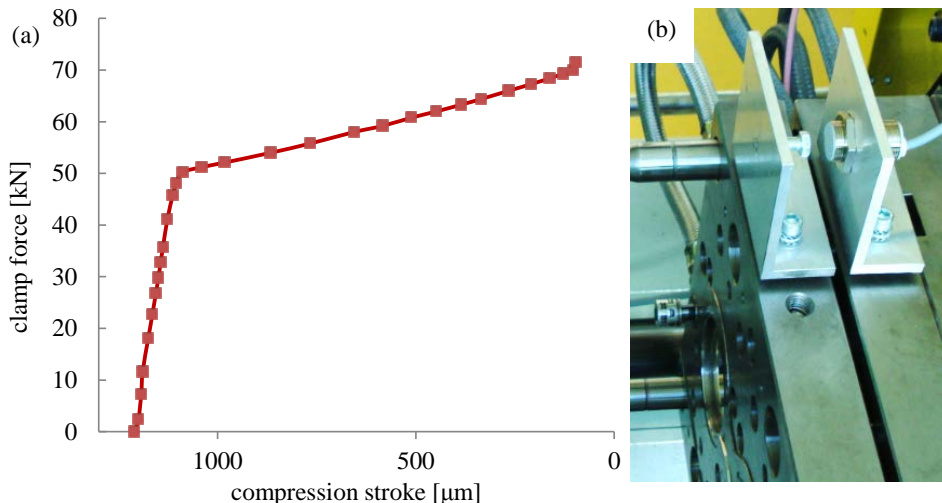


Fig. 3.20: (a) Spring characteristic: Measured clamp force dependent on the compression stroke; (b) inductive distance sensor (IWRM 18U9513) from Baumer (Frauenfeld, Switzerland), with a measuring range of 1.25 mm on the ejection side for a precise compression stroke control.

Alternatively to springs the compression stroke could be controlled hydraulically which is more precise, but also more expensive.

3.4.2 Processing parameters

For all processes the melt temperature was kept constant. In order to measure viscosities online dependent on shear rates, the injection speed was varied. The replication fidelity was predominantly compared at $15 \text{ cm}^3 \text{ s}^{-1}$.

Table 3-8: Set and measured injection moulding parameters applied for all processes and simulated polymer processing melt temperature T_P in the cavity.

Material	Cylinder/ melt temperature $T_{cyl.} / T_P [^{\circ}\text{C}]$	Injection speed $v_{inj} [\text{cm}^3 \text{ s}^{-1}]$	Set/measured mould temperature at ejection $T_{mould} [^{\circ}\text{C}]$
A-PA	280/283	10, 15, 30, 60	70 / 67
PMMA	250/253	10, 15, 30, 60	80 / 77
PP	220	10, 15, 30, 60	40 / 38
COC	280	10, 15, 30, 60	120 / 116
PS	230	15	60 / 57
POM	205	15	90 / 87

The mould temperature T_{mould} was measured in contact with the melt on the injection side with sensors T_A and T_B as shown in Fig. 3.13. The resulting polymer melt temperature was simulated with Autodesk Moldflow Synergy 2014 (Autodesk, 2014) additionally to measurements with sensors, as will be shown in Chapter 4 and used for the calculations of flow resistance and capillary pressure.

Various parameters like the holding pressure or the mould temperature at injection were specifically adapted to the different processes. The holding pressure and time was adjusted according the internal pressure curves taking care to find the optimum in order to prevent shrinkage on the one hand and high stresses in the part on the other hand. Low shrinkage is not only relevant for good dimensional accuracy but also for less demoulding issues (see also Chapter 7).

In isothermal compression moulding pretrials with PMMA and COC it turned out that a fast compression speed and a small compression stroke is favorable for the replication ratio RR, as can be seen in Fig. 3.21.

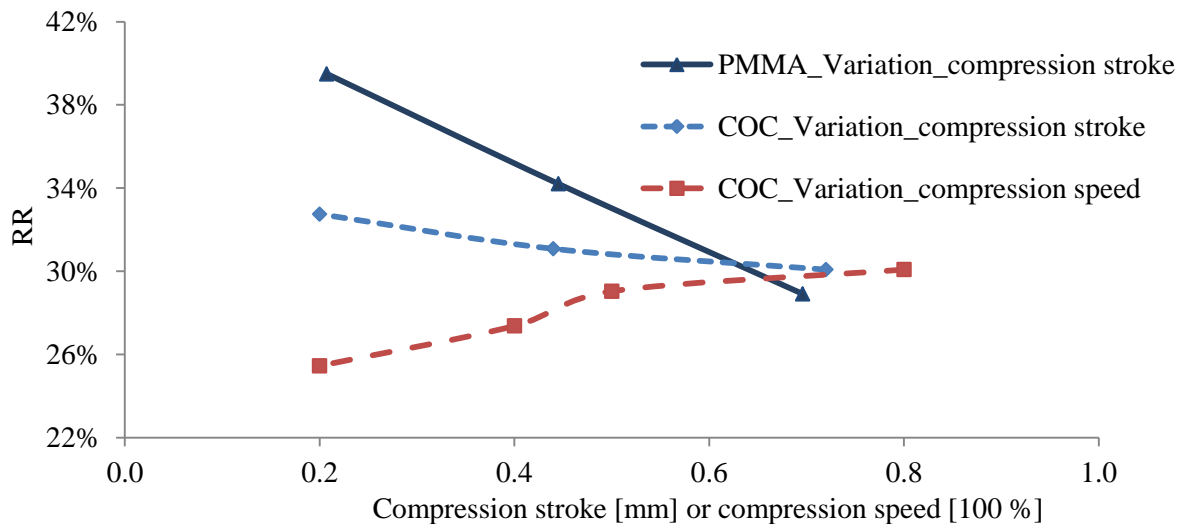


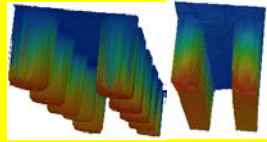
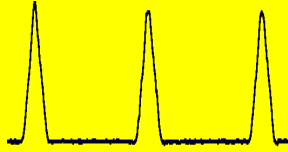
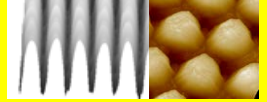
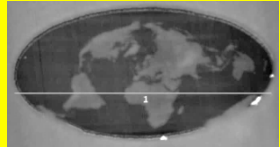
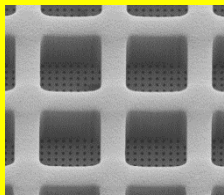
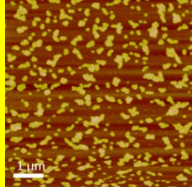
Fig. 3.21: Replication ratio RR of a laser-machined microstructure for isothermal injection compression moulding with COC and PMMA depending on compression stroke and compression speed showing that a high compression speed and a small compression stroke is favorable for the replication fidelity.

The positive effect of high compression speed and small compression stroke on the replication accuracy can be explained with the frozen-layer formation, which is less advanced if the compression of the polymer is conducted as fast as possible. The flow front speed and also the shear thinning effect are lower in a wider cavity which may be the reason why a small compression stroke is also favourable for a higher replication ratio. The results of the variations of compression speed are in good correlation with investigations of (Guan et al., 2012) and (Wu and Chen, 2006). This is why the compression speed was set to 100% ($\sim 10 \text{ mm s}^{-1}$). The compression gap was set to 0.5 mm instead of 0.2 mm on purpose in order to benefit from a lower filling pressure and less flow-induced residual stresses and birefringence during injection, as shown by (Lee et al., 2002). This high initial opening thickness was a balance between simplifying the processing and maximising the replication accuracy.

3.5 General overview of mould master inserts

The proper integration of the structured mould insert into the injection moulding tool is of high importance. Standard materials for nanostructured insert fabrication are silicon, quartz or nickel. Different methods for fixation of the insert were investigated: Bonding, vacuum, magnetic films, welding, soldering and clamping. The latter method turned out to be most promising as forces can be compensated that originate from different thermal expansion between steel frame and silicon, polymer or nickel insert. This is of high importance when using vario-thermal mould temperature control. In these investigations two highly polished CrNi steel (1.4301; roughness $R_a = 0.013 \mu\text{m}$) inserts without structures were used on the injection side. On the ejection side different mould-inserts with representative 2D and 3D micro- and nanostructures, manufactured by different processes, were clamped for the replication trials, summarized in Table 3-9 together with the intention of the respective trial.

Table 3-9: Overview of inserts used, showing the geometries and intention of the trial.

Process Structure design	Isothermal		Variothermal		Polymers of different viscosity and surface tension
	Injection moulding	Injection compression moulding	Injection Moulding	Injection compression moulding	
	IIM	IICM	VIM	VICM	
Micro-milled channels and holes	Size range: $w = 500 \mu\text{m}$, $h = 1 \text{ mm}$ (AR = 2) Intention: Reference for macro filling				
Direct laser-machined gradient v-groove micro structure	Size range: $w \sim 9 - 45 \mu\text{m}$; $h = 123 \mu\text{m}$ (AR = 5.6) Intention: Investigation of filling on the microscale dependent on flow resistance, viscosity and wetting				
Nano pillar & line array → UV photolithography + electroplating	Size range: $w \sim 150 - 600 \text{ nm}$; $h = 150 - 550 \text{ nm}$ (AR = 1 - 2) Intention: Investigation of filling on the nanoscale in comparison to microscale additionally: capillary effect				
3D nanostructures → thermal scanning probe lithography	Size range: $w \sim 50 - 600 \text{ nm}$; $h = 60 \text{ nm}$ (AR = 0.1 - 1) Intention: Replication of 3D nanostructures using a new master fabrication technology				
Hierarchical Ni structures	Size range: $w \sim 600 \text{ nm} - 20 \mu\text{m}$; $h = 400 \text{ nm} - 25 \mu\text{m}$ (AR = 0.5 - 1) Intention: Filling and demoulding behaviour of combined micro and nanostructures				
Sintered SiO ₂ nano-dots on Si transferred to PPSU	Size range: $w \sim 72 \text{ nm}$; $h \sim 60 \text{ nm}$ (AR ~ 1) Intention: Filling and demoulding behaviour of nanostructures using polymer inserts				

4. PROCESS VARIATIONS: ISO- AND VARIOTHERMAL INJECTION (COMPRESSION) MOULDING

The objective of the investigations described in this Chapter is to compare the replication quality of micro- and nanostructures for four different injection moulding processes (*IIM*, *IICM*, *VIM*, and *VICM*) using different masters with defined structures ranging from micro- to nanoscale, employing polymers differing in rheology and surface energy. The main question is if and how far variothermal injection compression moulding shows better replication quality and less demoulding issues compared to the other injection moulding methods.

In Chapter 4.5 the replication of macrostructures is demonstrated as starting position for the replication of more challenging micro- and nanostructures. In Chapter 4.6 the results of replication of various microstructures (Chapter 4.6.2) and nanostructures (Chapter 4.6.4 to 4.6.6) are presented and discussed in the context of replication accuracy (height and shape of the structures), homogeneity, defects, stresses and suitability for mass production (stability, demouldability and filling pressure). Finally, it is investigated in Chapter 4.6.7 to which extent melt viscosity and capillary effect influence the replication quality of microstructures compared to nanostructures.

4.1 Injection moulding processes

All trials were carried out on an Arburg 320 A injection moulding machine from Arburg (Lossburg, Germany). The variothermal injection compression mould (described in detail in 3.3) was designed internally and produced at AdvalTech FOBOHA (Muri, Switzerland). The mould was equipped with four temperature and three piezoelectric pressure sensors from Priamus (Schaffhausen, Switzerland) allowing precise process control as well as online monitoring and data extraction during the moulding process. The main principle of the online measurement of polymer viscosity was described in detail in Chapter 3.3.3, and the injection compression moulding process was explained in Chapter 3.4.

4.2 Mould master inserts: Structure design and fabrication technology

4.2.1 V-groove microstructures

A gradient microstructure composed of three parallel v-shaped microgrooves with increasing depth along the flow direction of the polymer melt was implemented (Fig. 4.1). The maximum average aspect ratio was 5.6 with an average structure width w_1 of 22 μm (45 μm at the top and 9 μm at the bottom) and a depth h of $123 \pm 6 \mu\text{m}$. This structure was laser-machined into brass ($\text{CuZn}_{39}\text{Pb}_3$; 2.0401; roughness $R_a = 0.034 \mu\text{m}$) with a picosecond-pulsed laser (Duetto; wave length $\lambda = 355 \text{ nm}$, pulse repetition rate $f = 200 \text{ kHz}$) from Time Bandwidth (now Lumentum, Milpitas, USA).

The design of this insert is representative for micro-optics or microfluidic analysis systems as for example investigated by (Matteucci et al., 2013) and was used as a reference structure throughout all experiments.

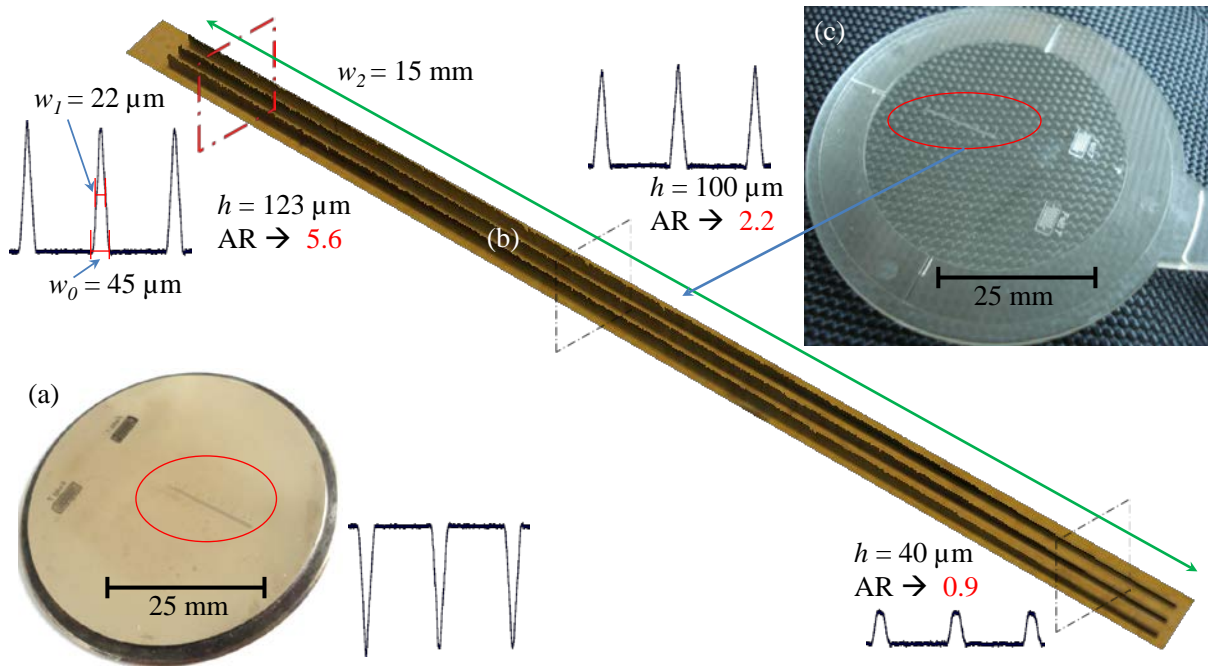


Fig. 4.1: a) Photograph and confocal laser-scanning height profile of laser-machined brass insert featuring three v-microgrooves with progressive depth; b) confocal laser-scanning micrograph of the replicated gradient structure with three representative cross-sections showing different height h and aspect ratios AR and c) photograph of the corresponding polymer replica.

The local surface increase in the area of the highest aspect ratio is almost seven times, which has of course a tremendous influence on the local heat transfer.

4.2.2 Nickel inserts produced by mask based displacement Talbot UV photolithography

Two different nickel inserts were produced by mask based displacement Talbot UV photolithography generating an optical image with a large depth of focus, explained in more detail in Fig. 4.2.

This technology, developed by Eulitha AG (Würenlingen, Switzerland), enables the production of regular nanostructure arrays over large areas.

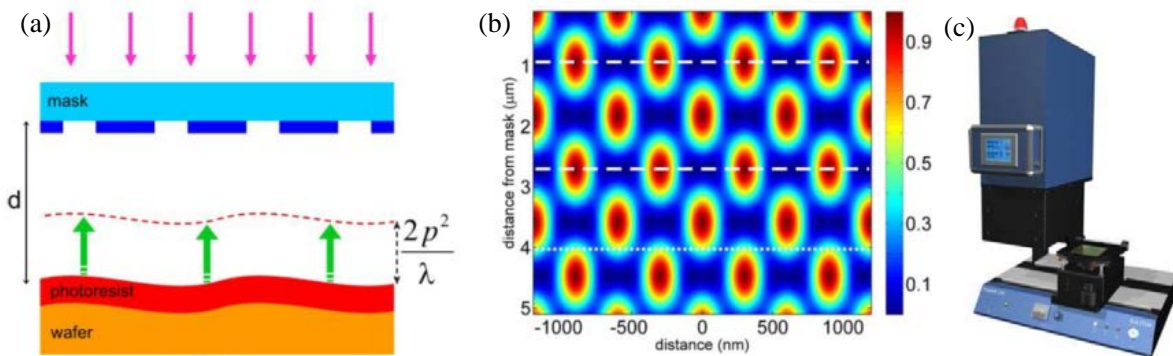


Fig. 4.2: (a) Schematic diagram illustrating the Talbot UV photolithography method. The photoresist-coated substrate is moved towards the mask by one Talbot period p during the exposure ($\lambda =$ wave length); (b) calculated intensity distribution after a linear grating. Two self images are marked with dashed lines at distances $0.9 \mu\text{m}$ and $2.7 \mu\text{m}$ from the grating. The dotted horizontal line below marks the position of a Talbot sub-image with twice the frequency of the original grating (Solak et al., 2011); (c) Phabler 100 device used for the Talbot UV photolithography (source: Eulitha AG).

For the insert with nanopillars a field of 44 x 44 mm was structured on a 4" silicon wafer (Fig. 4.3a). The hexagonal array of nano-holes ($D = 300 \text{ nm}$, $p = 600 \text{ nm}$, $h = 537 \pm 52 \text{ nm}$) was then transferred into a nickel shim ($D_{top} = 45 \text{ mm}$) through electroplating by applied microSWISS AG (Triesen, Liechtenstein). Perfluoro-octanephosphonate (PFOP) from Sigma-Aldrich (St. Louis, USA) was dip coated from tert-butyl-methylether (tBME) as an anti-sticking layer (Padeste et al., 2014), see also Chapter 7.3.

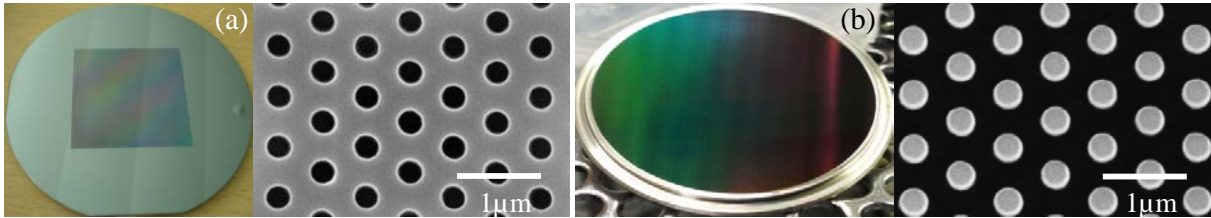


Fig. 4.3: (a) 4" Silicon master macro and SEM picture; (b) electroplated nickel-palladium macro and SEM picture of the injection moulding insert ($D_{top} = 45 \text{ mm}$) showing good structure transfer quality of large-area nanostructures with around 5 billion nanopillars.

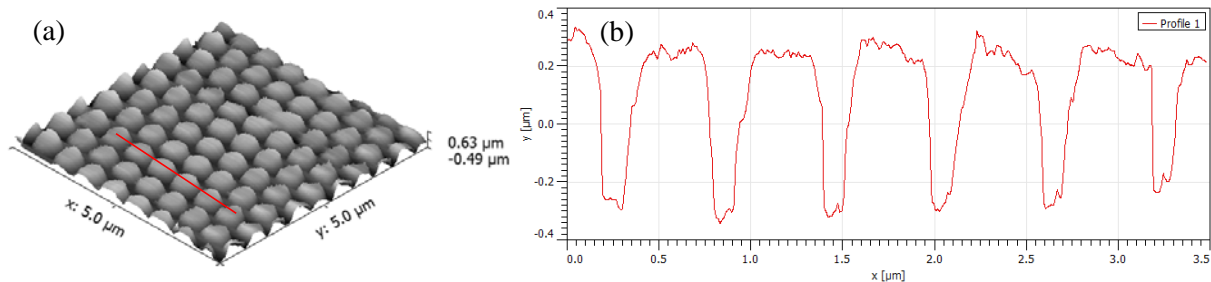


Fig. 4.4: (a) 3D AFM picture of the electroplated nickel-palladium (Ni-PD) insert showing in (b) the cross-section with a pillar height variation of $519 \pm 52 \text{ nm}$ and a structure pitch of 600 nm .

These large area structures could be used to increase the efficiency of LEDs or solar cells as demonstrated by (Chen et al., 2014) but also for adhesion and growth tests of cells or bacteria as investigated by (Curtis et al., 2004).

The mask based displacement Talbot UV photolithography is not only limited on pillar structures. Also nano-line structures can be produced and replicated, as will be shown in Chapter 4.6.6.

4.2.3 Nickel insert produced by thermal scanning probe lithography and electroplating

Another mould insert was prepared by mask-less thermal scanning probe lithography, capable of fabricating 3D nanostructures below 100 nm resolution. These nanostructures were written with a hot cantilever into a polyphthalaldehyde (PPA) thermal resist layer, developed by SwissLitho AG, Zürich, Switzerland (Paul et al., 2011). PPA has a thermodynamically unstable backbone and unzips into monomers upon breakage, which happens at the glass transition temperature of 150°C. The chemical structure of the resist material is shown in Fig. 4.5.

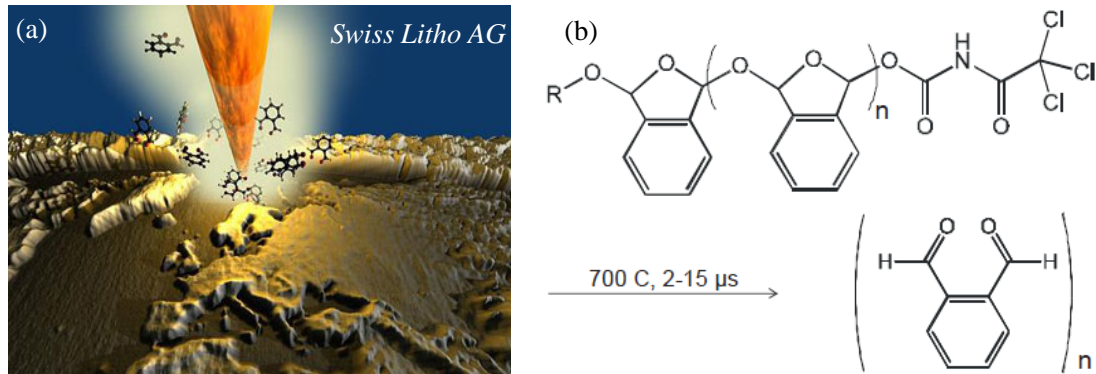


Fig. 4.5: (a) Illustration of a hot cantilever writing into polyphthalaldehyde (PPA) and creating a 3D nanostructure; (b) chemical structure of PPA resist (Coulembier et al., 2009).

Fundamentals about scanning probe lithography can be found in the review paper of (Garcia et al., 2014). In Fig. 4.6 the nickel-palladium insert is shown with two examples of transferred 3D nanostructures. Palladium was used as starter layer for the electroplating process. Such complex 3D nanostructures may find use for copy protection or for biological research.

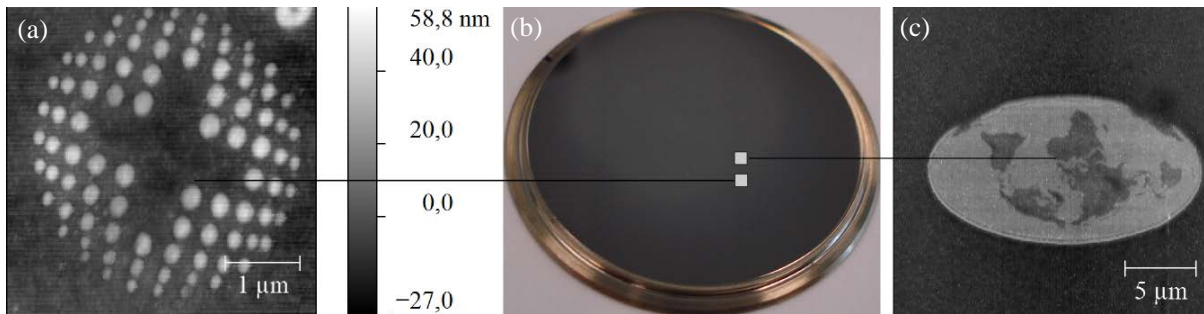


Fig. 4.6: (b) Nickel-palladium insert ($D_{top} = 45 \text{ mm}$) with 3D nanostructures produced by mask-less thermal scanning probe lithography, and (a), (c) AFM topography analysis of two example fields.

4.3 Processing parameters

For the comparison of all four processes the melt temperature, injection speed and mould temperature at ejection were kept constant. The mould temperature T_{mould} was measured in contact with the melt on both, the injection and ejection side.

Table 4-1: Set and measured injection moulding parameters applied for all processes and simulated polymer processing melt temperature T_P in the cavity.

Material	Cylinder/melt temperature	Injection speed	Set/measured mould temperature at ejection
	$T_{cyl.} / T_P$ [°C]	v_{inj} [cm ³ /s]	T_{mould} [°C]
A-PA	280/283	15	70 / 67
PMMA	250/253	15	80 / 77

Various parameters like the holding pressure or the mould temperature at injection were specifically adapted to the different processes.

Table 4-2: Process related parameters: Mould temperature (T_{mould}) at injection; holding pressure (P_{hold}); compression force (F_{comp}); compression stroke (s_{stroke}); compression speed (v_{comp}).

Process	A-PA					PMMA				
	T_{mould} [°C]	P_{hold} [bar]	F_{comp} [kN]	v_{comp} [%]	s_{comp} [mm]	T_{mould} [°C]	P_{hold} [bar]	F_{comp} [kN]	v_{comp} [%]	s_{comp} [mm]
IIM	70	800	0	0	0	80	800	0	0	0
IICM	70	400	300	100	0.5	80	400	300	100	0.5
VIM	135	800	0	0	0	130	800	0	0	0
VICM	135	400	300	100	0.5	130	400	300	100	0.5

Note: F_{comp} , v_{comp} and s_{comp} were optimized in the pre-study shown in Chapter 3.4.2.

In addition to direct measurements with sensors, the resulting polymer melt temperature was simulated with Autodesk Moldflow Synergy 2014, as shown in Fig. 4.7 and consequently used for the calculation of flow resistance, capillary pressure and spreading coefficient, respectively.

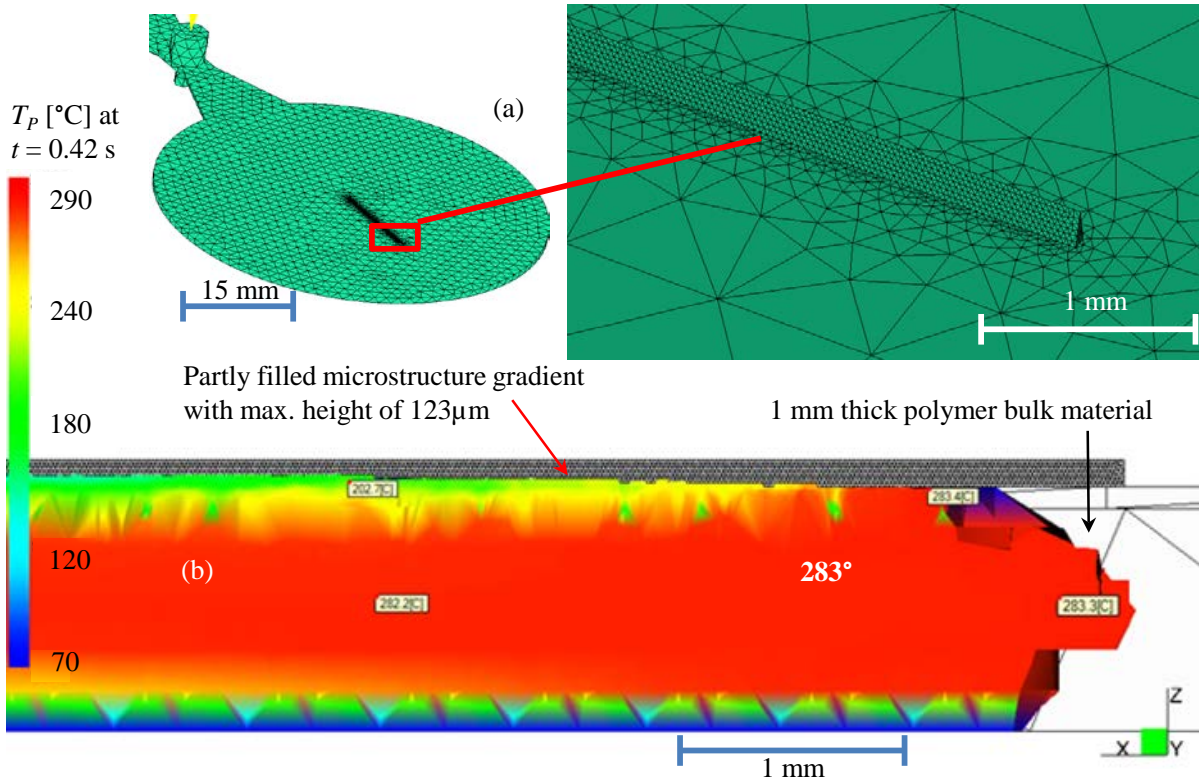


Fig. 4.7: Simulation of polymer melt temperature T_P for injection moulding of A-PA after $t = 0.42$ s: (a) part showing low mesh density in the bulk and high mesh density in the microstructure; (b) cross-section of bulk and microstructure.

The macroscopic bulk part and the v-microgroove were fitted with 8.4 million 3D volume tetrahedrons. Polymer data like viscosity, pVT-behaviour (modified 2-domain Tait-model) and thermal transition were already implemented in the data base. The viscosity was described by the Cross-WLF model (Chapter 2.2) based on the incompressible Navier-Stokes viscous fluid motion taking into account the shear and temperature dependence.

4.4 Polymers and polymer properties

Mainly two different polymers with the same glass transition temperature T_g of 110°C were used for the replication trials: Polymethylmethacrylate (PMMA, Plexiglas[®] 7N) from Evonik (Marl, Germany) and an amorphous polyamide (A-PA, Grilamid[®] TR55LX) from EMS-Chemie (Domat-Ems, Switzerland). For the pre-trials of the investigation of the mould temperature, additionally polystyrene (PS, PS 158K) from BASF (Ludwigshafen, Germany) was evaluated.

The surface tensions σ_L of the polymer melts were determined by the pendant drop method and the contact angle θ of the polymer melt on the brass and nickel inserts by the sessile drop method. Both measurements were carried out in a hot chamber with a drop shape analysis system (DSA100B) from Krüss (Hamburg, Germany) described in detail in Chapter 3.2.2.

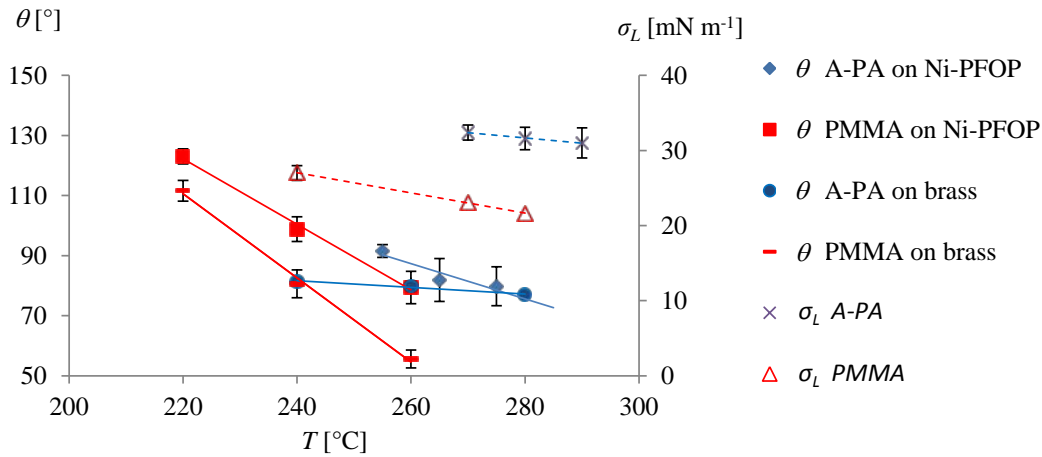


Fig. 4.8: Surface tension σ_L (dashed lines) and polymer melt contact angle θ measurements of A-PA (blue solid lines) and PMMA (red solid lines) at different temperatures and on two mould inserts used for calculations of spreading coefficient and capillary pressure; good wetting behaviour corresponds to low contact angle and high surface tension.

The measured surface energies and contact angles were used to calculate the capillary pressure P_C and the spreading coefficient S as a function of temperature for both materials. Thermal properties of the polymers for calculations were taken from the Autodesk Moldflow Synergy 2014 database.

The average viscosities of the polymers were determined online with two sensors as explained in Chapter 3.3.3 and the results are shown in Table 4-3. It can be seen that PMMA displays a lower viscosity compared to A-PA. The values for both materials are higher compared to the Cross-WLF values of the Moldflow database. But the online viscosity measurements represent more precisely the fast cooling of the polymer contacting the colder mould, which naturally has significant influence on the viscosity.

Table 4-3: Online viscosity measurements with temperature and pressure sensor in the mould depending on different injection velocities; values at shear rates of 601 s^{-1} and 678 s^{-1} resulted from injection speed = $15\text{ cm}^3\text{ s}^{-1}$ (marked red) and were used for calculations.

Shear rate s^{-1}		120	140	423	601	678	715	1206
PMMA $T_p=283^\circ\text{C}$	viscosity [Pa s]	3800±54		1129±21		597±12		270±10
	$\tau = \dot{\gamma} \cdot \eta$ [MPa]	0.46		0.48		0.40		0.33
A-PA $T_p=253^\circ\text{C}$	viscosity [Pa s]		4630±115		994±15		689±13	
	$\tau = \dot{\gamma} \cdot \eta$ [MPa]		0.65		0.60		0.50	

In reality, shear rates decrease and viscosities increase rapidly after contact with the cold mould. But that leads only to a small change in the shear stress τ as can also be seen in Table 4-3.

The no-flow temperatures T_{no} of both polymers were determined with a MFI measuring device MI-2 from Göttfert (Buchen, Germany) by detecting the melt temperature at which a zero melt flow mass rate (MFR) was observed (explained in detail in Chapter 3.2.1). Results for PMMA and A-PA are shown in Table 4-4. According to this investigation T_{no} for PMMA is approximately 130°C and that of A-PA 150°C.

Table 4-4. Adapted melt flow rate (MFR) measurements for the determination of T_{no} of A-PA and PMMA measured with a load of 21.6 kg for 45 min by weighing the extruded material after 45 min at different temperatures.

Temperature [°C]	160	150	140	130
MFR of PMMA [mg / 45 min]	527	40	22	0
MFR of A-PA [mg / 45 min]	59	0	0	0

Although both materials have the same T_g , the determined T_{no} for PMMA is 20°C lower than that of A-PA. This, of course, has a significant influence on the viscosity and the frozen-layer formation during filling of micro- and nanostructures.

4.5 Pre-trials: Replication of macrostructures and variation of mould temperatures

4.5.1 Replication of macro-grooves and pillars

The filling of macrostructures was investigated for a better understanding of the replication of micro- and nanostructures. For this purpose, 500 μm wide channels and holes were manufactured into brass (CuZn39Pb3; 2.0401; roughness $R_a = 0.034 \mu\text{m}$) by micro-milling (Fig. 4.9a) and filled by standard injection moulding, carrying out short shots (Fig. 4.9b & c) with A-PA.

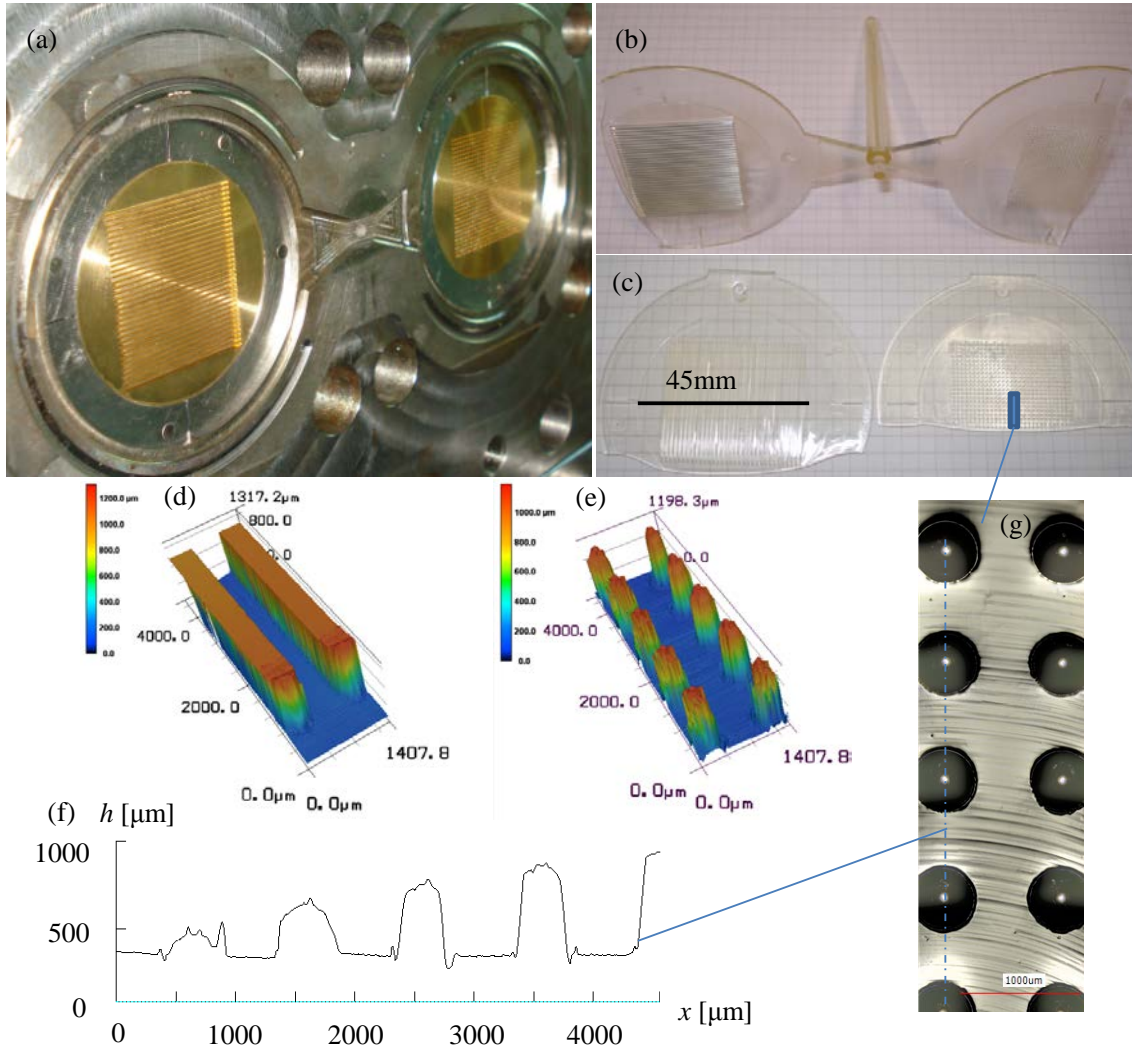


Fig. 4.9: (a) Machined brass insert with macro channels ($w = 500 \mu\text{m}$, $AR = 2$) and macro holes ($d = 500 \mu\text{m}$, $AR = 2$); (b) and (c) A-PA short-shots showing better flow into the channel structure compared to the hole structure; (d) and (e) CLSM pictures of completely filled channels and holes near the gate and (g), (f) partially filled pillars towards the flow front.

In the short shots, one can clearly see that channels in flow directions are filled easier compared to holes, the replicated pillars of which decrease in height from 1 mm to 140 μm towards the flow front. Interestingly, there was no change in height in the short-shots when increasing the mould temperature from 70°C to 115°C (above T_g). This shows that a macro-sized fluid centre dominates compared to heat transfer effects at the mould/melt interface.

Despite an aspect ratio of two, both structures can be filled to 100% applying standard moulding conditions (isothermal mould temperature $T_{mould} = 70^{\circ}\text{C} < T_{no}$). The reason is that although a frozen layer is formed (Fig. 4.10), there is still enough fluid-centre for the polymer to fill the structures completely, before the structure would be completely blocked by the solidified polymer. (Berger et al., 2011) used the model of (Dietz et al., 1978) to calculate the frozen layer thickness:

$$\delta(t) = 1.9 \frac{T_{no} - T_{mould}}{T_P - T_{mould}} \sqrt{a_{eff} \cdot t_c} \quad (4-1)$$

$$a_{eff} = \frac{k}{\rho_m \cdot c_p} \quad (4-2)$$

Where T_{no} is the no-flow temperature, T_{mould} the mould surface temperature, T_P the polymer melt processing temperature, and a_{eff} and t_c refer to the thermal diffusivity of the polymer and the contact time, respectively. The thermal diffusivity was calculated based on data from Moldflow 2014 using the coefficient of thermal conductivity k , the polymer melt density ρ_m and the specific heat capacity c_p , all of which are summarized in Table 4-5.

Table 4-5: Parameters used for calculation of frozen layer thickness.

	T_{no} [°C]	T_{mould} [°C]	T_P [°C]	k [W m ⁻¹ K ⁻¹]	ρ_m [kg m ⁻³]	c_p [J kg ⁻¹ K ⁻¹]	a_{eff} [m ² s ⁻¹]
PMMA	130	80, 115	253	0.19	1057	2120	$8.5e^{-8}$
A-PA	150	70, 115	283	0.20	950	2200	$9.6e^{-8}$

With lower T_{no} less polymer freezes in the same time which has a positive effect on the filling of a structure.

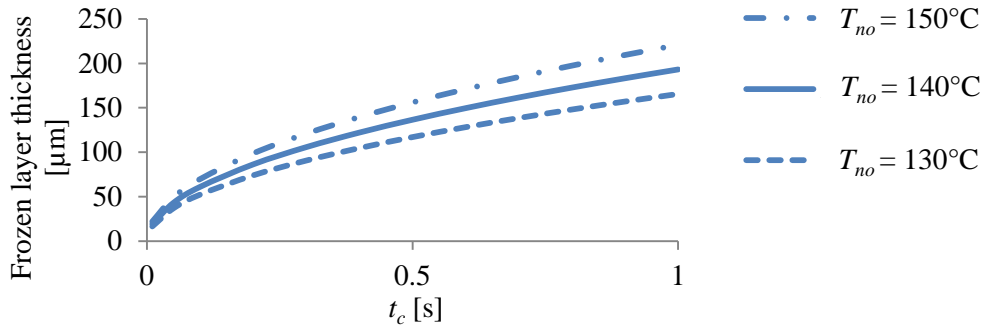


Fig. 4.10: Calculated frozen layer thickness as function of contact time t_c for A-PA assuming different no-flow temperatures T_{no} .

4.5.2 Dependence of microstructure replication fidelity on mould temperature

The variothermal process is based on increasing the mould temperature in the moment of initial melt contact. In pre-trials with different mould temperatures shown in Fig. 4.11, the tremendous influence of T_{mould} on the filling height was confirmed.

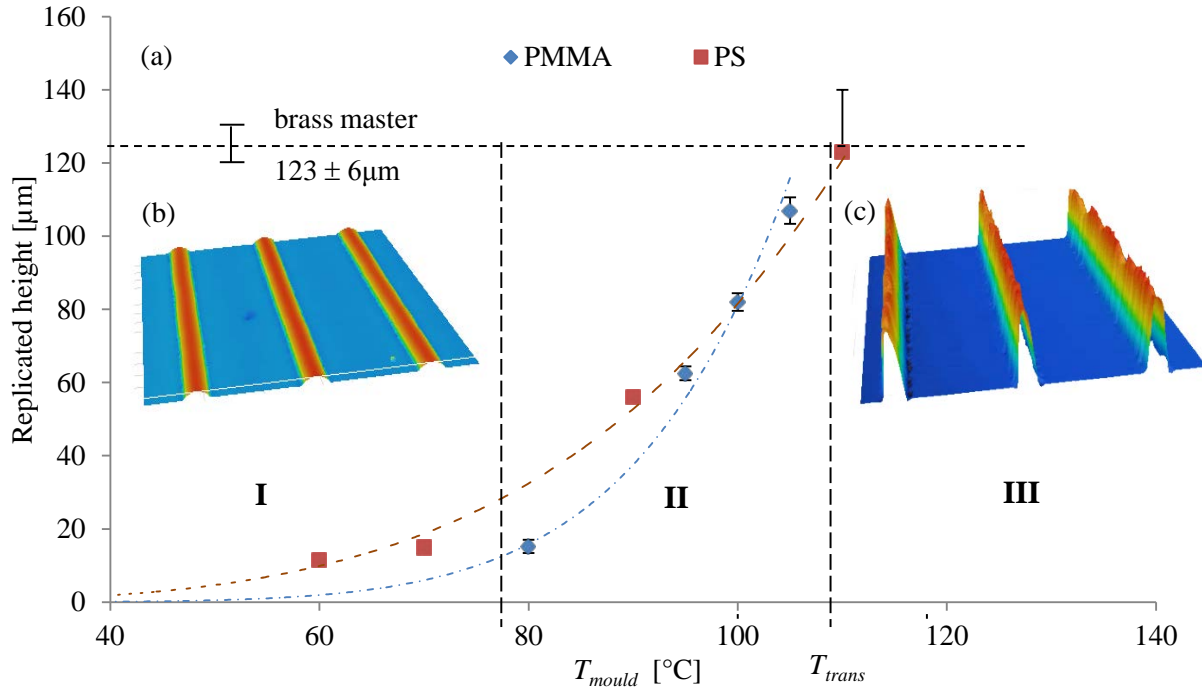


Fig. 4.11: (a) Replicated height of a v-groove microstructure in PS and PMMA depending on the mould temperature T_{mould} with an injection velocity of $15 \text{ cm}^3 \text{ s}^{-1}$; (b) CLSM micrograph of a PS replica at $T_{mould} = 60^\circ$; (c) CLSM micrograph of a PS replica at $T_{mould} = 110^\circ\text{C}$.

The dependence of the replicated height on temperature can be divided into three regimes:

- Regime I: Low replication quality because of high ΔT between polymer melt and mould temperature resulting in a very fast cooling and rapid freezing of the polymer.
- Regime II: Monotonic increase of the replicated height until the transition temperature T_{trans} is reached.
- Regime III: Perfect replication due to complete filling at mould temperatures exceeding the transition temperature. Structures may be stretched if the ejection temperature is chosen too high. This is the reason why the error bar for the PS replica in Fig. 4.11 is up to $140 \mu\text{m}$ despite the maximum height of the master is $123 \pm 6 \mu\text{m}$. For materials with high no-flow temperatures significantly above T_{trans} or T_g , a higher mould temperature could be necessary to achieve a 100% replication with high aspect ratio structures as will be shown in Chapter 4.6.2.

Regime I and II can also be fitted with power functions (red and blue dashed line in Fig. 4.11) with the general structure $RR = A \cdot (T_{mould})^B$; A and B would be fitting parameters for different polymers.

4.6 Results and discussion: Variation of moulding processes and structure geometries

Various micro- and nanostructures were replicated with four different processes and two different materials. Internal stresses, replication ratio and demoulding issues were compared to each other.

4.6.1 Pressure and frozen-in stresses

The melt pressure was measured in front of the screw and in the cavity, respectively. The higher the necessary pressure the more the polymer chains are oriented and the more inhomogeneous frozen-in stresses, part deformation and demoulding issues occurred.

Table 4-6: Switch over pressure P_{so} and internal pressure P_{int} (near the gate) depending on the process showing much higher values without compression (IIM and VIM).

Process	IIM	IICM	VIM	VICM
P_{so} [bar] A-PA	1440	860	1380	840
P_{int} [bar] A-PA	680	400	750	375
P_{so} [bar] PMMA	1160	700	1120	750
P_{int} [bar] PMMA	650	380	630	380

From Table 4-6 it becomes evident that parallel compression phase significantly reduced the switch over pressure P_{so} as well as the internal pressure in the cavity P_{int} , leading to a substantial reduction in internal stresses (Fig. 4.12), which translates into less demoulding issues. In stark contrast, injection moulding without additional compression stroke caused high internal pressures resulting from the high holding pressure required to compensate the shrinkage during solidification and to prevent formation of pronounced sink marks that would reduce both the overall part quality as well as the replication accuracy. Frozen-in stresses were visualized with polarized light and are compared in Fig. 4.12 for the four process variants.

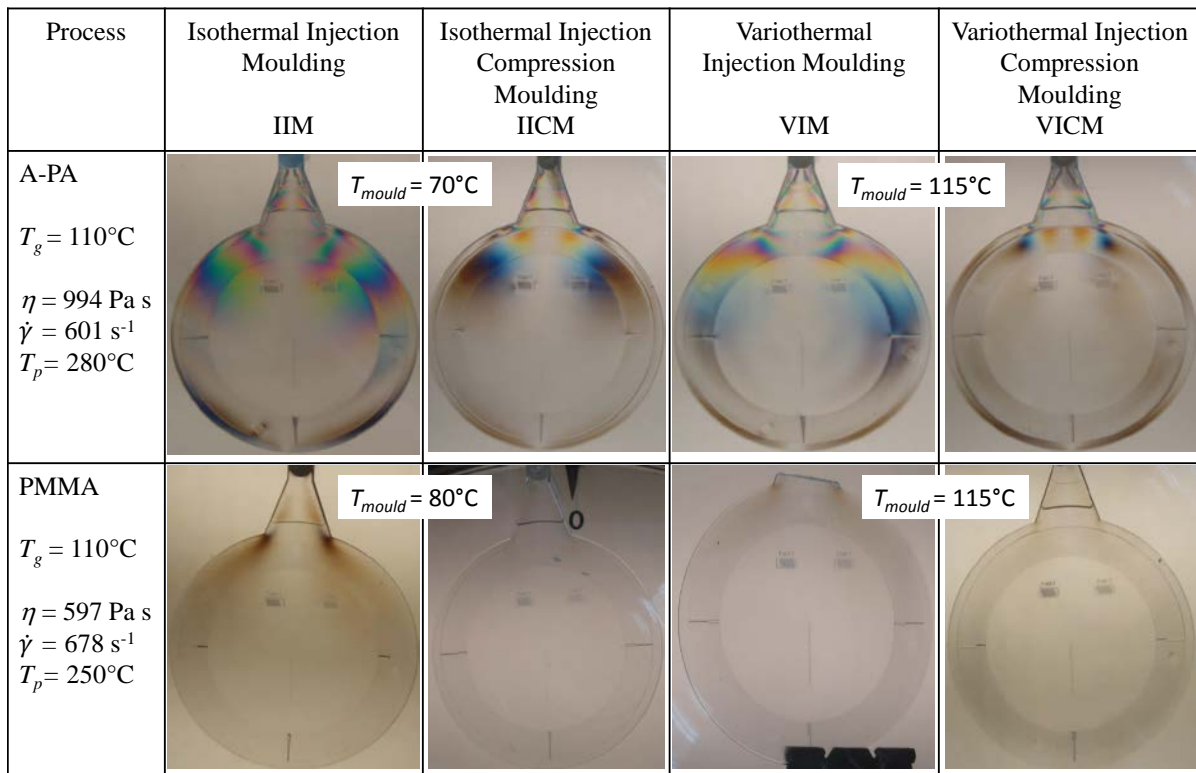


Fig. 4.12: Frozen-in stresses viewed under polarized light depending on the replication process and polymer viscosity (from online measurements) showing that lower viscosity, additional compression and variothermal moulding reduce internal stresses because of less molecule orientation.

The lower viscous PMMA can be fabricated with all processes almost without internal stresses, compared to the higher viscous A-PA, which clearly shows stresses that are highest when using isothermal injection moulding and are lowest when using variothermal injection compression moulding. These results show the differences in birefringence of the different processes and correspond well to the investigation of (Kim and Isayev, 2013), who measured and simulated residual birefringence of PS and PC replicated by IIM and IICM.

The reason for the lower pressure and less stresses using processes with compression lies to some extent in the wider cavity because of the compression gap, when the polymer is injected. But even more important is the fact that the polymer shrinkage is compensated in a more uniform way when applying a planar compression stroke instead of a holding pressure through a narrow gate. The pressure, volume and temperature situation can be visualized in pvT-curves (Fig. 4.13), showing the influence of pressure on the specific volume of the polymer melt depending on the respective injection process and the melt temperature:

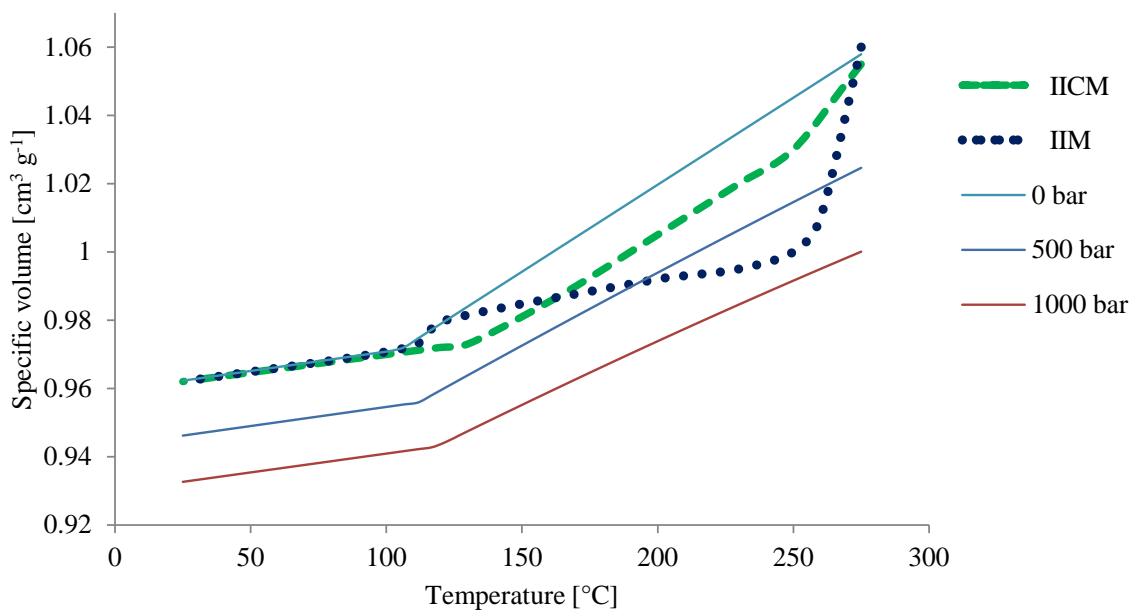


Fig. 4.13: pvT-curves of A-PA (full lines) taken from Moldflow, sketching the difference of the pressure-volume-temperature change for isothermal injection moulding (IIM) compared to isothermal injection compression moulding (IICM) showing a significant higher internal injection cavity pressure for IIM (dotted line).

With the IICM process (green dashed line) the pressure in the cavity increases to a low level (400 bars) and remains fairly constant until the polymer is solidified. In the IIM process (dotted line) the pressure in the cavity first rises to a peak value and decreases again afterwards, which results in inhomogeneous molecule orientations, leading to undesired birefringence and ultimately to warpage of the part.

4.6.2 Replication of v-groove microstructure: Variation of processes and materials

Comparing four different processes, the replication accuracy of microstructures with isothermal processes was rather poor for both polymers, A-PA and PMMA. With variothermal processes a 100% replication (including the sharp top) of the high aspect ratio microstructure was only achieved with the lower viscous PMMA. No influence on the replicated structure height could be measured, when applying an additional compression stroke, which is in good agreement with the investigations of (Michaeli et al., 2008).

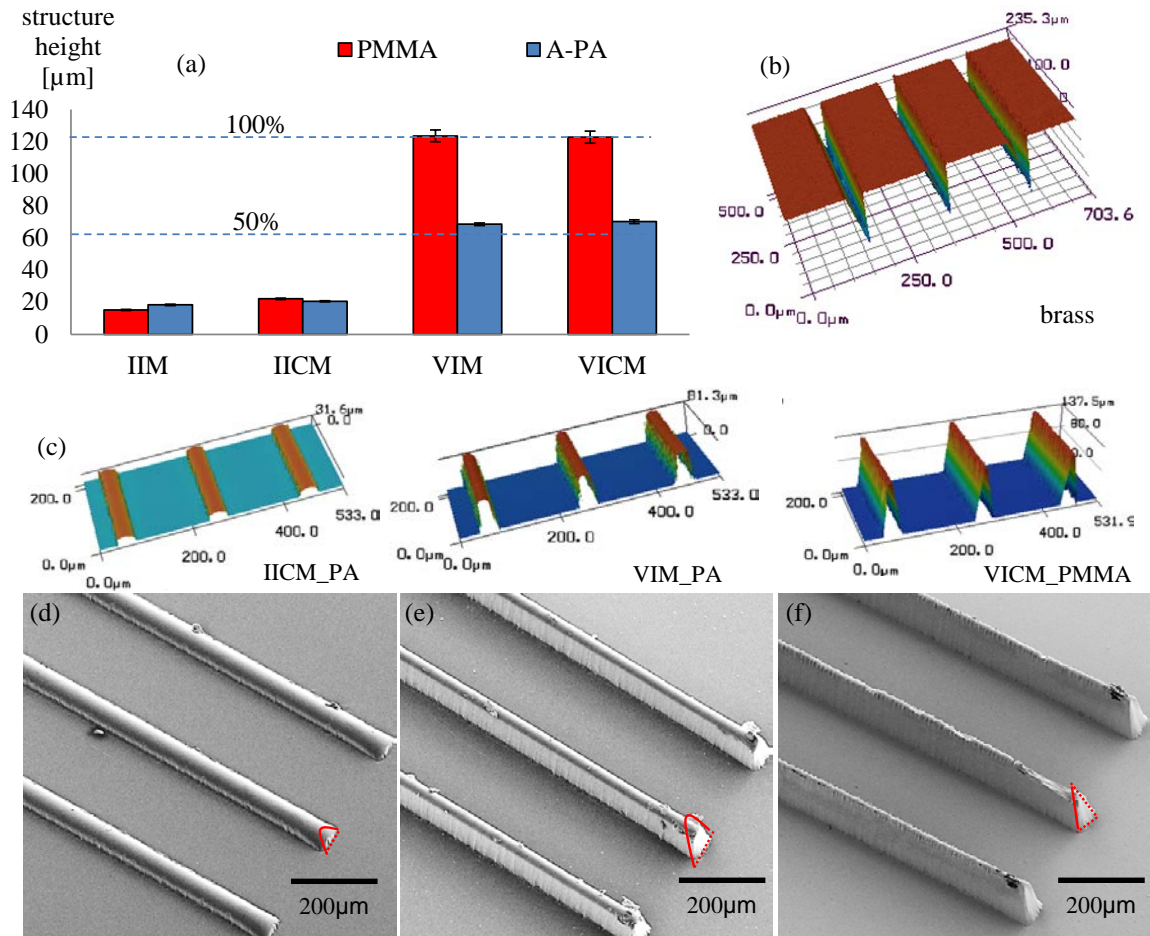


Fig. 4.14: (a) Replication quality of microstructures observed for different processes and materials compared to brass master structure height (100% $\cong 123 \mu\text{m} \pm 6 \mu\text{m}$); CLSM measurements of (b) master (made from brass) and (c) replica prepared by different process variants; and (d, e, f) corresponding 20° tilted SEM pictures of replicated microstructures, displaying 17%, 52% and 100% replication, respectively (cross-sections indicated in red).

The negligible effect of compression on the replicated height can be explained by the rapid formation of a frozen polymer layer due to fast cooling upon contact with the cold mould as observed, for instance, by (Suzuki et al., 2012). This frozen layer prevents further filling of the micro-cavities in the mould during the compression phase. The influence of frozen layer formation is most evident when comparing variothermal with isothermal injection moulding. The cooling time of the polymer is longer in a mould with a temperature above no-flow temperature resulting in a much better replication quality.

It becomes evident from equation (4-1) for the calculation of the frozen-layer thickness, that for mould temperatures above the no-flow temperature no frozen layer formation occurs. The determined T_{no} of A-PA is approximately 20°C higher than that of PMMA which has a significant effect on the frozen layer thickness formation demonstrated in Fig. 4.15. The difference in T_{no} can explain why A-PA using VICM with a mould temperature above T_g results in an incomplete filling compared to PMMA as shown in Fig. 4.14.

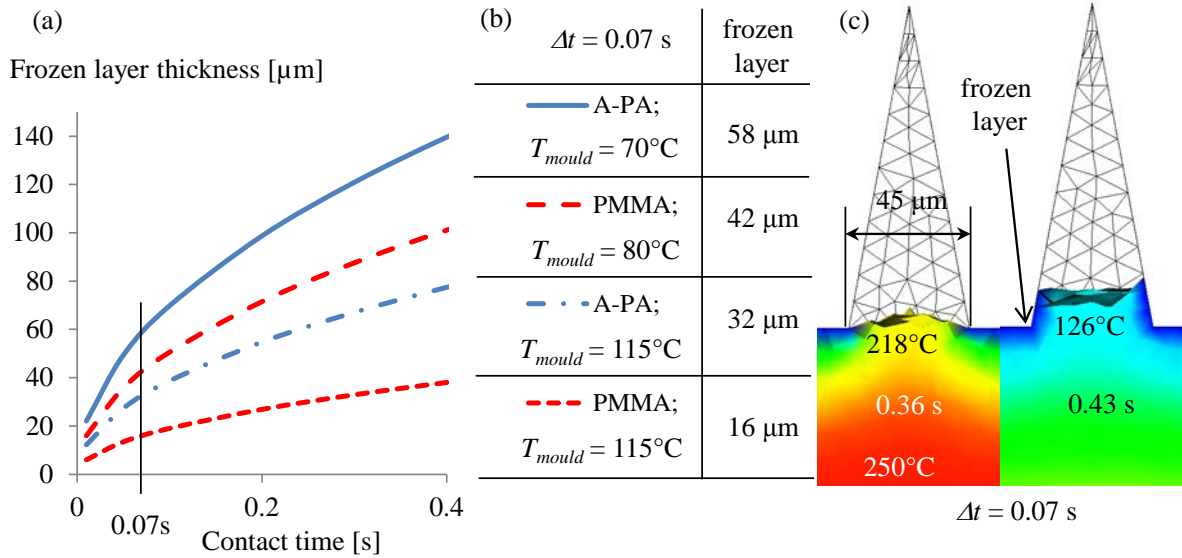


Fig. 4.15: (a) and (b): Calculated frozen layer thickness as function of contact time for PMMA (red dashed line) and A-PA (blue lines) for different no-flow and mould temperatures, showing a bigger frozen-layer thickness for A-PA ($T_{no} \sim 150^{\circ}\text{C}$) compared to PMMA ($T_{no} \sim 130^{\circ}\text{C}$); (c) simulated frozen layer formation for PMMA with a mould temperature of 80°C with Moldflow showing that after a time difference of 0.07 s, the material in the structures has cooled down below the no-flow temperature of 130°C.

The calculation of the frozen layer thickness is based on data shown in Table 4-5 and on two assumptions: First of all, the no-flow temperature is difficult to determine experimentally and the common assumption for amorphous materials $T_{no} = T_g + 30^{\circ}\text{C}$ varies in a wide spectrum, which substantially affects the resulting frozen layer thickness. Secondly, the polymer melt comes into physical contact with the mould surface during filling only in the unstructured areas. In stark contrast, in the vicinity of microgroove structures, there is an air gap between the polymer and the mould, reducing the heat transfer as can be seen in the simulated cross-sections of the v-microgroove (Fig. 4.16). But as soon as the polymer flows into the microgroove, the heat transfer is rapidly increased again and a frozen layer forms within the micro-cavity.

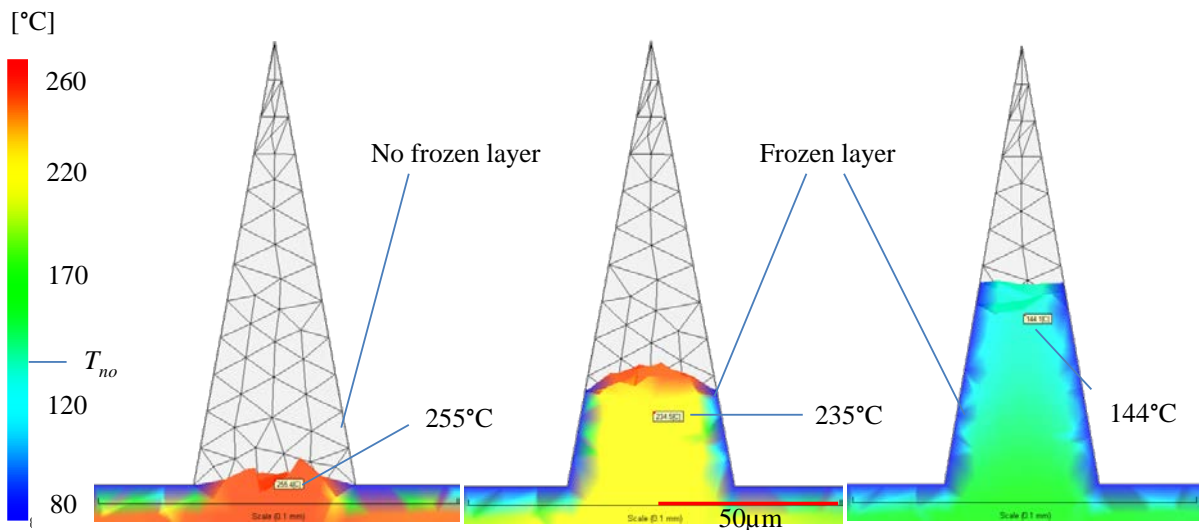


Fig. 4.16: Simulated temperature and frozen layer formation for PMMA applying IIM in the v-microgroove after 0.37 s, 0.38 s and 0.47 s filling time using Moldflow 2014.

4.6.3 Calculation of filling resistance and capillary force in the microstructure

Because of above mentioned reasons further explanations for different filling fidelity in the v-groove microstructures are needed. The filling is forced by injection pressure P_I resulting in a total cavity pressure P_{Total} and can be summarized as described in equation (4-3) and visualized in Fig. 4.17:

$$P_{Total} = P_I - P_{FR} \pm P_C \quad (4-3)$$

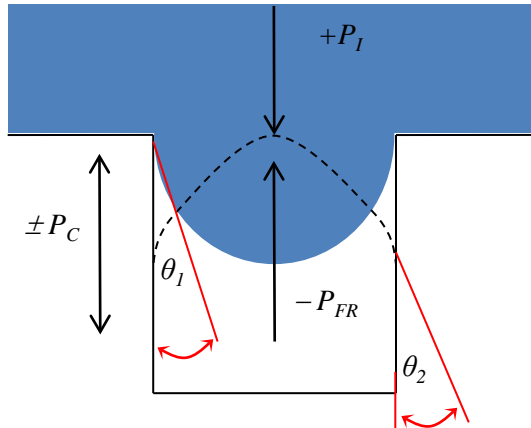


Fig. 4.17: Schematic filling of a micro- or nanostructure influenced by different pressures: The injection pressure P_I ; the flow resistance P_{FR} (defined as negative countering the polymer flow) and the capillary pressure P_C (defined as positive supporting the flow and as negative countering the flow).

During the filling phase, the pressure P_I at the flow front is at ambient, so the total pressure is a result of P_{FR} and P_C . But the pressure in the macro-cavity and in the structures increases rapidly when the polymer reaches the end of the cavity. The counter pressure caused by the flow resistance of the polymer in the cavity P_{FR} (defined in (4-6) and Fig. 4.17 as negative pressure) is given by the Hagen-Poiseuille equation for rectangular channels (as can be assumed in the case of the micro-groove).

$$P_{FRsquare} = \frac{\dot{V} \cdot 12 \cdot \eta \cdot h}{K \cdot w_1^3 \cdot w_2} \quad (4-4)$$

$$\dot{\gamma} = \frac{6 \cdot \dot{V}}{w_2 \cdot w_1^2} \cdot e_{rec} \quad (4-5)$$

$$P_{FR} = \frac{2 \cdot \dot{\gamma} \cdot \eta \cdot h}{K \cdot w_1 \cdot e_{rec}} \quad (4-6)$$

By combining equation (4-4) with equation (4-5), equation (4-6) can be used to calculate the flow resistance P_{FR} depending on the shear rate $\dot{\gamma}$, the polymer melt viscosity η and the depth of the structure h .

Where w_1 is the minimal and w_2 the maximum width of the structure (Fig. 4.1) and e_{rec} is a geometric factor ~ 0.77 (Pahl et al., 1991) for the rectangular channel shape for a non-parabolic velocity profile according to the Weissenberg-Rabinowitsch correction. The factor K (for this geometry $K = 0.99$) takes into account the ratio of the different widths of the channel and is 1 for very high ratio and 0.42 if $w_1 = w_2$ (Bruus, 2008).

The shear rate is a result of the injection speed, but becomes very low within the micro-cavities because the polymer flow is drastically reduced due to fast formation of frozen layer. As the polymer cools down quickly in contact with the mould, the shear rate is reduced accompanied by a concomitant increase in viscosity, despite only slight changes in the shear stress ($\tau = \dot{\gamma} \cdot \eta$, cf. Table 4-3). Therefore, the mean shear rate and viscosity was measured with the temperature and pressure sensors in the cavity and used for the calculation of the flow resistance within the structures. Based on the online viscosity measurements shown in Table 4-3 a flow resistance of 8.7 MPa for A-PA and 5.9 MPa for PMMA was calculated, which may explain, additionally to differences in the no-flow temperatures, why variothermal filling of A-PA is worse compared to PMMA for microstructures.

In addition to the filling resistance, which depends strongly on viscosity and thus on melt temperature, capillary forces P_C can play a significant role. Materials with a high surface energy tend to improve the filling behaviour whereas those with a low surface energy can prevent good filling. In the case of the v-groove microstructure the calculated capillary pressures P_C in the microstructure was less than 1 kPa according to equation (4-7) and thus can be neglected compared to the injection, holding or compression pressure and flow resistance, summarized in Table 4-7.

$$P_C = \pm \sigma_L \left(\frac{2 \cdot \cos \theta}{w_1} + \frac{2 \cdot \cos \theta}{w_2} \right) \quad (4-7)$$

Table 4-7: Calculated flow resistance P_{FR} and capillary pressure P_c in the microstructure with an aspect ratio $AR = 5.6$.

Material	P_{FR} microchannel [MPa]	P_c microchannel [kPa]
A-PA	8.7	0.65
PMMA	5.9	0.84

4.6.4 Large - area transcription from Ni-pillars to polymer holes

With all four processes a stable replication with virtually defect-free polymeric parts was possible. But after 200 cycles small scratches on the Ni-master were observed that originated from broken nickel pillars. Especially in variothermal processes the adhesion between polymer and master structures can be substantially higher because of the more precisely replicated surface. This increased contact area results in higher friction forces compared to isothermal processes that, in turn, cause more demoulding issues, in particular more breakage of the master structures (in this case broken, pulled out and sheared off nickel nano-pillars). The breakage of the nickel pillars was evaluated qualitatively by microscope analysis with stitching software for the investigation of large areas and SEM analysis in the regions of broken pillars as described in Chapter 3.2.3. Exemplarily, a defect free large area and an area with broken pillars on the nickel master after the injection moulding trials is shown in Fig. 4.18.

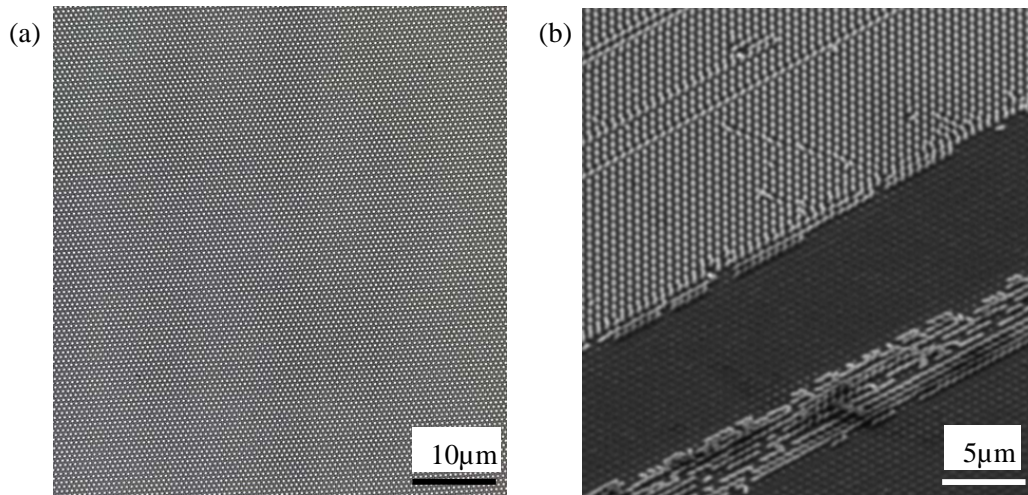


Fig. 4.18: (a) Small section of a stitched CLSM picture showing a defect free nano-pillar structure; (b) SEM picture of a defect showing a scratched nano-pillar array; both pictures were taken after the injection moulding trial.

An anti-adhesion coating like PFOP, as mentioned in Chapter 4.2.2, reduces adhesion forces by about 30% and thus pillar breakage. Calculation of adhesion forces will be shown in Chapter 7.4 based on contact angle measurements on polymer plates and the mould material. Additionally, less injection and packing pressure, as it is the case when applying VICM instead of VIM, also reduces the pillar breakage.

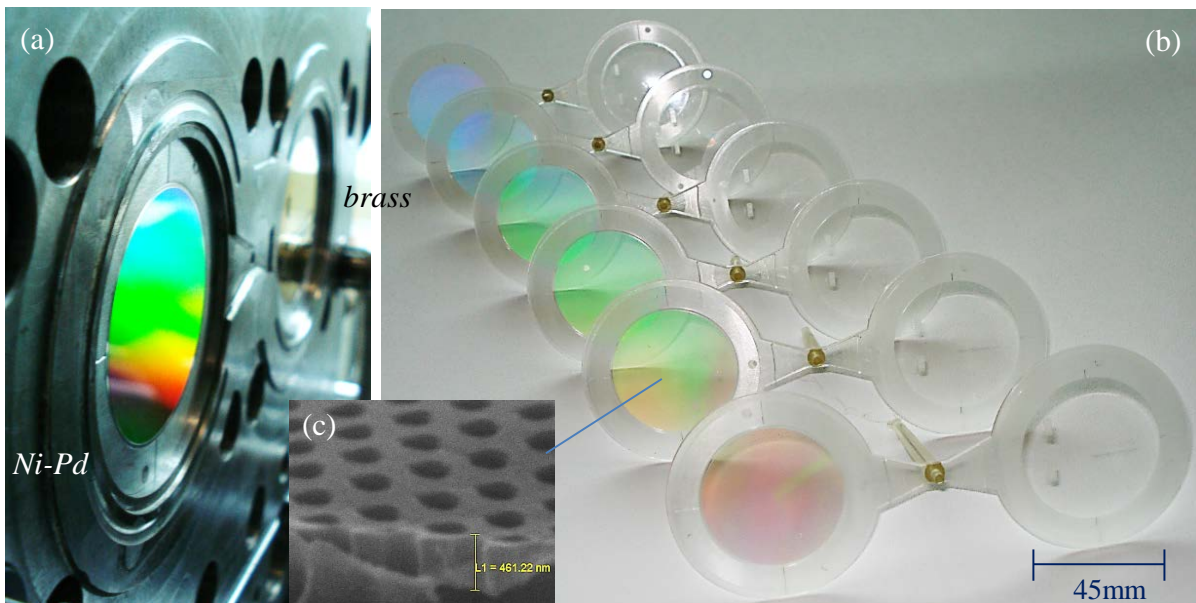


Fig. 4.19: (a) Ejection side of the mould with brass microstructure and nickel-palladium nanostructure master inserts; (b) PMMA replica macro picture and (c) SEM picture showing holes with a depth ≥ 460 nm.

Substantial differences in the replicated structure depths between isothermal and variothermal methods were observed. With isothermal injection moulding only 27% to 50% of the maximum structure height was replicated, whereas 100% was achieved with variothermal injection replication as can be seen in Fig. 4.20 and Fig. 4.21.

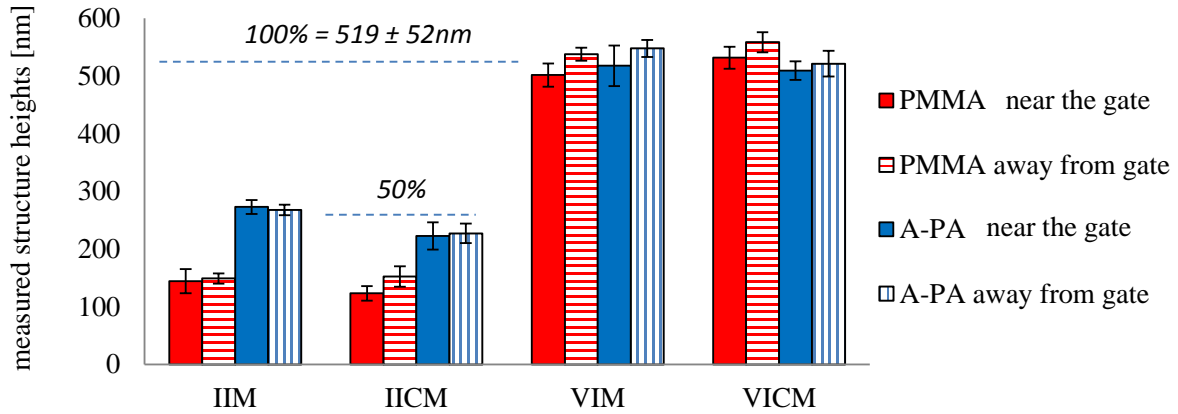


Fig. 4.20: AFM structure height measurements of PMMA and A-PA replica produced by various injection moulding methods.

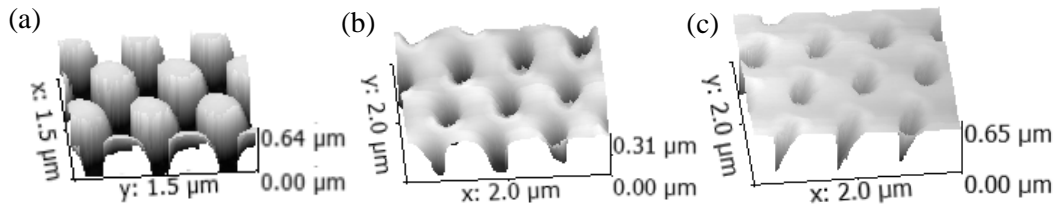


Fig. 4.21: AFM measurements of (a) Ni-Pd master structure, and comparative examples of A-PA replica prepared by (b) isothermal injection moulding and (c) variothermal injection compression moulding, respectively.

Fig. 4.21 shows superior surface quality and flatness for the sample produced by variothermal injection compression moulding (VICM). Moreover it can be clearly seen in Fig. 4.21c that the replication was much better compared to the sample produced by isothermal injection moulding (IIM), which is displayed in Fig. 4.21b.

With the replication of nanostructures some of the results observed during the replication of microstructures were confirmed: Additional compression seemingly does not improve the replication accuracy. Variothermal moulding leads to improved replication fidelity in terms of feature size and surface flatness, as the bottom of the nickel pillar array was fully reached by the polymer melt, which is not the case with isothermal injection moulding.

Spreading coefficient, flow resistance and capillary forces in nanostructures

The better replication of large area nano-pillars with A-PA compared to PMMA with low mould temperature could be explained by a better wetting behaviour of A-PA. The higher the spreading coefficient, the better the filling of the structure is supposed to be. Because of the high heat dissipation of the polymer melt in contact with the substantially colder mould, a strong decrease of the spreading coefficient means a lower filling. When the polymer melt enters the cavity, the melt temperature of A-PA is 283°C and that of PMMA 253°C. In that moment the spreading coefficient for both materials is almost on the same level ($S_c \sim -25$), calculated with equation (4-8) and shown in Fig. 4.22. The spreading coefficient of PMMA decreases faster compared to A-PA in contact with the cold mould because of a stronger increase of the contact angle. This can be the reason why the isothermal replication of nanostructures with A-PA, as shown in Fig. 4.20, is better than that with PMMA.

$$S_c = \sigma_L (\cos \theta - 1) \quad (4-8)$$

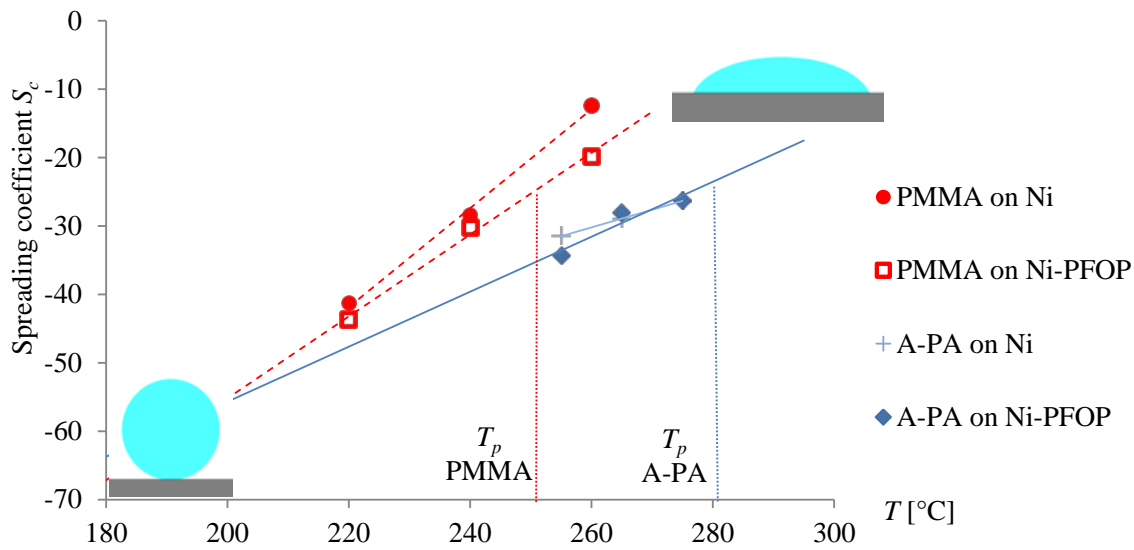


Fig. 4.22: Calculated spreading coefficient S_c for A-PA (blue solid line) and PMMA (red dashed line) on pure nickel and Ni-PFOP surfaces, as a function of the polymer melt temperature T_p . It can be seen that the temperature dependence of S_c is more pronounced in the case of PMMA which could have a negative impact on the filling if the polymer is cooled down quickly in contact with the cold mould.

Obviously the spreading coefficient correlates well with the capillary pressure as they both are strongly influenced by the surface interactions between polymer melt and mould insert. The capillary pressure can be calculated with equation (4-9) for the polymer melt, flowing between the nickel pillars.

$$P_C = \pm \frac{2 \cdot \sigma_L \cdot \cos \theta}{r} \quad (4-9)$$

For the calculations, the same surface energy σ_L and contact angle θ were used from Fig. 4.8 as for the microstructures. Assuming a cylindrical hole with a radius r of 150 nm for the capillary volume between Ni pillars, the capillary pressures amount to 115 kPa for A-PA and only 23 kPa for PMMA, (see Table 4-8). This seems not a lot compared to injection pressure or the resulting flow resistance P_{FR} , calculated with (4-10), but considering that melt pressure at the flow front is very low, this relatively low capillary pressure can improve the filling in the first milliseconds when the melt comes into contact with the mould surface.

$$P_{FR} = \frac{2 \cdot \dot{\gamma} \cdot \eta \cdot h_n}{r \cdot e_{circle}} \quad (4-10)$$

The depth h_n was determined with AFM, and shear rate and viscosity were taken from online measurements shown in Table 4-3. The dimensionless geometry factor e_o (~ 0.82) is needed for circular channels for non-parabolic velocity profile according to the Weissenberg-Rabinowitsch correction (Pahl et al., 1991).

Table 4-8: Calculated flow resistance P_{FR} and capillary pressure P_c in the nanostructure with $h_n = 519$ nm.

Material	T_p [°C]	P_{FR} nanochannel [MPa]	P_c nanochannel [kPa]
A-PA	253	5.0	23.2
PMMA	283	3.4	115.2

As the aspect ratio of the nanostructure was considerably lower ($AR_{nano} = 1.6$) than that of the microstructure ($AR_{micro} = 5.6$), the flow resistance in the nanostructure is consequently lower than that in the microstructure. In order to evaluate the capillary effect, the height of the nanostructures was measured at the flow front of a short shot (Fig. 4.23a), where the pressure is supposed to be zero.

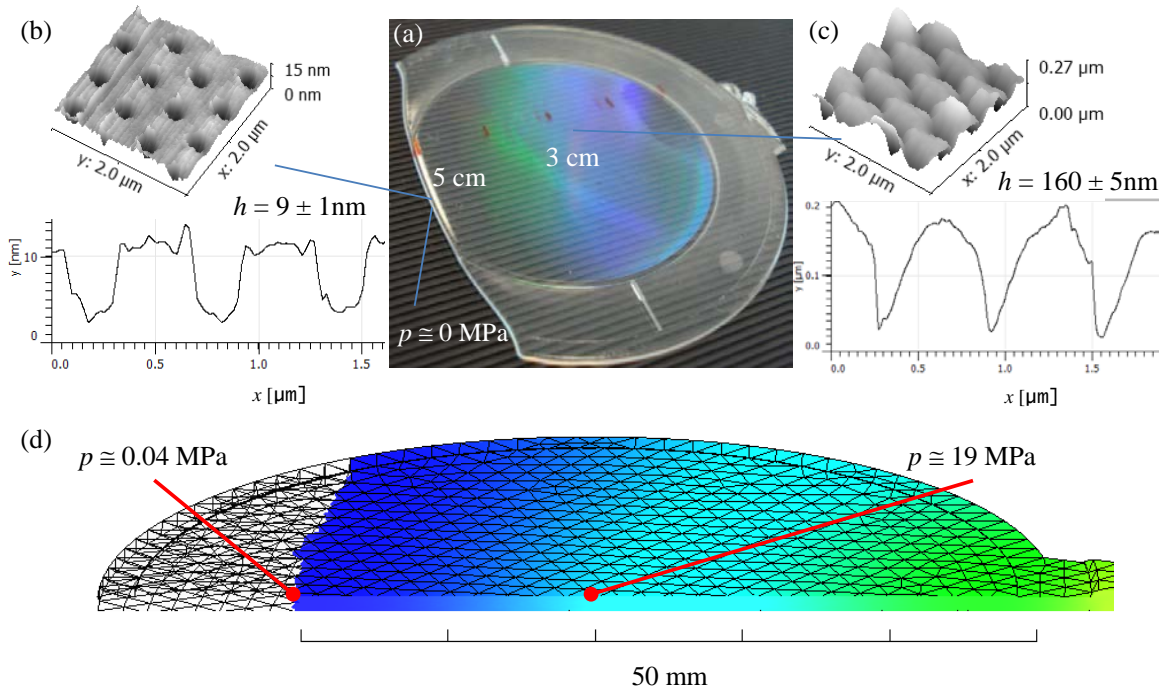


Fig. 4.23: (a) Photograph of a short-shot with A-PA ($T_{mould} = 115^\circ\text{C}$) showing AFM measurements of (b) already filled nanostructures at the flow front (5 cm from gate), where the pressure is supposed to be 0 MPa, compared to (c) replicated structures 3 cm from gate; (d) simulated pressure distribution for A-PA after 0.44 s filling time, showing almost no pressure (0.04 MPa) at the flow front in comparison to 19 MPa in the middle area.

From these investigations one could assume that the capillary pressure at the flow front could be partially the reason for the filling of 9 ± 1 nm. Interestingly this height is in good agreement with the calculations in Chapter 4.6.7, where it will be shown that for A-PA this value is in the regime where capillary effects dominate over the flow resistance. But also for the remaining filling, a good wetting at the side wall should improve the polymer flow, which is primarily forced by injection pressure. The influence of wetting will be investigated in much more detail in Chapter 5.

Comparison near and away from the gate of replicated nanostructures

Interestingly, no significant differences could be found between structures replicated near and away from the gate (Fig. 4.20), which contrasts investigations of (Lucchetta et al., 2014) who showed that the replication of microstructures near the gate was much better compared to those away from the gate. The reason for this discrepancy could be that the influence of capillary pressure in nanostructures cannot be neglected, contrary to microstructures, as already shown already in Table 4-7 and Table 4-8. Moreover, the melt pressure increases at the end of the cavity as soon as the melt fills the cavity completely and this pressure pulse could compensate the decreasing holding pressure profile with a maximum at gate, as can be seen in Fig. 4.24, showing the filling of A-PA by IIM with and without holding pressure:

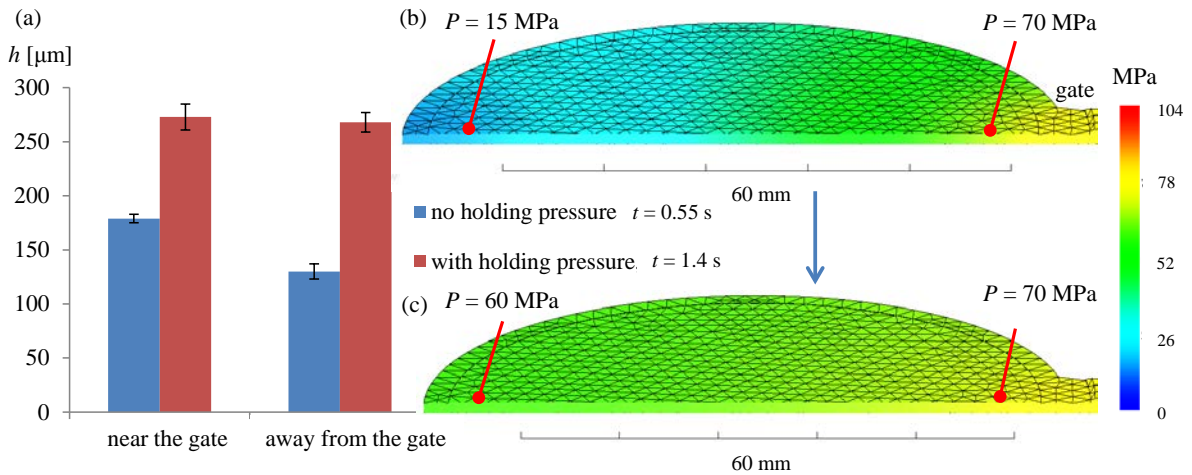


Fig. 4.24: (a) Filling height of A-PA nanostructures away and near the gate, with (red columns) and without holding pressure (blue columns); (b) Moldflow simulation of the pressure distribution after 0.55 s and (c) 1.4 s filling time showing an increase of the pressure away from the gate from 15 MPa to 60 MPa.

Fig. 4.24 explains why differences in heights between near and away from the gate can occur. If the difference in pressure is large enough ($\Delta P = 55$ MPa), as it is the case for the moment before applying the holding pressure (Fig. 4.24b), then the resulting height near the gate is 49 nm higher than away from the gate. As long as the holding pressure can still reach the end of the cavity ($\Delta P = 10$ MPa, Fig. 4.24c), these structures are then also filled to the same level as those near the gate, and explains why the height difference disappears after the holding pressure is applied. It is worth to point out, that the holding pressure has a significant influence on the isothermal filling of nanostructures, which is different from macro and micro filling. This observation will be confirmed in Chapter 4.6.6.

4.6.5 Transcription of Ni 3D nanostructures

The objective of the investigations presented in this Chapter was to evaluate a process chain for the replication of complex 3D nanostructures by injection moulding. In these experiments, the replication of 3D nanostructures prepared by mask-less thermal scanning probe lithography was studied for PMMA and A-PA. In Fig. 4.25 all three structures, from PPA-pre-master to Ni-Pd master and finally to the PMMA replica, are displayed:

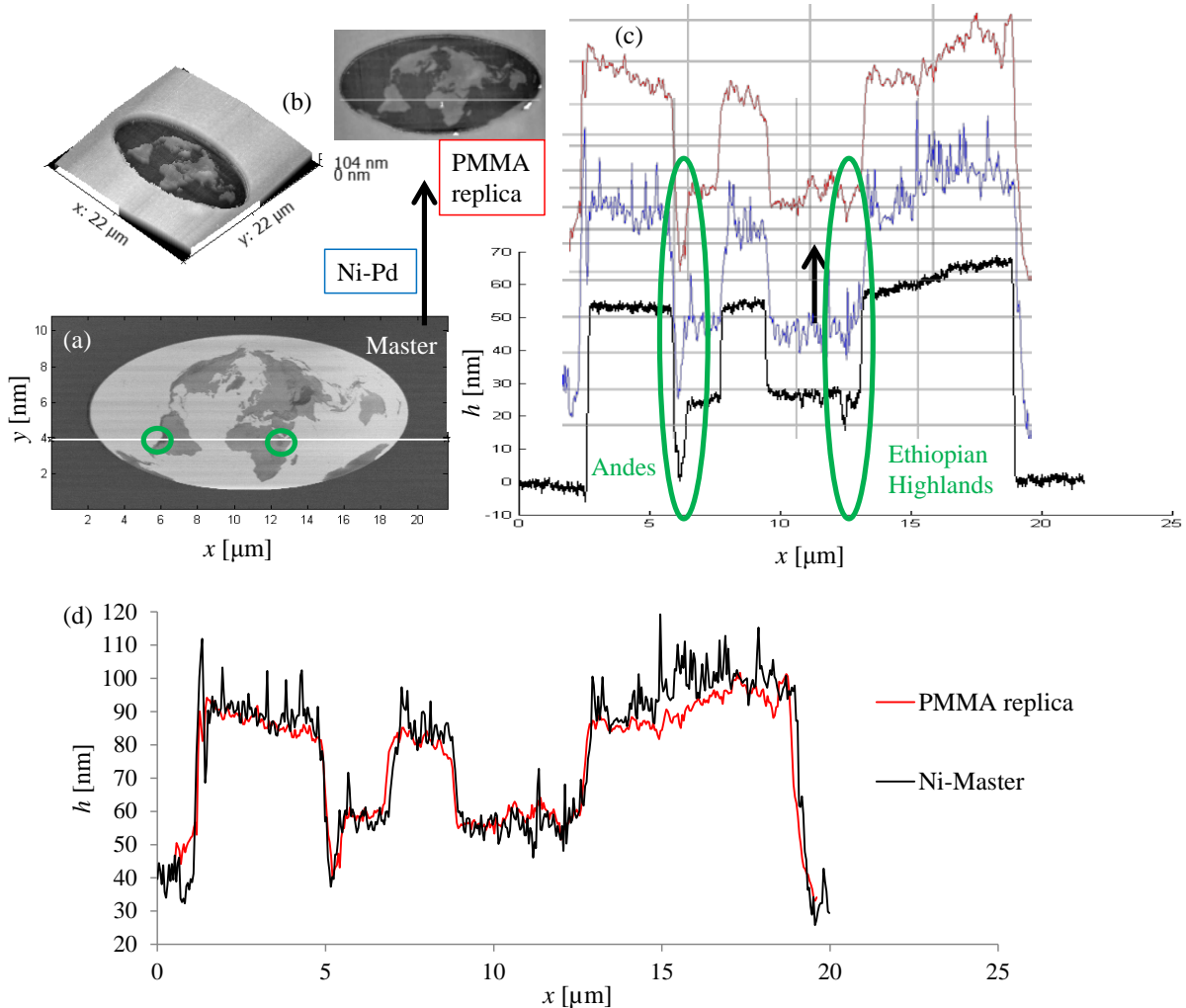


Fig. 4.25: (a) AFM picture of the PPA-pre-master; (b) AFM picture of the PMMA replica produced by VICM; (c) AFM profile comparing the PPA-pre-master (black line) with the Ni-Pd injection moulding master (blue line) and the PMMA replica (red line); the well replicated Andes and Ethiopian highlands through the whole process chain are marked green; (d) overlapped cross-section of the Ni-Pd master (red line) and the PMMA replica (black line) pointing out, once more, the precise replication quality.

In Fig. 4.25 the good replication quality over the whole process chain is clearly demonstrated. Moreover, it can be observed that the roughness increases in the copy process from PPA pre-master to the Ni-Pd master, but is then not completely transferred further into the PMMA.

Comparing VICM with IIM replication in Fig. 4.26, more demoulding defects (sharp peaks, green marking) and lower replication accuracy (red-marked area) can be observed using standard IIM.

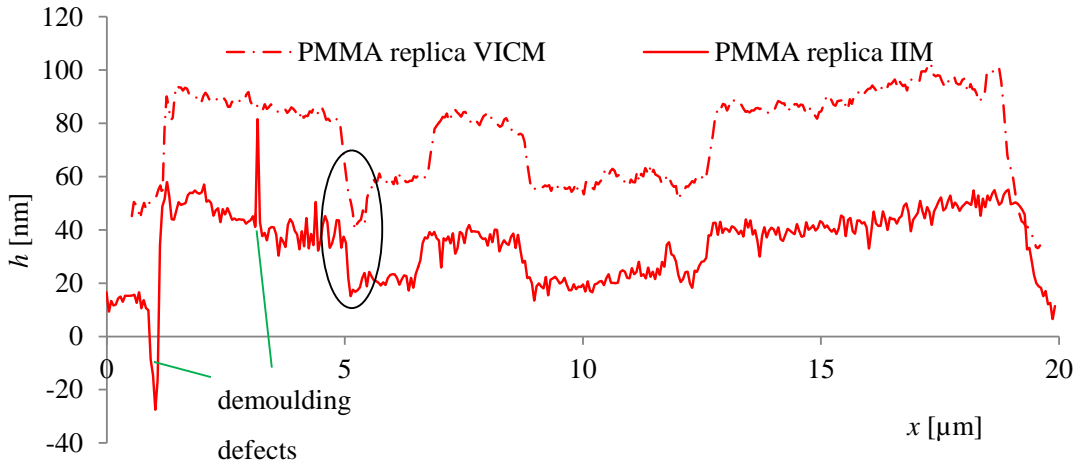


Fig. 4.26: Comparison between PMMA replica produced by VICM (dashed-dotted line) and IIM (full line) shifted by 30 nm in height for easier distinction, showing slightly better replication (black oval) by VICM and less demoulding defects (no peaks).

An additional comparison of AFM profiles of a hole-structure in a nickel-palladium master with the replicated pillars revealed that the 3D nanostructures were replicated to an RR between 70% and 83% depending on the polymer and the respective process, as shown in Fig. 4.27:

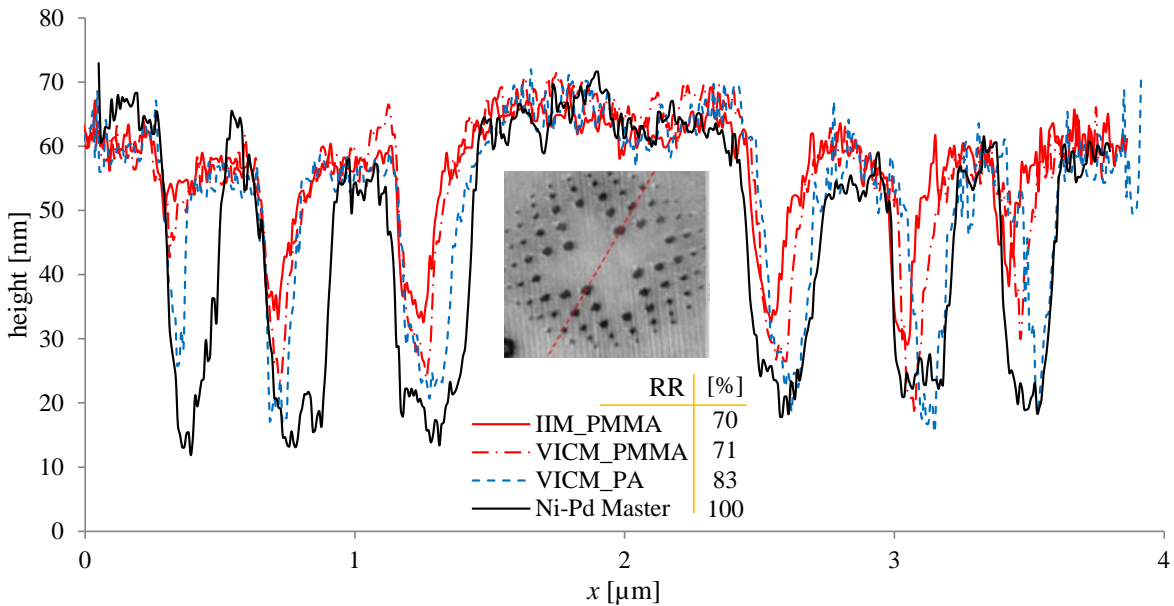


Fig. 4.27: AFM height profiles: Comparison between Ni-Pd master (reversed), PMMA and A-PA replica showing the highest replication ratio (RR) with A-PA produced by VICM (83%) and lower RR with PMMA produced by IIM and VICM (70 and 71%); RR was determined by integration of the total cross-section areas.

By variothermal injection compression moulding (VICM) the replication is slightly better compared to isothermal injection moulding (10 - 20 nm deeper structures).

Once more, it can be confirmed that VICM-replica show fewer demoulding defects at the top of the structures compared to IIM as can be also seen in Fig. 4.28b (red full line).

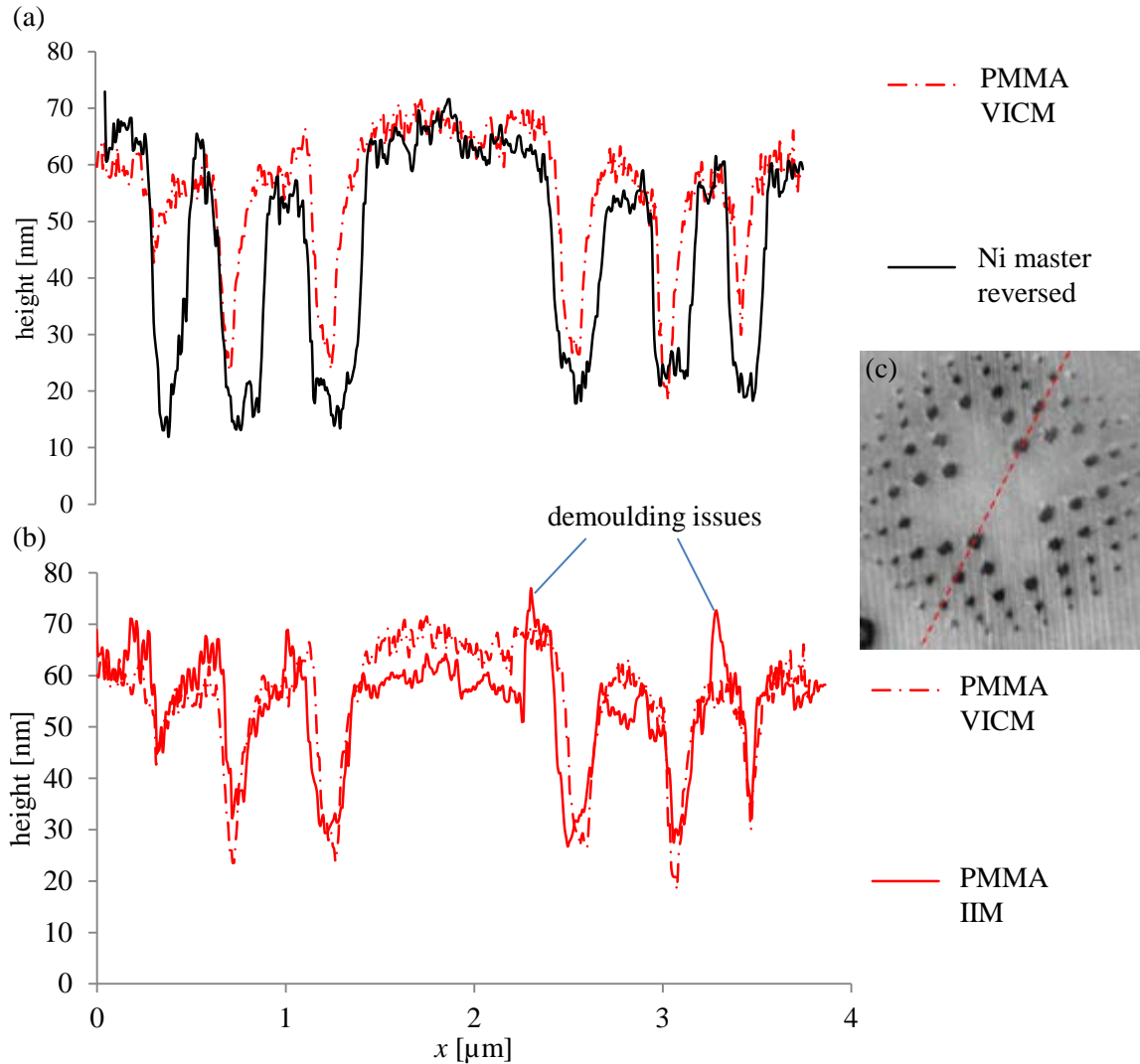


Fig. 4.28: (a) and (b) Comparison between Ni-Pd master and PMMA replica produced by IIM and VICM showing slightly better replication by VICM and less demoulding issues; (c) AFM picture of the replica indicating the cross-section of the profiles.

4.6.6 Transcription of Ni nanolines

The main goal of the replication of these nanolines was to find out, if the holding pressure in nanostructures has a different influence on the filling compared to microstructures. For that reason the replication ratio of nanostructures was evaluated with and without holding pressure for isothermal (IIM) and variothermal injection moulding (VIM).

The nanostructures were produced by mask based displacement Talbot UV photolithography followed by electroplating. The Ni-insert was clamped in the injection mould with lines being oriented parallel to the direction of polymer melt flow.

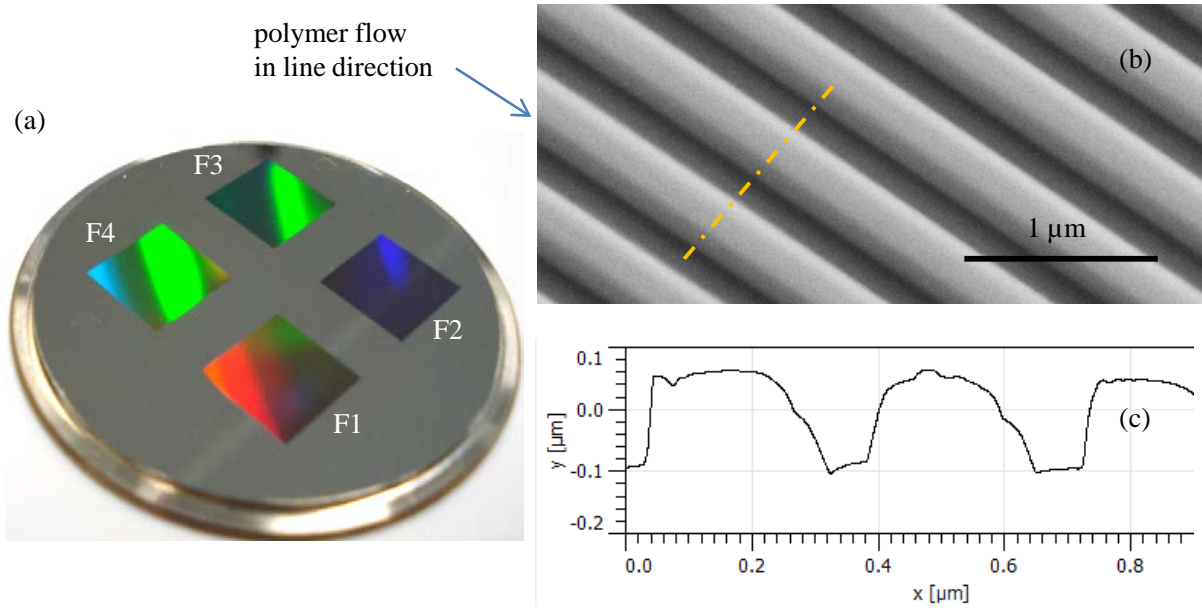


Fig. 4.29: (a) Nickel-paladium insert; (b) SEM picture (20° tilted) with nanolines (field F3); (c) AFM cross-section of the F3 line structure with a pitch of 300 nm.

Table 4-9: Pitch p , height h and aspect ratio AR of the four different fields shown in Fig. 4.29b.

Field	p [nm]	h [nm]	AR
F1	400	191±21	~ 1
F2	600	293±23	~ 1
F3	300	155±9	~ 1
F4	500	236±24	~ 1

This insert was replicated by iso- and variothermal injection moulding with PMMA. First, the part was filled to 99% and no holding pressure was applied (pressureless). This trial was compared to a standard isothermal and variothermal trial with holding pressure (with pressure).

In Fig. 4.30 it can be seen that there is almost no replication (5 - 10 nm) of nanolines using isothermal injection moulding (IIM) with pitches of 300 - 600 nm without holding pressure. When holding pressure is applied, the height increased by the factor of around 10 to structure heights of 48 - 99 nm. By increasing the mould temperature from 80°C to 115°C the filling without holding pressure increases to around 28 - 58 nm. Compared to the replication of microstructures the relevance of holding pressure on the replication accuracy is obviously much higher.

A reduction of pitch size results in a lower replicated height, but the h_r/w ratio remains almost constant. Thus, it seems that there is a linear correlation between the structure width and the replicated height.

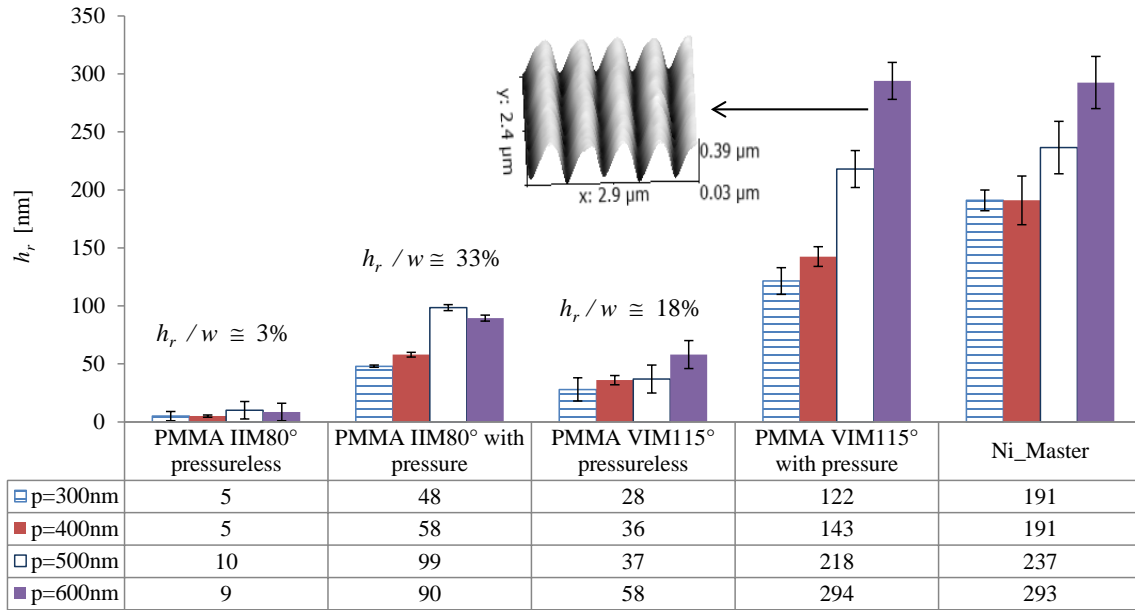


Fig. 4.30: Replicated structure height h_r for isothermal injection moulding process with a mould temperature of 80°C (IIM80°) with and without holding pressure (pressureless) compared to variothermal injection moulding with a mould temperature of 115°C (VIM115°).

Comparing the results of this trial for two different mould temperatures (80°C vs. 115°C) confirms that more polymer flows into the channel at 115°C , already before the holding pressure is applied, which results in a higher replicated height to width ratio (h_r/w). In contrast to the replication of microstructures the relevance of holding pressure on the replication accuracy is obviously quite high. A possible explanation is presented in Fig. 4.31. The holding pressure is essential for the filling of nanostructures because the shrinkage is in the range of the structure size.

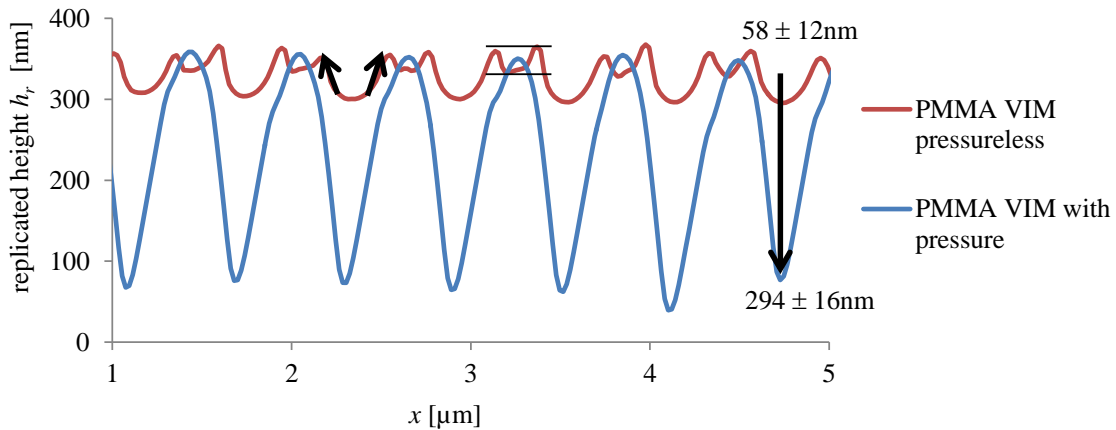


Fig. 4.31: AFM profile of a PMMA replica produced by variothermal injection moulding (VIM, $T_{mould} = 115^\circ\text{C}$) with (blue line) and without holding pressure (red line) showing that the structures with a pitch of 600 nm are only filled to 20% without holding pressure; the two black arrows indicate a shrinkage of around 30 nm.

4.6.7 Capillary and flow resistance regime depending on aspect ratio

As the 3D nanostructures shown in Chapter 4.6.5 with a maximum depth of $h_n = 50$ nm and a minimum feature size of 100 nm have a low aspect ratio ($AR < 0.5$), the flow resistance, which linearly depends on AR , is rather low and filling is less problematic compared to nanostructures with a higher AR , as discussed already in Chapter 4.6.4. The correlation of capillary pressure and flow resistance with capillary radius and aspect ratio is shown in Fig. 4.32 and Fig. 4.33. The better replication of A-PA compared to PMMA is again an indication for the relevance of wetting properties for the filling of nanostructures. With decreasing melt processing temperature T_p the contact angle of the polymer on the insert increased linearly (Fig. 4.8). Once it exceeds 90° the capillary pressure turns into negative counter-pressure acting in the same direction as the flow resistance P_{FR} , as can be seen in Fig. 4.32.

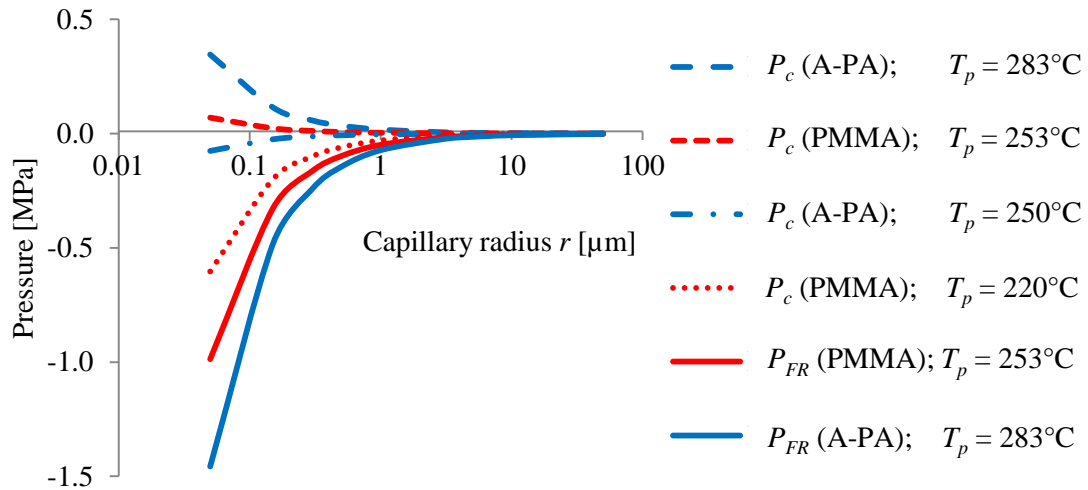


Fig. 4.32: Capillary pressure P_C and flow resistance P_{FR} (defined as negative pressure) vs. capillary radius r calculated from equation (4-9) and equation (4-10) respectively for PMMA (red) and A-PA (blue) melts with two different melt processing temperatures T_p on nanostructured ($h_n = 50$ nm) Ni with PFOP-coating showing a capillary pressure, assisting the polymer flow only at high melt temperatures (or in the very first milliseconds in contact with the mould).

By summing up P_{FR} and P_C at $T_p = 283^\circ\text{C}$ for A-PA and $T_p = 253^\circ\text{C}$ for PMMA and plotting versus the aspect ratio AR , it is possible to detect the cross over point AR_C from flow resistance ($P < 0$) to capillary dominated region ($P > 0$) depending on structure size and polymer as can be seen in Fig. 4.33.

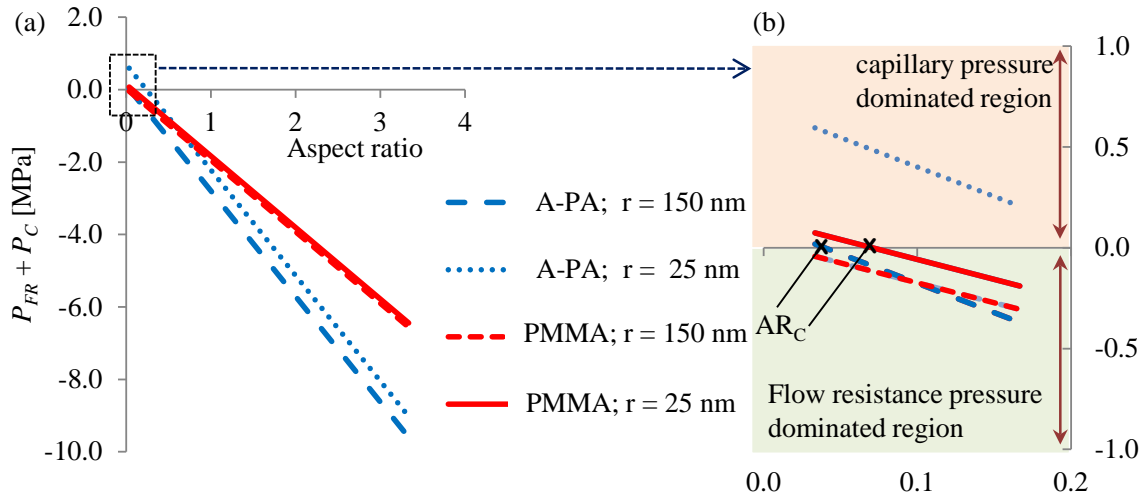


Fig. 4.33: (a) Sum of P_{FR} and P_C vs. AR for two different radii r ; (b) enlarged area showing the cross over point AR_C from flow resistance ($P < 0$) to capillary pressure dominated region ($P > 0$) depending on structure size and polymer.

A-PA has a higher surface energy which results in a higher capillary pressure compared to PMMA. The effect is getting more relevant for small structures (below capillary radius r of 150 nm). On the other hand the viscosity of A-PA is higher than that of PMMA resulting in a higher flow resistance P_{FR} at a given temperature.

The critical flow height h_{n0} is the point, when the flow resistance becomes smaller than the capillary pressure. Thus, by assuming $P_{FR} = P_C$, h_{n0} can be calculated from equation (4-11).

$$h_{n0} = \frac{\sigma_L \cdot \cos \theta \cdot e_0}{\eta \cdot \gamma} \quad (4-11)$$

$$r_C = \frac{h_{n0}}{2 \cdot AR_C} \quad (4-12)$$

For PMMA h_{n0} is 4 nm and for A-PA it is 12 nm because of better wetting behaviour of the latter one. From the critical flow height h_{n0} the corresponding critical radius r_C can be calculated with equation (4-12). The results are listed in the following table:

Table 4-10: Calculated critical radius r_C based on a critical flow height h_{n0} of 4 nm for PMMA and 12 nm for A-PA.

Aspect ratio AR	0.01	0.1	0.5	1	5
r_C for PMMA [nm]	176	18	4	2	0
r_C for A-PA [nm]	593	59	12	6	1

This means, for example that for the filling of a tubular structure with an aspect ratio of 0.1 and a radius r of 59 nm with A-PA, the capillary forces have to be taken into account as they would dominate versus the flow resistance. The calculations are in good correlation with experimental trials already described in Fig. 4.23.

4.7 Conclusions

Complementary to other studies on variothermal injection moulding the specific progress of this part of the thesis was to show the filling differences from micro to nanoscale of four different processes including variothermal injection compression moulding (VICM) on the same mould, taking into account the influence of exact online-determined melt viscosities and surface energies of different polymers, in order to calculate the flow resistance and capillary effect in micro- and nanostructures.

It was shown that high aspect ratio microstructures can be replicated with high accuracy using variothermal injection (compression) moulding only in combination with a polymer of sufficiently low melt viscosity and, thus, a low filling resistance in the cavity. In particular, it could be demonstrated that the actual no-flow temperature T_{no} , which can differ significantly from the glass temperature, plays a key role for the replication behaviour. The two studied polymers show similar T_g (both 110°C) but considerably different T_{no} . This is why the replication of microstructures with AR = 5.6 by VICM with an upper mould temperature slightly above T_g ($T_{mould} = 115^\circ\text{C}$) for A-PA ($T_{no} = 150^\circ\text{C}$) results in incomplete filling (only 52%) whereas PMMA with the same T_g but $T_{no} = 130^\circ\text{C}$ yields 100% replication. The lower T_{no} of PMMA causes slower frozen layer formation resulting in a lower melt viscosity within the cavity. Differences in wetting can be neglected for the filling of microstructures as the influence of viscosity is dominating.

On the contrary, capillary forces (driven by good wetting) seem to have a positive effect on the filling of nano-sized cavities and, thus, should not be neglected when investigating the replication behaviour of nanostructures. For this reason, nano-pillars were better replicated with A-PA that has a higher spreading coefficient at lower temperatures than PMMA. Capillary forces can even dominate versus flow resistance for feature sizes below 100 nm at least for low aspect ratio structures (AR < 0.1).

Although the replication fidelity of micro- and nanostructures cannot be improved significantly by an additional compression stroke (IICM, VICM), the well-known benefit of reduced pressure and internal stresses in the polymer part can be nicely combined with variothermal heating for best replication accuracy. The disadvantages of variothermal heating are a longer cycle time, more demoulding issues and complex mould design. However, demoulding issues like nano-pillar breakage can be minimised by an additional compression stroke because of the associated lower and more uniform stress distribution in the part. For that reason, defect-free large area replication of nano-pillars is possible, although electroplated nickel showed sensitivity to mechanical loads. If possible, structure geometries like sinusoidal grooves are preferable for a stable replication process instead of high aspect ratio nano-pillars.

Depending on the required precision of the functional structures, isothermal injection moulding may be sufficient for the replication of low aspect ratio 3D nanostructures. However, highest replication quality is achieved by variothermal injection (compression) moulding.

Comparing different publications, the influence of the holding pressure on the replication process has been discussed very contradictory. The results presented in this thesis clearly show that the effect of holding pressure strongly depends on structure size and on mould temperatures in relation to the no-flow temperature that influence the cooling speed and, thus, the duration of the pressure prior to freezing. The biggest influence of holding pressure was found for variothermal processes when replicating nanostructures in stark contrast to isothermal replication of macrostructures

The focus of this Chapter was on processes, parameters and structure variations. The influence of wetting, spreading, surface energy and viscosity on the replication quality was already mentioned, and correlations between these characteristics and replication will be discussed in greater detail in the next Chapter.

5. ON THE ROLE OF WETTING, STRUCTURE WIDTH AND FLOW CHARACTERISTICS IN POLYMER REPLICATION

The main objective of this Chapter is to show a correlation between the wetting characteristics, i.e. the measured surface tension and the calculated spreading coefficient of different polymers on different mould-insert materials with the replication ratio of various structure sizes covering both the micro- and nanoscale. As a result from these studies, a new characteristic value for polymers, the dewetting potential Ω_s , is proposed as a simple rationale for the differences in replicability of functional structures by injection moulding observed between different polymers (Chapter 5.2). For the calculation of Ω_s , no-flow temperatures (Chapter 5.2.1), contact angles and the surface tension of the polymers (Chapter 5.2.2) were determined experimentally.

Additionally to the influence of wetting and viscosity, the influence of the structure width on the replication behaviour is investigated in Chapter 5.3. The difference between variothermal and isothermal injection moulding in respect to the replication fidelity is once again discussed in Chapter 5.3.2, this time, for hierarchical structures.

The interfacial interaction of the mould's surface with the polymer melt has a huge impact in the context of manufacturing of polymeric micro- and nanostructures. It is of particular interest for the filling and demoulding of such structures, especially if features become very small. (Mosaddegh and Angstadt, 2008) proved the influence of interfacial wetting, showing differences in the filling behaviour of silicon sub-micron structures of three amorphous polymers without external pressure. The temperatures were adapted in a way that η_0 of all polymers were on the same level. According to these investigations the filling of PS and PMMA was superior to that of COC because of lower melt contact angles on silicon.

However, the influence of polymer wetting or spreading behaviour on the filling of micro- and nanostructure cavities has not been completely understood.

5.1 Materials and methods

5.1.1 Injection moulding processes and mould master inserts

All trials were carried out on an Arburg 320 A injection moulding machine from Arburg (Lossburg, Germany). The variothermal injection compression mould (described in detail in Chapter 3.3) was designed internally and produced at AdvalTech FOBOHA (Muri, Switzerland). The mould was equipped with four temperature and three piezoelectric pressure sensors from Priamus (Schaffhausen, Switzerland), allowing precise process control as well as online monitoring and data extraction during the moulding process. The main principle of the online measurement of polymer viscosity with a pressure and temperature sensor was described in detail in Chapter 3.3.3.

On the injection side two unstructured, highly polished chrome steel (CrNi 1.4301; roughness $R_a = 0.013 \mu\text{m}$) inserts were clamped. On the ejection side two different mould inserts with micro- and nanostructures were used. On one insert, a v-shaped microgroove was implemented (already explained in detail in Chapter 4.2.1).

Additionally to the brass insert, a nickel master with hierarchical micro- and nanostructures (Fig. 5.1a) was produced by electroplating at the Technical University of Denmark (DTU). For better demoulding, a plasma-polymerized perfluorocarbon nano-coating was applied. Further details about this monolayer coating can be found in the investigation of (Cech and Taboryski, 2012), who tested the durability of this particular coating on aluminium. After 500 moulding cycles with ABS and PS the surface

energy σ_s was still in the range of 20 mN m^{-1} and the presence of fluorine was additionally confirmed by x-ray photoelectron spectroscopy (XPS).

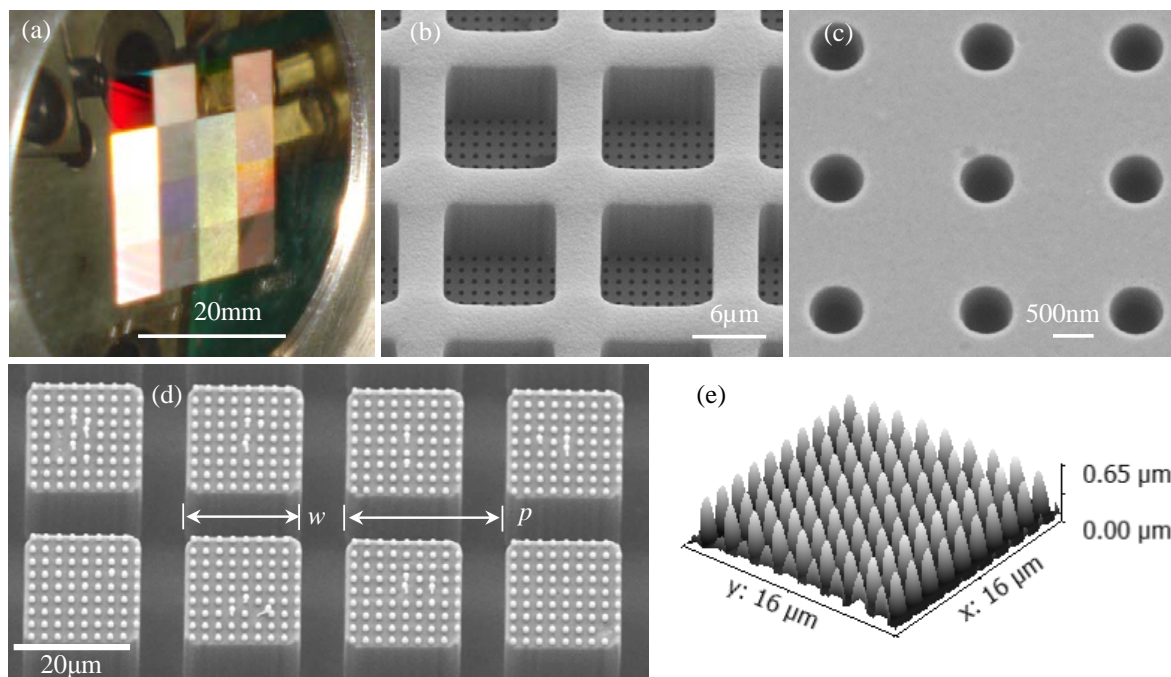


Fig. 5.1: (a) Photograph of Ni-master featuring a variety of hierarchical surface topographies; (b, c) SEM micrographs of selected fields on two different length scales and corresponding polymer replica of (d) hierarchical (SEM) and (e) nano-pillar structures (AFM).

Two of the 16 structure fields had only nanostructures (master and replica shown in Fig. 5.1c and e), whereas the others were squared hierarchical microstructures of different width w and pitch p with nanostructures on top of the squares (master and replica shown in Fig. 5.1b and Fig. 5.1d). An exemplary replica is shown in Fig. 5.2b. The nanostructures on top of the microstructures could only be replicated variothermally with elevated mould temperatures.

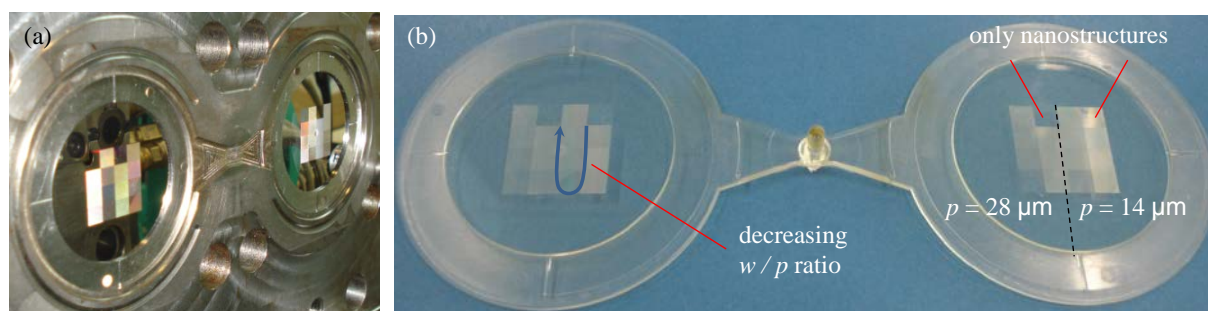


Fig. 5.2: (a) Injection mould with two electroplated Ni master inserts with different hierarchical micro- and nanostructures, manufactured at DTU; (b) A-PA replica showing structured fields with different pitches p and widths w .

5.1.2 Polymers and processing temperatures

Polymethylmethacrylate (PMMA, Plexiglas[®] 7N) from Evonik (Marl, Germany), amorphous polyamide (A-PA, Grilamid[®] TR55LX) from EMS-Chemie (Domat-Ems, Switzerland), cycloolefin copolymer (COC, Topas[®] 5013L-10) from Topas Advanced Polymers (Oberhausen, Germany), polypropylene (PP, PPC-711-70RNA) from Braskem (Sao Paulo, Brazil), polyoxymethylene (POM, Hostaform[®] C9021) from Celanese (Kaiserslautern, Germany) and polystyrene (PS, PS 158K) from BASF (Ludwigshafen, Germany) were used for the replication trials, pendant-drop tests, contact angle measurements and determination of surface tensions.

The melt and mould temperatures as well as the injection velocity were kept constant for all isothermal injection moulding trials, summarized in Table 5-1.

Table 5-1: Glass transition, melting and crystallization temperatures and set / measured injection moulding parameters applied for all trials; the mould temperatures were all set to the upper limit of the recommended temperature range.

Material	Glass or melting / crystallization temperatures			Cylinder temperatures T_{cyl} [°C]	Injection speed v_{inj} [cm ³ s ⁻¹]	Set / measured mould temperature at ejection T_{mould} [°C]
	T_g [°C]	T_{mb} [°C]	T_c [°C]			
A-PA	110	-	-	280	15	70 / 67
PMMA	100	-	-	250	15	80 / 77
PP	-	160	123	220	15	40 / 38
COC	130	-	-	280	15	120 / 116
PS	100	-	-	230	15	70 / 67
POM	-50	166	144	205	15	90 / 87

5.2 Correlation of dewetting potential with replicated height

Relevant polymer properties (online measured viscosity η , no-flow temperature T_{no} and surface tension σ_L) were determined either for a comparison with the filling height or for the calculation of the spreading coefficient S and the dewetting potential Ω_S . Afterwards η , σ_L and Ω_S were compared with the replicated height of micro- and nanostructures. Additionally to the influence of viscosity and wetting, the impact of the structure width w and pitch p on the filling height will be demonstrated and explained in comparison to common theoretical approximations.

5.2.1 No-flow temperature measurements

In Fig. 5.3 no-flow temperatures T_{no} of six different polymers were determined with a modified melt flow rate (MFR) measurement, explained in detail in Chapter 3.2.1.

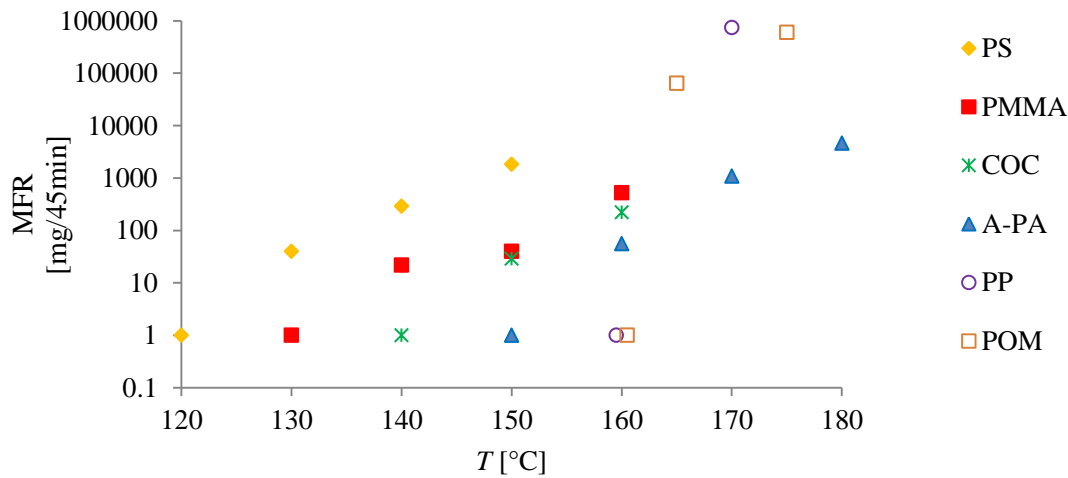


Fig. 5.3: Modified MFR measurements by weighing the extruded material after employing a load of 21.6 kg (corresponding to 33 MPa) for 45 min at different temperatures. Values for T_{no} were determined by extrapolation of the experimental data to an MFR value of 1 mg / 45 min (considered as no flow).

The measured T_{no} was compared with T_g and listed in Table 5-2.

Table 5-2: Determined T_{no} (measured) for various polymers in comparison to T_g and T_c (from data sheets, determined by dynamic scanning calorimetry DSC).

Material	PS	PMMA	COC	A-PA	PP	POM
T_{no} [°C]	120	130	140	150	160	165
T_g [°C]	100	110	130	110 / -	-10	-50
T_c [°C]	n.a.	n.a.	n.a.	n.a.	123	144
$\Delta T = T_{no} - (T_g \text{ or } T_c)$ [°C]	20	20	10	40	37	21

The smallest difference between T_g and T_{no} was measured for COC ($\Delta T = 10^\circ\text{C}$), the biggest for A-PA ($\Delta T = 40^\circ\text{C}$). T_{no} for the semi-crystalline PP corresponds exactly to the melting temperature of 160°C but is higher than T_c . At T_{no} it is expected that no polymer flow is possible, although even below T_{no} material could be pressed into the cavities by elastic deformation, forced by very high pressure. Furthermore, during injection moulding the measured pressure in the cavity was up to 60 MPa. Therefore, the T_{no} values may be somewhat lower for higher pressures than the 33 MPa as applied in the modified MFR measurement.

5.2.2 Comparison of surface tension and polymer viscosity with replicated height

In most injection moulding investigations the effect of surface tension, which can lead to different wetting at the interface of the polymer and mould is neglected. By determination of the surface tension of the polymer melt and the contact angle of the melt on the mould material, it is possible to estimate the effect of wetting on the filling quality. For that reason the spreading coefficient S_c , which is defined as the difference between the free energies of cohesion ΔG_c and adsorption ΔG_a (Trojer et al., 2013), was calculated with equation (5-2).

$$S_c = \Delta G_c - \Delta G_a = \sigma_S - (\sigma_L + \sigma_{SL}) \quad (5-1)$$

$$S_c = \sigma_L(\cos \theta - 1) \quad (5-2)$$

Equation (5-2) is a combination of equation (5-1) and the Young's equation (3-4).

For the calculation of S_c according to equation (5-2) the surface tension σ_L and the contact angle θ of the polymer melt on the mould material needs to be known. In Fig. 5.4 four exemplary graphs with contact angle measurements on brass are shown.

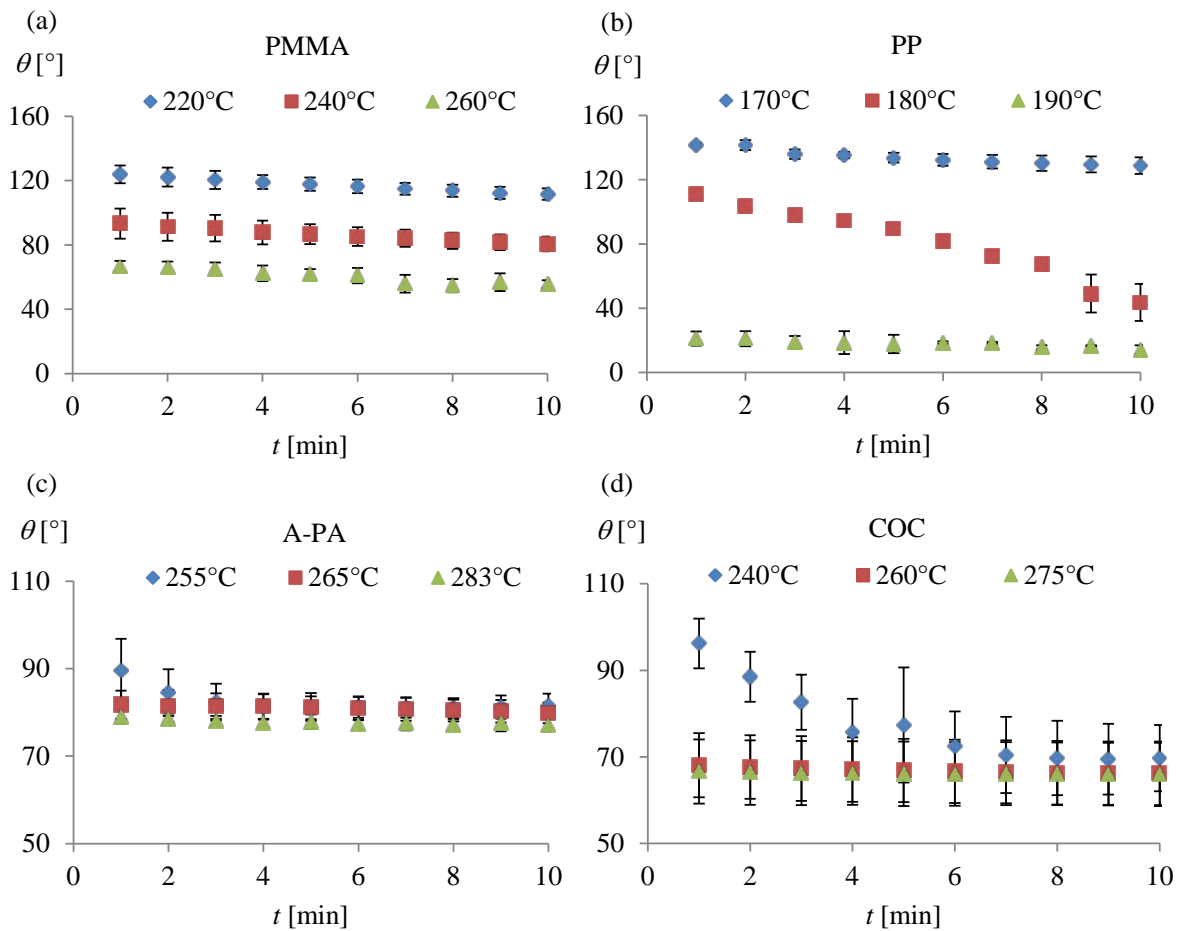


Fig. 5.4: Time-dependent contact angle measurements for different polymer melts on brass: (a) PMMA, (b) PP, (c) A-PA and (d) COC; (SD of 5 measurements).

The values used for subsequent calculation of the spreading coefficient were always taken after 10 min measuring time, where the contact angles had stabilized in most cases. It was assumed that, after this time, the drop was in thermal hydro-mechanical equilibrium and thermal degradation would not have influenced the measurement yet. These contact angles are plotted as a function of T in Fig. 5.5 for different mould metal surfaces.

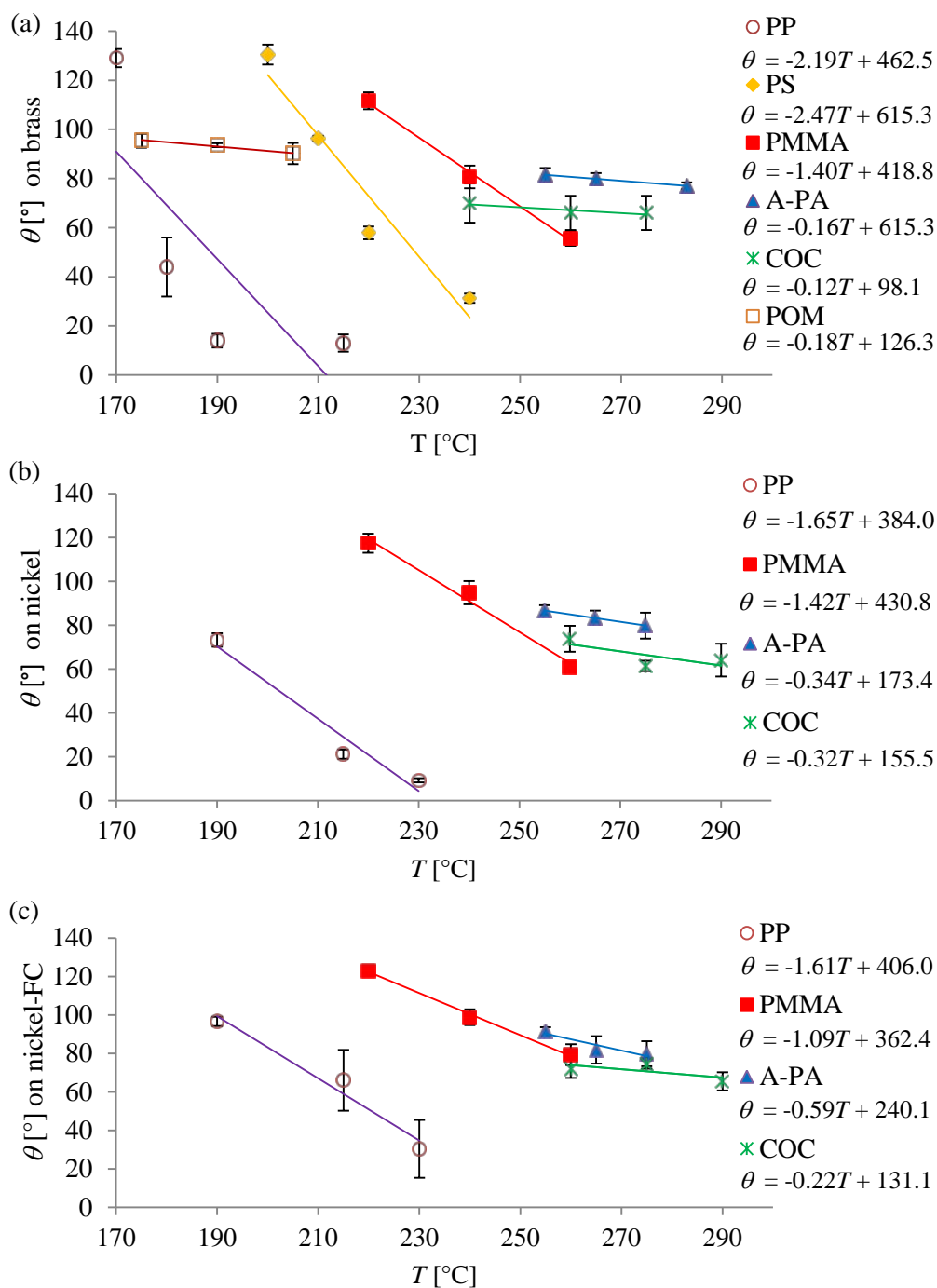


Fig. 5.5: Polymer melt contact angle measurements on various surfaces (brass, nickel and nickel with a perfluorocarbon anti-sticking coating = nickel-FC) at different temperatures, determined with sessile drop method;. (SD of 3 measurements, fitted with linear regression curves).

Fig. 5.6 shows the temperature dependence of the surface tension for the different polymers investigated in this study. Values for the surface tension in the molten (σ_L) and in the solid state (σ_S) were determined by the pendant and sessile drop method, respectively, as described in Chapter 3.2.2.

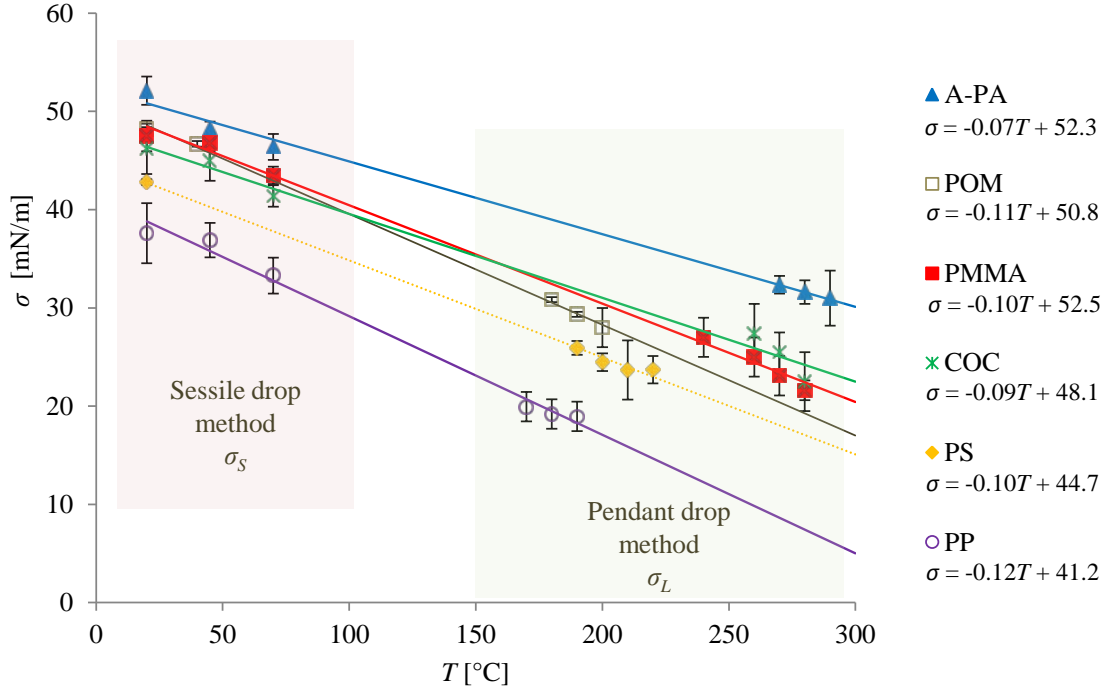


Fig. 5.6: Surface tension σ_L and σ_S of different polymers as a function of temperature determined from sessile and pendant drop measurements; (SD is based on minimum 3 experiments).

Generally, the surface tension decreases with increasing temperature. This could be explained with heat energy disrupting surface bonds like e.g. hydrogen bonds. Moreover, the surface energy is a function of surface internal energy U , the temperature T and the surface entropy S . According to equation (5-3) (Ragone, 1995), the surface tension decreases with increasing T :

$$\sigma = U - T \cdot S \quad (5-3)$$

The material with the lowest surface tension is PP, the one with the highest A-PA. Although data between sessile and pendant drop method were just interpolated, it seems that the decrease of surface tension with increasing temperature is linear which would be in accordance with studies of (Yang et al., 2010).

Additionally to the surface tension, as shown in Fig. 5.6, other polymer properties can affect the melt flow into small cavities. According to common knowledge, a low viscosity improves the filling in macro injection moulding. For that reason, it is of interest to plot the observed filling height in micro- and nanostructures versus the online viscosity and the surface tension at the respective polymer processing temperature, which is shown in Fig. 5.7 and Fig. 5.8.

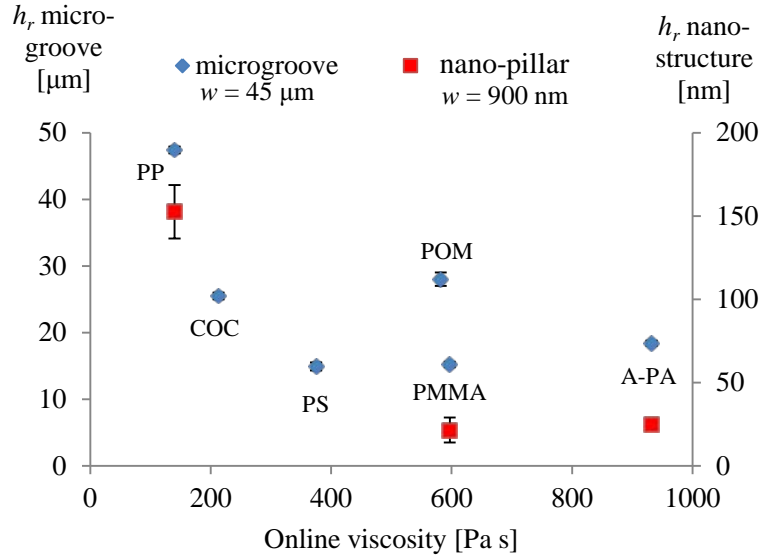


Fig. 5.7: Replicated height of v-groove microstructure with a width of $45 \mu\text{m}$ at the entrance (blue symbols) and nano-pillars with a diameter of 900 nm (red symbols) vs. online viscosity (determined at melt processing temperature) showing no clear correlation; (SD of 3 measurements).

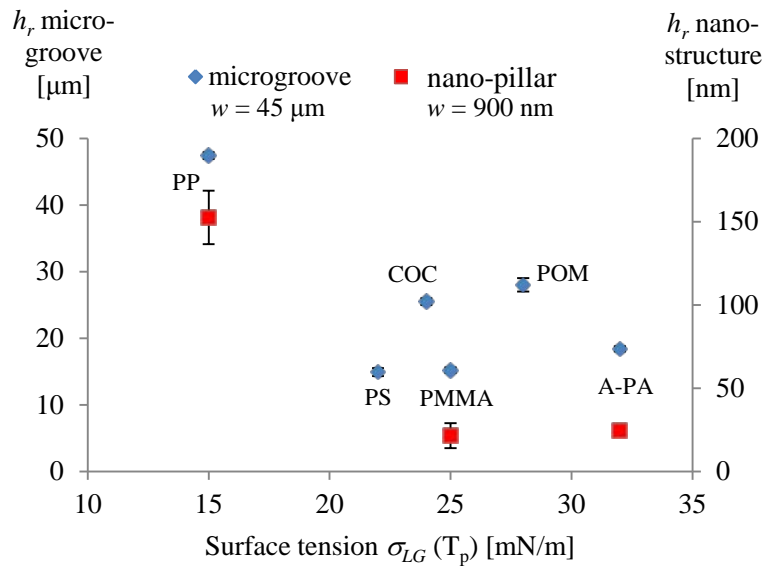


Fig. 5.8: Replicated height of v-groove microstructure with a width at the entrance of $45 \mu\text{m}$ (blue symbols) and nano-pillars with a diameter of 900 nm (red symbols) vs. surface tension of the polymer melt at processing temperature T_p both showing no good correlation; (SD of 3 measurements).

Fig. 5.7 clearly reveals that a low melt viscosity is favourable for the filling of micro- and nano-sized cavities. On the contrary, the effect of the surface tension of the polymer melts on the replicated height (Fig. 5.8) seemingly does remain unclear at least for microstructures. This indicates that other parameters besides of viscosity and contact angle at the polymer/mould interface have to be taken into account to explain the replication behaviour. Therefore, other explanations are presented.

5.2.3 Correlation of dewetting potential with replicated height of microstructures

A separate consideration of viscosity or surface tension is only useful to a certain extent for the explanation of polymer replication on the micro- and nanoscale. However, the spreading coefficient S_c (Equation (5-2) above) combines not only the surface tension but also the contact angle of the melt on the mould surface and could therefore be an interesting characteristic to be correlated with the replicability.

In Fig. 5.9 the spreading coefficient is plotted for different polymers on different mould surfaces:

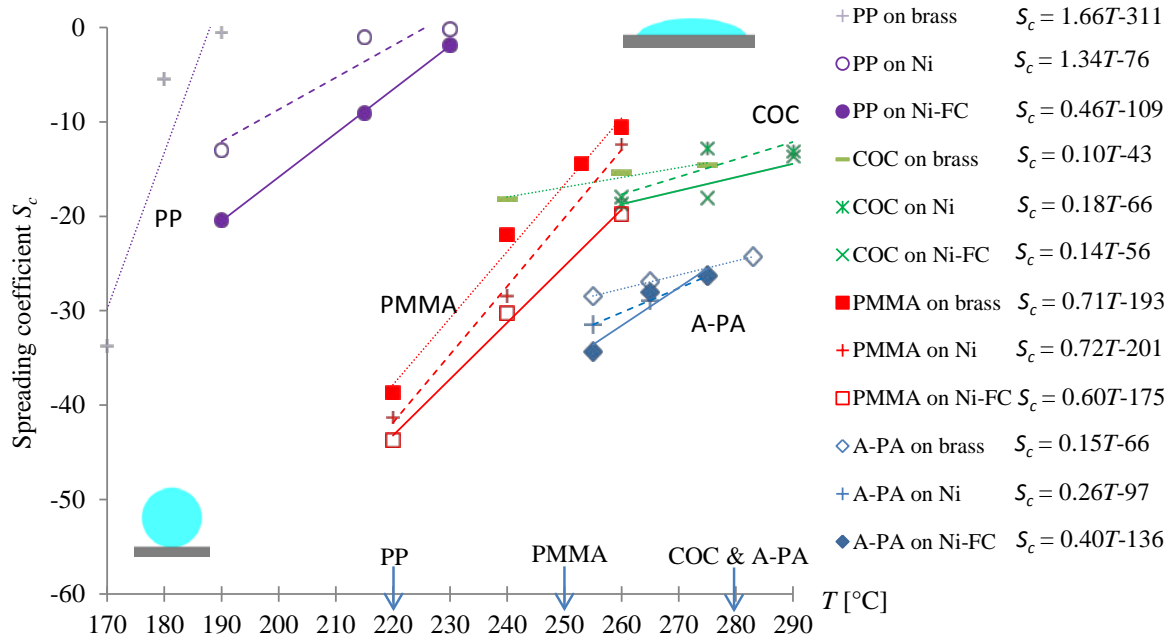


Fig. 5.9: Spreading coefficients of different polymers on various mould materials: brass, nickel (Ni), nickel with perfluorocarbon based anti-sticking coating (Ni-FC); fitted with linear regression curves, also used for the calculation of the dewetting potential. The blue arrows indicate the respective polymer melt processing temperature T_p .

For all polymers the spreading (low spreading coefficient) was best on brass and worst on nickel coated with a fluorocarbon anti-sticking layer (highest spreading coefficient). As the polymer melt comes in contact with the mould surface and rapidly cools down, S_c changes within milliseconds, i.e. the polymer melt undergoes a gradual dewetting process behaviour (corresponding to the slope dS_c/dT) until it freezes at the no-flow temperature. As can be seen from Fig. 5.9, this gradual dewetting can vary substantially between the different polymers investigated in this thesis. In an attempt to quantify this effect, we assumed that integration of S_c over the temperature range from T_p (initial melt temperature upon contact with the mould) to T_{no} (temperature at which polymer stops to flow) yields to the dewetting potential Ω_s :

$$\Omega_s = \int_{T_{no}}^{T_p} S_c dT \quad (5-4)$$

Based on this assumption the graph shown in Fig. 5.10c can be plotted and correlated with the replicated height of the v-groove microstructure.

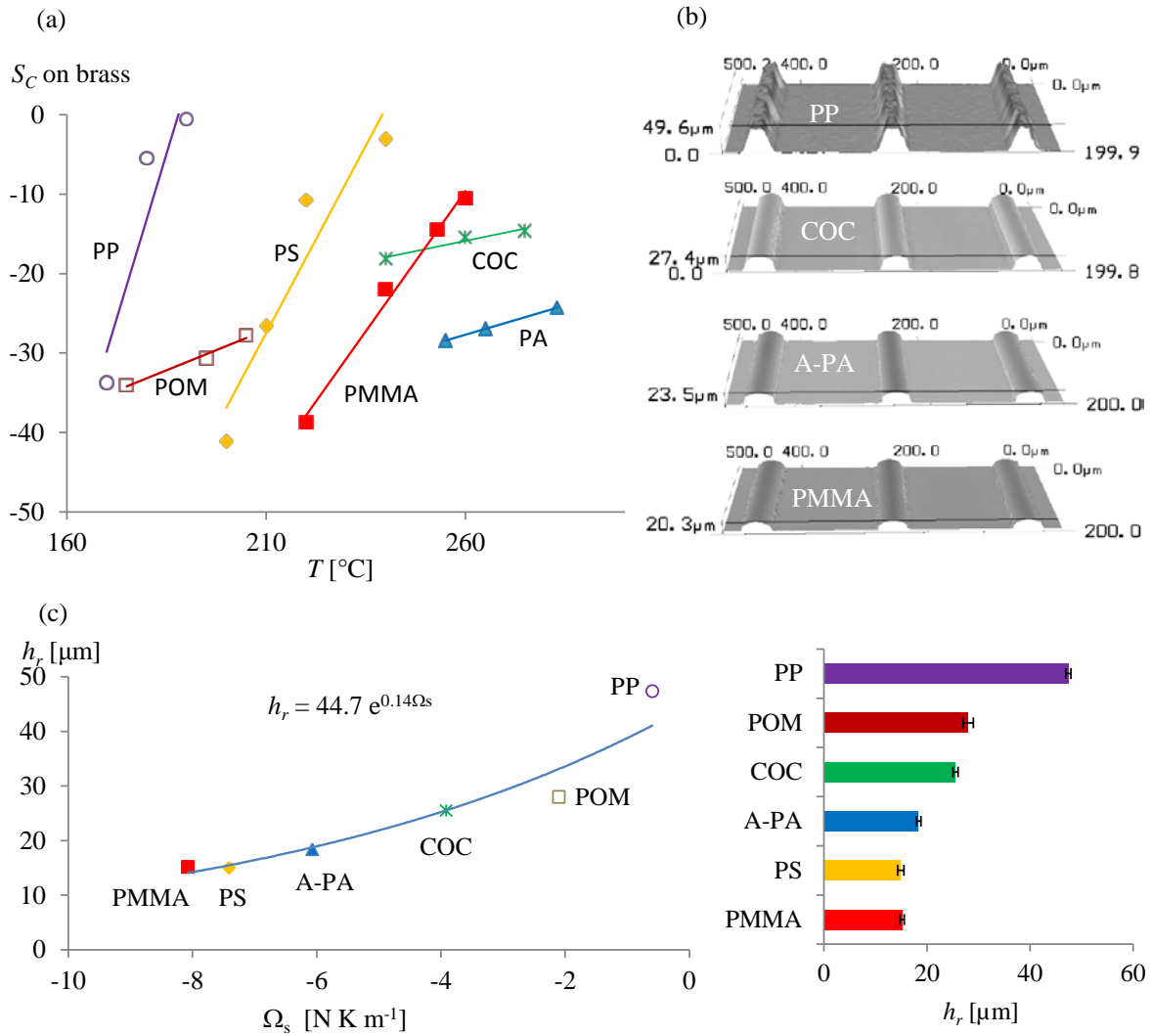


Fig. 5.10: (a) Calculated spreading coefficient S_C on brass as a function of melt temperature for six different polymers that were replicated into a v-groove microstructure on a brass mold, showing a good correlation with (b) 3D CLSM micrographs of the four replicated polymers (PS is equal to PMMA and POM is only slightly higher than COC, therefore, not shown here); (c) replicated height vs. dewetting potential (SD of 3 measurements, exponential fit).

In Fig. 5.10 the spreading coefficients on brass are plotted as a function of temperature next to CLSM micrographs of replica obtained from standard isothermal injection moulding. Interestingly, the replicated height h_r correlates very well with the dewetting potential Ω_s as can be seen in Fig. 5.10c, showing the lowest dewetting potential for PP and the highest for PMMA. Thus, Ω_s (the integrated spreading coefficient) seems to be an appropriate characteristic to describe the filling potential of microstructures for a given polymer.

5.2.4 Correlation of dewetting potential with replicated height of nanostructures

Additionally to the replication of brass microstructures, the replicated heights of micro- and nanostructures were also investigated on Ni surfaces coated with anti-adhesion layers based on fluorocarbons. The differences between the replicated height to width ratio of micro- and nanostructures can be seen in Fig. 5.11a.

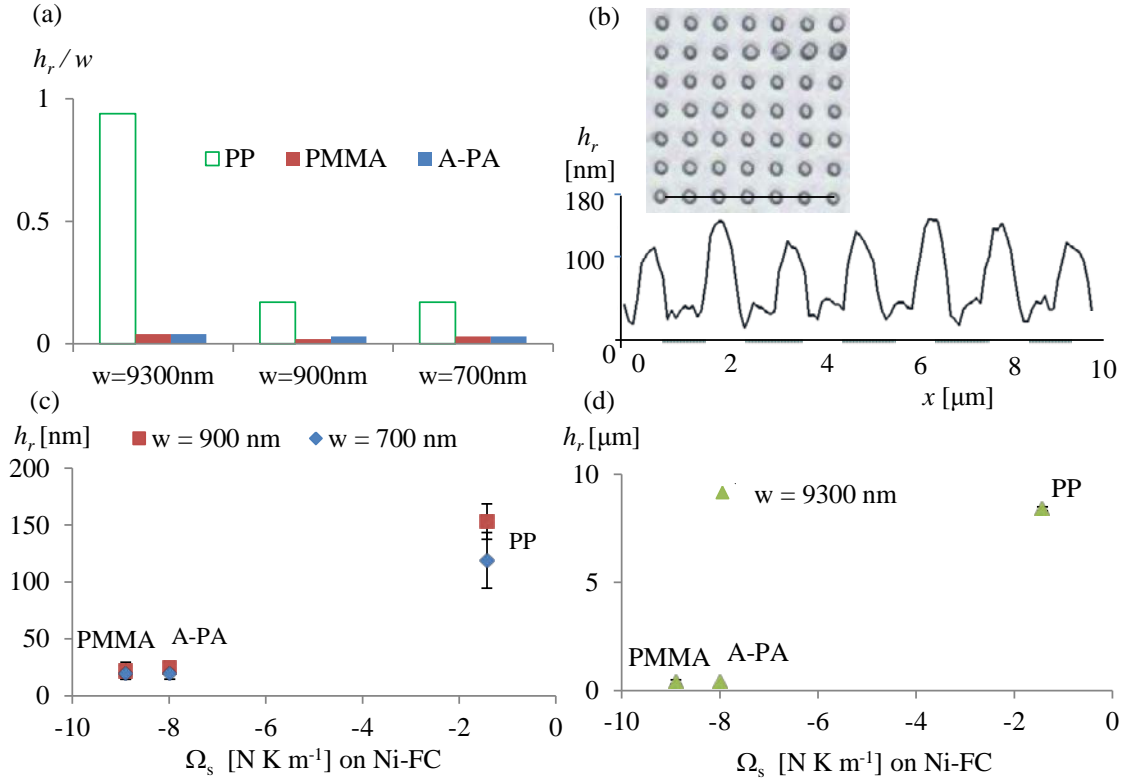


Fig. 5.11: (a) Difference between nanostructure ($w = 700\text{ nm}$ and $w = 900\text{ nm}$; mold master = Ni-FC) and microstructure ($w = 9300\text{ nm}$; mold master: Ni-FC) replication (isothermal), showing the influence of the width on the h_r/w replication ratio in correlation with (c & d) the dewetting potential of three different materials; (b) exemplary CLSM cross-section of PP structures with a width of 700 nm showing a height of $119 \pm 25\text{ nm}$.

Obviously, nanostructures are more difficult to fill than microstructures resulting in a lower achievable height to width ratio (h_r/w), likely because of rapid cooling and faster heat transfer in small structures. This effect seems to be less pronounced for materials with a lower dewetting potential like PP in comparison to A-PA or PMMA, referring to Fig. 5.11a&c. Moreover, it is worth to underline once more that the differences in replication accuracy between the three materials correlate well with the dewetting potential (Fig. 5.11c&d). Thus, the theory of dewetting potential was evaluated with four different structures (two in the micro and two in the nano range), on two selected surfaces (brass and Ni with fluorocarbon nano-coating) and five different materials (PP, PMMA, A-PA, PS, COC) with various spreading coefficients.

5.3 Replicability of hierarchical structures

5.3.1 Influence of width to pitch ratio on replication height of micro-squares

Additionally to viscosity and wetting, effects discussed in previous Chapters, the dimensions of micro- or nano-cavity structures, in particular the width w influence the maximal replication ratio (RR) that can be achieved in isothermal injection moulding. Different analytical or empirical approaches to approximate that RR of micro- and nanostructures have been proposed. (Xu et al., 2005) tried to correlate the RR with the Fourier number Fo (cf. equation (5-5) below), which represents the ratio between heat conduction and thermal energy storage.

$$\text{Fo} = \frac{a_{eff} \cdot \Delta t}{w^2} \quad (5-5)$$

$$a_{eff} = \frac{k}{\rho_m \cdot c_p} \quad (5-6)$$

Where a_{eff} is the thermal diffusivity, Δt is the time needed by the polymer to flow from the structure with a width w to the end of the cavity, k is the coefficient of thermal conductivity, c_p is the specific heat capacity and ρ_m is the melt density. It was shown that a lower Fo number results in a lower RR, effectively scaling with w^{-2} .

The Graetz number Gz can be defined as the ratio within the polymer melt filling the cavity and the heat conduction into the surrounding mould:

$$\text{Gz} = \frac{\dot{\gamma} \cdot w^2}{a_{eff} \cdot h_r} \quad (5-7)$$

Where h_r is the characteristic length, in this case the filling height; $\dot{\gamma}$ is the shear rate.

The smaller Gz the more dominant the cold mould gets in comparison to the convection of heat from the polymer melt leading to a freezing in the micro-channel. The higher the width w of the structure and the higher the injection speed (or the shear rate $\dot{\gamma}$) the higher will be the Graetz number, ultimately resulting in a better filling. As Gz scales with w^2 the influence of structure dimensions on the replication ratio will become dominant compared to fast injection strategies preventing the melt from freezing. This is the reason why especially high mould temperatures can significantly improve the filling in micro- and nano-cavities. (Yao and Kim, 2005) discussed the influence of Gz and the freezing time t_f (cf. equation (5-8), below) on the filling of microstructures.

$$t_f = \frac{w^2}{\pi^2 a_{eff}} \ln \left(\frac{4}{\pi} \cdot \frac{T_p - T_{mould}}{T_{no} - T_{mould}} \right) \quad (5-8)$$

All three equations have in common that the influence of w on h_r scales with the power of two.

Also (Cui et al., 2014) and (Young, 2005) proposed a parabolic relation in their calculations between filling height and structure width, but without proving it experimentally.

As can be seen in Fig. 5.12a, a quadratic dependence of h_r on w on the microscale was confirmed experimentally, which is in good agreement with the influences of the Graetz and Fourier numbers as well as the empirical freezing time, c.f. equation (5-5) - (5-8). As expected, the parabolic dependence approaches the maximum structure height of the master structures (9.5 μm) asymptotically at $w = p$.

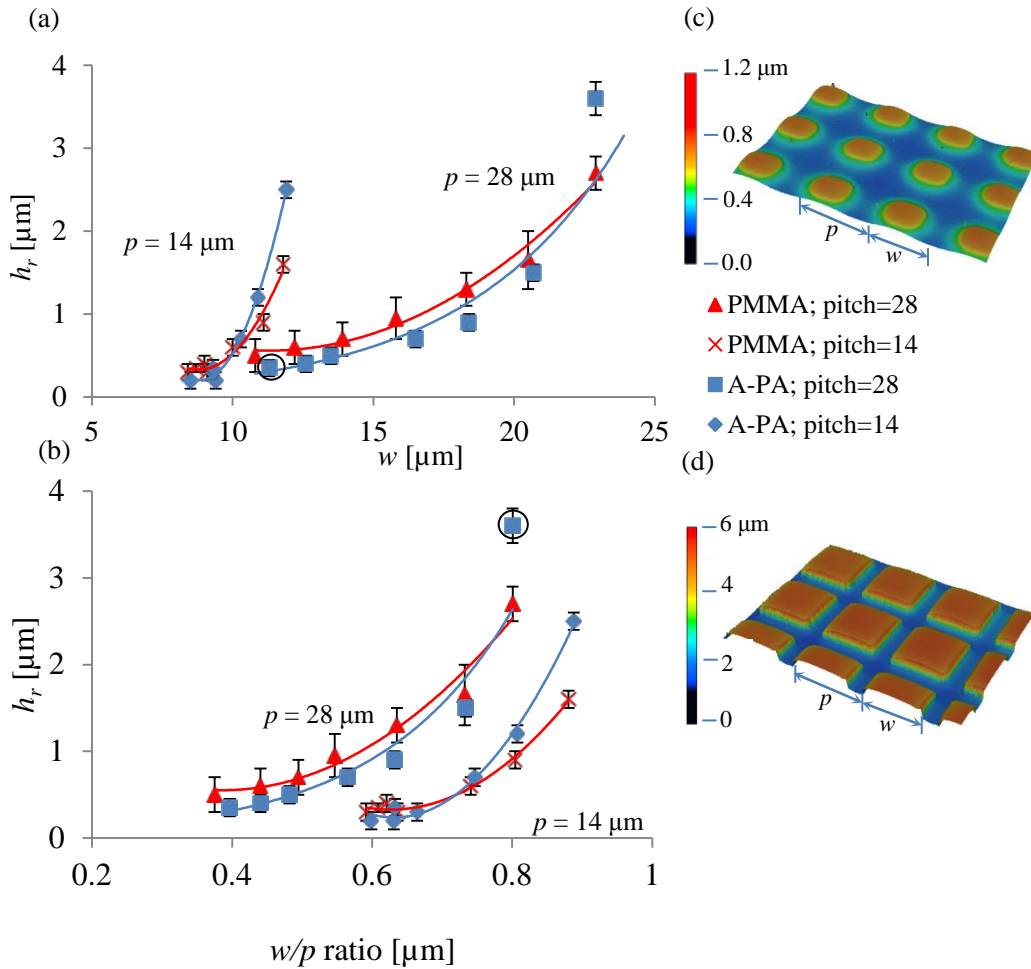


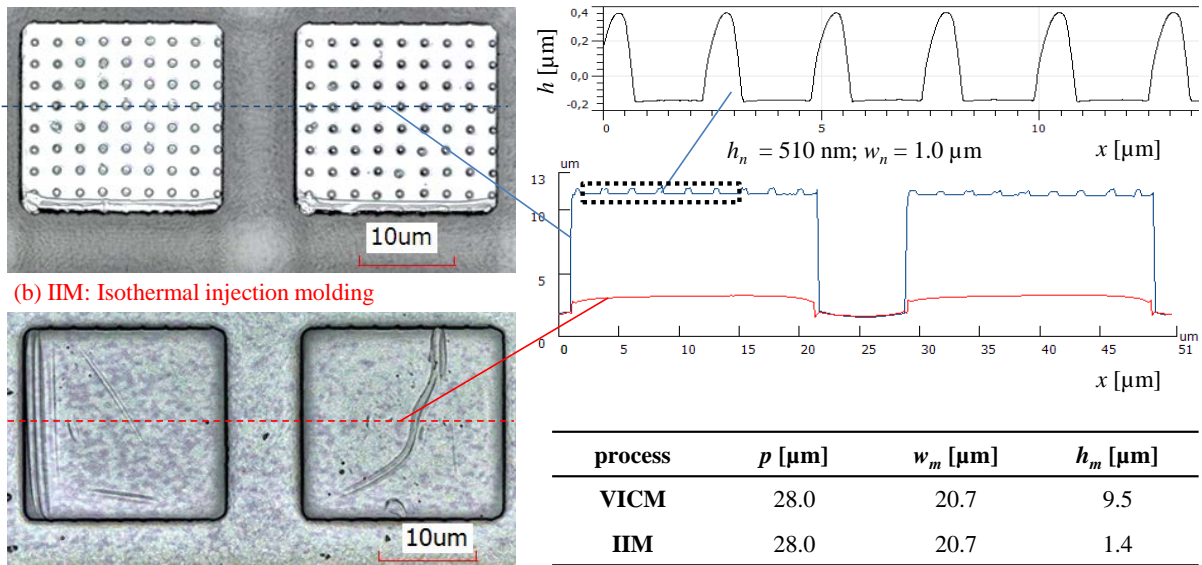
Fig. 5.12: Replicated height h_r as a function of (a) the width w of micro-cavities, and (b) the width to pitch ratio w/p of the master structure for a series of rectangular pillar arrays with two different pitches moulded from PMMA (red symbols) and A-PA (blue symbols); (c), (d) selected 3D CLSM micrographs of two A-PA replica ($p = 28$ μm) marked with black circles (Results fitted with quadratic functions; SD of 3 measurements).

Fig. 5.12b shows that the ratio w/p also influences the achievable replication height. The comparison of the replicated height of the two populations differing in p at a constant value of w/p (e.g. 0.75) confirms that bigger micro-cavities are filled to a larger extent under standard processing conditions. This can readily be understood by considering the local heat losses, where the melt is in direct contact with the mould. For a constant w/p , a similar contact area results in similar heat fluxes. However, the widths of the single cavities to be filled are double for $p = 28$ μm and, thus, it takes substantially more time to cool down the polymer melt to the no-flow temperature. This effect was also observed in investigations of (Xu et al., 2005), who discussed the influences of structure geometry on the replication of microstructures.

5.3.2 Replication of hierarchical structures by variothermal injection moulding

Another conclusion which was drawn from the results shown in Fig. 5.12 is the fact that such microstructures cannot be replicated by standard injection moulding. A 100% replication was once again only possible with variothermal mould heating. As can be seen in Fig. 5.13, only 1.4 μm of the microstructure were replicated by IIM, whereas both the micro- and nanostructure of the hierarchical structures were fully replicated by VICM reaching the maximum height of 9.5 μm .

(a) VICM: variothermal injection compression molding; $w/p = 0.74$



(c) VICM: variothermal injection compression molding; w/p - ratio = 0.48

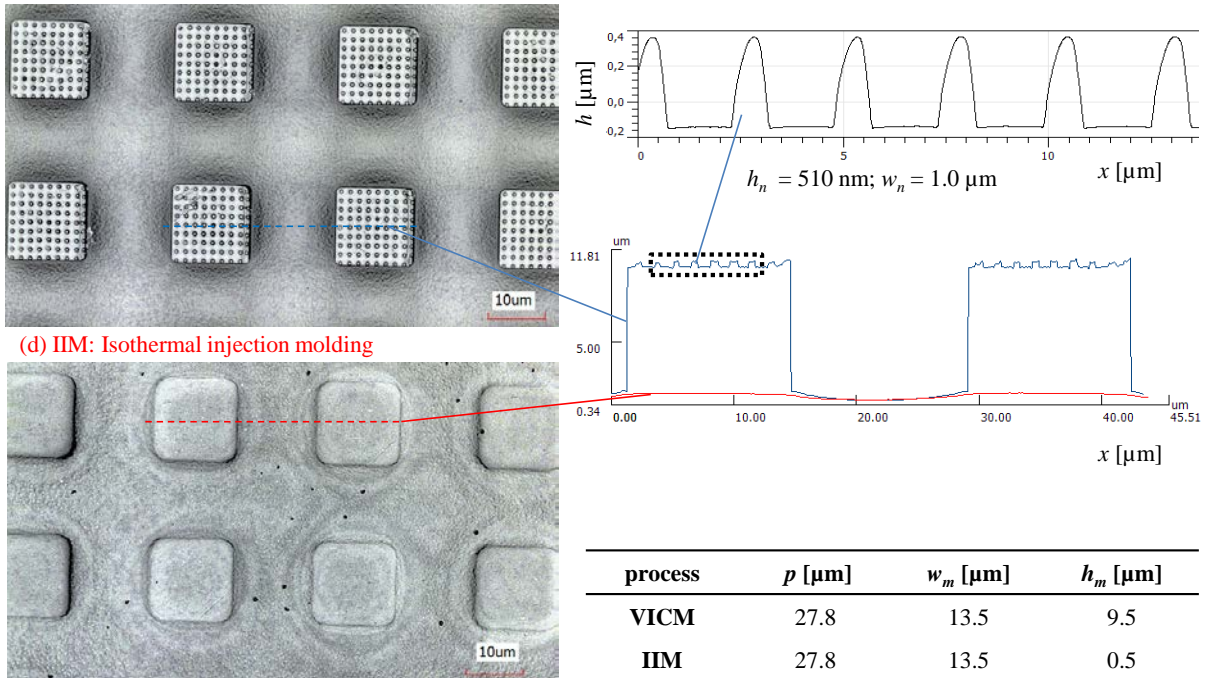


Fig. 5.13: Comparison of variothermal ($T_{\text{mould}} = 115^\circ\text{C}$) and isothermal ($T_{\text{mould}} = 70^\circ\text{C}$) replication of hierarchical structures with two different w/p ratio with A-PA: (a) and (c) CLSM micrographs of fully replicated hierarchical structures by VICM with a height of 9.5 μm and a w/p ratio of 0.74 and 0.48 respectively (blue lines in the profile); (b) and (d) CLSM micrographs of unfilled structures replicated by IIM with a resulting structure height of only 1.4 μm and 0.5 μm respectively (red line in the profile); the profiles of the structures on top with a height of $h_n = 510$ nm and a width $w_n = 1$ μm were determined with AFM.

Similar to the nanostructures on top of the microstructures, as shown in Fig. 5.13, other fields of interest covered merely with nanoholes can also only be replicated by applying variothermal mould heating as can be seen in Fig. 5.14.

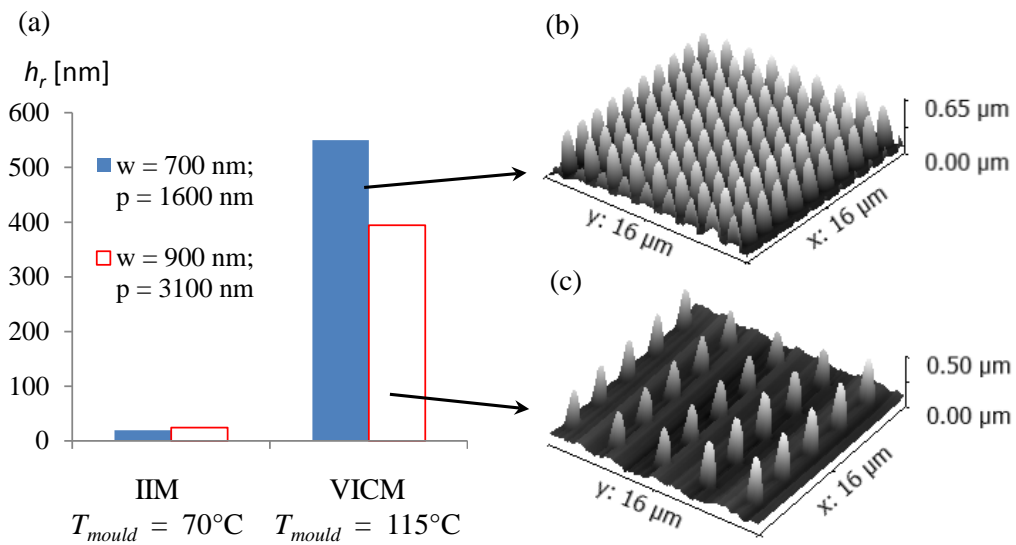


Fig. 5.14: (a) Replicated height h_r of two different submicron structures with A-PA produced by IIM in comparison to VICM; (b) AFM picture of replicated pillars in A-PA by VICM with a diameter w of 700 nm, a pitch p of 1700 nm and a height h_r of 550 nm; (c) AFM picture of replicated pillars in A-PA by VICM with $w = 900$ nm, $p = 3100$ nm and $h_r = 395$ nm.

5.4 Conclusions

The importance of low viscosity for good replication of micro- and nanostructures known from previous studies was confirmed, but the role of surface energy has been hardly investigated in detail to date. As a result of this part of the thesis, the dewetting potential Ω_s (integrated spreading coefficient) is proposed as a simple rationale for the estimation of suitability of a given polymer for the replication of micro- and nanostructures. Based on Ω_s the influence on the replication accuracy could be assessed, i.e. when changing polymers or applying an anti-adhesion coating.

In order to calculate Ω_s , contact angles of polymers on various mould materials and the surface energies of these polymers as a function of temperature need to be determined. Based on these measurements the spreading coefficient can then be calculated. The advantage of the spreading coefficient is that it represents the gradual decrease in wetting behaviour that a polymer melt undergoes as a result of cooling upon contact with mould surface. The lower the dewetting potential of a polymer, the better the replication can be expected. Thus, the spreading coefficient and the calculated dewetting potential seem to be appropriate values to describe the filling potential of micro- and nanostructures for different polymers on various surfaces. For the determination of the dewetting potential the effect of the mould temperature was not implemented yet. As the filling is highly influenced by the fast cooling of the polymer, which is again dependent on the difference between the melt and the mould temperature, it is inconvenient to compare the different polymers. One possibility would be to combine the equation for the spreading coefficient with the equation for the freezing time, where the differences between melt, mould and no-flow temperature are implemented. Mainly amorphous polymers were investigated. It would be of high interest to evaluate the role of dewetting potential with further semi-crystalline materials, such as PA66 or PE.

Besides viscosity and wetting, the influence of structure geometry (in particular the width) on the filling was investigated. On the microscale, a parabolic dependence of the replicated height on the structure width was confirmed, which is in good agreement with the influences of the Graetz and Fourier numbers as well as the empirical freezing time. Consequently, nanostructures were more difficult to fill than microstructures. In addition, the width/pitch ratio has an influence on the filling because of variations in the local heat losses, depending on where the melt is in direct contact with the mould. This knowledge is advantageous for the development of micro- or nanostructures in respect to functionality and replication fidelity. Usually, there is a trade-off between the replication fidelity of a structure (achieved easier with larger structures) and the optimum functionality, i.e. the optical effect in diffractive optical elements (DOEs) or the resulting capillary force in microfluidic analysis systems.

6. 3D MULTI-SCALE SIMULATION IN COMPARISON TO INJECTION MOULDING TRIALS

In this part of the thesis, the 3D flow in a macro part is simulated in Moldflow and scaled down to be able to simulate the filling of single micro- and also nanostructures with simple cut-outs in order to save computational time. Basic validations of simulated filling time, pressures, viscosities and shear rates on macroscale with experiments are presented in Chapter 6.4. Additionally, Comsol is used to evaluate adapted boundary conditions such as variation in heat transfer coefficient (Chapter 6.5) and wall wetting instead of no-slip conditions (Chapter 6.6.5). The goal was to get a good correlation to injection moulding trials with different polymers when changing the injection speed (Chapter 6.6.2) and increasing the mould temperature from below to above the transition temperature of the polymer, which represents isothermal and variothermal filling, respectively (Chapter 6.6.3). The transition temperature was adapted to real no-flow temperature measurements and the polymer flow of two sequences, "Fill" and "Pack", is shown. Most of the published simulations deal with macro- and microstructures. In the investigations shown in this section, which were published in (Rytka et al., 2016a), results are not only presented for microstructures but also for nanostructures (Chapter 6.6.4 & 6.6.5).

6.1 Motivation and state-of-the-art

The motivation of using simulations for the filling of micro- and nanostructures is to be able to predict differences of the melt flow in structures of various sizes, taking into account different polymer properties like viscosity or the transition temperature from melt to solid state. Moreover, the development time for polymeric parts with functional surface topographies would be substantially decreased if sufficiently robust simulation results allowed determination of the replication fidelity, influenced by changes in geometry (width, height, aspect ratio) and processing parameters (injection speed, mould temperature, holding pressure) without the necessity of carrying out extensive real injection moulding trials.

Various 3D computer-aided engineering (CAE) software tools such as Moldflow, Mouldex3D, Simpoe, Sigmasoft, Cadmould or Rem3D have been used to simulate macroscopic cavity-filling during injection moulding for fast evaluation of part design and polymer melt flow behaviour. Some simulations can also be found that address filling of cavities in the micron range. (Shen et al., 2008), for example, simulated with Moldflow the filling process of an array of micro-columns with diameters of 150 μm and heights of 11 μm . However, because of the low aspect ratio (< 0.1) and the rather coarse meshing, these structures were easily filled and no significant differences in filling were shown. (Chen et al., 2000), on the other hand, used the Hele-Shaw fluid flow model to simulate the filling of mould cavities without structures during the injection compression moulding. It was shown that faster compression speed, smaller compression stroke and a thinner wall thickness result in lower part shrinkage and better shrinkage uniformity. (Yu et al., 2004) found that the Hele-Shaw model does not correctly represent the flow in microstructures and developed a hybrid numerical method showing the importance of the heat transfer coefficient for a good correlation with experiments. (Kim and Turng, 2006) used a two-step macro-micro filling approach for the filling analysis of a part with a micro-surface feature, in order to avoid excessive numbers of elements and long computational time and discussed the dependence of pressure and temperature on the flow velocity, filled volume, time and heat transfer coefficient. Usually a cold frozen layer at the wall with no slip boundary condition is assumed, while the polymer flows in a fluid centre. Only in some approaches wall adhesion, surface tension or wall slip effects are taken into account. (Choi and Kim, 2011) implemented wall slip and surface tension and simulated a multi-scale flow in Moldflow and Comsol. They concluded that a slip model is required for channel diameters below 10 μm , and capillary effects are only visible in the

submicron range. (Tofteberg and Andreassen, 2010) used Moldflow combined with Ansys and carried out a multi-scale simulation of 2D optical gratings with 3 μm period in COC, applying a high heat transfer coefficient ($30000 \text{ W m}^{-2} \text{ K}^{-1}$).

(Lin et al., 2010) simplified their model by assuming that most of the filling takes place during the packing phase and showed good correlations with replication trials. However, this assumption only partly represents the reality, as depending on the settings (especially mould temperature) and polymer a large part of the filling process can also occur before packing (as already shown in Chapter 4). Instead of Cross-WLF, the Phan-Thien-Tanner (PTT) rheology model was applied by (Cao et al., 2011). Although slip boundaries and surface tensions were included, the agreement with real micro-injection moulding was only fair. (Kuhn et al., 2010) developed an analytic flow model taking the power-law material model into account and considering the flow in the surface structures separately from the main cavity. An important conclusion was that for small structures the main part of the filling occurred during the holding stage. Interestingly, a low heat transfer coefficient was used ($850 \text{ W m}^{-2} \text{ K}^{-1}$). (Cui et al., 2014) used the generalized Hele Shaw model and simulated the influence of the heat transfer coefficient, mould temperature and flow velocity on the filling of micro-channels but without experimental validation.

Most of the investigations listed above deal with the filling simulation of microstructures, but especially 3D simulations of nanostructures (as presented in this section) have been rarely carried out.

6.2 Polymers and process

Two different polymers with the same glass transition temperature T_g of 110°C were used for the replication trials: Polymethylmethacrylate (PMMA, Plexiglas[®] 7N) from Evonik (Marl, Germany) and an amorphous polyamide (A-PA, Grilamid[®] TR55LX) from EMS-Chemie (Domat-Ems, Switzerland).

6.2.1 Mould master inserts

On the injection side two unstructured, highly polished chrome steel (CrNi 1.4301; roughness $R_a = 0.013 \mu\text{m}$) inserts were clamped. On the ejection side two different mould inserts with micro- and nanostructure were used. On one insert a v-shaped microgroove was implemented (already explained in detail in Chapter 4.2.1). Additionally, a nickel insert was produced by a mask based displacement Talbot UV photolithography and electroplating. The dimensions of the nanostructures were already visualized in detail in Chapter 4.2.2. The gaps between the nickel pillars were approximated in the simulation with pillars of 300 nm diameter. It was assumed that the most critical dimension for filling is the smallest distance between the pillars on the master, which is 300 nm. A pillar was the simplest geometry for a quick simulation, being aware that, in reality, the heat transfer was delayed in one dimension compared to the pillar model. However, every other geometry would boost the mesh number resulting again in much longer calculation times. Finally the goal of this investigation was to evaluate a simulation method that speeds up the development phase and to investigate the main influencing factors in the multiscale approach.

6.2.2 Processing parameters

For the injection moulding trials and the simulations the parameters shown in Table 6-1 were used:

Table 6-1: Injection moulding parameters applied for all processes.

Material	Cylinder temperature T_{cyl} [°C]	Injection speed v_{inj} [cm ³ s ⁻¹]	Ejection temperature T_e [°C]	Mould temperature T_{mould} [°C]	Holding pressure P_{hold} [MPa]	Holding pressure time t [s]
A-PA	280	15	70	70, 115	80	15
PMMA	250	15, 30, 60, 90, 120	80	80, 95, 100, 105, 115	80	15

For isothermal injection moulding (IIM) the mould and ejection temperatures were equal, whereas in the variothermal process (VIM) the material was injected at the respective mould temperatures and ejected at low ejection temperatures T_e as listed in Table 6-1.

6.2.3 No-flow temperature

For the determination of the filling behaviour of functional structures, it is important to know the accurate temperature at which the polymer stops to flow. This so-called no-flow temperature T_{no} or transition temperature T_{trans} (terminology used e.g. by Moldflow) has a high influence on the replication fidelity but is rather difficult to determine. T_{no} is of utmost importance for definition of the proper mould temperatures for the injection moulding process. Table 6-2 shows the experimentally determined T_{no} in comparison to T_g and T_{trans} from Moldflow.

Table 6-2: Determined T_{no} for PMMA and A-PA in comparison to T_g and T_{trans} .

Material	PMMA	A-PA
T_{no} [°C] (measured with 33 MPa and 41.5 MPa)	130	150
T_g [°C] (from data sheets, determined with DSC in heating mode, +10 K/min)	110	110
T_{trans} [°C] (Moldflow database, determined with DSC in cooling mode, -10 K/min)	105	103

Although the glass transition temperatures of PMMA and A-PA are similar, a pronounced difference is observed for the measured T_{no} . At T_{no} , it is expected that no polymer flow is possible anymore. However, even below T_{no} material could possibly be pressed into the cavities by elastic deformation of the solidified polymer, forced by a very high pressure. Therefore, the values may be lower for a higher pressure than 33 MPa as applied in this test, because the measured pressure in the cavity during injection moulding was up to 60 MPa. Probably the real no-flow temperature is in the range of the measured T_{no} and T_{trans} from the Moldflow data base. The proper choice of T_{trans} is important for the correct simulation of the filling of micro- and nanostructures, especially in the holding pressure phase, as will be shown in the next Chapters.

6.3 Simulation settings with Moldflow and Comsol

A multi-scale approach combining Moldflow and Comsol was chosen with particular focus on PMMA. In a first step, temperatures, pressures, shear rates, and viscosities were determined in the macroscopic regime through conventional filling simulations in Moldflow. These values were subsequently used as boundary conditions for filling simulations on the micro- and nanoscale. It can be assumed that micro- and nano-features will hardly affect the macroscopic flow. However, the micro-flow will be influenced by the macro-flow in terms of flow front velocity, filling pressure, and packaging. Therefore, it is essential to apply correct boundary conditions for model downscaling.

For the simulation of the filling behaviour of the macro-part and the microstructure, the commercial FEM simulation software Autodesk Moldflow Insight 2014 with a coupled 3D solver was used. The polymer parts were meshed with 3D volume tetrahedrons in order to represent the laminar flow of the melt adequately. It was reported that a 3D simulation can give a more accurate result of the temperature convection, especially in corners (Kennedy and Zheng, 2013). Polymer data like viscosity, pressure-volume-temperature (PvT) behaviour and thermal transition are implemented in the data base. The viscosity is described by the Cross-WLF (Williams-Landel-Ferry) model (already explained in detail in 2.2).

Inertia and gravity effects can be included into the simulation. Compared to the inertia term, viscous stresses in the polymer melt are very large because of the high viscosity of polymers. Therefore, the inertia term can be neglected in injection moulding (Gujrati and Leonov, 2010). Also gravity forces are insignificant compared to other forces, which result from the high injection or holding pressure.

In comparison to standard filling simulation software like Moldflow, the main advantage of Comsol is the possibility to combine multiple-physical effects like surface tension between mould and polymer to the numerical simulation field. But in general it is not very common to use Comsol for flow simulations, which explains why only few approaches can be found in literature.

(Moguedet et al., 2009) used a two phase flow (polymer/air) level set to simulate the flow in microstructures. Non-Newtonian flow behaviour was represented by the Cross-WLF law. Air-trapping was considered by a pseudo-compression law (low Mach number) for the air and the level set method was used to accurately track the melt flow front.

In this thesis, additionally to the 3D Moldflow filling simulation, the computational fluid dynamic (CFD) and heat transfer (HT) modules of Comsol Multiphysics 5.0 were used to simulate the Non-Newtonian multi-phase flow (polymer/air). The 2D models were meshed using triangular elements. The nanostructure was meshed with a maximum element size of 1.3 nm and a maximum growth rate of 1.1. The flow was calculated with the laminar two-phase flow level-set method combined with the heat transfer in fluids. Polymer viscosities were obtained from the Cross-WLF model using similar parameters as in Moldflow.

6.3.1 Governing equations

The general governing equations are as follows:

1. Mass continuity equation:

$$\frac{\partial \rho}{\partial t} + \nabla \cdot \rho \mathbf{u} = 0 \quad (6-1)$$

Where ρ is the density, t is the time, \mathbf{u} is the velocity vector and ∇ represents the 3-dimensional Nabla operator. Assuming incompressibility, equation (6-1) reduces to $\nabla \cdot \mathbf{u} = 0$.

2. Momentum equation including gravity force and surface tension:

$$\rho \frac{\partial \mathbf{u}}{\partial t} = -\nabla P + \nabla(2\eta\psi) + \rho \mathbf{g} + \Pi \quad (6-2)$$

$$\Pi = \nabla \left(\sigma (I - NN^T) \delta(\Gamma, x) \right) \quad (6-3)$$

Where ψ is the strain tensor, \mathbf{g} is the standard gravity and Π is the surface tension vector (equation (6-3)) that can be included only in Comsol simulations (Comsol, 2012), but not in Moldflow. I is the identity matrix, σ is the surface tension, N is the interface normal and $\delta(\Gamma, x)$ is a Dirac delta function localizing the surface tension forces to the interface Γ (Peskin, 1977).

3. Energy or heat equation:

$$\rho c_p \left(\frac{\partial T}{\partial t} + (\mathbf{u} \cdot \nabla) T \right) = \nabla \cdot (k \nabla T) + \beta T \left(\frac{\partial P}{\partial t} + (\mathbf{u} \cdot \nabla) P \right) + 2\eta \dot{\gamma}^2 \quad (6-4)$$

$$\dot{\gamma} = \left(2\psi : \psi^T \right)^{1/2} \quad (6-5)$$

With k being the thermal conductivity, c_p the heat capacity, β the thermal expansion coefficient and $\dot{\gamma}$ the shear rate tensor.

The flow front was tracked using the phase variable ϕ initially having the value 1. According to (Comsol, 2012) the motion of the air/polymer interface is described by:

$$\frac{\partial \phi}{\partial t} + \mathbf{u} \cdot \nabla \phi = \phi \nabla \cdot \left[\kappa \nabla \phi - \phi(1-\phi) \frac{\nabla \phi}{|\nabla \phi|} \right] \quad (6-6)$$

Where ϕ is the reinitialization parameter that stabilizes the level set function depending on the magnitude of \mathbf{u} and κ is a parameter controlling the interface thickness.

Polymers are considered as incompressible fluids for pressures below 100 MPa (Gujrati and Leonov, 2010).

In the packing phase, the compressibility cannot be neglected anymore and the continuity and the momentum equations need to be adapted for a compressible fluid according to (Xie et al., 2011) to yield equation (6-7) and (6-8), respectively:

$$-\nabla \cdot \mathbf{u} = \chi \left(\frac{\partial P}{\partial t} + \mathbf{u} \cdot \nabla P \right) - \beta \left(\frac{\partial T}{\partial t} + \mathbf{u} \cdot \nabla T \right) \quad (6-7)$$

$$0 = -\nabla P + \nabla \left(2\eta\psi - \frac{2}{3}\eta I \nabla \cdot \mathbf{u} \right) + \rho \mathbf{g} + \Pi \quad (6-8)$$

Where χ is the compressibility coefficient.

6.3.2 Analysis sequences

Different standard analysis sequences are implemented in Moldflow simulations:

1. Fill: Very important as most of the replication takes place during this sequence.
2. Pack: More important for variothermal processes as cooling of the polymer is delayed and material can still be pressed into the cavities.
3. Cool: For the cooling sequence a cooling circuit needs to be defined (Fig. 6.1). This sequence is helpful for getting a better understanding of the thermal transfer between polymer melt and mould, since the heat from the polymer is conducted into the mould and then into the water cooling circuit.
4. Warp: Essential for the deformation of the macroscopic part but not important for the filling of micro- or nanostructures. However, warpage can influence the functionality of, for example, optical microstructures as shown by (Wu and Chen, 2006).

The mould cooling used in these investigations was approximated by rectangular channels with heights of 8 mm, widths of 4 mm, distances of 3 mm to the part, and 8 mm to each other. Two inlets and outlets with a total flow-rate of 10 l min^{-1} were set.

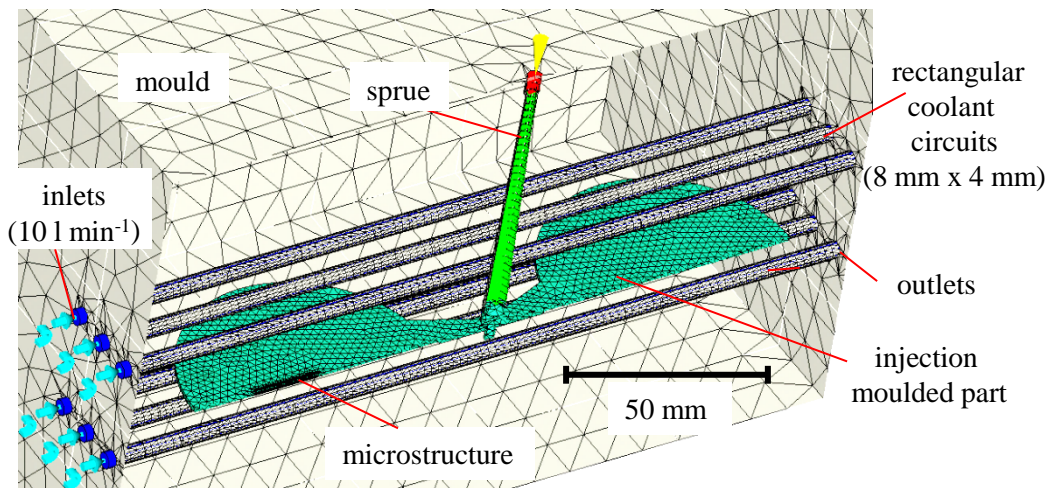


Fig. 6.1: Moldflow cross-cut of the part showing the mould and the cooling circuits.

It turned out that the simulation of the cooling and warp sequence is less relevant for the filling of micro- and nanostructures. For that reason only "Fill" and "Pack" sequences were simulated, in order to keep the required memory space and simulation time on a reasonable level. Furthermore, the sprue was found to have no influence on structure replication and was, therefore, neglected in most simulations.

6.3.3 Mesh density and model scaling

The FEM-mesh of the simulated part was split in areas with a wide (bulk) and areas with a very narrow mesh. Especially the micro- and nanostructures need to be meshed tightly in order to run a precise simulation. In the transition zone between large and small elements the element size needs to be changed gradually. For this reason, the mesh for the macro-part was generated in Nastran, NX 8.0 or Comsol 5.0 and not directly in Moldflow. The exported Nastran-file (.nas) was imported into Moldflow as a 3D-file.

The mesh was balanced in such a way that 9 million elements were not exceeded as otherwise Moldflow may not run accurately. On the other hand, as many elements as possible should be generated in order to achieve maximal simulation accuracy.

In Fig. 6.2 an exemplary comparison is shown between two meshes consisting of 1.4 and 8.3 million elements, respectively.

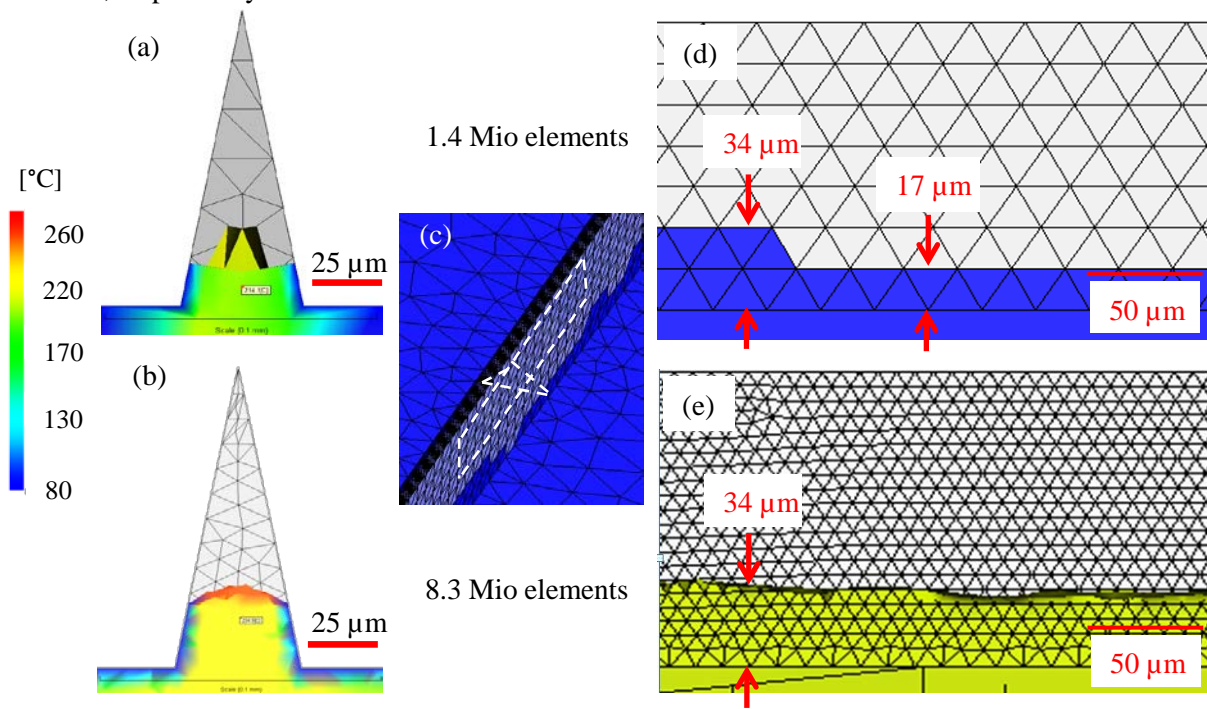


Fig. 6.2: Exemplary Moldflow simulation of the temperature distribution of injected A-PA using IIM in the v-microgroove after 0.43 s filling time showing huge differences in resolution for (a) 1.4 million elements compared to (b) 8.3 million elements; (c) 3D plot of the microstructure showing the location of the parallel and perpendicular cross-section cut used for height determination of the polymer flow with (d) 1.4 million elements and (e) 8.3 million elements.

Laminar flow in the microstructure can only be clearly identified when applying a high mesh density, as can be seen in Fig. 6.2b in comparison to Fig. 6.2a. Moreover, the determination of the replicated height is less accurate for low mesh densities as the resolution is given by the size of the elements (Fig. 6.2d). By increasing the number of elements significantly, the flow within the microstructures is represented much more realistically, as can be seen in Fig. 6.2e. On the other hand, the simulation time can be drastically reduced when using a coarse mesh and the results may still be precise enough dependent on the purpose of the simulation.

The v-groove microstructure and nano-pillars were simulated with the three models shown in Fig. 6.3.

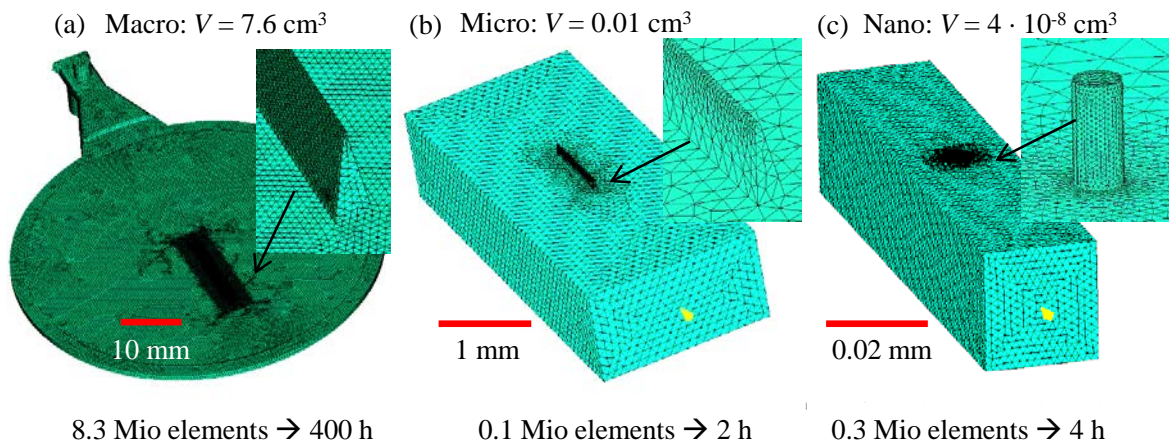


Fig. 6.3: (a) Macro, (b) micro and (c) nano model used for the filling simulation of the v-microgroove structure and of nanopillars. The main model mesh is a single continuous mesh with different mesh densities for the macro and micro/nano scale.

If the size of the model is scaled down in volume and number of elements from macro (Fig. 6.3a) to micro (Fig. 6.3b) or nano size (Fig. 6.3c) to reduce calculation time, it is of absolute importance to transfer the boundary conditions accurately. In particular, the values for local flow velocities and local temperatures need to be extracted from a macro simulation and implemented as boundary conditions in the downscaled model.

6.3.4 Simulation parameters in Moldflow

Various parameters turned out to be important for the simulation (marked in bold in Table 6-3), others were set as default. Especially the parameter *maximum % volume to fill per time step* is important to resolve the intermediate filling steps in the microstructure. The heat transfer coefficient has a drastic influence on the replicated height. In Moldflow, a 3-stage mould-melt heat transfer coefficient h_{tc} is implemented. Assuming a very high h_{tc} in agreement with (Tofteberg and Andreassen, 2010), (Xu et al., 2005) and (Nguyen-Chung et al., 2008), the h_{tc} value in the early filling phase was changed from 5000 to 30000 $\text{W m}^{-2} \text{K}^{-1}$ and the results were compared with each other.

Table 6-3: Program (Moldflow) and material specific parameters with significant impact on the simulation results (marked bold).

Programme specific parameters	default	adapted
Minimum number of elements through the thickness:	6	
Maximum % volume to fill per time step	4%	0.05%
Maximum iterations per time step (filling)	50	
Convergence tolerance (scaling factor)	1	
Material specific parameters	default	adapted
h_{tc} filling [$\text{W m}^{-2} \text{K}^{-1}$]	5000	30000
h_{tc} packing [$\text{W m}^{-2} \text{K}^{-1}$]	2500	
h_{tc} detached (pressure = 0) [$\text{W m}^{-2} \text{K}^{-1}$]	1250	
Transition temperature T_{trans}		
A-PA	103	130°C
PMMA	105	105°C

In Fig. 6.4 the tremendous influence of h_{tc} and the number of elements on the filling height is shown. The results from the injection moulding trial can only be simulated correctly by increasing the h_{tc} from $5000 \text{ W m}^{-2} \text{ K}^{-1}$ to $30000 \text{ W m}^{-2} \text{ K}^{-1}$ and applying a high mesh density. The reason why it is necessary to increase the heat transfer coefficient will be explained in more detail in Chapter 6.5.

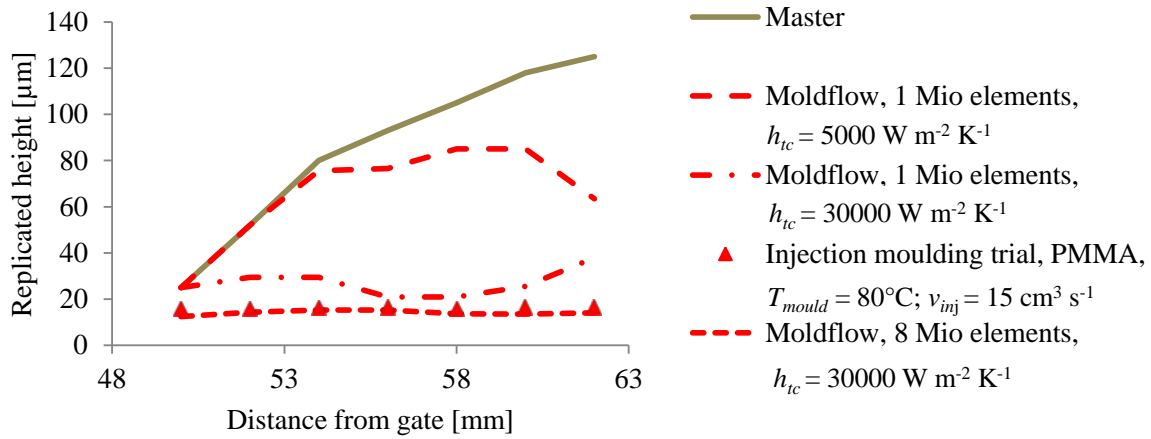


Fig. 6.4: Simulation of the filling height of PMMA in a v-microgroove showing the influence of different h_{tc} and various amount of finite elements (lines) in comparison to isothermal injection moulding (symbols) with a mould temperature $T_{mould} = 80^\circ\text{C}$ and an injection velocity v_{inj} of $15 \text{ cm}^3 \text{ s}^{-1}$.

6.4 Validation of macroscopic boundary conditions

In order to validate the macroscopic model, simple preliminary simulations were carried out and compared with previous experiments. First of all, the fill time and switch over pressure were compared to each other. In the simulation with PMMA the melt reached the v-groove structure after 0.33 s and the end of the cavity after 0.86 s.

Table 6-4: Plausibility check: Comparison of fill time and switch over pressure observed in experiments and simulations (including the sprue).

PMMA	Moldflow	IIM
Fill time [s]	0.86	0.89
Switch over pressure near the gate [MPa]	690	680

Both, the injection speed and the switch over pressure near the gate showed good correlation of simulated and experimental results for isothermal injection moulding (IIM). Note that these values are only valid for the simulation including the sprue; otherwise the simulated fill time is reduced by 0.35 s.

6.4.1 Shear rates

In comparison to the simulation (Fig. 6.5), the shear rate between point A and B was determined online with a pressure and a temperature sensor as explained in Chapter 3.3.3. The online determined shear rate of 678 s^{-1} for an injection speed of $15 \text{ cm}^3 \text{ s}^{-1}$ (cf. Table 4-3) represents a good averaged value through the whole part.

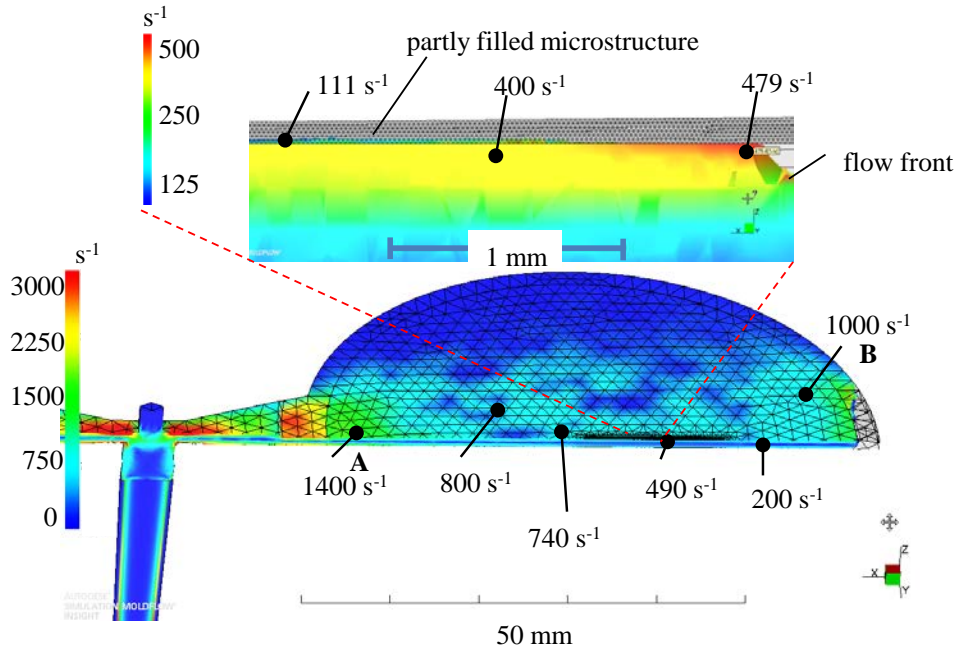


Fig. 6.5: Moldflow simulation for the determination of the shear rate in the bulk and in the microstructure exemplary for PMMA with an injection velocity of $15 \text{ cm}^3 \text{ s}^{-1}$.

With a constant injection volume speed, the shear rate changes depending on the cross section of the part. Therefore the highest shear rate (up to 3000 s^{-1}) is generated in the gate area, decreases in the middle area to 740 s^{-1} and increases again towards the end of the cavity to more than 1000 s^{-1} . The shear rate is higher close to the wall in contrast to the centre area, where low shear rates ($\sim 200 \text{ s}^{-1}$) are formed. The shear rates at the entrance of the microstructure are rather small, around 479 s^{-1} at the flow front, continuously decreasing to 111 s^{-1} after a few milliseconds.

6.4.2 Viscosities: Comparison of simulation with online measurements

Similar to the shear rate, the viscosity of PMMA at a volume flow rate of $15 \text{ cm}^3 \text{ s}^{-1}$ and a mould temperature of 80°C was validated with a Moldflow simulation (Fig. 6.6). A very good correlation could be found, when comparing the online measured viscosity (Table 4-3) at a shear rate of 678 s^{-1} being $597 \pm 12 \text{ Pa s}$, with the simulated value of 590 Pa s (marked red in Fig. 6.6).

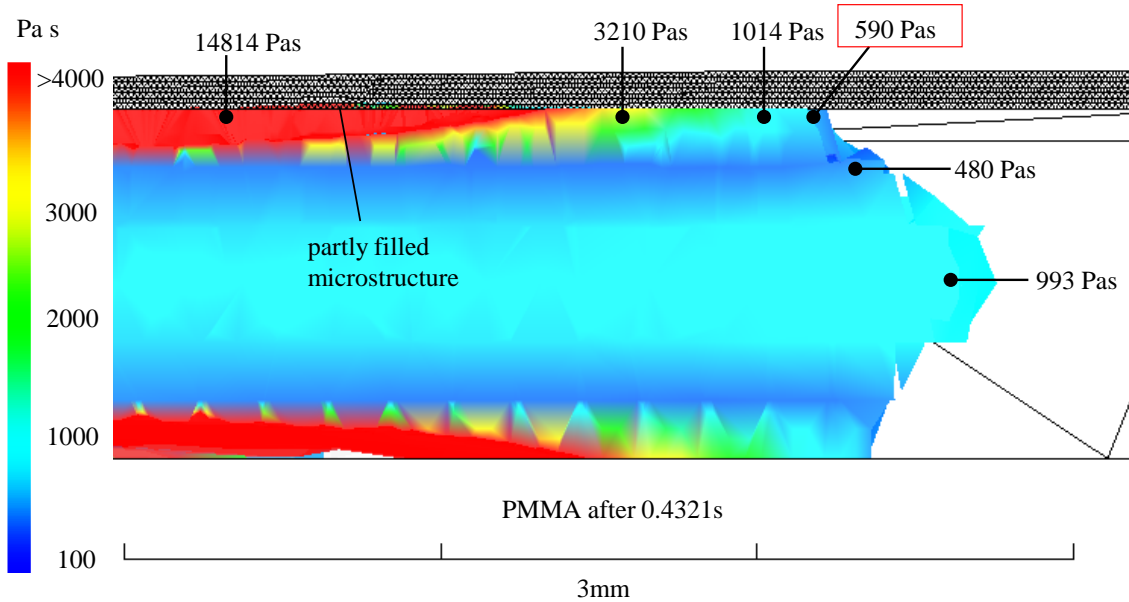


Fig. 6.6: Viscosity cross-section of simulated PMMA flow after 0.43 s showing a very good correlation of the viscosity entering the microstructure (marked red) in comparison to the online viscosity measurement shown in Table 4-3.

Applying an injection volume flow rate of $15 \text{ cm}^3 \text{ s}^{-1}$ the melt front moves 2 mm within 0.02 s. During this time the viscosity increases from 590 Pa s to 14814 Pa s at the same position in the v-microgroove. This confirms once more the fast solidification speed of the polymer in contact with the cold mould. The viscosity of 590 Pa s can be used as control value in further simulations.

6.4.3 Flow front velocities

For an injection volume flow rate of $15 \text{ cm}^3 \text{ s}^{-1}$, the resulting flow front speed at the different positions of the macro part (the flow at the entrance of the round plate is much faster than in the middle section). Especially in the cross-section of the part the flow differs between 0.5 and 10.9 cm s^{-1} as can be seen in Fig. 6.7. At the entrance of the microstructure the flow velocity is reduced to around 0.5 cm s^{-1} . Consequently this flow front velocity, determined in the macro simulation at a specific point, needs to be transferred accordingly to the micro or to the nano cut-out model by adapting the injection time. With this measure the shear rate and the melt temperature (which can increase because of shear) are represented correctly as well as the melt viscosity based on the Cross-WLF model.

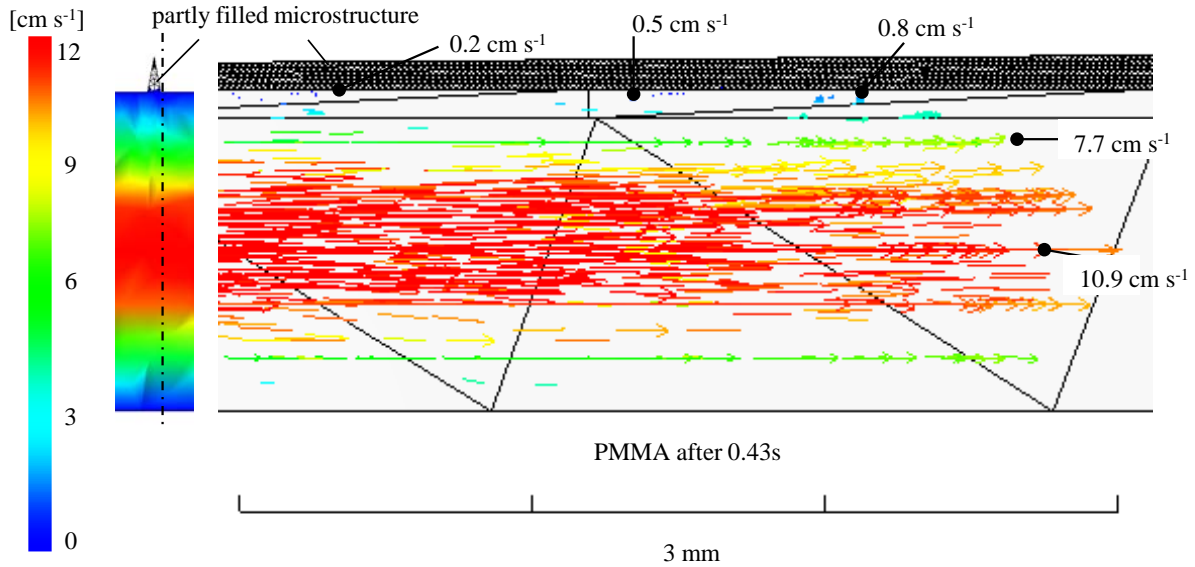


Fig. 6.7: Moldflow simulation ($T_{mould} = 80^\circ\text{C}$) of resulting PMMA flow front velocity in cross-section showing rather low flow velocities in the microstructure compared to the bulk.

The flow front velocity in the 1 mm thick cavity is much higher compared to the one within the microstructure because of lower flow resistance in the bulk. This is also the reason why the thick cross-section is being filled first. As soon as the melt reaches the end of the cavity, the pressure builds up and the polymer is pressed into the microstructures having much higher flow resistance, provided that the melt is not yet completely frozen. Otherwise, if the no-flow temperature was already reached, the structure would not be filled.

The velocity has a huge impact on the filling of structures. Therefore, the determination of the flow front velocity in the macro part is essential for the implementation of correct boundary conditions for the micro and nanoscale sub models, already shown in Fig. 6.3b & c. Based on the macroscopic simulations, the resulting averaged flow front speed in the microstructure is 0.01 cm s^{-1} for a volume flow rate of $15 \text{ cm}^3 \text{ s}^{-1}$ and increases to 0.41 cm s^{-1} for $v_{inj} = 60 \text{ cm}^3 \text{ s}^{-1}$.

6.4.4 Pressure

As can be seen in Fig. 6.8, the pressure in a microstructure correlates to the power of two with the position of the flow front, which corresponds to the filling time t .

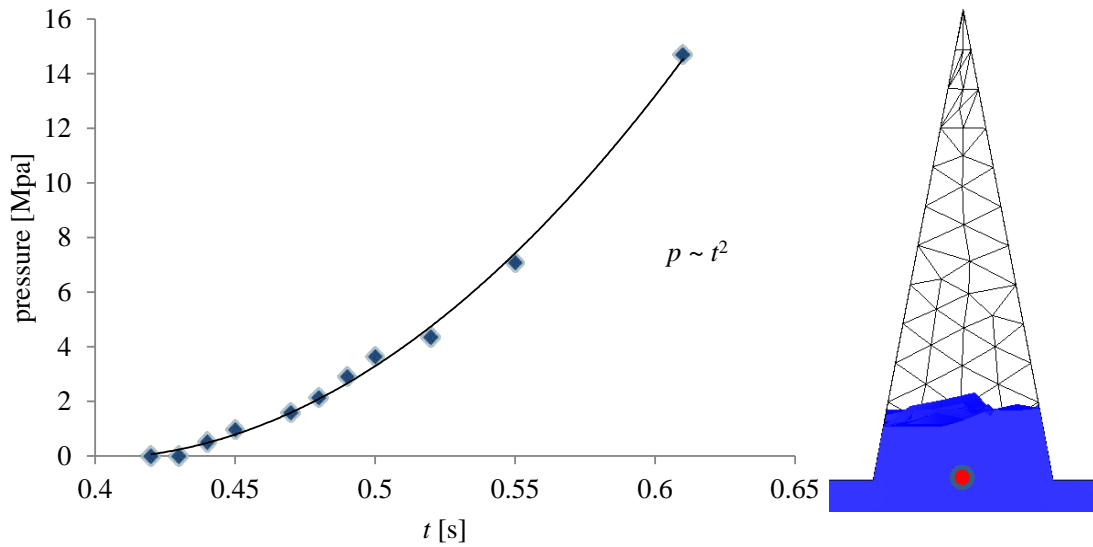


Fig. 6.8: Simulated pressure at the entrance of the microstructure as a function of filling time for PMMA with a mould temperature of 80°C and a volume flow rate of $15\text{ cm}^3\text{ s}^{-1}$.

6.5 Heat transfer and cooling rate of micro- and nanostructures

In the first milliseconds of polymer contact, which are important for the filling of micro- and nanostructures, the melt cools down very fast as the temperature gradient is maximal; but then the heat flux at the interface stagnates due to the instantaneous formation of a frozen insulation polymer layer detaching from the mould which leads to a substantial reduction in h_{ic} . For macroscopic mould filling, the first milliseconds of melt contact with the mould surface are less important. This is probably the reason why a moderate value for h_{ic} is used per default in Moldflow, in order to represent the total filling time, which can be in the range of up to some seconds for thicker parts. However, in microscopic cavity filling, the influence of the heat transfer at the polymer-mould interface on the filling of the structures is much more pronounced.

In Fig. 6.9 the Comsol model that was used to determine the cooling speed in micro- and nanostructures depending on the mould temperature is shown. For simplification, it was assumed that the structure has been completely filled. The water channel (material: steel) was simulated with *heat transfer in fluids* and the brass/PMMA interface with *heat transfer in solids*. Both heat transfer models are based on the energy equation (6-4) without considering thermal expansion and shear heating. The only difference is that in *heat transfer in fluids* also the impact of fluid-flow with the velocity field u is also included. The initial values for the temperature of the PMMA melt and the mould were set to 250°C and 80°C , respectively (at 0 ms).

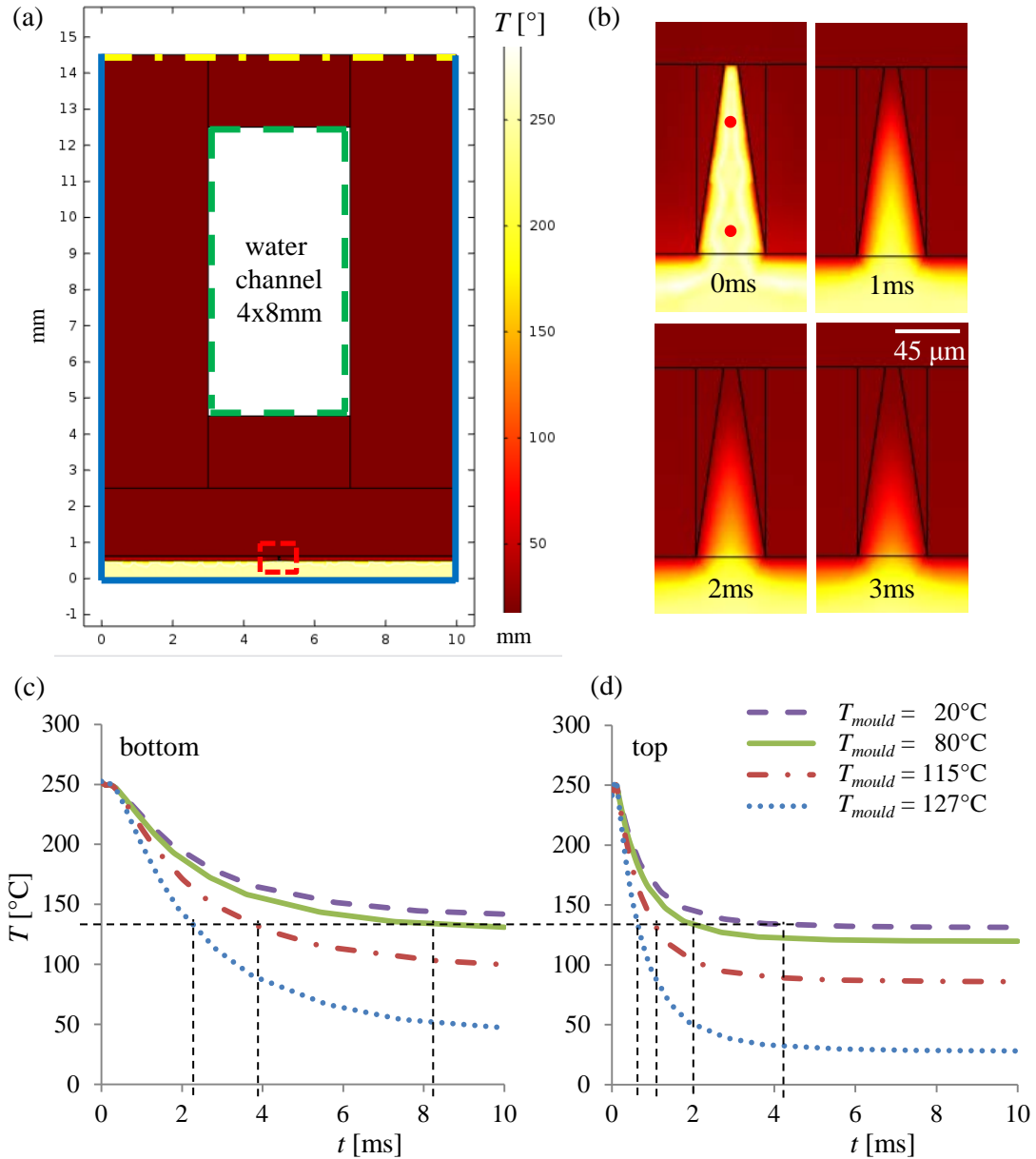


Fig. 6.9: (a) Heat transfer model of the relevant part of the mould with applied boundary conditions (blue solid line in the centre of the macro cavity = symmetry; green dashed line = heat transfer in fluids; yellow dashed-dotted line = thermal insulation) and a completely filled micro-cavity shown in detail in (b) together with the temperature evolution of the polymer melt after indicated contact times with the brass insert; (c, d) simulated cooling curves of PMMA at the bottom (c) and the top (d) of a v-groove microstructure with indicated measuring points (red dots) in (b); dashed black lines in (c) and (d) visualize the duration after which the no-flow temperature is reached for different mould temperatures.

Based on the model shown in Fig. 6.9a, the time until T_{no} is reached can be determined from the temperature evolution over time at different positions as shown in Fig. 6.9b-d assuming perfect heat transfer with implemented cooling channel. In the above model a perfect heat transfer is assumed by applying two temperatures in the polymer mould interface as boundary condition. This model was compared with a simplified model without implementing the cooling channel (boundary condition at the polymer interface = "heat flux") and the heat transfer coefficient was varied (Fig. 6.10). It can be clearly seen in Fig. 6.10b-d that using a high heat transfer coefficient of $30000 \text{ W m}^{-2} \text{ K}^{-1}$ (green col-

umns) instead of $5000 \text{ W m}^{-2} \text{ K}^{-1}$ (red columns) at the interface of the simplified model gives a much better correlation with the model including the cooling channel (blue columns).

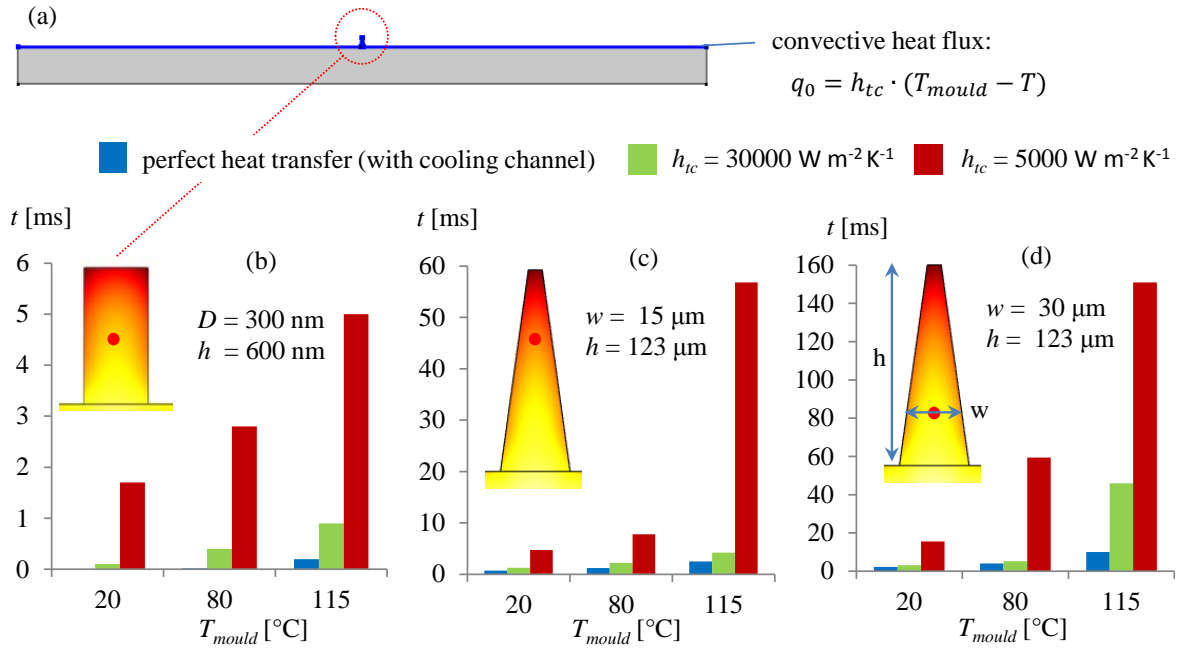


Fig. 6.10: (a) Simplified model for the filling of micro- and nano-cavities assuming a convective heat flux boundary condition at the polymer-mould interface; (b), (c) and (d) comparison of the cooling times after which the no-flow temperature ($T_{no}=130^\circ\text{C}$ for PMMA) is reached for different mould temperatures between a model with cooling channel (blue columns, cf. Fig. 6.9) and the simplified model with two different heat transfer coefficients: $30000 \text{ Wm}^{-2}\text{K}^{-1}$ (green columns) instead of $5000 \text{ Wm}^{-2}\text{K}^{-1}$ (red columns, standard value used by Moldflow). A better correlation is observed for the high heat transfer coefficient.

These substantially simplified simulations confirm that the cooling time in nanostructures (Fig. 6.10b) is much lower than in microstructures (Fig. 6.10c&d). Moreover, the top of the microstructures cools down faster than the bottom. Whether the structure is completely filled or not depends on the necessary filling time of the respective structure which should be shorter than the cooling time. Therefore the simulation of the filling of micro- and nanostructures is much better represented with a high heat transfer coefficient, at least for the very first few milliseconds when the polymer contacts the mould. Then the heat transfer coefficient decreases continuously. The assumption of a higher heat transfer coefficient is in good agreement with investigations of (Nguyen-Chung et al., 2008) who found that h_{tc} increases with decreasing cavity thickness.

As already mentioned above, h_{tc} of $5000 \text{ W m}^{-2} \text{ K}^{-1}$ is used per default in Moldflow which works sufficiently well for macroscopic filling simulations because of the slower heat transfer within the bulk. In contrast to the situation directly at the polymer/mould interface where the melt freezes within milliseconds only, the cooling time until T_{no} is reached throughout the bulk lies in the range of several seconds. This is illustrated in Fig. 6.11 which shows results from simulations in the bulk (0.45 mm away from the interface).

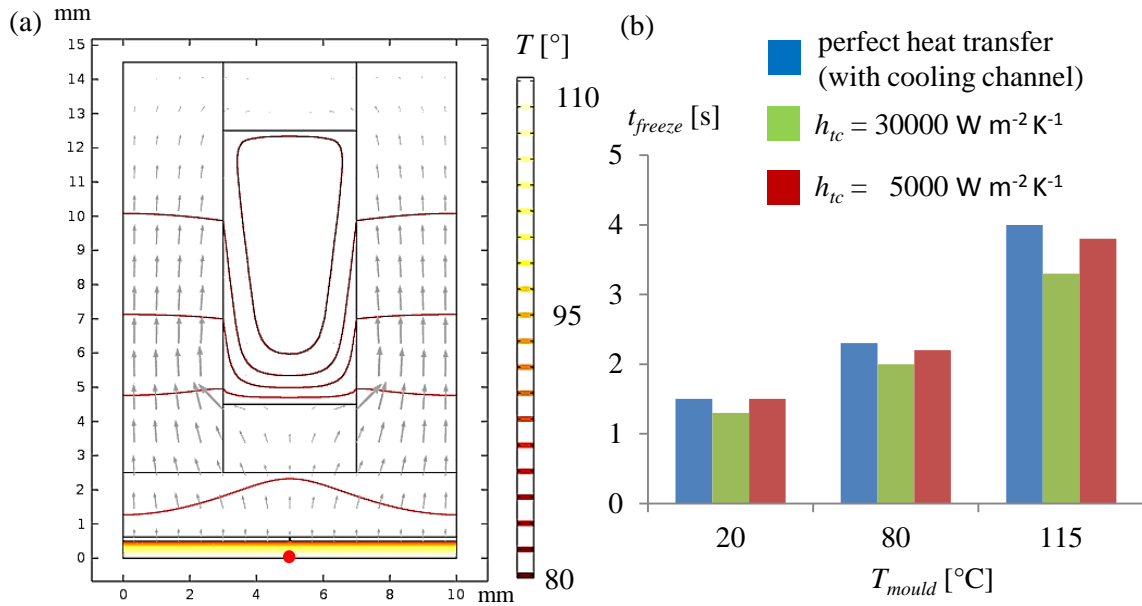


Fig. 6.11: (a) Heat flux (grey arrows) and temperature distribution in a PMMA heat transfer model with a cooling channel after 3 s cooling time; (b) comparison of the cooling time until T_{no} is reached (t_{freeze}) for different mould temperatures between a model with cooling channel (blue columns), a simplified model with a high h_{ic} of $30000 \text{ W m}^{-2} \text{ K}^{-1}$ (green columns) and low h_{ic} of $5000 \text{ W m}^{-2} \text{ K}^{-1}$ (red columns), measured 0.45 mm away from the brass interface with the microstructure (red dot).

As can be seen in Fig. 6.11b the difference in cooling time observed for micro- or nanostructures for different values of h_{ic} is much less pronounced far away from the melt/mould interface. Interestingly, applying an h_{ic} of $5000 \text{ W m}^{-2} \text{ K}^{-1}$ in the simplified model even yields better agreement with the model including the cooling channel. These model simulations thus provide a rationale for the default value settings in Moldflow.

6.6 Correlation of experiments with simulation

6.6.1 Short-shot: Replication of microstructures during the filling phase

Short-shots were carried out to shed light on the early stages of microstructure replication during the initial mould filling process. Depending on the injected volume, the pressure at the entrance of the microstructure cavity increases with time which forces the molten polymer to slightly penetrate the microstructure:

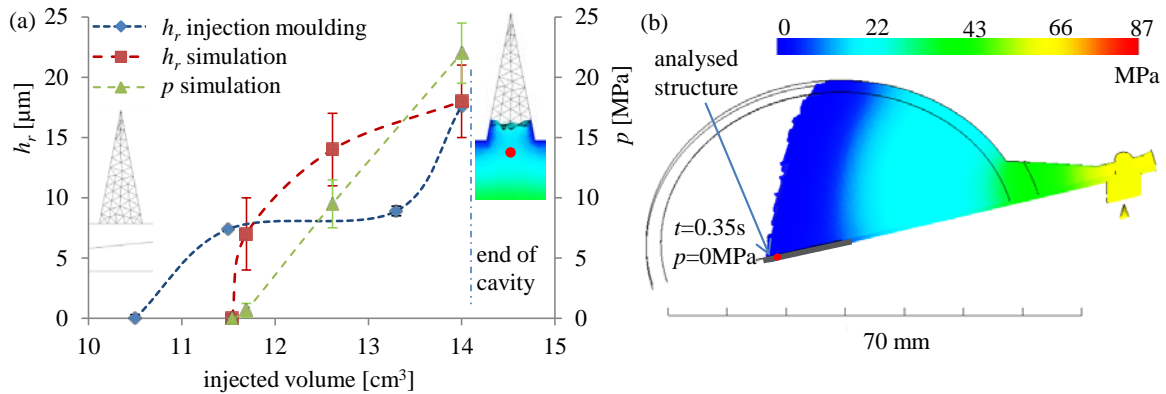


Fig. 6.12: (a) Replicated height of a PMMA microstructure as a function of injected volume ($T_{\text{mould}} = 80^\circ\text{C}$; $h_{\text{rc}} = 30000 \text{ W m}^{-2} \text{ K}^{-1}$) comparing isothermal injection moulding (IIM, blue dashed line) with Moldflow simulations (red line) and simulated pressure increase (green line) at the measuring point marked in red; (b) corresponding Moldflow simulation with pressure profile after 0.35 s with 0 MPa pressure at the flow front increasing to 24 MPa at the red measuring point when reaching the end of the cavity.

In Fig. 6.12a, the replicated heights of the v-groove microstructure obtained from the experimental short-shots (blue dashed line) are shown together with simulation results (red full line), revealing a fairly good correlation. It is interesting to note that the v-groove micro-cavity is filled to a height of around 8 μm even at low pressures long before the melt front reaches the end of the macroscopic cavity. These experimental results are confirmed by the simulations. In the analysed point (red dot in Fig. 6.12b) of the microstructures the pressure increases from 0 MPa to 24 MPa before switching to holding pressure.

6.6.2 Impact of injection velocity on microstructure replication

Filling simulations were carried out for PMMA under variation of the injection speed at constant $T_{\text{mould}} = 80^\circ\text{C}$. Detailed results are shown in Fig. 6.13 and Fig. 6.14 for injection (volume) velocities of $15 \text{ cm}^3 \text{ s}^{-1}$ and $60 \text{ cm}^3 \text{ s}^{-1}$, respectively.

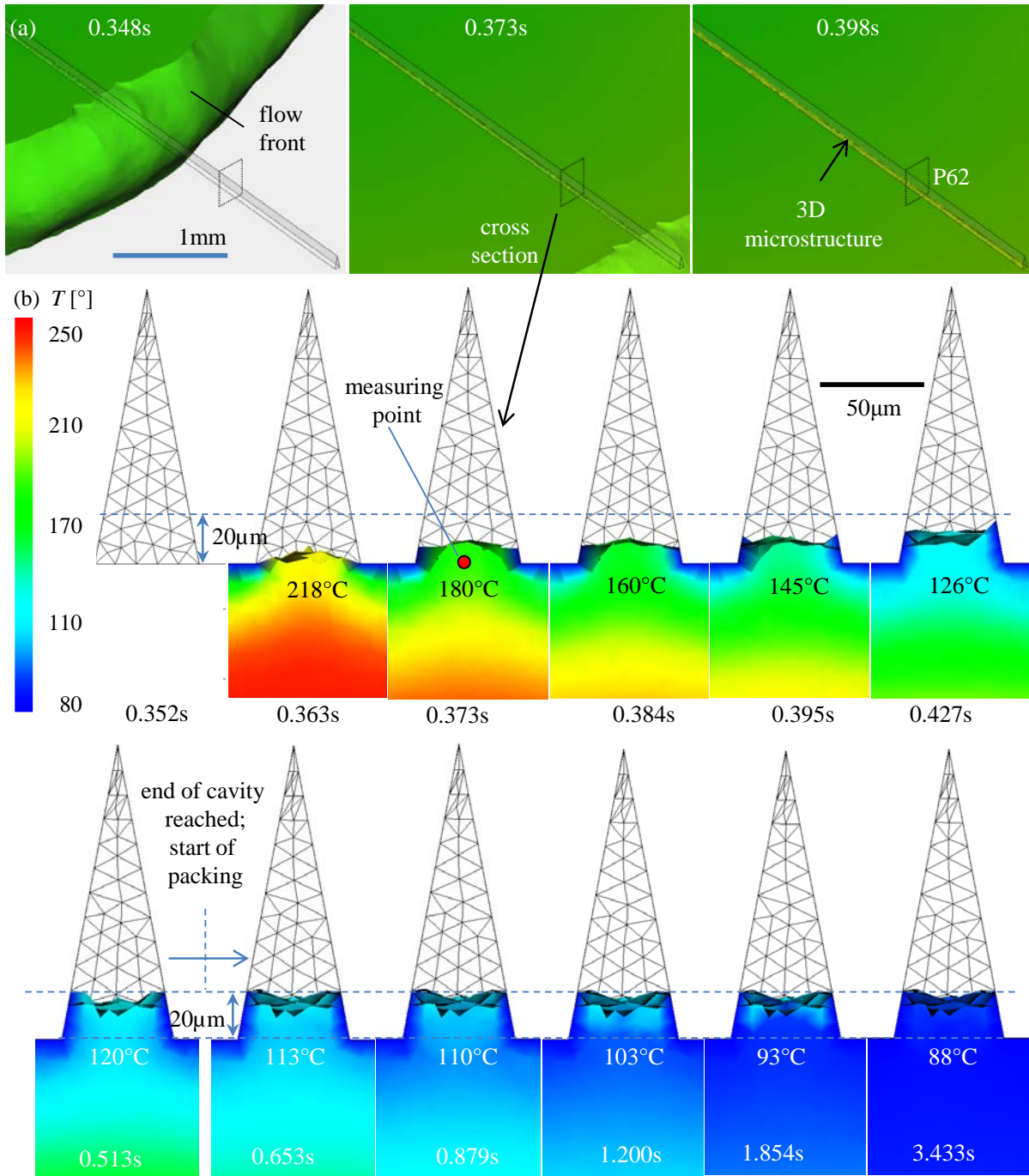


Fig. 6.13: (a) 3D simulation of the PMMA flow front partially filling the v-microgroove at an injection speed of $15 \text{ cm}^3 \text{ s}^{-1}$ ($T_{\text{mould}} = 80^\circ\text{C}$; $h_{\text{tc}} = 30000 \text{ W m}^{-2} \text{ K}^{-1}$; $T_{\text{trans}} = 105^\circ\text{C}$); (b) cross-sections with time dependent filling and temperature progress showing that when the end of the cavity is reached after $\Delta t = 0.16 \text{ s}$ and the packing phase is started, most of the filling process is finished because of the fast frozen layer formation with low mould temperatures.

As can be seen in Fig. 6.13, the micro-cavity is continuously being filled as the melt front proceeds and the pressure accordingly rises at the location of the cross-section indicated in Fig. 6.13a. The final filling height is only $18 \mu\text{m}$ for an injection velocity of $15 \text{ cm}^3 \text{ s}^{-1}$. The packing phase is less relevant for the filling of the microstructure for mould temperatures below the no-flow temperature, because the polymer in the cavity has cooled down below T_{no} after about 0.5 s, which prevents further filling of the microstructure during the packing phase.

With increasing injection velocity the micro-cavity filling becomes faster and more instantaneous as can be seen in Fig. 6.14.

At an injection velocity of $60 \text{ cm}^3 \text{ s}^{-1}$ most of the micro-cavity filling takes place within the first 3 ms. These results are in good agreement with (Han and Yokoi, 2006) who used a mould with a glass insert to monitor the filling of v-microgrooves (pitch 100 and $50 \mu\text{m}$) with an ultrahigh-speed video camera and concluded that filling is almost completed within the first 3-4 ms for injection velocities exceeding $50 \text{ cm}^3 \text{ s}^{-1}$.

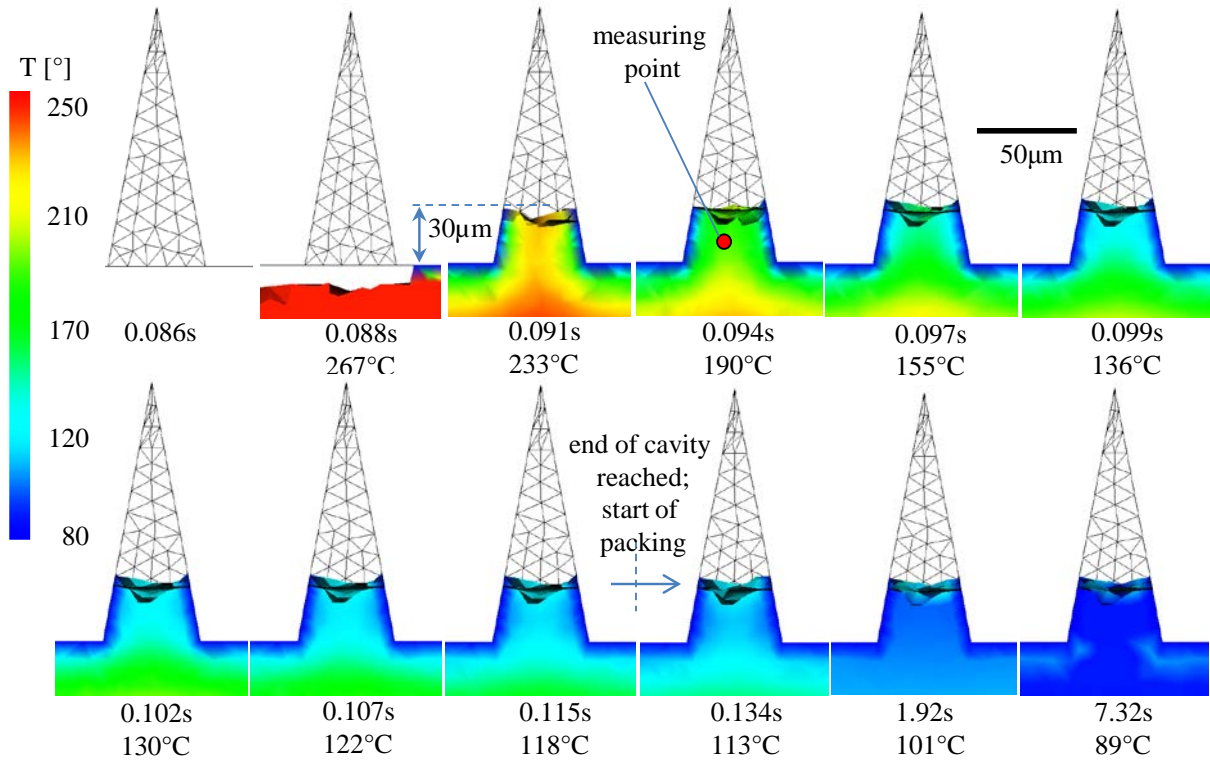


Fig. 6.14: Simulated filling of a v-groove microstructure with PMMA for an injection velocity of $60 \text{ cm}^3 \text{ s}^{-1}$ ($T_{\text{mould}} = 80^\circ\text{C}$; $h_{\text{ic}} = 30000 \text{ W m}^{-2} \text{ K}^{-1}$; $T_{\text{trans}} = 105^\circ\text{C}$) resulting in a filling height of $33 \mu\text{m}$, showing that $30 \mu\text{m}$ were already filled in the first 3 ms.

The evolution of the filling height and the temperature in the microstructure for both injection velocities are compared in Fig. 6.15.

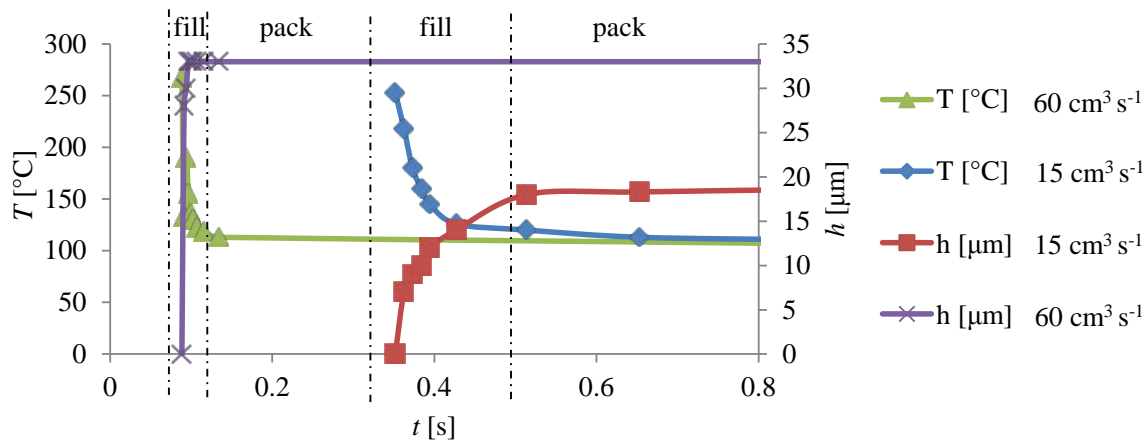


Fig. 6.15: Plotted temperature T in the microstructure vs. time t at P62 and filling height for two simulations with PMMA applying different injection velocities: $15 \text{ cm}^3 \text{ s}^{-1}$ and $60 \text{ cm}^3 \text{ s}^{-1}$.

As illustrated by Fig. 6.13, Fig. 6.14 and Fig. 6.15, a faster injection velocity generally improves the filling of micro-structures during the early phase of mould filling, which has already been addressed experimentally, among others, by (Pranov et al., 2006). The reason is that the pressure builds up faster at the entrance of the micro-cavity while the melt temperature is still high and, thus, the viscosity remains low enough to fill the structures to a higher extent. As soon as T_{no} is reached, the polymer melt ceases to flow into the structure, independent of the flow velocity. A comparison of the simulated results with experimental injection moulding trials are shown in Fig. 6.16.

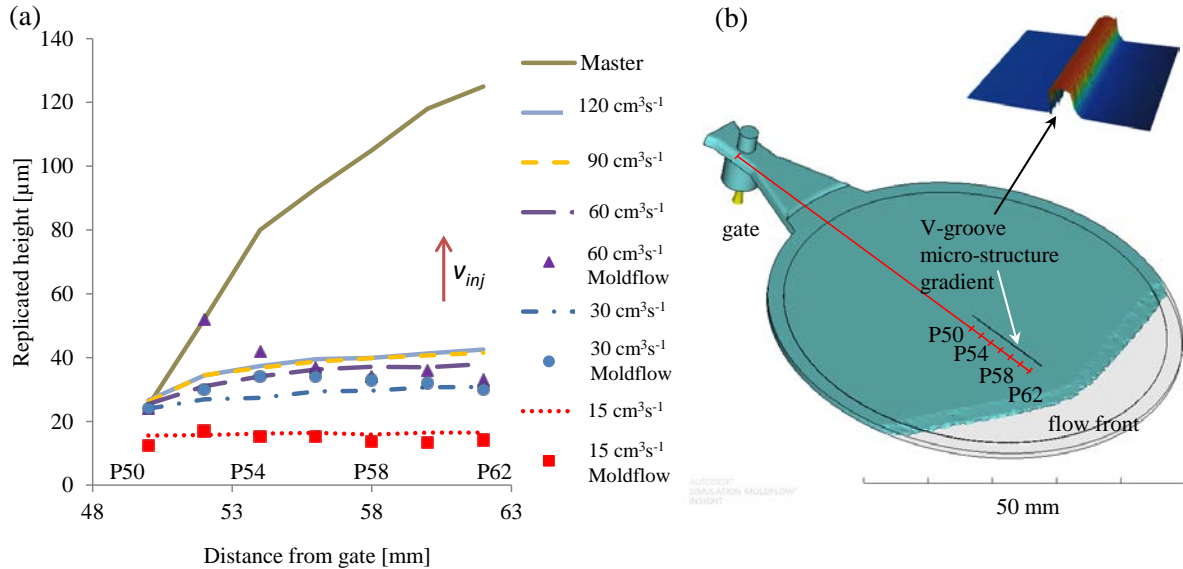


Fig. 6.16: (a) Replicated height of a v-groove microstructure for PMMA ($T_{mould} = 80^{\circ}\text{C}$; $h_{tc} = 30000 \text{ W m}^{-2} \text{ K}^{-1}$; $T_{trans} = 105^{\circ}\text{C}$) at varying distance from gate experimentally determined for different flow velocities in comparison to Moldflow simulation (symbols); (the standard deviation in the simulation (height of cross-section) and in experiments varies from 2-5 μm and was not included in the graph for better clarity); (b) Moldflow macro-filling model showing the positions at which the microstructures were analysed.

In contrast to the replication of macrostructures, the filling of these microgrooves is much more difficult. Even for very high flow velocities, the replicated structure height does not reach an aspect ratio larger than one, still far away from the depth of the master structure. The correlation between injection moulding trials and Moldflow simulation is very good for all positions at a flow velocity of $15 \text{ cm}^3 \text{ s}^{-1}$ (red dotted line and red squares). For $v_{inj} = 30$ and $60 \text{ cm}^3 \text{ s}^{-1}$ the correlation is also fairly good except for the two measuring points.

In Fig. 6.17 the cross-sections of replicated microstructures at measuring point P62 are compared to the cross-sections obtained from simulations.

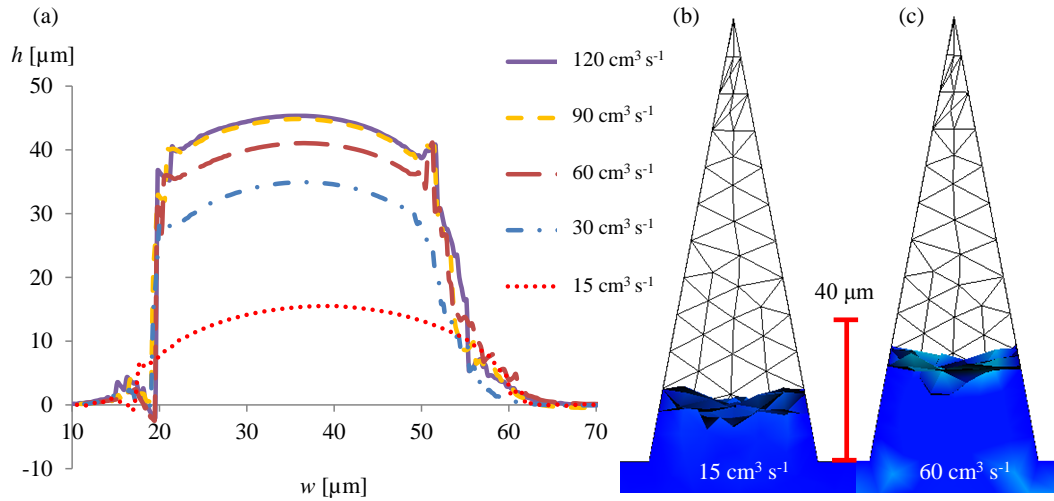


Fig. 6.17: CLSM cross-sections of the v -microgroove at position P62 depending on different flow velocities; (a) IIM trials; (b) Moldflow simulation with $15 \text{ cm}^3 \text{ s}^{-1}$; (c) Moldflow simulation with $60 \text{ cm}^3 \text{ s}^{-1}$.

Of course, the replication is better with higher injection speed, although a 100% structure transcription is not even possible with the highest volume flow velocity of $120 \text{ cm}^3 \text{ s}^{-1}$ (Fig. 6.17, violet continuous line). In contrast to macrostructures where the replication of an $\text{AR} = 2$ was easily accomplished, a microstructure (width = $45 \text{ }\mu\text{m}$) with an aspect ratio of one appears to be very difficult to replicate with a mould temperature below the no-flow temperature, despite applying very high injection velocities. In Fig. 6.18a, the viscosity η is plotted versus the injection velocity v_{inj} showing the typical decrease in viscosity due to shear thinning.

The replicated height or volume correlates inversely proportional with the polymer viscosity as it is presented in Fig. 6.18b: RR_h or $\text{RR}_{vol} \sim 1/\eta$.

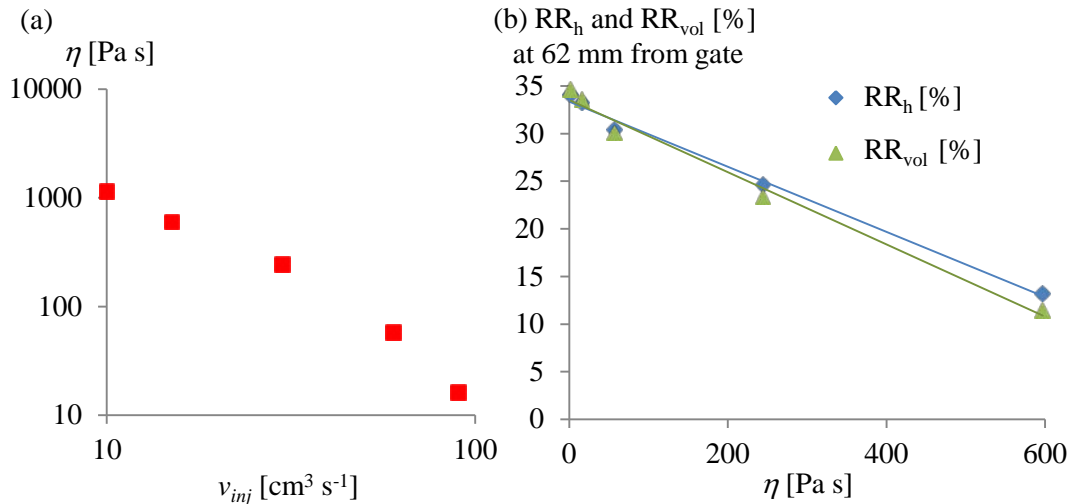


Fig. 6.18: (a) Plotted viscosity η (measured online) of PMMA vs. injection velocity (v_{inj}); (b) replication ratio based on structure height (RR_h) and the structure volume (RR_{vol}), respectively, at measuring point P62 (62mm from gate) in the microstructure vs. η .

In contrast to simulations of (Young, 2005) who did not carry out any experimental verifications, the correlation of the filling distance (or replication ratio) with the filling rate is not linear but logarithmic; thus RR_h or $\text{RR}_{vol} \sim \ln(v_{inj})$.

This correlation was verified with three polymers as can be seen in Fig. 6.9.

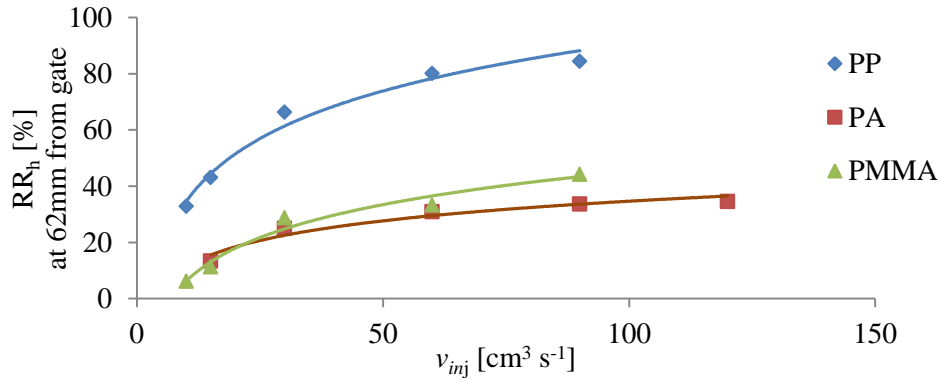


Fig. 6.19: Correlation between replication ratio RR_h and injection velocity v_{inj} in $\text{cm}^3 \text{s}^{-1}$ displaying a logarithmic behaviour for three different polymers.

6.6.3 Variation of mould temperature

The replication of the v-groove microstructure with PMMA as a function of mould temperature was also compared with Moldflow simulations. As can be seen from Fig. 6.20, a fairly good correlation between experiments and simulation was found when simulating the full part with 8.3 million elements (blue bars in Fig. 6.20a), but this required very long calculation times (300 - 400h). Attempts to reduce the simulation time by a reduction of the simulated volume with only 0.1 million of elements (green bars in Fig. 6.20a) resulted in a less accurate differentiation between the different mould temperatures.

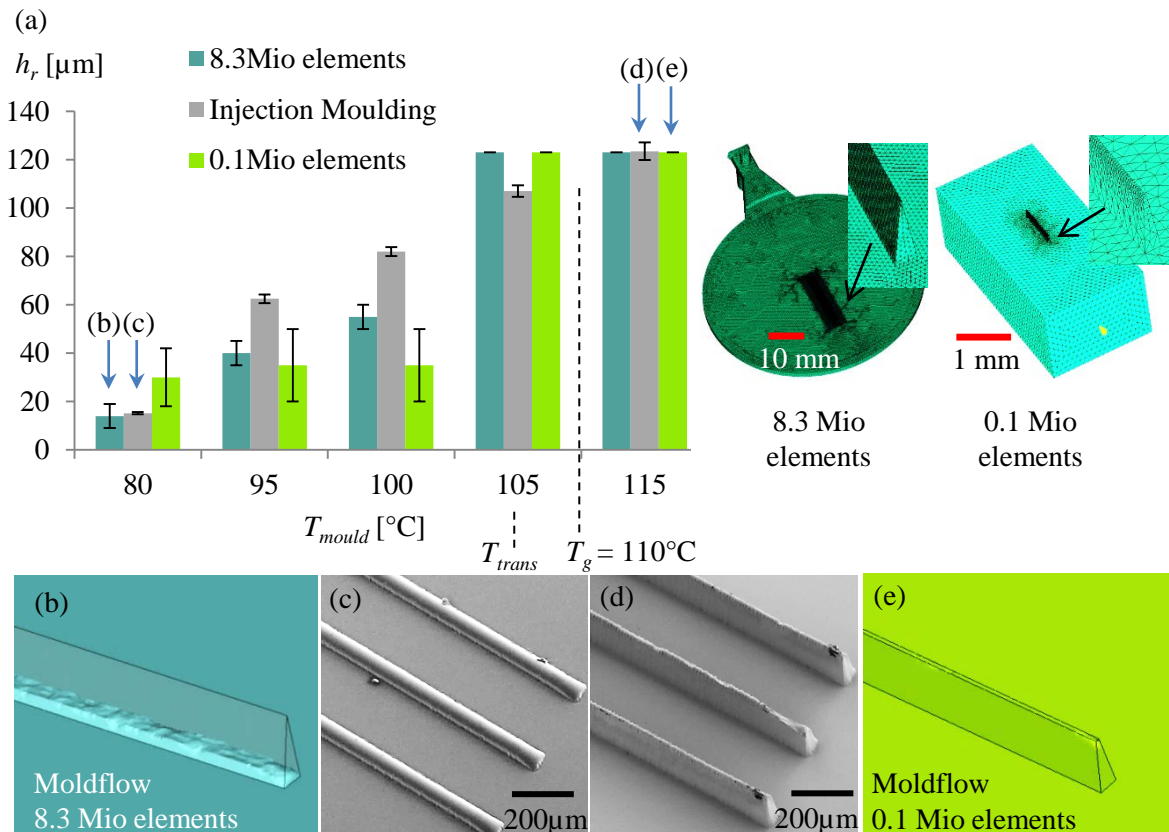


Fig. 6.20: (a) Comparison of replicated height h_r as a function of temperature from injection moulding and Moldflow simulations ($h_{tc} = 30000 \text{ W m}^{-2} \text{ K}^{-1}$) with good correlation; (c), (d) SEM pictures of injection moulded PMMA v-groove microstructures and simulation results for (b) the macro model with 8.3 million elements (here shown for $T_{mould} = 80^{\circ}\text{C}$) and I the simplified micro model with only 0.1 million elements (shown for $T_{mould} = 115^{\circ}\text{C}$).

One can see in Fig. 6.20 that the replicated height continuously increases with rising mould temperature. The structure was finally filled for a mould temperature of 115°C which is above T_{trans} (105°C) and T_g (110°C). If T_{mould} exceeds T_{trans} , the cooling is delayed and the molten material can still be pressed into the cavity by the holding pressure that builds up rapidly once the cavity is completely filled. The influence of the holding pressure can be observed when looking at short-shots as visualized already in Fig. 6.21.

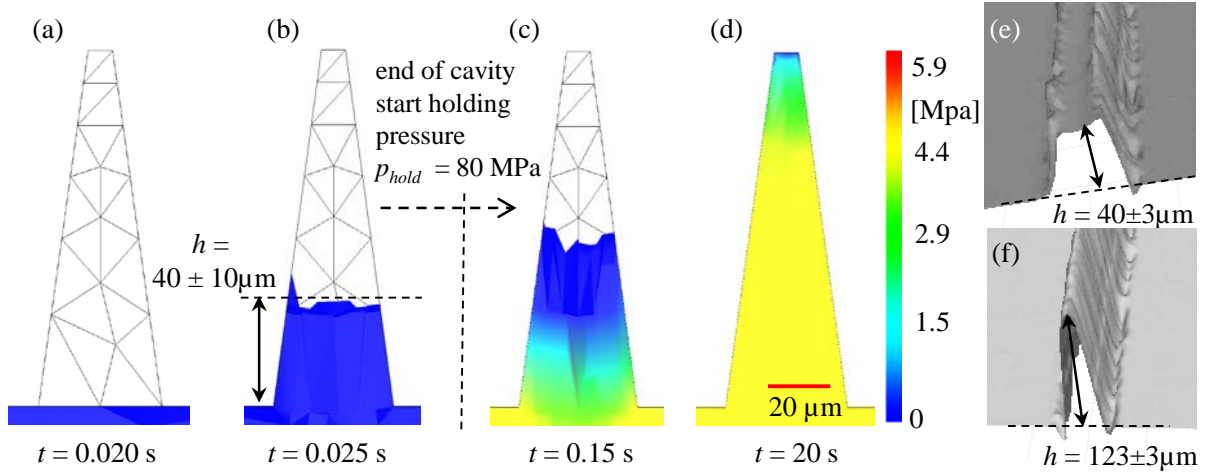


Fig. 6.21: Volume dependent filling (short-shots) with a mould temperature of 115°C showing good correlation of the filling height h before applying the holding pressure between (b) simulation and (e) 3D-CLSM micrograph of injected PMMA; (c) and (d) show the simulated increase in height when applying a holding pressure of 80 MPa in good correlation with (f) 3D-CLSM micrograph of a fully replicated PMMA v-groove microstructure prepared by variothermal injection moulding.

If T_{trans} in Moldflow is set above T_{mould} , almost no material is pressed into the cavity by the holding pressure because a significant volume of the polymer freezes before. In reality, T_{trans} corresponds to T_{no} , which is not necessarily similar to T_g . For PMMA T_{trans} seemingly is in the range of T_g , although the measurements shown in Table 6-2 revealed a T_{no} of 130°C. Probably, the experimental value of T_{no} is just too high because of the lower applied pressure in the test (33MPa) compared to the resulting cavity pressure during injection moulding (60MPa). However, a difference of $\Delta T = 20^\circ\text{C}$ was measured for T_{no} of PMMA compared to A-PA. The importance of the higher T_{no} of A-PA is evident when looking at the filling of the same v-microgroove with A-PA in Fig. 6.22 for different values of T_{trans} applied in the filling simulation.

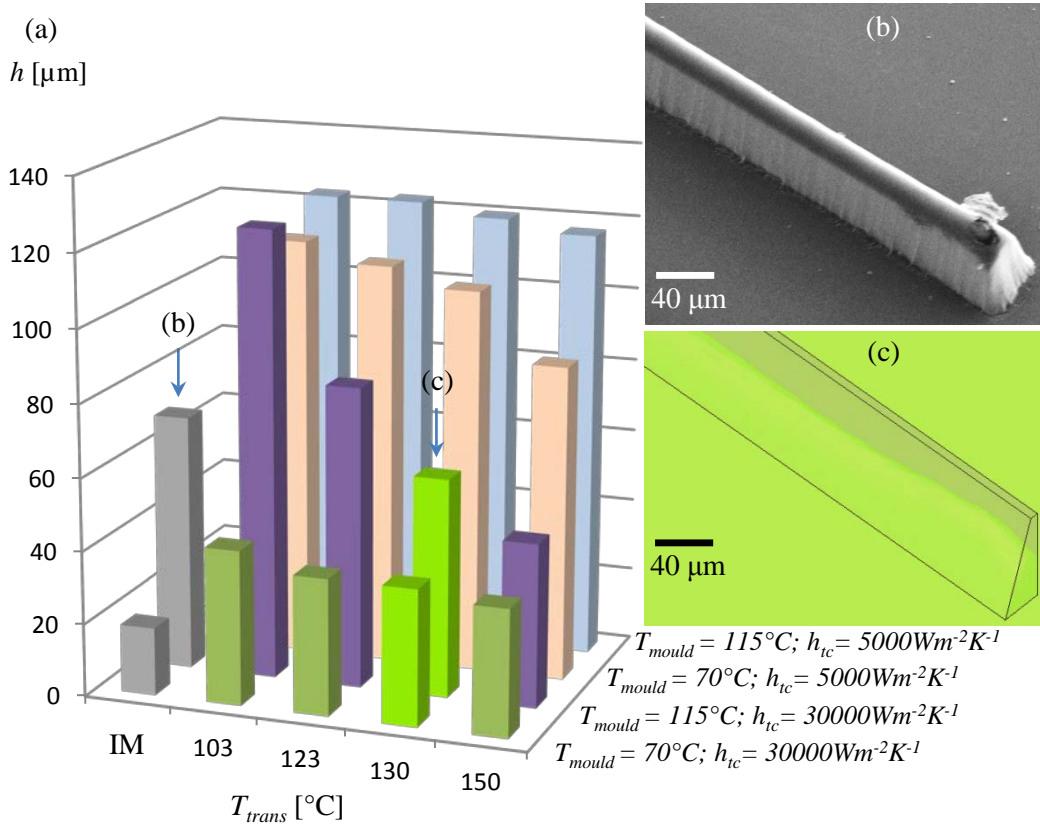


Fig. 6.22: (a) Comparison of isothermal ($T_{mould} = 70^{\circ}\text{C}$) and variothermal ($T_{mould} = 115^{\circ}\text{C}$) injection moulding (grey) with filling simulations (green) for different values of T_{trans} and h_{ic} ; (b) SEM picture of variothermally injection moulded A-PA microstructure with $T_{mould} = 115^{\circ}\text{C}$; (c) simulated structure height of variothermally injection moulded A-PA microstructure with $T_{mould} = 115^{\circ}\text{C}$.

Same as the isothermal filling of PMMA, the filling simulation of A-PA with $T_{mould} = 70^{\circ}\text{C}$ is hardly influenced by T_{trans} because the polymer within the microstructures is already frozen when the packing sequence starts. For variothermal replication the correlation of experiments and simulation was only good if T_{trans} was increased from 103°C to 130°C . If T_{trans} of A-PA in the simulation was set below T_{mould} the polymer could be still pressed into the structure. As the measured T_{no} of A-PA is 20°C higher than that of PMMA (Table 6-2), T_{trans} needs to be adapted accordingly and the h_{ic} (same as for PMMA) needs to be increased from 5000 to $30000\ \text{W m}^{-2}\text{K}^{-1}$ to obtain good correlations with real injection moulding.

As already shown for h_{ic} , also an adaption of T_{trans} for macroscopic filling simulations is less important, because the filling of a macro-part is less influenced by interfacial interactions.

6.6.4 Replication of nanostructures

The gaps between the nickel pillars (Fig. 4.21a) were approximated in the simulation with pillars of 300 nm diameter. Most important for a correct simulation is a precise knowledge of the flow front velocity, which needs to be transferred as a boundary condition from the macro to the micro or nano model, as shown in Chapter 6.3.3. In Fig. 6.23 one can see that the nano-moulding trials both iso- and variothermal also correlate well with the simulation for two different polymers if the flow front velocity in the bulk of 7.7 to 10.9 cm s⁻¹ was approximated with an injection time of 0.0013 s for a volume of $V = 4 \cdot 10^{-8}$ cm³:

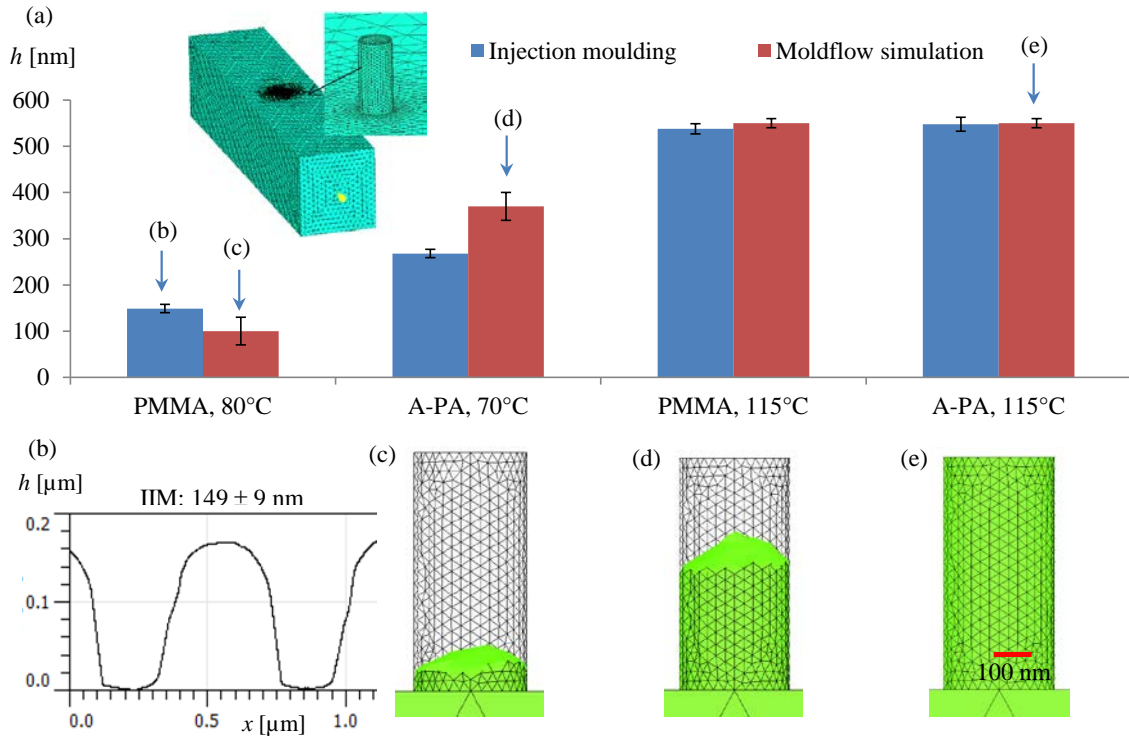


Fig. 6.23: (a) Comparison of injection moulded nanostructures (blue) with Moldflow simulations (red); (b) AFM profile of replicated PMMA at 80°C mould temperature; (c)-(e) simulated filling of nanostructures: (c) PMMA, 80°C isothermal; (d) A-PA 70°C isothermal; (e) A-PA 115°C variothermal.

Moreover, the values for h_{rc} and T_{trans} were adjusted as for the micro-moulding. The heat transfer coefficient during filling was set to 30000 W m⁻² K⁻¹ for both materials. On the basis of the T_{no} shown in Table 6-2 revealing a difference in T_{no} of at least 20°C, the transition temperature for PMMA was used as default (105°C) whereas T_{trans} for A-PA was increased from 103°C to 130°C.

In Fig. 6.24 the simulated flow of PMMA into a nanostructure is shown in more detail and the values of pressure P , temperature T and viscosity η at the entrance of the nanostructure (red dot marking) is documented for selected times:

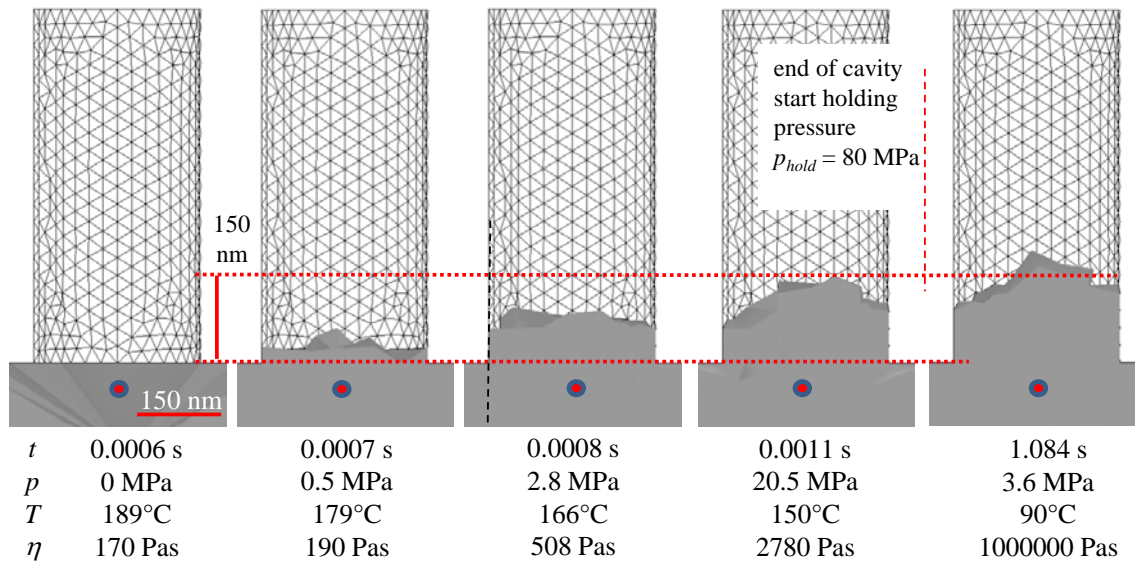


Fig. 6.24: Simulated flow behaviour for PMMA with 80°C mould temperature: The pressure P , temperature T and viscosity η at the entrance of the nanostructure is documented depending on time t .

Because of the fast temperature decrease of the melt in contact with the much colder mould cavity ($T_{mould} = 80^\circ\text{C}$), p and η increase within milliseconds. In that moment, when the holding pressure phase starts, the melt still has a temperature of 150°C which is above T_{trans} (105°C), and thus, some material can be still pressed into the cavity, as can be seen in the two figures to the right in Fig. 6.24.

6.6.5 Influence of wall boundary condition

For macro injection moulding the assumption of no-slip boundary condition is generally accepted. If the shear stress reaches a critical value, a wall slip model might represent the polymer flow more realistically, although the online viscosity measurements for PMMA and A-PA, already shown in detail in Table 4-3, revealed a constant or lower stress level with increasing shear rates and decreasing polymer viscosities. Therefore, the influence of wall slip was neglected but the role of wetting on the polymer/mould interface was investigated. The simulation shown in Fig. 6.25 was carried out to determine the influence of the wall boundary conditions on the filling of the nanostructure. For this purpose, the boundary condition in the laminar two-phase flow level set model was varied (no slip vs. wetted wall). In order to maximize wetting effects, the cavity side wall temperature (green dashed line in Fig. 6.25) was set equal to the polymer melt temperature of PMMA (250°C). Whereas a small difference between no slip and wetted wall can be detected, there seems to be no substantial influence of the actual contact angle.

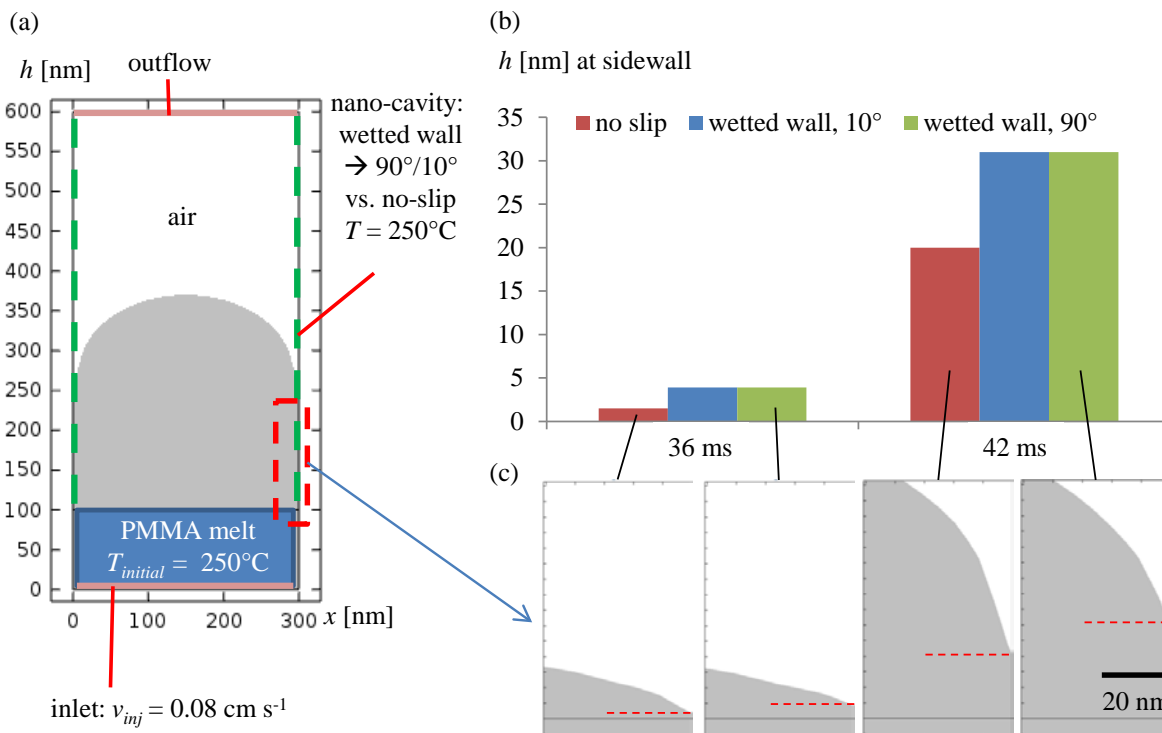


Fig. 6.25: (a) Comsol 2-D model for the filling (grey) of a nano-pillar with a diameter of 300 nm with PMMA (blue rectangular area is PMMA melt at the entrance of the nano-pillar); (b) differences in melt advancement at the sidewall after 36 and 42 ms, respectively, with different wall boundary conditions showing a lower filling height with no slip boundary compared to a wetted wall boundary; (c) cut-outs at the height of the polymer at the side wall (red dashed square in (a)).

In contrast to the experimental investigations shown in (Rytka et al., 2016b) the influence of the wall boundary in the flow simulation was not significant. Only small differences can be seen between no slip and wetted wall independent of the contact angle. Also (Moguedet et al., 2009) found no influence of the surface tension on the filling of microstructures when varying between 20 and 60 mN m^{-1} .

6.7 Conclusions

The simulation of micro- and nano-cavity filling was discussed using different models. With such models the development of polymeric products with functional polymeric structures can be accelerated, as it would be possible to provide quick answers which process, material, and parameter are best suited to achieve a perfect replication of structures of different sizes and geometries without the necessity of carrying out real injection moulding trials. Good correlation between experimental findings and simulations was achieved for different processing conditions, i.e. varying mould temperatures and injection velocities with two amorphous polymers, namely PMMA and A-PA. In order to reduce calculation time and memory space, the models were scaled down, taking care of transferring the correct boundary conditions, such as temperature, pressure, viscosity, and flow front velocities. While full simulations can still be done with microstructured parts, the downscaling of the model for nanostructured parts is inevitable. There are two key parameters that need to be adjusted, in order to achieve the good correlation between simulations and experiments:

First, the heat transfer coefficient h_{ic} needs to be increased from $5000 \text{ W m}^{-2} \text{ K}^{-1}$ to $30000 \text{ W m}^{-2} \text{ K}^{-1}$, at least for initial contact of the polymer melt with the mould. Ideally, h_{ic} should be represented by a fast decreasing value over time to reach a value of $5000 \text{ W m}^{-2} \text{ K}^{-1}$ which is experienced by the bulk, where cooling times are in the range of seconds rather than milliseconds. In order to confirm the necessity of a high h_{ic} , a heat transfer simulation was carried out in Comsol Multiphysics. Additionally to the simulations with Moldflow, it was clearly shown that filling and cooling of the polymer in micro- and nanostructures take place within milliseconds and T_{no} is reached earlier for smaller structures.

Secondly, the transition temperature T_{trans} needs to be adjusted to the no-flow temperature measurements, although the experimentally determined values cannot be used directly in Moldflow simulations. Differences between polymers ($\Delta T = 20^\circ\text{C}$), as observed for A-PA and PMMA, should be considered accordingly by adapting T_{trans} ideally in the same range. T_{trans} influences the replication in the packing phase especially where $T_{mould} > T_{trans}$, in the case of variothermal processes. In the case of an isothermal process ($T_{mould} < T_{trans}$), the influence of T_{trans} is much smaller in the packing phase, as most of the filling takes place in the very first milliseconds and the polymer at the mould interface is already frozen once the holding pressure is applied.

In the 3D Moldflow simulations only amorphous polymers were simulated. It remains to be shown whether transition temperatures and heat transfer coefficients can be adapted in the same way for semi-crystalline materials.

Finally, different wall boundaries ("no slip", "wetted wall 10° ", "wetted wall 90° ") were compared with the FEM software Comsol, which is not possible with Moldflow. Whereas some small differences in the advancement of the melt at the side wall were observed between "no slip" and "wetted wall" conditions, no significant influence of the actual contact angles could be identified. However, it should be noted that only contact angles at the side wall were varied, while an implementation of the surface tension of the polymer was neglected because of convergence issues.

7. DEMOULDING OF MICRO- AND NANOSTRUCTURES

Once the structures have been filled, the replica need to be demoulded. This can be an even bigger challenge than the actual filling of micro- and nanostructures. The demoulding of the part is as important as the filling and gets even more difficult with increasing aspect ratio, or more generally, with increasing surface to volume ratio. As the fracture toughness of the mould material is crucial for demoulding, different materials are compared in Chapter 7.2. Anti-adhesion coatings can reduce ejection problems and are discussed in Chapter 7.3. In Chapter 7.4 the work of adhesion is proposed as an indicating value for potential demoulding issues that are finally explained and discussed in Chapter 7.5.

7.1 Introduction

Examples for typical demoulding issues are illustrated in Fig. 7.1. High adhesion forces between mould and replica can lead to a complete destruction of the polymer part (Fig. 7.1a) in the demoulding phase. Another common issue is related to polymer residues on the master originating from broken polymer structures during ejection (Fig. 7.1b). These imperfections would be transferred into the next polymer replica (Fig. 7.1c).

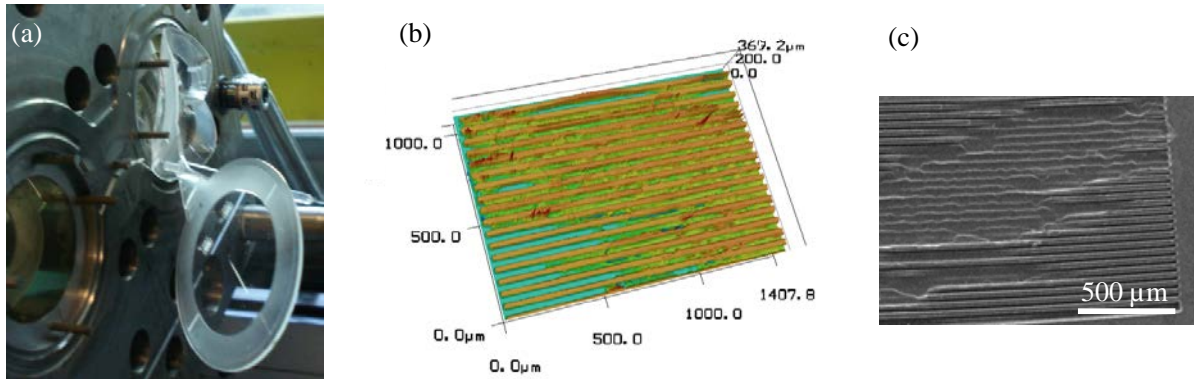


Fig. 7.1: Demoulding issues with COC on uncoated Ni: (a) macropicture of a deformed COC part in the injection mould; (b) CLSM 3D micrograph of the Ni master structure (blue) with stuck COC material (brown); (c) COC replica from same Ni master showing the replicated surface defects.

For the replication of thousands of parts a material is needed, which is highly resistant to thermal and mechanical fatigue. Moreover, the demands on tooling materials are getting higher with smaller feature size. Of course it would be convenient to use silicon as a stamp material as it is readily available in a good quality (monocrystalline) with perfect purity of more than 99.99%. Additionally the processes to structure silicon, as for example photo- and e-beam-lithography, are well established. However, silicon is very fragile (Fig. 7.2a), but also electroplated nickel or nickel-phosphate (Ni-P) is sensitive especially if the design of the structures is unfavourable (high aspect ratios), as already shown in Fig. 4.18b.

Some examples of broken nano-pillars after injection moulding are shown in Fig. 7.2. High aspect ratio pillars for example are much more sensitive compared to low aspect ratio sinusoidal diffractive microgroove patterns (Fig. 7.2c).

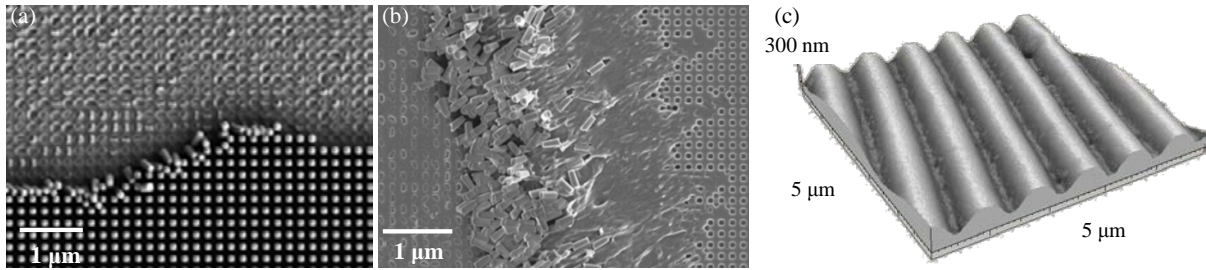


Fig. 7.2: (a) SEM picture of broken Si nanopillars produced by e-beam lithography after injection moulding; (b) SEM picture of the polymer replica with Si nanopillars ripped off from the Si master; (c) CLSM micrograph of an exemplary low aspect ratio sinusoidal diffractive microgroove pattern.

Steep side walls without draft angles or with undercuts that most of the times originate from uncontrolled etching are even more critical than high aspect ratio structures. Such a structure, as can be seen in Fig. 7.3, would either break or would be pulled apart immediately during demoulding if being replicated with polymers.



Fig. 7.3: SEM picture of Ormostamp resist (micro resist technology GmbH, Berlin, Germany) on nickel showing undercuts because of improper lithography process (courtesy of Victor Cadarso, PSI).

7.2 Fracture toughness and demoulding issues of different mould materials

The fracture toughness K_{Ic} and the elongation at break ε_B can be considered as good indicators for the durability of a mould material (see Fig. 7.4) instead of only comparing the elastic modulus E , which could lead to false interpretations. The correlation between K_{Ic} and E is given for plane stress as:

$$K_{Ic} = \sqrt{EG_c} \quad (7-1)$$

Where G_c is the critical strain energy release rate.

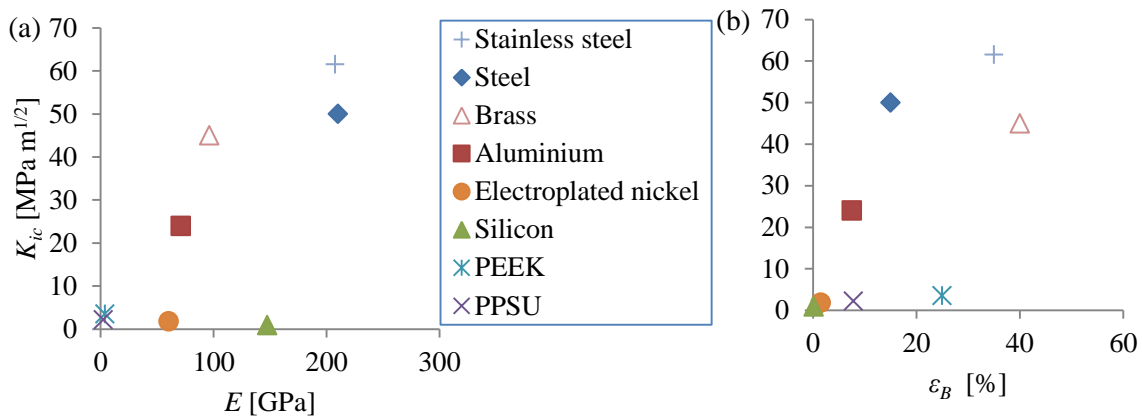


Fig. 7.4: Fracture toughness K_{Ic} plotted vs. (a) elastic modulus E and (b) elongation at break ε_B of different mould insert materials proving the best performance of steel compared to silicon or electroplated Ni (source: CES Edupack Software 2013 data base, granta design and material data sheets; values for electroplated nickel were taken from (Sade et al., 2011)).

High K_{Ic} and ε_B combined with a good corrosion resistance are the reasons why stainless steel is strongly preferred for industrial injection moulding tools, but is very difficult to functionalise with micro- and nanostructures. Possible direct structuring methods for metal are direct precision technologies, laser ablation, focused ion beam (FIB), laser sintering and ion etching. Because of the polycrystalline nature of steel, the resolution of such structuring processes is often limited by the grain size (Gadegaard et al., 2003).

Alternatively, bulk metallic glass (BMG) have been proposed for direct structuring by (David et al., 2012). (Kumar et al., 2009) showed that feature sizes as small as 13 nm can be transferred from porous alumina into BMG by hot embossing. (Zhang et al., 2012) investigated the stability of microstructured BMG-moulds and observed severe destruction after 20000 cycles, especially for structural features oriented perpendicular to the flow direction. Several research groups, e.g. (Saarikoski et al., 2009) investigated nano-porous anodized aluminium oxide (AAO) membranes as mould masters for the fabrication of high aspect ratio nanopillars. But also AAO is rather brittle, very difficult to handle and demoulding is almost impossible without destroying the master (Yoo et al., 2009). Compared to AAO, silicon and glass, glassy carbon is much more stable and can also be micro- and nanostructured as demonstrated by (Prater et al., 2014), (Prater et al., 2015). Similar to silicon, glassy carbon is also difficult to integrate into the mould.

7.3 Anti-adhesion coatings for better demoulding

In various studies the positive effect of anti-adhesion coatings was examined for demoulding. (Matschuk et al., 2010) improved the replication fidelity of 50 and 100 nm wide holes by applying a 10 nm plasma-polymerized fluorocarbon based anti-sticking coating on a nickel mould. Without coating, micro-cracks, regular nanoscale defects and distortions occurred during demoulding. (Kosuke et al., 2010) investigated a silicone release agent in comparison to an alkoxy-silane-terminated perfluoropolyether for thermal nano-imprint lithography with polystyrene. Whereas the silicone layer on SiO_2 nano-pillars showed no reduction of adhesion forces, demoulding and adhesion forces were reduced significantly with a perfluoro-polyether surface. (Cech and Taboryski, 2012) tested the durability of a perfluoro-decyltrichlorosilane (FDTS) molecular coating on aluminium. After 500 cycles with ABS and PS the surface energy was still in the range of 20 mN m^{-1} and the presence of fluorine was additionally confirmed with x-ray photoelectron spectroscopy (XPS).

Also in this thesis different anti-adhesion coatings were investigated in order to prevent demoulding issues:

1. Perfluoro-octanephosphonate (PFOP) from Sigma-Aldrich (St. Louis, USA)
2. Heneicosafuoro-dodecylphosphate (HFDP), synthesized at PSI (Villigen, Switzerland)

Both chemicals were dip coated from tert-butyl-methylether (tBME) at PSI as described in detail by (Padeste et al., 2014). In contrast to commercial anti-adhesion coating systems like chromium nitride (CrN), diamond like carbon (DLC) or titanium nitride (TiN) that are typically applied by physical vapour deposition (PVD), the PFOP-coating is only a few nm thick and therefore well suitable for nanostructures that would otherwise be covered by commercial coatings. PFOP reduces the surface energy of the mould insert surface and therewith the work of adhesion. Unfortunately, the coating is not very stable as can be seen in Fig. 7.5. In order to determine the stability, sessile drop measurements (explained in detail in Chapter 3.2.2) were carried out on unstructured surfaces of the insert material (here nickel) before injection and after 100, 200 and 350 shots with COC and PS. Every 100 shots the material was changed, and the inserts were cleaned mechanically with the cleaning agent Lusin Clean L101F from Chem Trend (Maisach, Germany) and ultrasonic bath in ethanol in order to accelerate the coating failure. In injection moulding the cleaning of critical mould areas is common for polymers with volatile additives to remove deposited residuals.

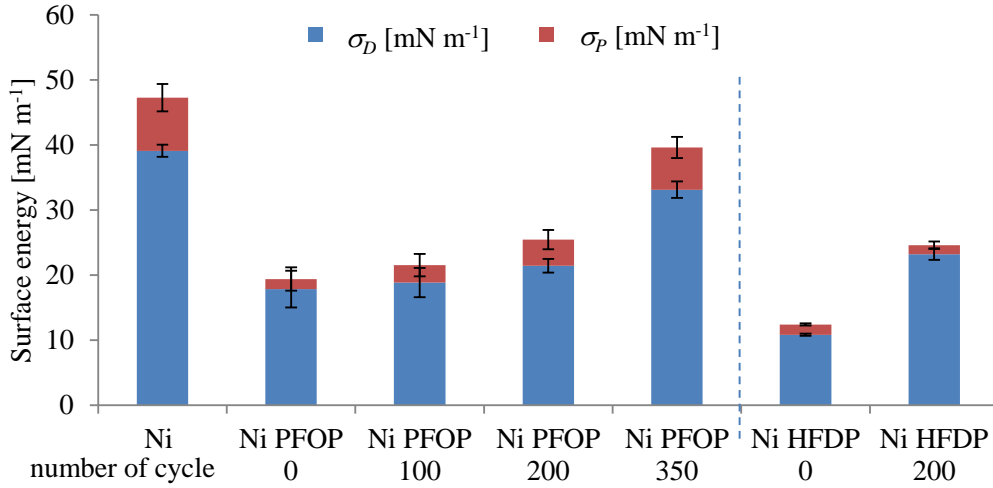


Fig. 7.5: Sessile drop measurements with water and diiodomethane on Ni-PFOP and Ni-HFDP showing a significant increase of both the dispersive (σ_D) and the polar (σ_P) part of surface energy already after 200 shots.

Because of the increase of surface energy after 200-350 shots, both anti-adhesion coatings could be suitable for the production of a hundred of samples for research purpose, but rather not for mass production.

7.4 Correlation of demoulding issues with work of adhesion and adhesion forces

A good filling and spreading of the polymer in the structures could result in strong adhesion forces and significant demoulding issues. The work of adhesion could be used to quantify the adhesion forces between the solidified polymer and the cavity during the ejection phase according to:

$$W_A = \sigma_L \cdot (1 + \cos\theta) = 2 \cdot \left(\sqrt{\sigma_S^D \cdot \sigma_L^D} + \sqrt{\sigma_S^P \cdot \sigma_L^P} \right) \quad (7-2)$$

Where σ_L is the surface energy of the polymer; θ is the contact angle; σ_S^D is the dispersive and σ_S^P is the polar part of the surface energy of the substrate; σ_L^D is the dispersive and σ_L^P is the polar part of the surface energy of the polymer.

(Jeong et al., 2006) used equation (7-2) to correlate the work of adhesion with the aspect ratio for the fabrication of stretched PMMA nano-hairs (radius $R = 45$ nm, $W_A = 100$ mJ m⁻²) without disrupting them from a polyurethane acrylate (PUA) mould. In the same investigation the work of adhesion for a single nano-hair was measured with a flat AFM-tip in force-distance mode and correlated with the calculated adhesion force F_{adh} of a single structure with the Johnson-Kendall-Roberts equation (Johnson et al., 1971):

$$F_{adh} = \frac{3}{2} \pi \cdot R \cdot W_A \quad (7-3)$$

It turned out that the adhesion force of a single nano-hair is around 20 nN. High work of adhesion W_A or high force of adhesion F_{adh} can lead to undesirable sticking or breaking of the polymer part or the structures likewise. The interfacial forces between polymer and mould can be represented with the work of adhesion. Therefore, equation (7-2) was used to calculate W_A at different ejection temperatures (T_e). The calculations are based on contact angle measurements on polymer plates (interpolated to T_e) and mould inserts (at 23°C) with water and diiodomethane.

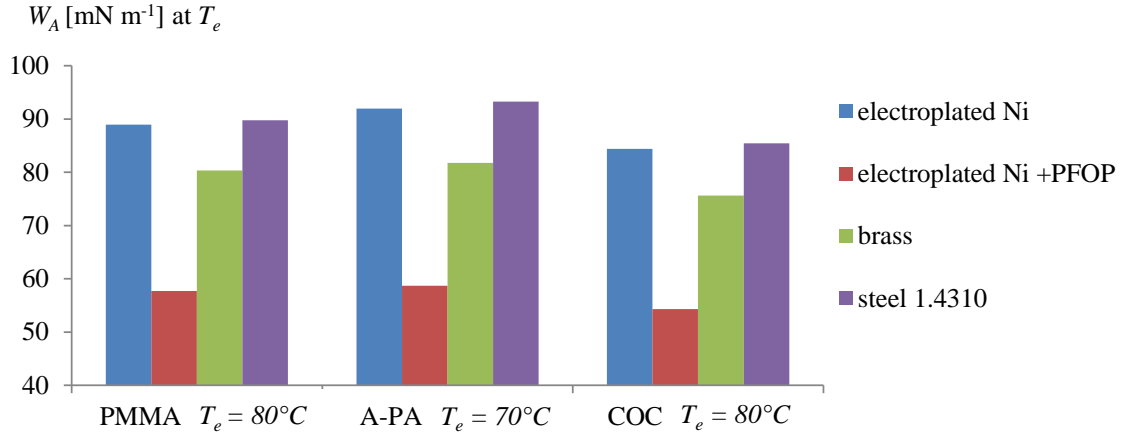


Fig. 7.6: Calculated work of adhesion W_A for three different polymers (PMMA, A-PA, COC) at the respective ejection temperature T_e in contact with various insert surfaces (Ni, Ni with PFOP anti-adhesion coating, brass, and steel 1.4310) showing a huge reduction of W_A when applying an anti-adhesion coating.

The lowest W_A values in general were calculated for COC and the highest for A-PA. Moreover, it can be clearly seen that a PFOP coating reduces the work of adhesion and could therefore prevent demoulding issues. The ejection problems showed in Fig. 7.1 were eliminated by applying the PFOP coating on nickel and, thus, the calculated reduction of W_A was confirmed experimentally. The detailed values for the calculation can be found in Table 7-1:

Table 7-1: Detailed values for the determination of W_A .

substrate	polymer	σ_S^D at 23°C [mN m ⁻¹]	σ_S^P at 23°C [mN m ⁻¹]	T_e [°C]	σ_L^D interpolated to T_e [mN m ⁻¹]	σ_L^P interpolated to T_e [mN m ⁻¹]	W_A at T_e [mN m ⁻¹]	F_{adh} pillar [nN]	F_{adh} on $D = 45$ mm [N]
electroplated Ni	PMMA	39.1	8.2	80	40.0	3.0	89	63	314
electroplated Ni	A-PA	39.1	8.2	70	38.6	6.2	92	65	325
electroplated Ni	COC	39.1	8.2	120	34.2	3.9	84	60	298
electroplated Ni +PFOP	PMMA	17.8	1.6	80	40.0	3.0	58	41	204
electroplated Ni +PFOP	A-PA	17.8	1.6	70	38.6	6.2	59	41	207
electroplated Ni +PFOP	COC	17.8	1.6	120	34.2	3.9	54	38	192
brass	PMMA	34.4	3.2	80	40.0	3.0	80	57	284
brass	A-PA	34.4	3.2	70	38.6	6.2	82	58	289
brass	COC	34.4	3.2	120	34.2	3.9	76	53	267
steel 1.4310	PMMA	38.8	10.2	80	40.0	3.0	90	63	317
steel 1.4310	A-PA	38.8	10.2	70	38.6	6.2	93	66	330
steel 1.4310	COC	38.8	10.2	120	34.2	3.9	85	60	302
steel 1.4310	COC	38.8	10.2	90	36.6	3.8	88	62	310
steel 1.4310	COC	38.8	10.2	50	39.7	3.8	91	64	321

These calculated values for W_A are clearly higher than those reported by (Anastasiadis and Hatzikiriakos, 1998) who determined an adhesion energy of high density polyethylene (HD-PE) on steel in the order of 30 mN m⁻¹. However, the values are in very good agreement with investigations of (Pedersen et al., 2015) who calculated the W_A of PC and PS on SU-8 in the order of 87 mN m⁻¹ and those on fluorinated silicon nitride (SiN) in the order of 61 mN m⁻¹.

Using the values for W_A from Fig. 7.6 the adhesion forces F_{adh} for single nano-pillars can be calculated with equation (7-3). Thus, depending on the polymer/mould interface, the adhesion force would be between 38 nN to 66 nN for pillars with a radius of 150 nm. Considering that there are around 5 billion pillars on the total surface of the one insert used in these investigations the total adhesion force would be between 192 to 329 N as can be seen in the following figure:

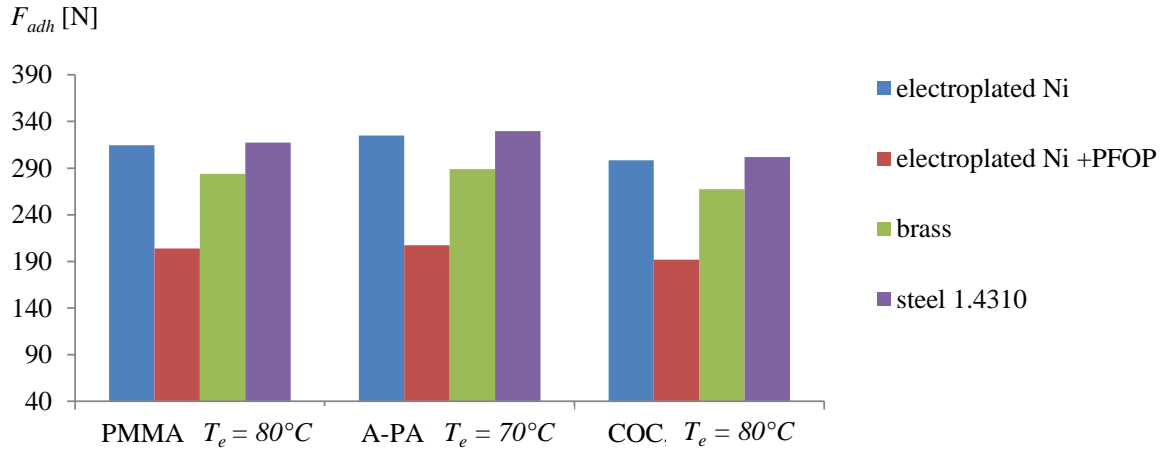


Fig. 7.7: Calculated adhesion forces F_{adh} for an insert with 5 billion nanopillars on an area of $15,2 \text{ cm}^2$.

These results are interesting in the context of replication of large-area nano-pillars, which was previously presented in Chapter 4.6.4. In these trials the ejection forces at the ejector plate were varied. No ejection was possible with an ejection force of 1000 N, but with 2000 N instead. Thus, the theoretical calculated value seems to be in the right range, particularly, when considering additional frictional forces in the second cavity, at the edges of the plates and especially in the conical support pin.

7.5 Explanations for demoulding issues

Demoulding issues can result from both, deformation and deflection, that originate from shrinkage effects (Fig. 7.8) and friction forces between the solidified polymer and the micro- and nanostructures featuring on the mould (Fig. 7.10).

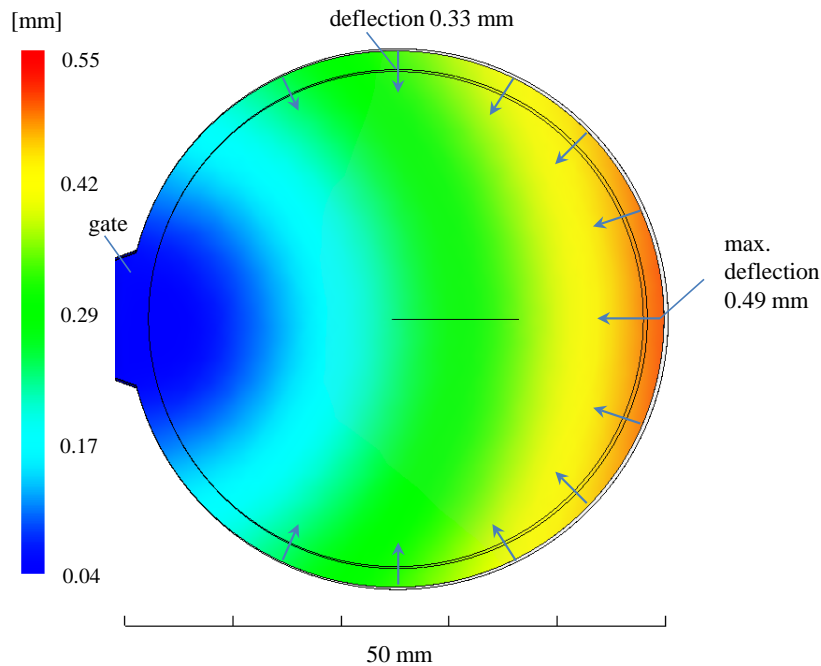


Fig. 7.8: Simulated deflection, caused by polymer shrinkage for isothermal injection moulding (IIM) with PMMA.

Consequently, the most deflected structures can be expected away from the gate. Such deflections can be minimized by injection compression moulding as already shown in the investigation of (Wu and Chen, 2006) who fabricated more accurate diffractive gratings with less warpage by IICM in comparison to IIM. Additionally to shrinkage effects, demoulding issues can arise during ejection, if the structures are deformed asymmetrically either during the initial opening of the tool or due to insufficient or unfavourably positioned ejector pins, illustrated in Fig. 7.9.

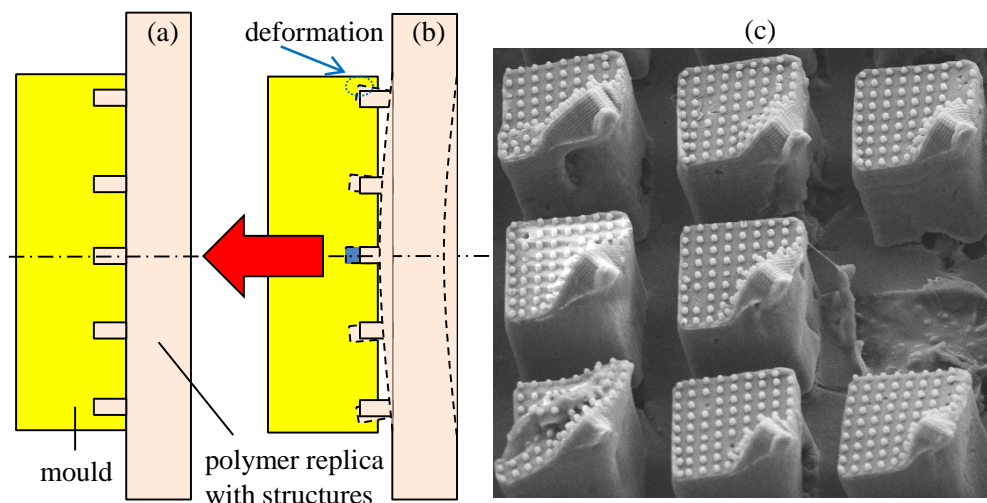


Fig. 7.9: Demoulding issues caused by deformation: Structured mould and polymer replica (a) before ejection and (b) during ejection showing asymmetrical deformation of the structures with the result of demoulding defects, exemplarily shown in (c) SEM picture of a PP replica (courtesy of Nis Korsgard, Technical University of Denmark (DTU)).

(Ito et al., 2009) determined the birefringence of a cross-section with 1 mm thickness and measured values almost four times higher at the edges compared to the centre caused by demoulding issues. Depending on the manufacturing method of the mould master, especially the side wall roughness can be very high which can lead to elastic or plastic deformation during demoulding because of high friction forces. On very smooth surfaces intermolecular forces, such as van-der-Waals, dipole-dipole or hydrogen bonds can also cause demoulding problems, which is illustrated schematically in Fig. 7.10.

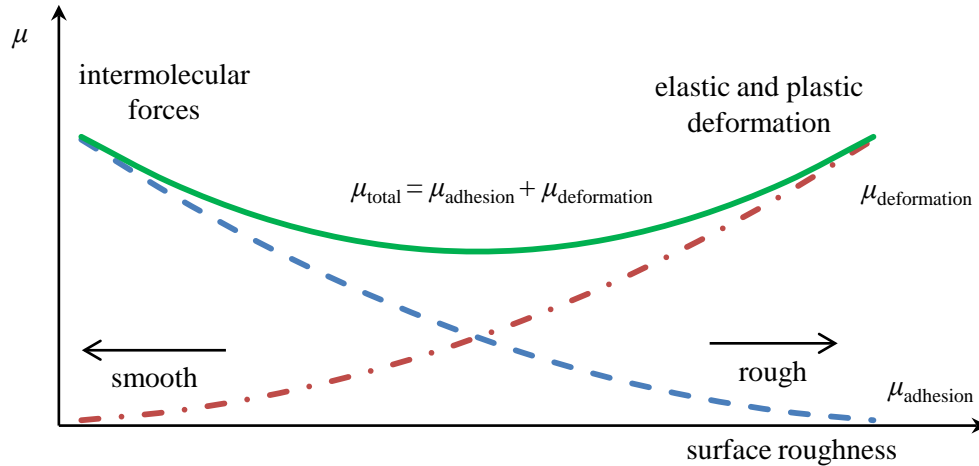


Fig. 7.10: Friction forces μ (green) as a result of adhesion $\mu_{adhesion}$ (blue) and deformation $\mu_{deformation}$ (red) depending on the surface roughness, showing a minimum at a specific moderate roughness where neither deformation nor intermolecular forces are dominant (Böhm, 2008).

7.6 Conclusions

Additionally to the filling of micro- and nanostructures also the demoulding of the structured replica imposes significant challenges. In this context the geometry of the structure, the adhesion and friction between the polymer and the mould surface play an important role. In addition to adhesion forces, which can be derived from the work of adhesion at the polymer/mould interface, deflections originating from shrinkage and friction can cause severe deformation of the replicated polymer structures but also of the master structures in the tool. Ejection forces can be reduced by applying draft angles to the structures and anti-adhesion coatings. However, draft angles may not be applicable due to geometric constraints given by the targeted application and the long-term stability of thin (some nm) anti-adhesion coating is still not sufficient for use in mass fabrication.

As already discussed in Chapter 4, demoulding issues like nano-pillar breakage or deformed ridges around micro-channels can be also minimized by application of an additional compression stroke, because this leads to substantially lower and more homogeneously distributed stresses in the part.

Brittle materials like silicon or glass with low fracture toughness are less suitable for injection compared to nickel or steel. Whereas the transfer of nanostructures from silicon to Ni by LIGA is already well established, the transfer into tool steel is not yet commercially feasible. Nonetheless, robust steel masters with integrated functional micro- and nanostructures can still be considered the Holy Grail, which is sought after by industry and academia likewise, as they would reduce premature structure failure.

8. POLYMER MOULDS FOR THE FAST FABRICATION OF NANOSTRUCTURED POLYMERIC SAMPLES FOR CELL GROWTH TESTS

For cell-adhesion tests, structured polymer plates are needed that are coated with titanium prior being tested. Currently, the sintered silicon/SiO₂ dots are transferred to PDMS and in a second step to epoxy. This process is very time-consuming, not very reproducible and results in many faulty samples. Injection moulding offers the possibility of being much more efficient and precise for the production of identical structured samples.

Consequently, the goal of the investigations presented in this Chapter was to develop a fast and cheap but reproducible process chain for the manufacturing such plates with nanopillars below 100 nm diameter for cell growth tests. For this purpose, sintered silicon nanostructures were transferred into polyphenylsulfone (PPSU) and polyetheretherketone (PEEK) by hot embossing and subsequently replicated in different polymers (Chapter 8.2). The quality of the replica was assessed by the replication fidelity and defect density and related to the time of the contact temperature above no-flow temperature of the polymer (Chapter 8.4 and Chapter 8.5). The contact temperature was calculated and additionally simulated with Comsol.

8.1 Introduction

For the replication of thousands of parts by injection moulding, a material which is highly resistant to thermal and mechanical fatigue is needed. Most of the time silicon is transferred into more ductile materials like nickel. But the electroplating process is not a quick process and rather expensive.

On the contrary, for the production of several hundred of samples, polymers like PPSU, PEEK, polyetherimide (PEI) or resist materials like SU8 or Ormostamp could be interesting as mould materials. Compared to electroplating this method offers fast and cost-efficient master structures directly replicated from silicon or other brittle and sensitive materials like glass. Additionally, this technology offers potential advantages for transferring patterns from metal moulds that are difficult to produce. For example, the laser-machining of micro-hemispheres with different heights that are standing out, is more challenging compared to microspheres ablated into the metal. Thus, with the transfer from metal to polymer, master structures can be produced fast and cost-efficient. In the study of (Kim et al., 1995) polyurethane (PU) and epoxy (EP) structures were produced by capillary filling of PDMS structures with pre-polymers. (Stormonth-Darling and Gadegaard, 2012) replicated hybrid inlays made of polyimide (PI) claiming sufficient stability for 2000 cycles replication. Another replication process with a polymer master was proposed by (Kim et al., 2013) who used a polyvinyl alcohol (PVA) film as a disposable master for injection moulding. In a first step a PVA-water solution was casted onto a silicon master. After evaporation, the residual PVA film with nanostructures was over-moulded with PC. Finally, the PVA was dissolved in water again. (Nagato, 2014) produced nanostructured moulds for UV-NIL from cycloolefin copolymer by isothermal compression moulding. (Jena et al., 2012) used epoxy and COC (Topas 6017) as mould material for the replication of several samples in a different COC grade with a lower T_g (Topas 8007).

Another advantage of polymer inserts is the lower heat transfer resulting in a much higher contact temperature, when the polymer melt initially contacts the mould and forms the structures. Therefore, the replication quality of such structures is comparable to results obtained from variothermal injection moulding. In the PhD thesis of (Stormonth-Darling, 2013) the cooling time of a hybrid Cirlex/SU-8 tooling was simulated showing a much slower cooling speed for the polymer cooling in comparison to the nickel reference. (Hobæk et al., 2015) tested a ceramic coating with a lower heat transfer than nickel to enhance the contact temperature at the mould-melt interface and showed improved replication of nanostructures compared to nickel.

8.2 Injection moulding and mould insert process chain

The process conditions, i.e. the melt and mould temperatures and the injection velocity used in this part of the thesis are summarized in Table 8-1.

Table 8-1: Set and measured injection moulding parameters.

Material	Cylinder temperature $T_{cyl.}$ [°C]	Injection speed v_{inj} [cm ³ s ⁻¹]	Set/measured mould temperature at ejection T_{mould} [°C]
A-PA	280	15	50 / 47
			60 / 57
PP	220	15	35 / 32
			45 / 42

A silicon wafer with sintered SiO₂ nano-particles with an average diameter of 72 nm, manufactured at the Eidgenössische Technische Hochschule (ETH, Zürich, Switzerland) by Rebecca Huber, was transferred by hot embossing (240°C, 4h) into 2 mm thick plaques of PPSU (Ultrason P3010) from BASF (Ludwigshafen, Germany) and PEEK (Victrex 450G) from Victrex (Lancashire, UK) respectively, and then used as inserts for injection moulding trials, schematically shown in Fig. 8.1.

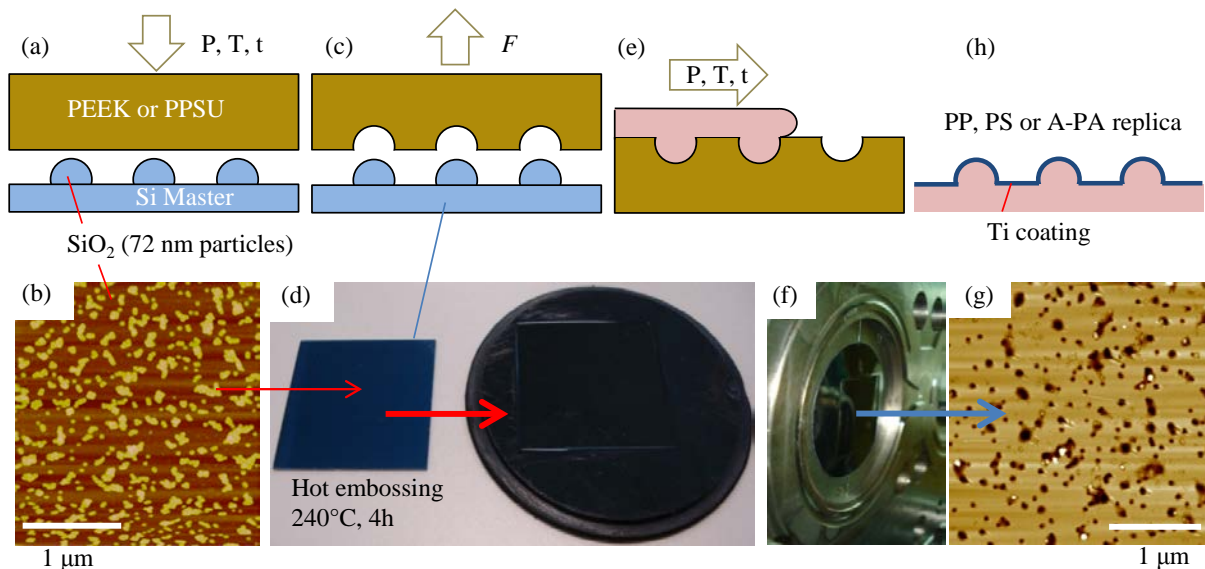


Fig. 8.1: Process chain for the fabrication of replica from a silicon master: (a) Hot embossing of sintered Si master into PEEK or PPSU; (b) AFM picture of Si master with SiO₂ nanoparticles (light brown); (c) demoulding; (d) picture of Si chip and hot embossed PPSU insert; (e) injection moulding with (f) clamped PPSU insert; (g) AFM picture of PPSU insert with nanoholes (black); (h) replicated nanostructured polymer samples with Ti coating for cell tests.

8.3 Thermal properties of mould materials

In Table 8-2 the most important thermal properties of some mould materials are compared, i.e. brass, tool steel, nickel and PPSU. The values heat capacity, heat conductivity and density were used for simulations and calculations of the contact temperatures.

Table 8-2: Properties of various mould materials used for injection moulding trials and for simulations in Moldflow and Comsol; data were taken from material data sheets and Moldflow data base. Significant differences are observed between polymer inserts like PPSU and metals like brass, tool steel or nickel.

Material	Glass transition temperature T_g [°C]	Elastic modulus E [Mpa]	Heat capacity c_p [J kg ⁻¹ K ⁻¹]	Heat conductivity k [W m ⁻¹ K ⁻¹]	Density ρ [kg m ⁻³]
Brass (CuZn39Pb3)		100000	385	123	8470
Tool steel P-20		205000	460	29	7800
Nickel		200000	455	91	8908
PPSU Ultrason P3000	220	2360	1500	0.2	1240

8.4 Contact temperatures at the polymer melt/mould interface

The mould temperature is essential for the replication quality of micro- and nanostructures and with a dynamic heating process the filling can be improved. However, because of economic reasons, the mould temperature is usually set to a constant temperature, as low as possible, to get short cycle times. In this context, the term *isothermal* only partly represents the reality because in contact with the hot polymer melt the temperature will increase to a contact temperature that is substantially higher than the mould temperature before injection. This can be seen in the following exemplary measurement of an isothermal injection moulding process:

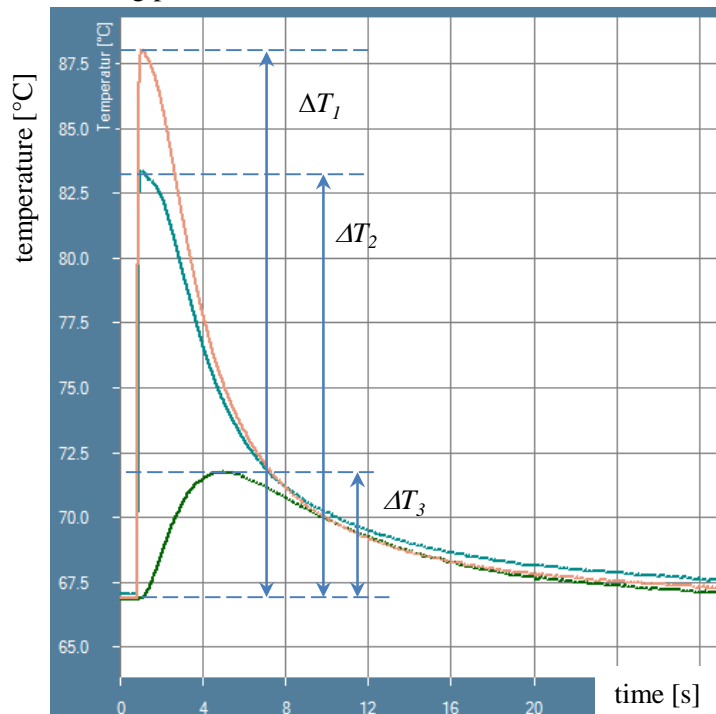


Fig. 8.2: Temperature increase ΔT because of hot polymer melt, measured at different sensor positions showing a maximum mould temperature increase of $\Delta T_1 = 20^\circ\text{C}$ very near the gate in direct contact with the hot polymer melt and a small temperature increase of $\Delta T_3 = 5^\circ\text{C}$, 1 mm behind a 2 mm thick metal mould insert.

The example of a standard IIM cycle shown in Fig. 8.2 reveals no difference between the temperatures at the three positions after 10 s. This is important for the demoulding to make sure that the temperature at the interface corresponds to the mould temperature behind the insert, close to the cooling channel. However, dependent on the mould insert material, the contact temperature at the initial moment of the filling can vary over a wide range, because of the differences in the thermal effusivity b , which is the ability of the material to exchange thermal energy with its surrounding. The thermal effusivity or heat penetration coefficient b can be defined according equation (8-1), (Baehr and Stephan, 2013).

$$b = \sqrt{k \cdot \rho \cdot c_p} \quad (8-1)$$

Metals, for example, have a very high thermal effusivity. For this reason, the heat is transported quickly from the polymer through the insert to the mould and the cooling or heating system. Consequently, the contact temperature at the interface of the polymer and the mould insert is rather low compared to a mould made out of an insulating material like glass or high temperature resistant polymers, such as PPSU, as can be seen in Fig. 8.3.

The contact temperature can be calculated with equation (8-2) according to (Baehr and Stephan, 2013), considering two semi-infinite one-dimensional bodies with the initial temperatures of the mould T_{mould} and the polymer melt T_p brought into perfect thermal contact at $t = 0$.

$$T_{contact} = \frac{T_{mould} \cdot b_{mould} + T_p \cdot b_p}{b_{mould} + b_p} \quad (8-2)$$

This simple equation can be used for a fast and simple approximation of the contact temperature in the very first milliseconds. In Fig. 8.3 the calculated contact temperatures of PP and PA are compared for various mould-insert materials.

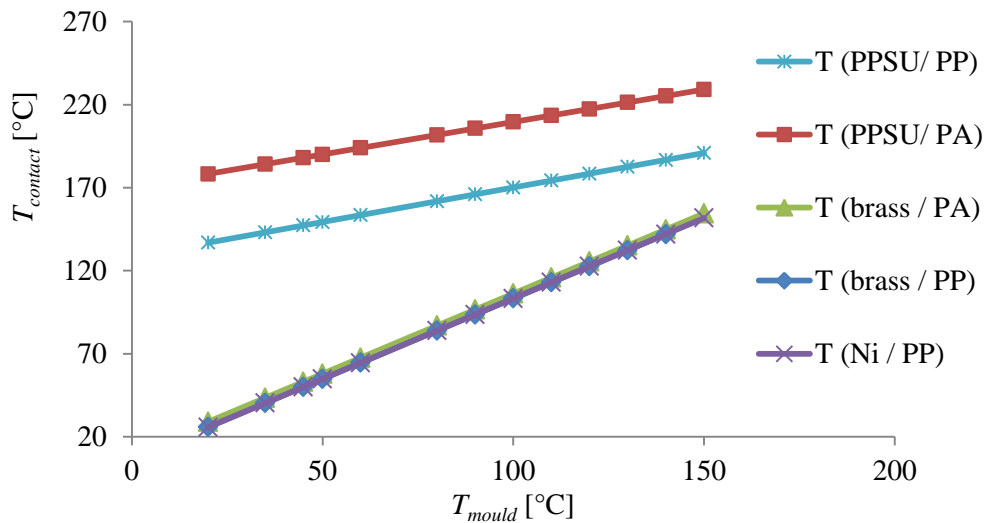


Fig. 8.3: Calculated contact temperatures $T_{contact}$ for two different polymers (T_p of PA = 280°C; T_p of PP = 220°C) and various mould-materials showing much higher contact temperatures for PPSU inserts compared to nickel or steel inserts because of the much lower thermal effusivity (material data as listed in Table 3-3 and Table 8-2).

It can also be seen that with increasing mould temperature, the differences in contact temperature between metal and polymer moulds become smaller. Additionally, the polymer melt processing temperature (T_p) has a much higher influence on the contact temperature when using polymer moulds compared to metal moulds, which is evident when comparing the pairings PPSU/PP (blue line with stars) and PPSU/PA (red line with squares).

8.5 Replication of sintered nano-dots for cell tests

The structured PPSU and PEEK masters were replicated with PP and A-PA by injection moulding. Because of its semi-crystalline morphology, PEEK was less suitable as a mould material compared to amorphous PPSU. As can be seen in Fig. 8.4 and Table 8-3, the best quality and roundest particles were achieved with a PPSU master, replicated with A-PA at a mould temperature of 47°C.

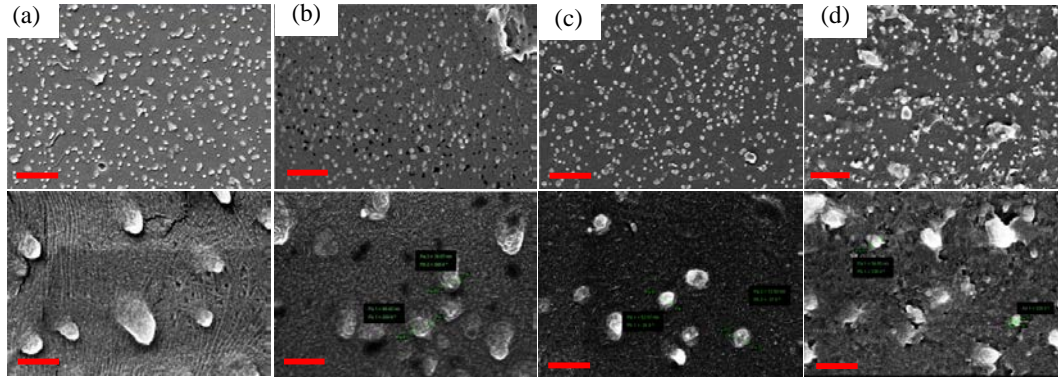


Fig. 8.4: SEM pictures of PP and A-PA replica prepared by injection moulding with a PPSU master, applying different mould temperatures T_{mould} : (a) PP, $T_{mould} = 32^\circ\text{C}$; (b) PP, $T_{mould} = 42^\circ\text{C}$; (c) A-PA, $T_{mould} = 47^\circ\text{C}$; (d) A-PA, $T_{mould} = 57^\circ\text{C}$; (red scale bars top = 1 μm ; bottom = 200 nm; courtesy of R. Huber, ETH).

As already explained in Chapter 8.4, polymer inserts have a lower thermal effusivity which is the reason why the resulting contact temperature of the polymer melt with the polymer insert is much higher compared to metal inserts. The calculation with the simple equation (8-2) gives only a rough value for the contact temperature. Therefore, $T_{contact}$ was additionally simulated with Comsol and the time until the no-flow temperature T_{no} is reached was extracted. T_{no} can vary over the range of 123-160°C for PP and 110-150°C for PA depending on the pressure, as already shown and discussed in previous Chapters. The extracted cooling curves for both materials as well as, adjusted mould temperatures are shown in Fig. 8.5.

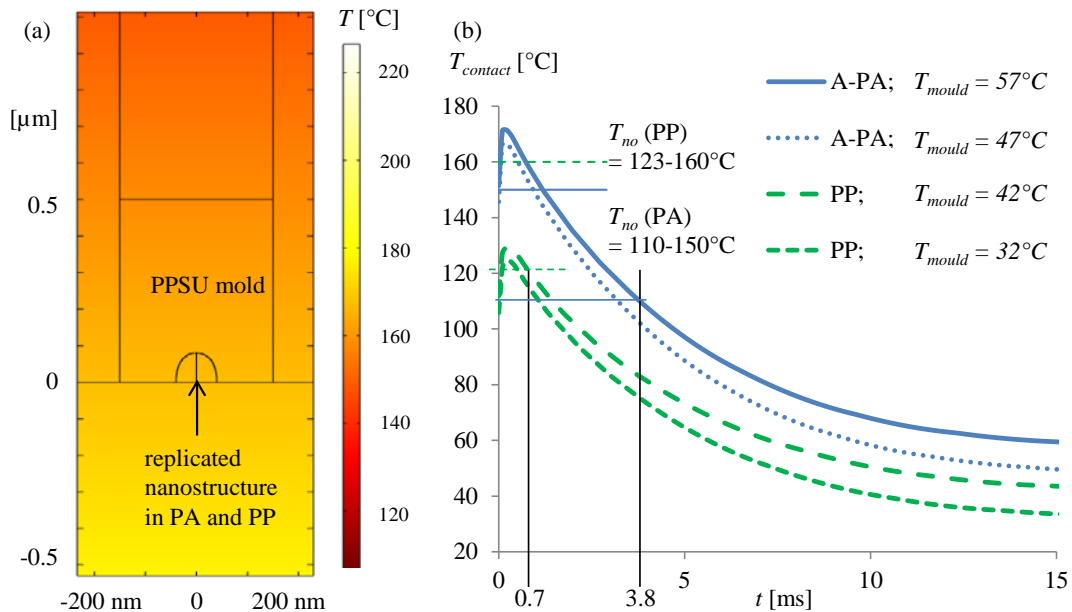


Fig. 8.5: (a) Comsol model used for the determination of the contact temperatures $T_{contact}$ and the time t until the polymer melt reaches T_{no} ; (b) Extracted cooling curves for A-PA and PP for different mould temperatures T_{mould} showing two exemplary cooling times (3.8 ms for PA and 0.7 ms for PP) when reaching the lower level of the no-flow temperature T_{no} .

In contrast to the amorphous A-PA, PP undergoes crystallization, associated with substantial shrinkage, which ultimately leads to pronounced sample deformation and possibly even warpage. High contact temperatures above T_g and close to T_{no} generally lead to more sticking.

Table 8-3: Replicated heights h and replication ratio RR resulting from different contact temperatures $T_{contact}$ at the interface of the PPSU mould and the polymer.

	PP		A-PA	
	$T_m = 161^\circ\text{C}$		$T_g = 110^\circ\text{C}$	
T_{mould} [$^\circ\text{C}$]	35 (32)	45 (42)	50 (47)	60 (57)
h [nm]	41 ± 11	37 ± 10	63 ± 18	83 ± 15
RR [%]	68	62	105	138
$T_{contact}$ [$^\circ\text{C}$] *	142	146	189	193
$T_{contact}$ [$^\circ\text{C}$] #	124	129	167	172
$t > T_{no}$ [ms]	0 - 0.4	0 - 0.7	0.9 - 3.2	1.1 - 3.8

*calculated with equation (8-2); #simulated with Comsol; T_{mould} in brackets = measured value

The incomplete replication of structure heights with PP most probably does not result from deformation and shrinkage, but rather is caused by the very short time of the polymer melt above T_{no} resulting in a premature solidification before the filling of the nanostructure is completed.

8.6 Conclusions

In this Chapter of the thesis, the knowledge on nanostructure replication was transferred to an exemplary application for life science research. Especially the importance of heat transfer and no-flow temperature was proven once again, both for metallic and polymeric moulds.

Moreover, it was shown that it is possible to reproducibly replicate more than 100 parts with PP and A-PA from a PPSU insert with nanostructures that were previously transferred from a silicon master by hot embossing. The transfer is simple, cheap, takes less than a day and could therefore find use in the product development phase for small series of specialized products or more generally for fast iterations. Not surprisingly, it turned out that the mould temperatures need to be adapted with regards to the increased contact temperatures at the polymer/mould interface. Finally, a good correlation between the replication ratio and the time of the polymer above the no-flow temperature was once again demonstrated.

9. SUMMARY, CONCLUSIONS AND OUTLOOK

9.1 Summary

The integration of functional micro- and nanostructures on polymeric surfaces offers a wide range of potential applications for different markets ranging from consumer goods to life sciences. Most important applications are microfluidic diagnostic devices, sensors and optical structures. The realisation of these applications in polymers requires fast and efficient mass production methods, which allow functional structures to be implemented into the product in a versatile and cost-effective manner. With increasing complexity of the functional topography, perfect replication becomes more difficult by standard injection moulding, especially with highly viscous polymers.

Thus, the goal of this work was to compare theoretical considerations and models with practical tests on the injection compression moulding machine, running four different variations of injection moulding with the same mould. Complementary to other studies on variothermal injection moulding, the specific progress of this work was to thoroughly investigate the differences in filling and demoulding behaviour when reducing the structure size from macro- and micro- to nano-scale. The filling and the heat transfer in micro- and nanostructures were simulated with two FEM programs, Autodesk Moldflow and Comsol Multiphysics. In the experimental part, pressures, temperatures and injection velocities were varied. Moreover, the spreading behaviour of different polymers on various mould material surfaces was taken into account. Overall, processes and polymers were evaluated in the context of replication accuracy (height and shape of the structures), homogeneity, defects, stresses and suitability for mass production (stability, demouldability, and filling pressure).

As a reference for macrostructures, it was shown that pillars and channels with widths of 500 μm can be easily filled with aspect ratios above one which turned out to be much more difficult for micro- and nanostructures. In order to find the consistent explanations, a detailed determination of polymer properties is crucial. Therefore, melt viscosities were measured online during injection moulding. Additionally, no-flow temperatures, contact angles of polymers on various mould materials and surface energies of the different polymers were determined. Based on these measurements, the spreading coefficient, the flow resistance and capillary effect in micro- and nanostructures were calculated and related to the replication quality.

Finally, the knowledge gained on the replication of nanostructures was transferred to an exemplary application for a life science research product. Especially the importance of heat transfer and no-flow temperature was once again proven, this time for the use of polymeric mould inserts.

The most relevant results and conclusions are summarized in the following.

9.2 Conclusions

Influence of injection moulding processes and parameters

The replication quality of micro- and nanostructures are significantly influenced by moulding parameters and moulding processes.

The best replication quality, when comparing four different processes was achieved by **variothermal injection compression moulding (VICM)**, because of best replication accuracy, lowest pressure, low and homogenous distribution of internal stresses in the polymer part and notably less demoulding issues. These results were proven with a broad range of structure design for micro- and nanostructures with different polymers.

From all processing parameters the **mould temperature** has the biggest influence on the replicated height, which was shown both experimentally and with simulations. Of course, this has been known for a long time. However, the relation between the mould and the no-flow temperature, which can differ significantly from the glass transition temperature, plays a key role for the replication behaviour. This was investigated in more detail and simulated for micro- and nanostructures with 3D models.

Comparing different publications, the influence of the **holding pressure** on the replication process has been discussed very contradictory. The results presented in this thesis clearly show that the effect of holding pressure strongly depends on both structure size and mould temperatures in relation to the no-flow temperature that influence the cooling speed and, thus, the duration of pressure transfer prior to freezing. The biggest influence of the holding pressure on replication ratio was found for variothermal processes when replicating nanostructures, in stark contrast to the isothermal replication of macrostructures.

Influence of structure geometry on the replication fidelity

One of the main aims of this thesis was to answer the question, if nanostructures are more difficult to fill than micro- and macrostructures.

It was shown that **macrostructures** ($> 200 \mu\text{m}$) can easily be replicated with aspect ratios above one, applying standard moulding conditions. The reason is that despite the formation of a frozen layer, there is still enough fluid-centre for the polymer to fill the structures completely. In **microstructures** ($200 \mu\text{m} \rightarrow 1 \mu\text{m}$) the frozen-layer formation becomes dominant as the fluid centre is reduced drastically. Because of a much faster heat transfer, **nanostructures** ($1 \mu\text{m} \rightarrow 1 \text{nm}$) are even more difficult to be filled.

For industrial applications, designers of functional structures need to know what happens to the replication ratio if the structure size is reduced. In this thesis a **parabolic dependence of the replicated height on the structure width** was confirmed at least for the microscale. This is in good agreement with the influence of dimensionless Graetz and Fourier numbers as well as the empirical freezing time. In addition, the width/pitch ratio has an influence on the filling because of varying local heat losses, where the melt is in direct contact with the mould.

On the **nanoscale**, the parabolic dependence between replicated height and structure width could not be confirmed, the correlation seems rather linear. Wetting effects could interfere on this scale with flow resistance and frozen-layer formation, which warrants further consideration.

Influence of spreading, wetting and capillary forces

The influence of wetting characteristics on the replication behaviour has been investigated far less than the impact of processing parameters.

As a result of this thesis, the **dewetting potential** Ω_s (integrated spreading coefficient area) of a polymer is proposed as a simple rationale for the estimation of the replicability of micro- and nanostructures. Based on Ω_s the influence on the replication accuracy could be assessed, i.e. when changing polymers or applying an anti-adhesion coating. The lower the dewetting potential of a polymer, the better the replication accuracy can be expected.

Capillary forces, driven by good wetting, seem to have a positive effect on the filling of nano-sized cavities and, thus, should not be neglected when investigating the replication behaviour of nanostructures. Capillary forces can even dominate versus flow resistance for feature sizes below 100 nm, at least for low aspect ratio structures ($AR < 0.1$).

Filling simulations

Especially 3D simulations of nanostructures have been rarely carried out. However, with such models the development of polymeric products with functional surface structures can be accelerated, as it would be possible to provide quick answers to which process, material, and parameters are best suited to achieve a perfect replication of structures of different sizes and geometries, without the necessity of carrying out real injection moulding trials.

In this thesis, the modelled filling of micro- and nanostructures showed good correlation to experiments with two amorphous polymers under different processing conditions, i.e. mould temperatures, holding pressure and injection velocities. In order to reduce calculation time and memory space, the models can be scaled down, but one has to take care of transferring the correct boundary conditions, i.e. flow front velocity. While full simulations can still be done with microstructured parts, the **downscaling** of the models for nanostructured parts is inevitable.

There are two main prerequisites to achieve a good correlation between simulation and experiments:

The **heat transfer coefficient** h_{ic} needs to be substantially increased. Ideally the h_{ic} should be represented by a fast decreasing profile, starting at a high value (e.g. $30000 \text{ W m}^{-2} \text{ K}^{-1}$) for the first milliseconds, after which the h_{ic} should decrease to a lower value ($5000 \text{ W m}^{-2} \text{ K}^{-1}$). The reason for this is the lower heat transfer in the bulk compared to the interface. The role of the heat transfer coefficient was confirmed in a separate simulation with the FEM software Comsol.

The **transition temperature** T_{trans} needs to be adjusted to the measured no-flow temperature, although the experimentally determined values cannot be used directly in Moldflow simulation. T_{trans} influences the replication especially in the packing phase if the mould temperature is above that transition temperature, which is predominantly the case in variothermal processes.

Polymer moulds for prototyping

The developed knowledge of filling and demoulding, focussing on heat transfer and no-flow temperature was applied to the reproducible production of nanostructured **samples for cell growth tests** and a fast prototyping method based on pattern transfer onto a high performance polymer was established.

More than 100 parts were replicated with PP and A-PA from a **PPSU insert** with nanostructures that were previously transferred from a silicon master by hot embossing. A good correlation between the replication ratio and the time of the polymer above the no-flow temperature was demonstrated.

9.3 Outlook

Various aspects of the replication of micro- and nanostructures were investigated in this thesis. Still there are several interesting topics that can be addressed in more detail.

Additionally to the filling of micro- and nanostructures also the **demoulding** of structured replica poses large challenges. In addition to adhesion forces, which can be derived from the **work of adhesion** at the polymer/mould interface, shrinkage and deflection of the part can cause severe deformation of the polymer structures, but also of the master structures, which can jeopardize the replication quality or even harm the mould. Long-term stable **anti-adhesion coatings** could reduce demoulding issues, but the interface of such coatings and the mould needs to be improved significantly. Whereas the structure transfer from silicon to nickel by LIGA is already well established, the **transfer of nanostructures into tool steel** is not yet commercially available. However, robust steel masters would reduce premature structure failure. Fortunately a couple of institutes and companies have already been working on that topic; e.g. Morphotonix (Ecublens, Switzerland).

In the 3D Moldflow simulations **only amorphous polymers** were simulated. It is questionable if the transition temperatures and heat transfer coefficients can be adapted in the same way for **semi-crystalline materials** or even additional material parameters come into play, e.g. because of the strong influence of the cooling rate on the crystallinity and thus, on the no-flow temperature.

The no-flow temperature T_{no} was implemented in various investigations in this thesis, e.g. for the calculation of the frozen-layer thickness, as boundary condition in 3D simulations or for the integration of the spreading coefficient to yield the dewetting potential Ω_s . However, the **correct determination of T_{no}** is rather difficult. In this thesis only rough measurements were carried out and compared with literature and simulation data base. Further measurements depending on pressure would be necessary to represent the flow behaviour of polymers at low flow front velocities and low temperatures.

The effect of packing on the filling of the structures was shown in dependence of the interface temperature. In this context the **compressibility** of the polymer in the range of the no-flow temperature may play a role, which was not further investigated in this thesis. This could be done by correlating the PvT-behaviour of the polymer with the replication accuracy, when applying mould temperatures close to the transition temperature from melt to solid.

With the FEM software Comsol different **wall boundaries** were compared. Whereas some small differences in the advancement of the melt at the side wall of nanostructures were observed between "no slip" and "wetted wall" conditions, no significant influence of the actual **contact angles** on the replication quality could be identified. However, it should be noted that only contact angles at the side wall were varied, while an implementation of the **surface tension** of the polymer was neglected, because of convergence issues. As the experiments clearly showed an influence of the wetting, it would be of certain interest to simulate this correlation ideally in 3D which was not yet possible.

Investigations related to **air inclusions** were not addressed properly. On the other hand various nanostructures were replicated to 100% without any indication that air reduces the replication quality. Nevertheless, a moulding process with **vacuum degassing** could probably facilitate the replication process with high injection velocities, especially if polymers are used that tend to release volatile components.

10. LIST OF SYMBOLS AND ABBREVIATIONS

a_0, a_1, \dots	Fitting parameters	-
a_{eff}	Thermal diffusivity	$\text{m}^2 \text{s}^{-1}$
A	Area	m^2
$A_1; A_2;$ $A_3; D_1;$ $D_2; D_3$	Data fitted viscosity coefficients	-
AR	Aspect ratio	-
b	Thermal effusivity or heat penetration coefficient	$\text{W s}^{1/2} \text{m}^{-2} \text{K}^{-1}$
b_R	Rabinowitsch correction	-
B	Pressure sensitivity used in 2-Domain Tait model	-
Br	Brinkman number	-
C	Universal constant equal to 0.894 used in 2-Domain Tait model	-
C_∞	Molecule enlargement factor	-
Ca	Capillary number	-
c_p	Specific heat capacity	$\text{J kg}^{-1} \text{K}^{-1}$
d	Depth of the rectangular structure	μm or nm
e_B	Bagley correction factor	-
e_{rec}	Geometric factor for rectangular channels	-
e_0	Geometric factor for tubular structures	-
E	Elastic modulus	MPa
F_{comp}	Compression force	N
F_{adh}	Adhesion force	N or nN
Fo	Fourier number	-
f_1, f_2, f_{\dots}	Data fitted degree of replication coefficients	-
g	Gravitational acceleration (negative for pendant drop)	kg s^{-2}
G	Surface free energy	mJ m^{-2}
G_c	Critical strain energy release rate	J m^{-2}
h; h_r ; h_m	Filling height or height of the replicated structure; height of the master	μm or nm
h_{tc}	Heat transfer coefficient or thermal transmittance	$\text{W m}^{-2} \text{K}^{-1}$
I	Identity matrix	-
k	Coefficient of thermal conductivity	$\text{W m}^{-1} \text{K}^{-1}$,
K	Factor for rectangular channels considering the ratio between w_1 and w_2	-
K_{Ic}	Fracture toughness	$\text{MPa m}^{1/2}$
q	Heat flow	W or J s^{-1}
m	Consistency index in the power law	-
MFR	Melt flow rate	mg min^{-1}
n	Power law index in the high shear rate regime, determined by curve fitting	-
N	Degree of polymerisation	-
Nu	Nusselt number	-
p	Pitch of the structure	μm or nm
P	Pressure	MPa or bar
Δp_{apex}	Pressure difference at apex	Pa or bar
Δp_P	Pressure difference at Point P (x,z)	Pa or bar
$P_{\text{L,H,C}}$	Resulting internal pressure from injection, holding or compression phase	MPa or bar
P_C	Capillary pressure depending on the wetting properties of the mould and the polymer	MPa or bar
P_{hold}	Holding pressure	MPa or bar
P_{FR}	Flow resistance of the polymer melt	MPa or bar
P_{so}	Switch over pressure	MPa or bar
P_{int}	Internal pressure	MPa or bar
q	Heat flux	J s^{-1} or W
Q	Heat sources other than viscous heating	J
$r_1; r_2$	Radii of curvature of a sectional area of the drop surface	mm
R	Radius of the capillary of pillar	nm
R_a	Surface roughness	nm
Re	Reynolds number	-

LIST OF SYMBOLS AND ABBREVIATIONS

S	Surface entropy	J K ⁻¹
S _c	Spreading coefficient	-
s	Stress tensor	N m ⁻²
s _{comp}	Compression stroke	mm
t _f	Freezing time	s
T _{contact}	Contact temperature	°C
T _{cyl}	Cylinder temperature	°C
T _e	Ejection temperature	°C
T _g	Glass transition temperature	°C
T _{no}	No-flow temperature	°C
T _p	Polymer processing melt temperature when entering the cavity	°C
T _m	Melt temperature	°C
T _{mould}	Mould temperature	°C
u	Velocity vector or flow velocity	m s ⁻¹
U	Surface internal energy	mN m ⁻¹
v	Velocity	m s ⁻¹
\dot{V} ; v _{inj}	Volumetric flow rate or injection speed	m ³ s ⁻¹
v _{comp}	Compression speed	%
V ₀	Specific volume at gauge zero	1 cm ⁻³
V _t	Specific volume decrease in 2-domain Tait model	1 cm ⁻³
w _{1,2} ; w _m	Width of rectangular channel; width of the master	mm, μm or nm
W _a	Work of adhesion	mN m ⁻¹
z	Part wall thickness	mm
Greek letters		
α	Thermal diffusivity	m ² s ⁻¹
α _T	Shift factor (C-WLF)	-
β	Thermal expansion coefficient	K ⁻¹
γ̇	Shear rate	1 s ⁻¹
γ̇ _{app}	Apparent shear rate determined with capillary viscometer	1 s ⁻¹
δ	Frozen layer thickness	μm
ε	Elongation at break	%
η	Polymer melt viscosity	Pa s
η ₀	Zero shear viscosity or the 'Newtonian limit' in which the viscosity approaches a constant at very low shear rates	Pa s
θ	Contact angle	° or rad
δ̇(Γ,x)	Dirac delta function	-
κ	Parameter controlling interface thickness	m
λ	time constant	-
μ	Friction	-
Π	Surface tension vector	mJ m ⁻²
ρ; ρ _m	Density an melt density	kg m ⁻³
Δρ _p	Difference in density between the drop liquid and its surroundings	kg m ⁻³
σ _L	Surface energy of the liquid	mJ m ⁻² or mN m ⁻¹ or g s ⁻²
σ _p	Surface tension of polymer melt	
σ _s	Surface energy of the solid	
σ _{LS}	Interfacial energy between liquid and solid ²	
τ	shear stress	Pa
τ*	Critical stress level at the transition to shear thinning, determined by curve fitting	Pa
φ	Reinitialization parameter. Stabilizes the level set function depending on the magnitude of u	m/s
φ	Air or polymer volume fraction used in Comsol simulations	%
χ	Compressibility coefficient	-
ψ	Strain tensor	%
Ω _s	Dewetting potential	N K m ⁻¹

11. BIBLIOGRAPHY

- Anastasiadis S H & Hatzikiriakos S G 1998 The work of adhesion of polymer/wall interfaces and its association with the onset of wall slip *Journal of Rheology* **42** 795-812
- Andersen N K & Taboryski R 2015 Multi-height structures in injection molded polymer *Microelectronic Engineering* **141** 211-4
- Attia U, Marson S & Alcock J 2009 Micro-injection moulding of polymer microfluidic devices *Microfluidics and Nanofluidics* **7** 1-28
- Autodesk 2014 Moldflow Insight
- Bader C & Zeller S 2010 Die Entdeckung der Schmelzfront *Kunststoffe* **6** 1-6
- Baehr H D & Stephan K 2013 Wärme- und Stoffübertragung *Springer*
- Baum M J, Heepe L & Gorb S N 2014 Friction behavior of a microstructured polymer surface inspired by snake skin *Beilstein Journal of Nanotechnology* **5** 83-97
- Bechert D W, Bruse M & Hage W 2000 Experiments with three-dimensional riblets as an idealized model of shark skin *Experiments in Fluids* **28** 403-12
- Bekesi J, Kaakkunen J J J, Michaeli W, Klaiber F, Schoengart M, Ihlemann J & Simon P 2010 Fast fabrication of super-hydrophobic surfaces on polypropylene by replication of short-pulse laser structured molds *Applied Physics A* **99** 691-5
- Bendada A, Derdouri A, Lamontagne M & Simard Y 2004 Analysis of thermal contact resistance between polymer and mold in injection molding *Applied Thermal Engineering* **24** 2029-40
- Berger G R, Gruber D P, Friesenbichler W, Teichert C & Burgsteiner M 2011 Replication of Stochastic and Geometric Micro Structures – Aspects of Visual Appearance *International Polymer Processing* **26** 313-22
- Bird R B, Armstrong R C & O. Hassager 1987 Dynamics of Polymeric Liquids, Vol. 1: Fluid Mechanics New York Wiley
- Bixler G D, Theiss A, Bhushan B & Lee S C 2014 Anti-fouling properties of microstructured surfaces bio-inspired by rice leaves and butterfly wings *J Colloid Interface Sci* **419** 114-33
- Böckh Von P 2011 Wärmeübertragung Karlsruhe *Springer*
- Böhm P 2008 Antihafbeschichtungen - ein neuer Weg zur wirtschaftlichen Entformung? MST Agion
- Bruus H 2008 Theoretical Microfluidics *OUP Oxford*
- Burr A, Müller A & Martin H 2003 Die Motte als Vorbild *Plastverarbeiter* **54** Nr.9 FH Heilbronn
- Cao W, Kong L, Li Q, Ying J & Shen C 2011 Model and simulation for melt flow in micro-injection molding based on the PTT model *Modelling and Simulation in Materials Science and Engineering* **19** 085003
- Cavalcanti-Adam E A, Aydin D, Hirschfeld-Warneken V C & Spatz J P 2008 Cell adhesion and response to synthetic nanopatterned environments by steering receptor clustering and spatial location *HFSP J* **2** 276-85
- Cech J & Taboryski R 2012 Stability of FDTS monolayer coating on aluminum injection molding tools *Applied Surface Science* **259** 538-41
- Chen B-C, Cheng Y-S, Gau C & Lee Y-C 2014 Enhanced performance of polymer solar cells with imprinted nanostructures on the active layer *Thin Solid Films* **564** 384-9
- Chen S C, Chen Y C & Peng H S 2000 Simulation of injection-compression-molding process. II. Influence of process characteristics on part shrinkage *Journal of Applied Polymer Science* **75** 1640-54
- Chien R D J, W.R.; Chen, S.C. 2005 Study on rheological behavior of polymer melt flowing through micro-channels considering the wall-slip effect *J. Micromech. Microeng.* **15** 1389-96

- Chin C D, Laksanasopin T, Cheung Y K, Steinmiller D, Linder V, Parsa H, Wang J, Moore H, Rouse R, Umvilighozo G, Karita E, Mwambarangwe L, Braunstein S L, Van De Wijgert J, Sahabo R, Justman J E, El-Sadr W & Sia S K 2011 Microfluidics-based diagnostics of infectious diseases in the developing world *Nature Medicine* **17** 1015-U138
- Choi S-J & Kim S 2011 Multi-scale filling simulation of micro-injection molding process *Journal of Mechanical Science and Technology* **25** 117-24
- Christiansen A B, Clausen J S, Mortensen N A & Kristensen A 2014 Injection moulding antireflective nanostructures *Microelectronic Engineering* **121** 47-50
- Comsol 2012 Multiphysics user's guide **4.3a**
- Coulembier O, Knoll A, Pires D, Gotsmann B, Duerig U, Frommer J, Miller R D, Dubois P & Hedrick J L 2009 Probe-Based Nanolithography: Self-Amplified Depolymerization Media for Dry Lithography *Macromolecules* **43** 572-4
- Cui Z-X, Si J-H, Liu C-T & Shen C-Y 2014 Flowing simulation of injection molded parts with micro-channel *Appl. Math. Mech. -Engl. Ed.* **35** 269-76
- Curtis A S G, Gadegaard N, Dalby M J, Riehle M O, Wilkinson C D W & Aitchison G 2004 Cells react to nanoscale order and symmetry in their surroundings *NanoBioscience, IEEE Transactions* **3** 61-5
- David J B, Dermot S, Michael D G & Cormac J B 2012 Bulk Metallic Glass Multiscale Tooling for Molding of Polymers with Micro to Nano Features: A Review *Metallurgical and Materials Transactions A* **44** 2021-30
- Dawson A, Rides M, Allen C R G & Urquhart J M 2008 Polymer-mould interface heat transfer coefficient measurements for polymer processing *Polymer Testing* **27** 555-65
- Delaunay D, Le Bot P, Fulchiron R, Luye J F & Regnier G 2000 Nature of contact between polymer and mold in injection molding. Part I: Influence of a non-perfect thermal contact *Polymer Engineering & Science* **40** 1682-91
- Dietz W, White J L & Clark E S 1978 Orientation development and relaxation in injection-molding of amorphous polymers *Polymer Engineering and Science* **18** 273-81
- Drabiniok E & Neyer A 2014 Bionic micro porous evaporation foil for photovoltaic cell cooling *Microelectronic Engineering* **119** 65-9
- Eliezer I & Hayman H J G 1957 Mean square length and mean square radius of gyration of 1,4'-polysaccharides and of polybutadienes *Journal of Polymer Science* **23** 387-402
- Eringen C A & Okada K 1995 A lubrication theory for fluids with microstructure *International Journal of Engineering Science* **33** 2297-308
- Feng J, Huang M & Qian X 2009 Fabrication of Polyethylene Superhydrophobic Surfaces by Stretching-Controlled Micromolding *Macromolecular Materials and Engineering* **294** 295-300
- Feng J, Lin F & Zhong M 2010 Stretching-Controlled Micromolding Process with Etched Metal Surfaces as Templates Towards Mass-Producing Superhydrophobic Polymer Films *Macromolecular Materials and Engineering* **295** 859-64
- Fischer J 2012 Handbook of Molded Part Shrinkage and Warpage *Elsevier Science*
- Fleger M & Neyer A 2006 PDMS microfluidic chip with integrated waveguides for optical detection *Microelectronic Engineering* **83** 1291-3
- Fowkes F M 1964 Attractive Forces at Interfaces *Industrial and Engineering Chemistry* **56** 40-52
- Franco D, Klingauf M, Bednarzik M, Cecchini M, Kurtcuoglu V, Gobrecht J, Poulikakos D & Ferrari A 2011 Control of initial endothelial spreading by topographic activation of focal adhesion kinase *Soft Matter* **7** 7313-24
- Gadegaard N, Mosler S & Larsen N B 2003 Biomimetic Polymer Nanostructures by Injection Molding *Macromolecular Materials and Engineering* **288** 76-83
- Garcia R, Knoll A W & Riedo E 2014 Advanced scanning probe lithography *Nat Nano* **9** 577-87

- Giboz J, Copponnex T & Mélé P 2007 Microinjection molding of thermoplastic polymers: morphological comparison with conventional injection molding *Journal of Micromechanics and Microengineering* **19** 025023
- Gorb S N, Sinha M, Peressadko A, Daltorio K A & Quinn R D 2007 Insects did it first: a micropatterned adhesive tape for robotic applications *Bioinspiration & Biomimetics* **2** S117-S25
- Graß B, Neyer A, Jöhnck M, Siepe D, Eisenbeiß F, Weber G & Hergenröder R 2001 A new PMMA-microchip device for isotachopheresis with integrated conductivity detector *Sensors and Actuators B: Chemical* **72** 249-58
- Griffiths C A, Dimov S S, Scholz S & Tosello G 2011 Cavity Air Flow Behavior During Filling in Microinjection Molding *Journal of Manufacturing Science and Engineering-Transactions of the Asme* **133**
- Guan W-S, Huang H-X & Wu Z 2012 Manipulation and online monitoring of micro-replication quality during injection-compression molding *Journal of Micromechanics and Microengineering* **22** 115003
- Gujrati P D & Leonov A I 2010 *Modeling and Simulation in Polymers* Wiley
- Han X & Yokoi H 2006 Visualization analysis of the filling behavior of melt into microscale V-grooves during the filling stage of injection molding *Polymer Engineering and Science* **46** 1590-7
- Han X, Yokoi H & Takahashi T 2006 Effects of cavity conditions on transcription molding of microscale prism patterns using ultra-high-speed injection molding *International Polymer Processing* **21** 473-9
- Hanemann T, Pflöging W, Haußelt J & Zum K H 2002 Laser micromachining and light induced reaction injection molding as suitable process sequence for the rapid fabrication of microcomponents *Microsystem Technologies* **7** 209-14
- Hansen H N, Hocken R J & Tosello G 2011 Replication of micro and nano surface geometries *CIRP Annals - Manufacturing Technology* **60** 695-714
- Hattori S, Nagato K, Hamaguchi T & Nakao M 2010 Rapid injection molding of high-aspect-ratio nanostructures *Microelectronic Engineering* **87** 1546-9
- Heckele M & Schomburg M W 2004 Review on micro moulding of thermoplastic polymers *J. Micromech. Microeng.* **14** R1-R14
- Hobæk T C, Matschuk M, Kafka J, Pranov H J & Larsen N B 2015 Hydrogen silsesquioxane mold coatings for improved replication of nanopatterns by injection molding *Journal of Micromechanics and Microengineering* **25** 035018
- Holzer C, Gobrecht J, Schiff H & Solak H 2010 Replication of Micro- and Nanostructures on Polymer Surfaces *Macromolecular Symposia* **296** 316-23
- Hong S, Min I, Yoon K & Kang J 2014 Effects of adding injection-compression to rapid heat cycle molding on the structure of a light guide plate *Journal of Micromechanics and Microengineering* **24** 015009 (15pp)
- Huang M-S & Chung C-F 2011 Injection Molding and Injection Compression Molding of Thin-Walled Light-Guided Plates with V-Grooved Microfeatures *Journal of Applied Polymer Science* **121** 1151-9
- Huovinen E, Takkunen L, Suvanto M & Pakkanen T A 2014 Fabrication and quantitative roughness analysis of hierarchical multiscale polymer surface structures *Journal of Micromechanics and Microengineering* **24** 055017
- Ito H, Satoh I, Saito T & Yakemoto K 2007 Development of a Novel Transcription Molding Process to Fabricate Sophisticated Polymer Products with Precise Microstructure and High Transparency Applicable to Display Devices and Bio-chips *International Polymer Processing* **22** 155-65
- Ito H, Suzuki H, Kazama K & Kikutani T 2009 Polymer structure and properties in micro- and nanomolding process *Current Applied Physics* **9** e19-e24
- Iturri J, Xue L, Kappl M, García-Fernández L, Barnes W J P, Butt H-J & Del Campo A 2015 Torrent Frog-Inspired Adhesives: Attachment to Flooded Surfaces *Advanced Functional Materials* **25** 1499-505

- Jena R K, Yue C Y, Lam Y C, Tang P S & Gupta A 2012 Comparison of different molds (epoxy, polymer and silicon) for microfabrication by hot embossing technique *Sensors and Actuators B: Chemical* **163** 233-41
- Jeong H E, Lee S H, Kim P & Suh K Y 2006 Stretched Polymer Nanohairs by Nanodrawing *Nano Letters* **6** 1508-13
- Johnson K L, Kendall K & Roberts A D 1971 Surface Energy and the Contact of Elastic Solids *Proceedings of the Royal Society of London. Series A, Mathematical and Physical Sciences* **324** 301-13
- Jung W-C, Heo Y-M, Yoon G-S, Shin K-H, Chang S-H, Kim G-H & Cho M-W 2007 Micro Machining of Injection Mold Inserts for Fluidic Channel of Polymeric Biochips *Sensors* **7** 1643-54
- Kalima V, Pietarinen J, Siitonen S, Immonen J, Suvanto M, Kuittinen M, Mönkkönen K & Pakkanen T T 2007 Transparent thermoplastics: Replication of diffractive optical elements using micro-injection molding *Optical Materials* **30** 285-91
- Kennedy P & Zheng R 2013 Flow Analysis of Injection Molds *Carl Hanser Verlag GmbH & Co. KG*
- Kim E, Xia Y & Whitesides G M 1995 Polymer microstructures formed by moulding in capillaries *Nature* **376** 581-4
- Kim N H & Isayev A I 2013 Birefringence in Injection-Compression Molding of Amorphous Polymers: Simulation and Experiment *Polymer engineering and science* **53** 1786-808
- Kim S-W & Turng L-S 2006 Three-dimensional numerical simulation of injection molding filling of optical lens and multiscale geometry using finite element method *Polymer Engineering & Science* **46** 1263-74
- Kim S H, Sul I H, Jeong J-H, Song Y S & Youn J R 2013 Robust fabrication and evaluation of nanopattern insert molded parts *European Polymer Journal* **49** 1437-45
- Kinoshita S, Yoshioka S & Miyazaki J 2008 Physics of structural colors *Reports on Progress in Physics* **71** 076401
- Kirchner R, Guzenko V A, Rohn M, Sonntag E, Mühlberger M, Bergmair I & Schift H 2015 Bio-inspired 3D funnel structures made by grayscale electron-beam patterning and selective topography equilibration *Microelectronic Engineering* **141** 107-11
- Klammt S, Neyer A & Müller H 2012 Redirection of sunlight by microstructured components - Simulation, fabrication and experimental results *Solar Energy* **86** 1660-6
- Kosuke K, Akihiro M & Hiroyuki S 2010 Resin Elongation Phenomenon of Polystyrene Nanopillars in Nanoimprint Lithography *Japanese Journal of Applied Physics* **49** 106505
- Kuhn S, Burr A, Kübler M, Deckert M & Bleesen C 2010 Study on the replication quality of micro-structures in the injection molding process with dynamical tool tempering systems *Microsystem Technologies* **16** 1787-801
- Kumar G, Tang H X & Schroers J 2009 Nanomoulding with amorphous metals *Nature* **457** 868-72
- Kwok D Y, Cheung L K, Park C B & Neumann A W 1998 Study on the surface tensions of polymer melts using axisymmetric drop shape analysis *Polymer Engineering & Science* **38** 757-64
- Lee L H 1991 Fundamentals of Adhesion New York Springer
- Lee Y B, Kwon T H & Yoon K 2002 Numerical prediction of residual stresses and birefringence in injection/compression molded center-gated disk. Part II: Effects of processing conditions *Polymer Engineering & Science* **42** 2273-92
- Lin H-Y, Chang C-H & Young W-B 2010 Experimental and analytical study on filling of nano structures in micro injection molding *International Communications in Heat and Mass Transfer* **37** 1477-86
- Liu F, Dong B Q, Liu X H, Zheng Y M & Zi J 2009 Structural color change in longhorn beetles *Tmesisternus isabellae* *Opt Express* **17** 16183-91
- Lovhagen O, Johansen I R, Bakke K a H, Fismen B G & Nicolas S 2004 Dedicated spectrometers based on diffractive optics: design, modelling and evaluation *Journal of Modern Optics* **51** 2203-22

- Lucchetta G & Fiorotto M 2013 Influence of Rapid Mould Temperature Variation on the Appearance of Injection-Moulded Parts *Journal of Mechanical Engineering* **59** 683-8
- Lucchetta G, Sorgato M, Carmignato S & Savio E 2014 Investigating the technological limits of micro-injection molding in replicating high aspect ratio micro-structured surfaces *CIRP Annals - Manufacturing Technology* **63** 521-4
- Magin C M, Cooper S P & Brennan A B 2010 Non-toxic antifouling strategies *Materials Today* **13** 36-44
- Mannella G A, La Carrubba V, Brucato V, Zoetelief W & Haagh G 2011 No-flow temperature in injection molding simulation *Journal of Applied Polymer Science* **119** 3382-92
- Massé H, Arquis É, Delaunay D, Quilliet S & Le Bot P H 2004 Heat transfer with mechanically driven thermal contact resistance at the polymer–mold interface in injection molding of polymers *International Journal of Heat and Mass Transfer* **47** 2015-27
- Matschuk M 2011 *All-Polymer Microfluidic Systems with integrated Nanostructures for Cell Handling* PHD DTU Nanotech
- Matschuk M, Bruus H & Larsen N B 2010 Nanostructures for all-polymer microfluidic systems *Microelectronic Engineering* **87** 1379-82
- Matschuk M & Larsen N 2013 Injection molding of high aspect ratio sub-100 nm nanostructures *J. Micromech. Microeng.* **23** 025003
- Matteucci M, Christiansen T L, Tanzi S, Østergaard P F, Larsen S T & Taboryski R 2013 Fabrication and characterization of injection molded multi level nano and microfluidic systems *Microelectronic Engineering* **111** 294-8
- Mezger T G 2014 *The Rheology Handbook* Hannover *Vincentz Network*
- Michaeli W, Heßner S, Klaiber F & Forster J 2007 Geometrical Accuracy and Optical Performance of Injection Moulded and Injection-compression Moulded Plastic Parts *CIRP Annals - Manufacturing Technology* **56** 545-8
- Michaeli W & Klaiber F 2010 Urformen und Funktionalisieren in einem Schritt *Kunststoffe* **10** 217-22
- Michaeli W, Klaiber F & Scholz S. Investigations in Injection Moulding of Micro Structures and Microstructured Surfaces. Proceedings of the Fourth International Conference on Multi-Material Micro Manufacture (4M), 2008 Oxford. Elsevier.
- Moguedet M, Le Goff R, Namy P & Béreaux Y 2009 *Excerpt from the Proceedings of the COMSOL Conference 2009 Milan*
- Mosaddegh P & Angstadt D 2008 Micron and sub-micron feature replication of amorphous polymers at elevated mold temperature without externally applied pressure *J. Micromech. Microeng.* **18** 035036
- Nagato K 2014 Injection Compression Molding of Replica Molds for Nanoimprint Lithography *Polymers* **6** 604
- Nagato K, Hamaguchi T & Nakao M 2011 Injection compression molding of high-aspect-ratio nanostructures *Journal of Vacuum Science & Technology B* **29** 06FG10-1-4
- Nguyen-Chung T, Jüttner G, Pham T, Mennig G & Gehde M 2008 The importance of precise boundary conditions for the simulation of micro-injection molding *Journal of Plastics Technology* **4** 1-25
- Padeste C, Bellini S, Siewert D & Schift H 2014 Anti-sticking layers for nickel-based nanoreplication tools *Microelectronic Engineering* **123** 23-7
- Padeste C, Özçelik H, Ziegler J, Schleunitz A, Bednarzik M, Yücel D & Hasırcı V 2011 Replication of high aspect ratio pillar array structures in biocompatible polymers for tissue engineering applications *Microelectronic Engineering* **88** 1836-9
- Pahl M, Gleißle W & Laun H M 1991 *Praktische Rheologie der Kunststoffe und Elastomere* *VDI-Verlag*
- Park K, Sohn D-H & Cho K-H 2010 Eliminating weldlines of an injection-molded part with the aid of high-frequency induction heating *Journal of Mechanical Science and Technology* **24** 149-52

- Paul P C, Knoll A W, Holzner F, Despont M & Duerig U 2011 Rapid turnaround scanning probe nanolithography *Nanotechnology* **22**, 275-306
- Pedersen R H, Xu Q, Stormonth-Darling J M & Gadegaard N 2015 Strategies for High Quality Injection Moulding of Polymer Nanopillars *Macromolecular Materials and Engineering* **300** 172-80
- Peskin C S 1977 Numerical analysis of blood flow in the heart *Journal of Computational Physics* **25** 220-52
- Piotter V, Mueller K, Plewa K, Ruprecht R & Hausselt J 2002 Performance and simulation of thermoplastic micro injection molding *Microsystem Technologies* **8** 387-90
- Pranov H, Rasmussen H K, Larsen N B & Gadegaard N 2006 On the injection molding of nanostructured polymer surfaces *Polymer Engineering & Science* **46** 160-71
- Prater K, Dukwen J, Scharf T, Herzig H P & Hermerschmidt A 2014 Surface Micro-Structuring of Glassy Carbon for Precision Glass molding of Diffractive Optical Elements *Current Developments in Lens Design and Optical Engineering Xv* **9192**
- Prater K, Dukwen J, Scharf T, Herzig H P, Ploeger S & Hermerschmidt A 2015 Multilevel Micro-Structuring of Glassy Carbon for Precision Glass Molding of Diffractive Optical Elements *Advanced Fabrication Technologies for Micro/Nano Optics and Photonics Viii* **9374**
- Ragone D V 1995 Thermodynamics of Materials New York *Wiley*
- Rohde M, Derdouri A & Kamal M R 2009 Micro Replication by Injection-Compression Molding *International Polymer Processing* **24** 288-97
- Rosenbaum E E & Hatzikiriakos S G 1997 Wall slip in the capillary flow of molten polymers subject to viscous heating *AIChE Journal* **43** 598-608
- Rytka C 2009 Development of a production and quality control method for micro- and nano-structured parts exemplary for microfluidic devices in transparent polyamides *Master Thesis*
- Rytka C, Kristiansen P M & Neyer A 2015 Iso- and variothermal injection compression molding of polymer micro- and nanostructures for optical and medical applications *J. Micromech. Microeng.* **25** 065008
- Rytka C, Lungershausen J, Kristiansen P M & Neyer A 2016a 3D Filling simulation of micro- and nanostructures in comparison to iso- and variothermal injection moulding trials *J. Micromech. Microeng.* **26** 065018
- Rytka C, Opara N, Andersen N, Kristiansen P M & Neyer A 2016b On The Role of Wetting, Structure Width and Flow Characteristics in Polymer Replication on Micro- and Nanoscale *Macromolecular Materials and Engineering* **301** 597-609
- Saarikoski I, Suvanto M & Pakkanen T A 2009 Modification of polycarbonate surface properties by nano-, micro-, and hierarchical micro-nanostructuring *Applied Surface Science* **255** 9000-5
- Sade W, Proença R T, Moura T D D O & Branco J R T 2011 Electroless Ni-P Coatings: Preparation and Evaluation of Fracture Toughness and Scratch Hardness *ISRN Materials Science* **2011** 6
- Schift H 2015 Nanoimprint lithography: 2D or not 2D? A review *Applied Physics A* **121** 1-21
- Schift H, David C, Gabriel M, Gobrecht J, Heyderman L J, Kaiser W, Köppel S & Scandella L 2000a Nanoreplication in polymers using hot embossing and injection molding *Microelectronic Engineering* **53** 171-4
- Schift H, David C, Gobrecht J, D' Amore A, Simoneta D, Kaiser W & Gabriel M 2000b Quantitative analysis of the molding of nanostructures *Journal of Vacuum Science & Technology B* **18** 3564-8
- Senn T, Esquivel J P, Lörger M, Sabaté N & Löchel B 2010 Replica molding for multilevel micro-/nanostructure replication *Journal of Micromechanics and Microengineering* **20** 115012
- Shahsavan H, Arunbabu D & Zhao B 2012 Biomimetic Modification of Polymeric Surfaces: A Promising Pathway for Tuning of Wetting and Adhesion *Macromolecular Materials and Engineering* **297** 743-60
- Shen Y-K, Chang C-Y, Shen Y-S, Hsu S-C & Wu M-W 2008 Analysis for microstructure of microlens arrays on micro-injection molding by numerical simulation *International Communications in Heat and Mass Transfer* **35** 723-7

- Solak H H, Dais C & Clube F 2011 Displacement Talbot lithography: a new method for high-resolution patterning of large areas *Opt Express* **19** 10686-91
- Sorgato M & Lucchetta G 2015 The evaluation of vacuum venting and variotherm process for improving the replication by injection molding of high aspect ratio micro features for biomedical application *AIP Conference Proceedings* **1664** 110008 (5 pp.)
- Steindorfer M A, Schmidt V, Beleggratis M, Stadlober B & Krenn J R 2012 Detailed simulation of structural color generation inspired by the Morpho butterfly *Optics Express* **20** 21485-94
- Stormonth-Darling J M 2013 *Fabrication of difficult nanostructures by injection moulding* PHD University of Glasgow
- Stormonth-Darling J M & Gadegaard N 2012 Injection Moulding Difficult Nanopatterns with Hybrid Polymer Inlays *Macromol. Mater. Eng.* **297** 1075-80
- Stormonth-Darling J M, Pedersen R H, How C & Gadegaard N 2014 Injection moulding of ultra high aspect ratio nanostructures using coated polymer tooling *Journal of Micromechanics and Microengineering* **24** 075019
- Stricker M, Pillwein G & Giessauf J 2009 Focus on Precision. Injection moulding optical components *Kunststoffe* **4** 30-4
- Sun C-C, Lee S-C, Hwang W-C, Hwang J-S, Tang I-T & Fu Y-S 2006 Surface Free Energy of Alloy Nitride Coatings Deposited Using Closed Field Unbalanced Magnetron Sputter Ion Plating *Materials Transactions* **47** 2533 to 9
- Suzuki H, Takayama T & Ito H 2012 Replication behavior for micro surface features with high aspect ratio and structure development in injection compression molding *International Journal of Modern Physics: Conference Series* **06** 563-9
- Tawfick S, De Volder M, Copic D, Park S J, Oliver C R, Polsen E S, Roberts M J & Hart A J 2012 Engineering of micro- and nanostructured surfaces with anisotropic geometries and properties *Adv Mater* **24** 1628-74
- Temiz Y, Lovchik R D, Kaigala G V & Delamarche E 2015 Lab-on-a-chip devices: How to close and plug the lab? *Microelectronic Engineering* **132** 156-75
- Tengler F-C, Jakubowsky M & Neyer A 2014 High transparent light guiding plate for single-sided light emission *Microelectronic Engineering* **119** 174-7
- Théry M 2010 Micropatterning as a tool to decipher cell morphogenesis and functions *Journal of Cell Science* **123** 4201-13
- Tofteberg T & Andreassen E 2008 Injection Moulding of Microfeatured parts *Proceedings of the Polymer Processing Society* **24**
- Tofteberg T R, Amédro H, Grytten F & Andreassen E 2010 Effects of Injection Molding Holding Pressure on the Replication of Surface Microfeatures *International Polymer Processing* **25** 236-41
- Tofteberg T R & Andreassen E 2010 Multiscale Simulation of Injection Molding of Parts with Low Aspect Ratio Microfeatures *International Polymer Processing* **25** 63-74
- Trojer M A, Mohamed A & Eastoe J 2013 A highly hydrophobic anionic surfactant at oil-water, water-polymer and oil-polymer interfaces: Implications for spreading coefficients, polymer interactions and microencapsulation via internal phase separation *Colloids and Surfaces a-Physicochemical and Engineering Aspects* **436** 1048-59
- Urquhart J M & Brown C S 2004 The Effect of Uncertainty in Heat Transfer Data in The Simulation of Polymer Processing *NPL Report DEPC-MPR* **001**
- Urwyler P, Pascual A, Kristiansen P M, Gobrecht J, Mueller B & Schift H 2013 Mechanical and Chemical Stability of Injection-Molded Microcantilevers Used for Sensing *Journal of Applied Polymer Science* **127** 2363-70
- Utoko P, Persson F, Kristensen A & Larsen N 2011 Injection molded nanofluidic chips: Fabrication method and functional tests using single-molecule DNA experiments *Lab on a Chip* **11** 303-8

- Wang S Q 1990 Shear induced deformation of polymers - calculation of radii of gyration *Journal of Chemical Physics* **92** 7618-24
- Wenzel R N 1936 Resistance of solid surfaces to wetting by water *Industrial and Engineering Chemistry* **28** 988-94
- Wu C H & Chen W S 2006 Injection molding and injection compression molding of three-beam grating of DVD pickup lens *Sensors and Actuators a-Physical* **125** 367-75
- Wulf M, Michel S, Jenschke W, Uhlmann P & Grundke K 1999 A new method for the simultaneous determination of surface tension and density of polymer melts *Physical Chemistry Chemical Physics* **1** 3899-903
- Xie L, Shen L & Jiang B 2011 Modelling and Simulation for Micro Injection Molding Process, Computational Fluid Dynamics Technologies and Applications, Prof. Igor Minin (Ed.) Croatia, Rijeka *Intech*
- Xu G, Yu L, Lee L J & Koelling K W 2005 Experimental and numerical studies of injection molding with microfeatures *Polymer Engineering & Science* **45** 866-75
- Yang D, Xu Z, Liu C & Wang L 2010 Experimental study on the surface characteristics of polymer melts *Colloids and Surfaces A: Physicochemical and Engineering Aspects* **367** 174-80
- Yao D, Chen S-C & Kim B H 2008 Rapid Thermal Cycling of Injection Molds: An Overview on Technical Approaches and Applications *Advances in Polymer Technology* **27** 233-55
- Yao D & Kim B 2005 Scaling Issues in Miniaturization of Injection Molded Parts *Journal of Manufacturing Science and Engineering* **126** 733-9
- Yao D K, B. 2002 Simulation of the filling process in micro channels for polymeric materials *J. Micromech. Microeng.* **12** 604-10
- Yoo Y E, Kim T H, Choi D S, Hyun S M, Lee H J, Lee K H, Kim S K, Kim B H, Seo Y H, Lee H G & Lee J S 2009 Injection molding of a nanostructured plate and measurement of its surface properties *Current Applied Physics* **9** e12-e8
- Young W B 2005 Simulation of the filling process in molding components with micro channels *Microsystem Technologies* **11** 410-5
- Yu L, Lee L J & Koelling K W 2004 Flow and heat transfer simulation of injection molding with microstructures *Polymer Engineering & Science* **44** 1866-76
- Zhang E S, Wang Y S, Lv T, Li L, Cheng Z J & Liu Y Y 2015 Bio-inspired design of hierarchical PDMS microstructures with tunable adhesive superhydrophobicity *Nanoscale* **7** 6151-8
- Zhang N, Chu J S, Byrne C J, Browne D J & Gilchrist M D 2012 Replication of micro/nano-scale features by micro injection molding with a bulk metallic glass mold insert *Journal of Micromechanics and Microengineering* **22** 065019
- Zhiltsova T V, Oliveira M S A & Ferreira J A 2013 Integral approach for production of thermoplastics microparts by injection moulding *Journal of Materials Science* **48** 81-94
- Zhou Z P, Xu J M, Song X B & Yan D Y 1992 Calculation of the mean-square radius of gyration for polymer-chains with side-groups *European Polymer Journal* **28** 1339-43

12. LIST OF OWN PUBLICATIONS & CONFERENCE PRESENTATIONS

Peer-reviewed publications

1. Rytka C., Lungershausen J., Kristiansen P. M., Neyer A., 2016, 3D filling simulation of micro- and nanostructures in comparison to injection moulding trials *J. Micromech. Microeng.*, 26, 065018.
2. Rytka C., Opara N., Andersen N. K., Kristiansen P. M., Neyer A., 2016, On the role of wetting, structure width and flow characteristics in polymer replication on micro- and nanoscale, *Macromolecular Materials and Engineering.*, 301, 597–609.
3. Rother, M., Barmettler, J., Reichmuth, A., Araujo, J. V., Rytka, C., Glaied, O., Pieleles, U. & Bruns, N. 2015. Self-sealing and puncture resistant breathable membranes for water-evaporation applications. *Adv. Mater.*, 27, 6620-4 doi:10.1002/adma.201502761.
4. Rytka C., Kristiansen P. M., Neyer A., 2015, Iso- and variothermal injection compression moulding of polymer micro- and nanostructures for optical and medical applications. *J. Micromech. Microeng.*, 25, 065008.

Articles

1. Kristiansen P.M., Rytka C., Cheung M.J., Schiff H., Schleunitz A., Spreu C., Solak H., 2011, Kleinste Strukturen in der Massenfertigung abformen, *PlasticsNow!*, 20-21.

Conference presentations (talks)

1. Rytka C., Kristiansen P. M., Neyer A., 2015, Multi-scale 3D filling simulation of micro- and nanostructures in comparison to real injection moulding trials, *2nd int. conference on Polymer Replication on Nanoscale (PRN 2015)*, DTU, Denmark.
2. Gobrecht J., Kristiansen M., Rytka C., 2014, Functionalization of Polymer Surfaces by Micro- and Nanopatterns, *Micro Nanotechnologies in Materials and Processes for the European Polymer industry*, Fribourg, Switzerland
3. Rytka C., Kristiansen P. M., Neyer A., 2014, High-quality Replication of Micro- and Nanostructures with variothermal injection compression molding, roll and hot embossing, *3rd International Conference on Polymer Processing and Characterization (ICPPC 2014)*, Mahatma Gandhi University, India.
4. Rytka C., 2014, Manufacturing and replication technologies of functional micro- and nanostructures, *Innovative Surfaces Workshop on Antimicrobial Surfaces*, Berne, Switzerland
5. Rytka C., Kristiansen P. M., Neyer A., 2014, Mass replication of nanopatterns in polymers. *Swiss Nano Convention (SNC 2014)*, Windisch, Switzerland.
6. Rytka C., Kristiansen P. M., Neyer A., 2014, High-quality Replication of 3D-nanostructures with variothermal injection compression molding, *1st int. conference on Polymer Replication on Nanoscale (PRN 2014)*, DTU, Denmark.

Poster presentations

1. P.M. Kristiansen, J. Köser, J. Schmidli, C. Rytka, S. Neuhaus, H. Schiff, J. Gobrecht, "Enabling technologies for mass manufacturing of micro- and nanostructured polymer surfaces", *i-net Innovation Landscape Nano Event*, MuttENZ, Switzerland, September 9, 2015
2. J. Köser, U. Bruggisser, R. Holtz, C. Rytka, M. Grob, S. Neuhaus, S. Beck, P. M. Kristiansen, "Cell instructive micropatterns: effects and limitations", *Swiss Nanoscience Institute - Annual Meeting*, September 3-4, 2015, Lenzerheide, Switzerland
3. C. Rytka, U. Bruggisser, S. Aubry, P.M. Kristiansen, "Advanced processing technologies and novel tooling concepts for the industrialization of increasingly complex diagnostic devices", *NanoBioTech 2014*, Montreux, Switzerland, November 17-19, 2014
4. H. Schiff, P. Urwyler, C. Rytka, P.M. Kristiansen, "Filling of surface-structured microcavities in thermoplastic injection molding", *NNT 2013 - The 12th International Conference on Nanoimprint & Nanoprint Technology*, Barcelona, Spain, October 21-23, 2013
5. C. Rytka, U. Bruggisser, P. Krämer, S. Aubry, P.M. Kristiansen, H. Schiff, K. Vogelsang, J. Gobrecht, "Tooling concepts for replication of micro- and nanoscale topographies by injection molding", *NNT 2013 - The 12th International Conference on Nanoimprint & Nanoprint Technology*, Barcelona, Spain, October 21-23, 2013
6. C. Rytka, P. Krämer, H. Schiff, J. Gobrecht, P.M. Kristiansen, "Injection molding of micro- and nanostructures using non-metallic molds", *MNE2013 - 39th International Conference on Micro and Nano Engineering*, London, Great Britain, September 16-19, 2013
7. C. Rytka, M. Kristiansen, M. Altana, H. Solak, J. Gobrecht, "High Fidelity Mass Replication of Nanostructures", *Nanotech-date Nordwestschweiz*, Baden, Switzerland, March 29, 2011
8. C. Rytka, U. Bruggisser, M. Kristiansen, H. Solak, J. Gobrecht, "Process Effects on Tool Stability in Nano-Injection Molding", *MNE 2010*, Genova, Italy, September 19-22, 2010
9. P. Urwyler, V. di Chiara, P.M. Kristiansen, C. Rytka, J. Gobrecht, "Micro- and Nano-Injection Molding for Bioanalytical Applications", *10th Austrian Polymer Meeting and 2nd Joint Austrian-Slovenian Polymer Meeting*, Leoben, Austria, September 8-10, 2010
10. C. Rytka, H. Schiff, H. Solak, C. Hofmann, J. Gobrecht, "Nano Injection Moulding: Process and Quality Control", *NNT 2009*, San Jose, USA, November 11-13, 2009

13. CURRICULUM VITAE

Christian Rytka Albert-Gersbach Allee 1 79713 Bad Säckingen Deutschland	
Education	
1996 – 2001	Studies in Polymer Technology at University of Applied Science, Würzburg, Germany
2006 – 2009	Master studies in Micro and Nanotechnology at Nano-Netzwerk Bodensee-Region , graduated as M.Sc. Micro- and Nanotechnology
2012 – 2016	Doctoral Studies on Replication by Injection Moulding at TU Dortmund (Prof. Dr. A. Neyer, Prof. Dr. P.M. Kristiansen)
Employment	
2001 - 2004	Materials Engineer and Deputy Head of Materials Technology at Georg Fischer, Switzerland
2004 - 2009	Development Engineer in Application Technology and Deputy Head of Processing Department at Ems Chemie, Domat-Ems Switzerland
2009 - 2016	Senior Research Engineer at the Institute of Polymer Engineering (IKT) and the Institute of Polymer Nanotechnology (INKA) of the FHNW University of Applied Sciences and Arts Northwestern Switzerland, School of Engineering, Windisch, Switzerland
2016 - present	Group leader polymer processing at the Institute of Polymer Engineering (IKT) and the Institute of Polymer Nanotechnology (INKA) of the FHNW University of Applied Sciences and Arts Northwestern Switzerland, School of Engineering, Windisch, Switzerland